UNIVERSITY OF GENOA

POLYTECHNIC SCHOOL

Dipartimento di ingegneria meccanica, energetica, gestionale e dei trasporti (DIME)

PhD Thesis
XXXI COURSE

"Fuel cell hybrid systems, dynamics and surge analysis"

Supervisor:
Chiar.mo Prof. Ing. Mario Luigi Ferrari

Co-Supervisor:
Chiar.mo Prof. Ing. Alberto Traverso

Candidate:

Alessio Abrassi

Year 2018

UNIVERSITÀ DEGLI STUDI DI GENOVA

SCUOLA POLITECNICA

Dipartimento di ingegneria meccanica, energetica, gestionale e dei trasporti (DIME)

Tesi di dottorato

DOTTORATO DI RICERCA IN INGEGNERIA DELLE MACCHINE E DEI SISTEMI PER L'ENERGIA, L'AMBIENTE E I TRASPORTI

CURRICULUM: INGEGNERIA DELLE MACCHINE E DEI SISTEMI PER L'ENERGIA, L'AMBIENTE E LA PROPULSIONE
XXXI CICLO

"Fuel cell hybrid systems, dynamics and surge analysis"

Supervisore:
Chiar.mo Prof. Ing. Mario Luigi Ferrari

Co-Supervisore:
Chiar.mo Prof. Ing. Alberto Traverso

Candidato:

Alessio Abrassi

Year 2018

Contents

Nomenclature

A	area/equivalent area	[m^2]
B	Greitzer's B parameter	[-]
C	source term for compressor	[Pa]
c_p	specific heat at constant pressure	[J/kgK]
c_v	specific heat at constant volume	[J/kgK]
Cv	valve flow coefficient	[-]
ER	turbine expansion ratio	[-]
F	source term for throttle momentum equation	[Pa]
FO	valve fractional opening	[-]
G	Greitzer's G parameter	[-]
h	enthalpy	[J/kg]
J	rotor mechanical inertia	[kgm^2]
k	specific heat ratio	[-]
kp	surge margin	[-]
K_p	controller proportional gain	[-]
L	length/equivalent length	[m]
LHV	lower heating value	[J/kgK]
$\dot{m}$	mass flow rate	[kg/s]
M	mass	[kg]
N	rotational speed	[rpm]
n	rotational speed	[rps]
P	power	[W]
p	pressure	[Pa]
PR	compressor pressure ratio	[-]
r	radius	[m]
R	valve rangeability	[-]
t	time	[s]
T	temperature	[K]
T_d	controller derivative time	[s]
TIT	Turbine inlet temperature	[K]
T_r	controller reset time	[s]
U	tangential speed of the impeller	[m/s]
V	volume	[m^3]
β	compressor pressure ratio	[-]
Δp	pressure difference	[Pa]
η	efficiency	[-]
ϕ	flow coefficient	[-]
σ	slip factor	[-]
τ	power coefficient/ torque	[-] [Nm]
ψ	work coefficient	[-]
ω	angular velocity	[rad/s]
Ω	volume versus mass flow ratio	[m^3/kgs^{-1}]

Subscripts

0	reference/null flow condition
01	inlet stagnation
02	outlet stagnation
2	compressor impeller exit
2s	static outlet condition
a	air
c/compr	compressor
comb	combustion/combustor
d.p.	design point
dim	dimensional
gen	generator
f	fuel
FO	fractional opening
in	inlet
loss	losses
max	maximum
meas	measured
out	outlet
p	plenum
red	reduced
ref	referred
T	throttle

turb	turbine

Acronyms

APU	Auxiliary Power Unit
ESD	Emergency Shut Down
FFT	Fast Fourier Transform
Hyper	Hybrid Performance Project
MGT	Micro Gas Turbine
m.s.t.	maximum slope tangent
PI	Proportional Integral
PID	Proportional Integral Derivative
SISO	Single Input Single Output
SOFC	Solid Oxide Fuel Cell
T RIG1	Test Rig 1
TPG	Thermochemical Power Group

Acknowledgments

I would like to thank all the people who accompanied me on this journey which lasted three years, I would like to remember here the Hyper guys who hosted me in Morgantown for two exciting months, all the DLR staff who welcomed me for three pleasant ones in Stuttgart, but above all the people who belong and collaborate with the research group that has made me grow professionally and personally, the Thermochemical Power Group, TPG.

I take this opportunity to thank two of the most deserving degree candidates with whom I had the pleasure to collaborate during these three years, Marco Enaudi from University of Genoa, Italy and Robin Ipek from Mälardalen University who hardly have been working on this topic with me.

It is important to underline that it is usually particularly difficult to obtain sensitive information from any industrial manufacturer, for this reason we thank the microturbine division of Ansaldo Energia and Garrett Advancing Motion that during this study and previous collaborations showed great willingness to provide valuable data and information.

Last but absolutely not the least I thank my family who has always supported me and encouraged in decisions and paths taken throughout my life.

Thank you

1. Introduction

The improvement of energy system performance has led to the development of efficient dynamic compressors able to achieve high compression ratios, high flow rates of fluid and reduced weights. As it normally happens by nature, the higher is the desired performance the more difficult is to achieve it; in the case of dynamic compression, the need to reach increasingly higher compression ratios and larger operational flexibility involves the occurrence of unsteady phenomena such as rotating stall and surge. These two problematic phenomena characterize compressors with violent decrease of performance and severe damage to machines, consequently the topic has been object of several studies over the years. The intensity and behavior of surge are tightly connected to the amount of volumes coupled to the turbo machinery during its operation. For this reason, surge phenomenon is strongly felt in fuel cell gas turbine hybrid system applications, where, primarily the fuel cell, then all the other components (e.g. heat exchangers if present), auxiliaries and connections constitute the vast majority of the volume contained in the system.

Fuel cell-micro gas turbine hybrid systems (FC-MGTs) are very high efficiency power plants, they can reach beyond 60% efficiency level and are characterized by very low emissions. FC-MGTs are strongly coupled systems where the operating condition of the MGT impacts on the performance of the fuel cell stack and vice versa. For this and other reasons it is difficult to study, design [1] and define control strategies [2] able to avoid dangerous operating conditions for both components. Surge is one of the main problems that may affect such kind of systems because of the energy stored in the fuel cell volume, in particular during transient operations [3]. At present, hybrid systems are very costly, with the most expensive and fragile component being the fuel cell stack. For this reason, in the last few years emulators have been assembled for research and development purposes. In such a solution, the fuel cell is only emulated and it is not physically present, therefore the real behavior of the plant can be replicated avoiding the risk of failures into the stack.

A significant part of this work was possible thanks to the experience on the theme of hybrid systems accumulated over the years thanks to the creation and use of emulators. Two of the three hybrid system emulators on which information has been published in recent years have been the subject of study in this work, in fact, the modeling activity started from data and knowledge concerning the hybrid system emulator Hybrid Performance (Hyper) operated at NETL, West Virginia, USA, and the Ansaldo Turbec T100 based hybrid system emulator built at the Innovative Energy Systems laboratory of University of Genoa, Italy. These two plants are deeply presented in the dedicated sections in this work. Hybrid system emulators at NETL, UNIGE and DLR have contributed so far to solve many control and dynamic issues for hybrid systems. Apart from experimental know-how, they provided unprecedented opportunities for validation of system dynamic models. Steady-state simulation models and tools are widespread and are used mainly for determining the operating limits and the operating properties for planning and designing the plant

In this specific field of research, the European research project Bio-HyPP (Biogas-fired Combined Hybrid Heat & Power Plant) fits perfectly, the goal of the project is to realize the

Hybrid Power Plant concept as a reliable, cost-effective and fuel-flexible micro combined heat and power (CHP) system. The main objective of this project is to develop and realize a full-scale technology demonstrator of a Hybrid Power Plant in a lab environment suitable for gaseous sustainable biomass feedstock derived from fermentation processes. The foreseen fuel includes the products of the fermentation of agricultural residues, sewage sludge, food waste as well as mixtures of biogas and natural gas. The output of the demonstration system will be in between 15 and 30 kW of electrical power (kWe).

The main objective that the project proposes is the realization of the so-called demonstrators of both top efficiency and top economic layouts. Between the two system concepts there are many differences but the main is the type of turbomachinery considered; while in the first one the fuel cell is coupled to an MGT in the second case the turbine is replaced by a turbocharger derived from automotive application. Even if this difference in plant layout may seem minimal, it has significant repercussions on operating strategies, on the control system and on the performance of the system. Additionally, the plant layout of the top-economic layout designed during the Bio-HyPP project is shown in Figure 1, the emulator of this system that will be realized at the Innovative Energy Systems laboratory of the University of Genoa is introduced in 10. Appendix C.

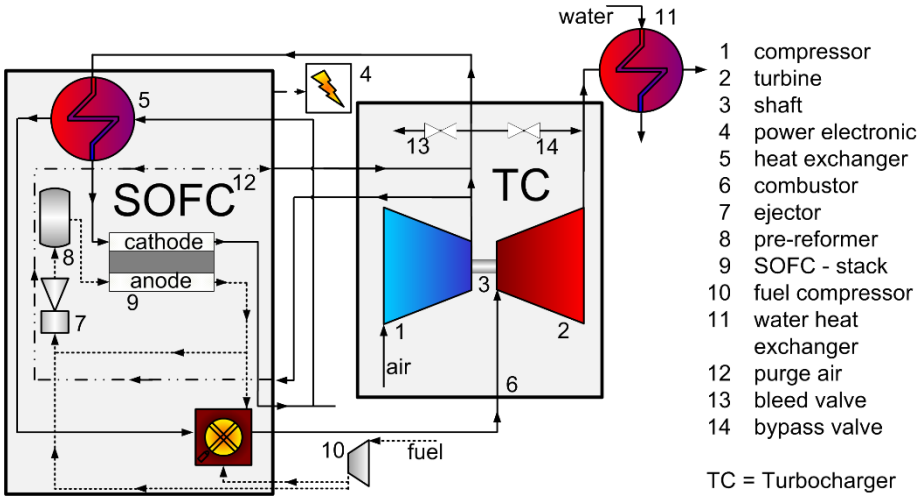

Figure 1: Block diagram of the top-economic layout planned in the Bio-HyPP project

From the dynamic modeling point of view, the surge topic implies different difficulties. The realization of a dynamic model able to correctly represent a real plant during the unstable operation caused by surge must take into account many aspects, for example: it must be robust and reliable enough to avoid to confuse purely mathematical instabilities, due to the incorrect resolution of the time varying equations, with the correct representation of the high frequency fluid-dynamic oscillations; on the other hand, it must be able to provide acceptable results in the shortest possible time, the modular nature that has been given to this tool must allow the realization of models based on complex systems that, once assembled, necessarily increase significantly the calculation effort; all the simulated components placed near the compressor must be able to handle very small mass flow rates and even negative flow values,

it is well known that compressors during deep surge oscillate between the positive and negative flow condition; moreover, where they are considered fundamental, interactions between flows with different temperatures must be taken into account. It is also essential to create a model that returns useful information for the understanding of the studied problem, it is therefore necessary to focus and choose the necessary parameters to correctly simulate the real plants and to avoid redundancy of information to make leaner the simulations. The models must be able to integrate as much information as possible, especially if derived from experimental test campaigns, for this reason the use of performance maps is used here to simulate both the compressor and the turbine. The availability and use of such information allow to begin from a good starting point to obtain results able to reflect the real operating conditions, as the data used derive from the direct experience obtained on the field and guarantee to the models a partial validation. An example of performance map is reported in Figure 2, typically this kind of performance map expresses the compressor pressure ratio (PR) as function of mass flow rate and rotational speed (N). The x-axis usually reports the compressor entry mass expressed as corrected (referred) flow or non-dimensional flow, while the y-axis is typically the pressure ratio or pressure rise across the compressor, the rotational speed is typically indicated as corrected rotational speed as well. The area that identifies the optimal operating of the compressor on this type of map is outlined by two lines whose identification allows to demarcate areas to avoid where a high risk of damage is present, these two lines are called surge line and choke line (or stonewall line). Each map is populated by the compressor operating curves at a constant speed, among which it is possible to identify the one which is, especially in stationary applications, the on-design curve. Moving away from the origin of the axes, the curves gradually identify increasing speed conditions.

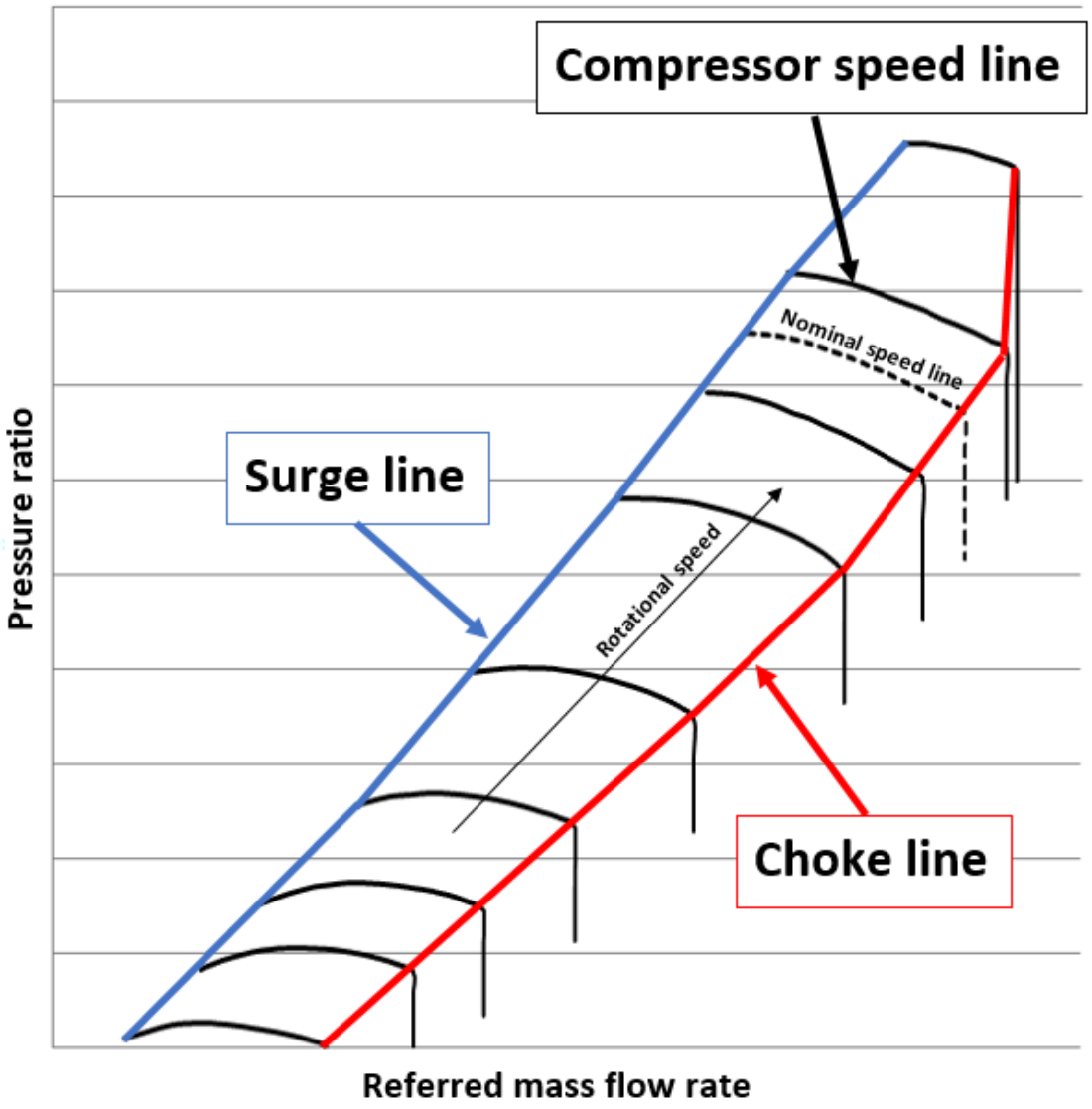

Figure 2: Example of compressor performance map, pressure ratio versus mass flow rate

As already introduced, Gas Turbine (GT) based Hybrid Systems (HS) consist of one or more turbomachines coupled with other technologies for energy production, such as high temperature Fuel Cells, where the operation of a single component strongly influences the behavior of the whole system. In contrast to a common Micro Gas Turbine (MGT) application [4] where the compressor and turbine are separated on the pressure side only by a combustor (and heat exchanger if recuperated), in a HS with pressurized Fuel Cell the dynamic behavior [5] of the rotating turbomachinery undergoes a radical change due to the coupling with a large volume between compressor discharge and turbine inlet. As briefly introduced before, a well-known example of a Hybrid System emulator plant is the Hybrid Performance (Hyper) facility that has been built at National Energy Technology Laboratory (NETL), West Virginia. The Hyper project utilizes a pressure vessel and a natural gas burner,

driven by real-time models, to simulate a 200kW to 700kW Solid Oxide Fuel Cell (SOFC) system coupled to a real 120kW MGT.

In this system configuration, compressor stability becomes a key constraint for operations, where maneuvers like load changes and speed ramps can have a significant impact. Compressor surge is a dangerous dynamic instability that may occur in compression systems for various reasons. Typically, the compressor surge margin parameter is used as an indicator to measure the distance between the current operating point and the surge line; the value of this quantity rapidly changes during transients and the way it changes is influenced by the size of the overall volume connected to the compressor. Moreover, the amount of volume affects the dynamic response of the system when an instability occurs, with effects on amplitude and frequency of the oscillations.

As it will be explained in chapter 2, according to [6] and [7], when the operating point crosses the surge line on the characteristic map of a compressor, and surge occurs, the overall annulus averaged mass flow varies with time, so that the entire compressor changes more or less in phase from being unstalled to stalled and back again. As soon as the pressure of the volume connected to the compressor is higher than compressor outlet pressure, the fluid tends to reverse or even flow back in the compressor. Eventually, the plenum pressure decreases to a value lower than compressor discharge and the flow reverses again.

Depending on the application, many different methods have been proposed to avoid compressor surge or to fully recover from it, a more detailed discussion of these topics is presented in chapter 5.2 Surge avoidance/recovery actions.

1.1. Thesis highlights

This thesis work is organized into three macro-chapters, each one is focused on a specific application. The descriptive organization follows the chronological order in which the case studies were addressed and follows the level of maturity of the research object of this program. Therefore, in the following chapters each single case study is presented and discussed separately. Before starting the description of the work conducted by the candidate along these years, two brief presentation are introduced to allow a better understanding of the topic and methodology at the base of the current research. Chapter 2 reports an introduction on the theme of the surge instability, which is then resumed by the discussions during each case study dissertation; while Chapter 3 is dedicated to the description of the work theorized by Greitzer in the 70s, on which current work lays its foundations.

The following list is thought to anticipate what are the main outcomes and learnings which will be encountered through the text. In this way the candidate wants to clearly summarize what can be considered as primary steps, contribution to the energy systems modeling research field and main outputs of this work:

- Mathematical descriptions for components development with integrations and improvements will be described application by application. Chapter 4.2, Chapter 5.3, Chapter 6.3.

- Description of the proposed steps followed by the methodologies used to extend compressor maps for surge simulation purposes. A mix of analytical and empirical methods will be suggested through this work. Chapter 4.4, Chapter 5.4 Chapter 6.2.

- A method for dynamic delays characterization of complex piping systems named τ-Flow approach have been proposed and applied to these studies. Chapter 4.3, Chapter 6.1.2.

- Parametric studies to investigate the effect of different parameters such as volume size, shaft inertia and equivalent lengths, on the surge cycles characteristics. Impacts of these characteristics will be analyzed in different control configurations where options are applicable. Chapter 4.6, Chapter 5.6.1, Chapter 5.6.2 Chapter 6.4.

- Simulation results, experimental comparison and validation will be presented at the end of each macro-chapter as completion of the analysis. Chapter 4.6, Chapter 5.6, Chapter 6.4, Chapter 6.5.

- The possibility to recover from a surge event acting on by pass valves will be also simulated and presented in the context of Hyper facility analysis. Chapter 5.6.3 and Chapter 5.6.4.

2. Compressor surge

Surge is an oscillation of the compressor flow that causes mass flow rate and pressure fluctuations, which combined they trace repetitive closed cycles on the compressor map. According to [6] and [7], when operating point overcomes the surge line on the characteristic map of compressor, and surge occurs, the overall annulus averaged mass flow varies with time, so that the entire compressor change more or less in phase from being unstalled to stalled and back again. As soon as the pressure of the volume connected to the compressor is higher than compressor outlet pressure, the fluid tends to reverse or even flow back in the compressor. Consequently, the plenum pressure will decrease, inlet pressure will increase and the flow reverses again.

Two types of surge are typically distinguishable, deep surge and mild surge. When Surge arises as violent to drag the operating point to the negative mass flow zone, it is called deep surge, Figure 3,. In the other hand, it may be very mild so that the operating point orbits in the positive mass flow rates domain, Figure 4. During some phases of the surge cycle, while the compressor is forced to operate at low mass flow, the flow may be transiently in rotating stall.

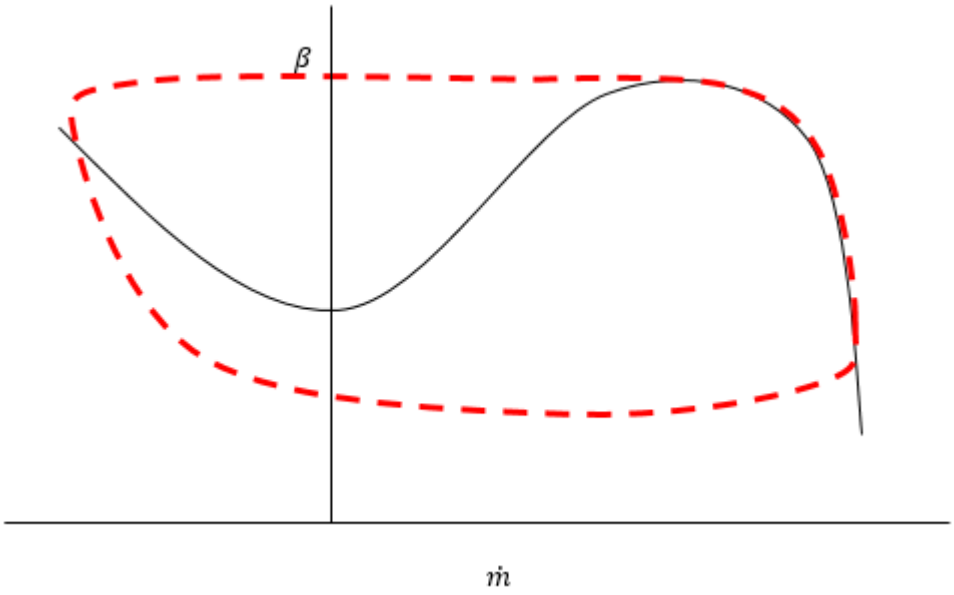

Figure 3: Example of deep surge cycle on compressor map

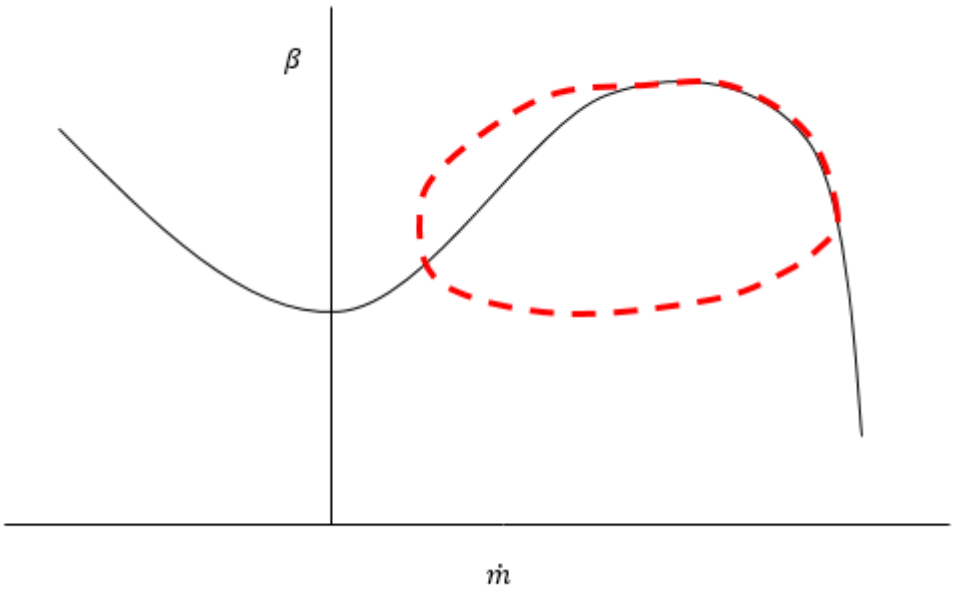

Figure 4: Example of mild surge cycle on compressor map

Both surge and rotating stall have a non-axisymmetric nature that brings to not balanced forces and torques, leading to vibration, blade rubbing and other damages.

The reason why this study is not limited in modeling just the compressor is linked to the fact that the way with which the compressor reaches the operating point at which the flow in the becomes unstable depends not only on the compressor map but also on system characteristics such as: the lengths of the ducts between compressor and turbine, the volumes, the throttle characteristic, turbine performance and control system reaction.

A clear difference between surge and rotating stall is based on dynamic operating matters. Because of the system hysteretic effects, if rotating stall occurs in any compressor sections, it is not possible to return in a not stalled condition simply increasing the flow rate decreasing the pressure drop downstream the compressor. However, if operating condition overcomes the surge line causing surge instability, this condition can be easier to recover acting on a discharge valve placed downstream to the compressor for example.

For this reason, one of the important problems associated with compressor stability is the determination of which of these two types of behavior will occur with a given axial flow compression system

3. Greitzer's modelling approach

This section reports the key steps of theory explained by Greitzer in [12]. This study, developed in 1976, reports a lumped model that predicts the response of a compression when the operating point changes its position from a steady state zone to an instable one and was undertaken to provide a more detailed look at the phenomenon of surge.

The compression system modelled by Greitzer is a simple test configuration and it is the starting point for this thesis; it consists of a compressor, a duct, volume and a throttle.

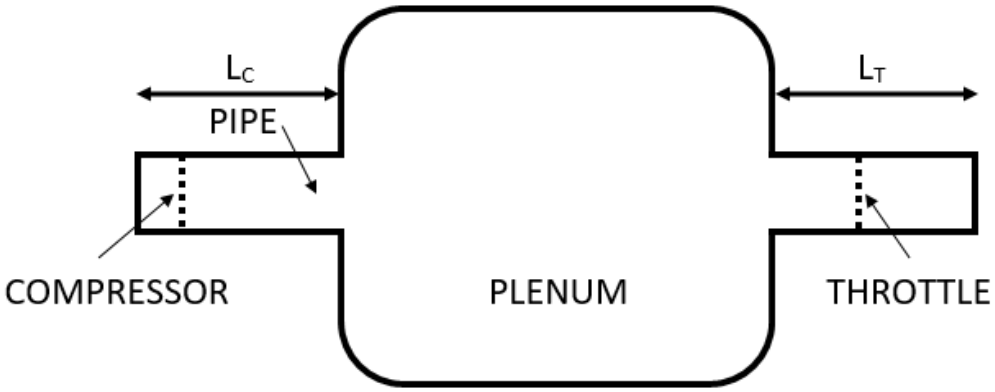

Figure 5: Example of the equivalent compression system used by Greitzer in [12]

All the kinetic energy of the oscillation is associated with the motion of the fluid in the compressor and throttle duct and the potential energy referred to the compression of the gas in the plenum.

Actuator disks and lengths of constant area pipe replace compressor, throttle and its ducting

Every single component of the compressor system is ruled by its equation of motion.

The rate of change of mass flow in the compressor duct can be related to the pressure difference across the duct and the pressure rise across the compressor, an analogous equation can be written to describe the flow in the throttle duct.

As regards to the plenum, Greitzer stated that, in this component, energy is present just in terms of potential energy so that velocities are negligible.

Another equation is introduced because the compressor does not respond quasi-steadily to change in mass flow but, when the stall limit line is reached, and the axisymmetric compressor flow field becomes unstable, there is a definite time lag τ between the onset of instability and the establishment of the developed rotating stall pattern. This time is equal to or longer than the order of several rotor revolution or equivalently the order of one or more revolution of a stall cell.

In these terms, a quasi-steady response is not adequate and Greitzer use a first order transient response to simulate this lag.

Becomes easier express these relations in a non-dimensionalized structure obtaining the set of equations here below:

$$\frac{d\dot{\tilde{m}}_c}{d\tilde{t}} = B\left(\tilde{C} - \Delta\tilde{p}\right) \quad \textbf{(1)}$$

$$\frac{d\dot{\tilde{m}}_T}{d\tilde{t}} = \left(\frac{B}{G}\right)\left(\Delta\tilde{p} - \tilde{F}\right) \quad \textbf{(2)}$$

$$\frac{d\Delta\tilde{p}}{dt} = \frac{1}{B}\left(\dot{\tilde{m}}_c - \dot{\tilde{m}}_T\right) \quad \textbf{(3)}$$

$$\frac{d\tilde{C}}{d\tilde{t}} = \left(\frac{1}{\tilde{\tau}}\right)\left(\tilde{C}_{ss} - \tilde{C}\right) \quad \textbf{(4)}$$

where:

$$B = \frac{U}{2\omega L_c} = \frac{U}{2a}\sqrt{\frac{V_p}{A_c L_c}} \quad \textbf{(5)}$$

$$G = \frac{L_T A_c}{L_c A_T} \quad \textbf{(6)}$$

$$\tau = \frac{N\ 2\pi\ r}{U} \quad \textbf{(7)}$$

$$\tilde{\tau} = \tau\omega = \left(\frac{\pi\ r}{L_C}\right)\left(\frac{N}{B}\right) \quad \textbf{(8)}$$

Equations (1), (2), (3) and (4) describe the dynamic of compression system using non-dimensional parameters.

Equation (7) says that the time lag in compressor response is proportional to constant N that is called rotor revolution where the value of N is usually taken from experimental data. As

for a given compressor the values N, R, and L_c are constant, the nondimentional time lag is proportional to B.

As typified, time variables are non-dimensionalized using the characteristic time $\frac{1}{\omega}$, where ω is Helmholtz frequency defined as below.

$$\omega = a\sqrt{\frac{A_c}{V_p L_c}} \qquad \textbf{(9)}$$

Greitzer uses Helmholtz frequency as a time scale to describe the phenomena because the proposed model is similar to the Helmholtz resonator 9.1, which is representative of the fluid dynamic oscillation of the model.

4. Modeling and validation of a free spool subject to compressor surge

Compressor surge is one of the main problems that may affect fuel cell gas turbine hybrid systems, because of the energy stored in the volume containing the high temperature pressurized fuel cell stack. The problem becomes even more crucial because in such kind of system, the fuel cell is the most sensitive and costly component that must be preserved by abrupt pressure changes.

To determine the behavior of a dynamic compressor in its whole range of operating conditions, a calculation model is developed in Matlab® Simulink using a modular approach similar to the one already used in TRANSEO, a software tool for transient and dynamic analysis of microturbine and fuel cell based-cycles [13].

The modeling procedure is derived from the Greitzer's 1976 nonlinear dynamic approach; the resulting T-RIG1 model predicts the transient response of a compression system and is able to simulate both normal and instable transient conditions. Several investigations have been done in order to characterize the impact of different parameters and configurations on the system response. The validation, in the frequency domain, is performed comparing calculations with experimental data measured from a dedicated test rig, where a small size turbocharger is operated in stable and unstable conditions.

In particular, the present work demonstrates the capability of the T-RIG1 model to simulate a free shaft turbocharger performance and instability, with the aim of carrying out the first step towards the development of feasible strategies for surge detection and recovery, applicable to turbocharger-based hybrid systems and then to the micro gas turbine-based ones.

As introduced This chapter is focused on the study of a model for turbocharger-based hybrid systems. The working principle is the same as for hybrid systems based on a MGT but, in this case, the hot exhaust gases coming from the fuel cell are directed to the turbine of a free spool turbocharger, which drives the compressor supplying air to the cathode side of the fuel cell. Many are the reasons in favor of such configuration. Figure 6 shows an example of turbocharger-based hybrid system layout (with SOFC emulator). More details on the final vessel designed by TPG for this type of emulator are reported in 9. Appendix .

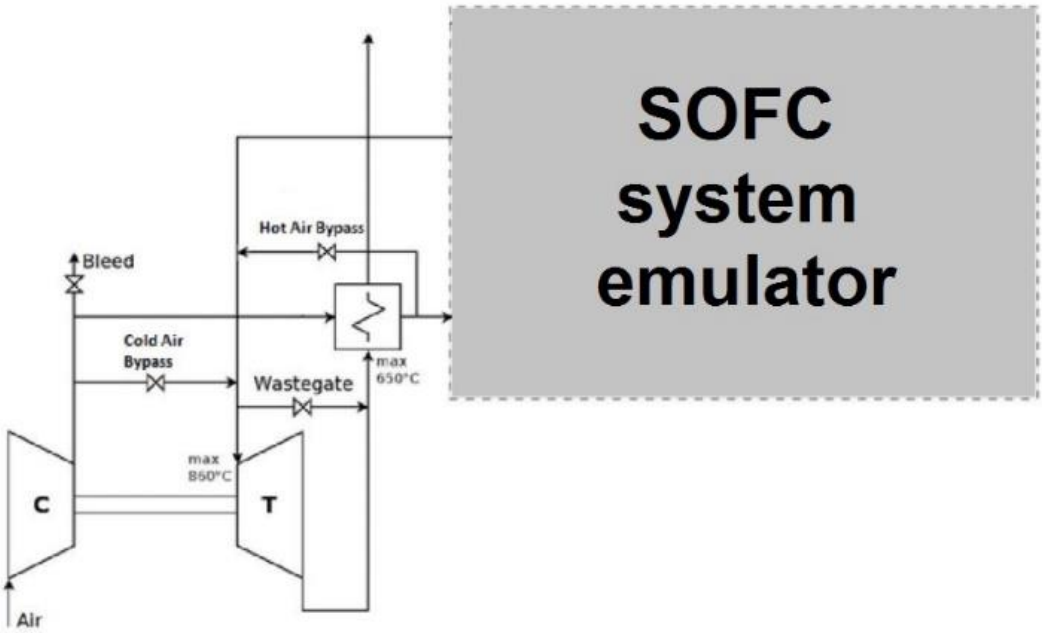

Figure 6: Turbocharger based hybrid system (if the fuel cell is not actually present, then it is SOFC emulator)

4.1. Test rig description and instrumentation

The modeling work is based on the new test rig assembled at the TPG Innovative energy system laboratory (IES lab) at the University campus of Savona. The T-RIG1 shown in Figure 7 is made up by a turbocharger operating in open loop (compressor discharge is not connected to turbine inlet), where a flow regulator feeds turbine combustor with compressed air. Hot compressed air, expanding into the turbine generates the necessary power to sustain the compression load. The turbocharger used in this study is a Garrett Advancing Motion prototype. It is a centrifugal compressor- centripetal turbine used for Passenger Vehicle (PV) automotive application. In the current layout, the compressor takes air from the ambient and sends it to a discharge valve utilized to modify the compressor load. Interconnecting pipes are located at compressor intake and compressor discharge. These elements impact on the system dynamics, therefore their dynamic characteristic must be carefully taken into account. In this paper, a method to reduce complex geometries through equivalent lengths and sections is proposed.

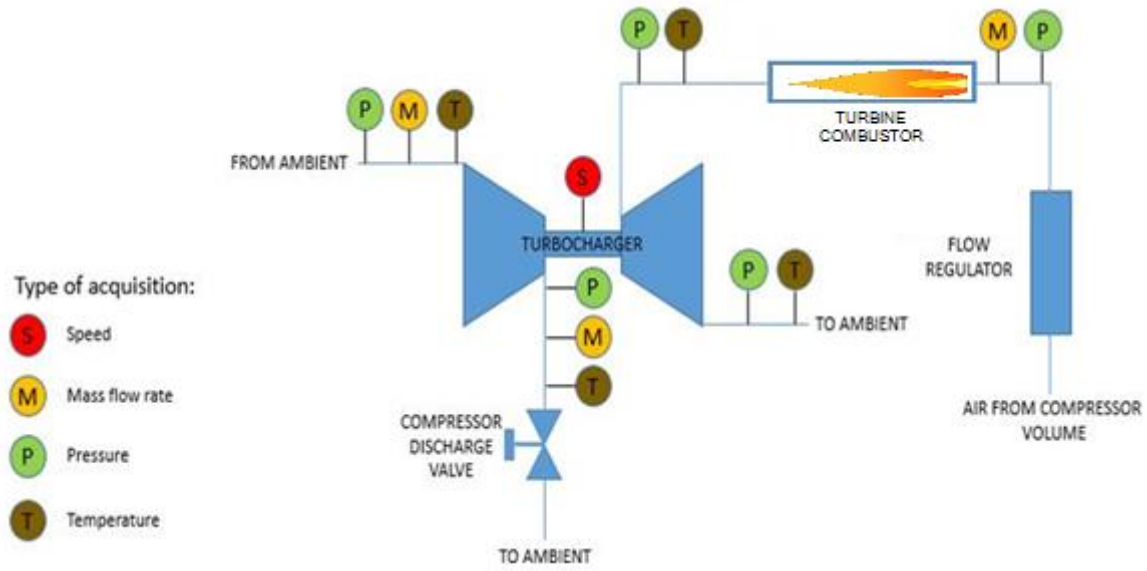

Figure 7: T-RIG1 layout

As shown by Figure 7, the test rig has been equipped with different sensors, probes and controllers in different positions of the plant. This is necessary to monitor and control the system during its operation. All the quantities such as pressures, mass flow rates and temperatures are acquired in real-time thanks to an acquisition system based on a CompactRIO hardware, an embedded industrial controller made by National Instruments for industrial control system that has been interfaced with a LabVIEW software. For the detailed description of the measurement and acquisition system please refer to 8. Appendix A.

4.2. T-RIG1 Model description

The complete real turbocharger test rig consists in a centrifugal compressor that takes fresh air from the ambient and it supplies compressed air to the following pipeline; these pipes connected to the discharge side of the compressor are also joint to a ball throttle at the end which is utilized to vary the pressure drop along the discharge line moving the compressor operating point on its map. The impeller of the compressor is directly connected to the shaft that is driven by a centripetal micro turbine operated in open cycle. This means that the combustion chamber is not directly fed by the centrifugal compressor of the machine, but an auxiliary external compressor feeds it. The T-RIG1 layout is reported in Figure 7.

During this work two different model layouts are modeled and studied. The first one is a simplified version of the test rig where only compressor, plenum and discharge valve are simulated. The second model instead simulates also shaft and turbine, it better represents the real system and permits to simulate the dynamics of a real turbocharger.

Both modelling approaches start from the work conducted by Greitzer in [7], [12].

Such papers describe a lumped model that well predicted the response of a compression system when the operating point changed its position from a steady-state zone to an instable one. The compression system modeled by Greitzer consisted of a compressor, a duct, a

volume and a throttle. These components can be found also in the T-RIG1 model, which also shares the following main assumptions:

- the kinetic energy of the fluid oscillation is associated with the motion of the air in the compressor and throttle duct and the potential energy referred to the compression of the gas in the plenum;
- actuator disks and lengths of constant area pipe replace compressor, throttle and their ducting;
- every single component of the compressor system is ruled by its equation of motion;
- the rate of change of mass flow in the compressor duct can be related to the pressure difference across the duct and the pressure rise across the compressor, and a similar equation can be used to describe the flow in the throttle duct;
- as regards to the plenum, Greitzer stated that, in this component, energy is present just in terms of potential energy so that velocities are negligible.

For the T-RIG1 model, the plenum represents the volume contained in the pipeline before and after compressor. The length of these pipes is considered in the compressor momentum equations as an equivalent length to correctly replicate the time flow delay of the entire line. Turbine receives as inputs mass flow, temperature, specific heat, gas constant and lower heating value information of the upstream flow returning expansion ratio, moreover it can calculate temperature, specific heat, gas constant at the outlet condition, efficiency and power.

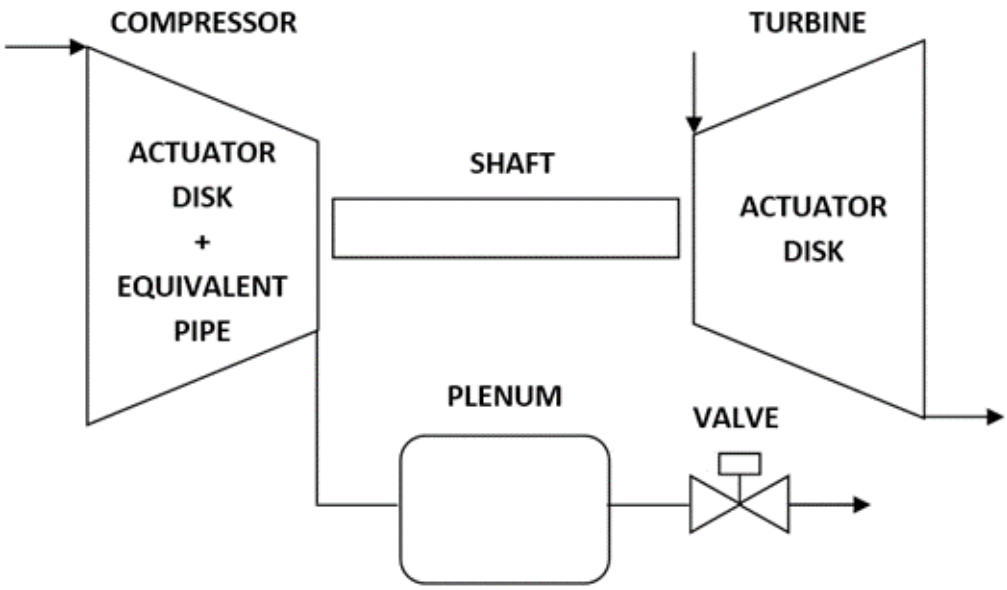

Figure 8: T-RIG1 model layout

T-RIG1 model has been developed in MATLAB-Simulink environment with a modular approach, each component has been built separately by including the corresponding code inside separated MATLAB functions.

4.2.1. Compressor

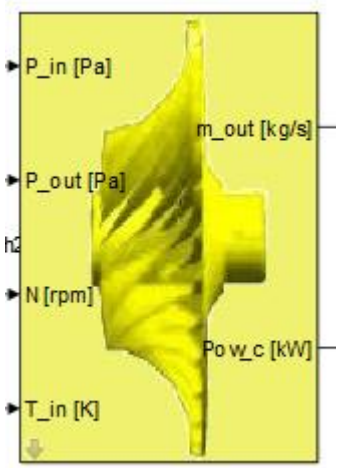

Figure 9: Compressor dynamic model developed in Simulink for T-RIG1

The compressor used in this study is a Garrett Advancing Motion prototype. It is a centrifugal compressor for automotive application. Main technical characteristics are reported in Table 1.

Table 1: Basic compressor technical data

Number of impeller blades	7
Trim	46
A/R	0.32
Radius	0.016 [m]
Speed Limit	325.8 [krpm]
Wheel Inertia	7.756E-07 [kg m^2]

According to [26], an actuator disk and a constant area pipe can properly replicate the dynamic behavior of a compressor: the first mimics the pressure rise due to the compressor while the second element considers the dynamics of the fluid through the compressor.

The differential equation that describes the fluid dynamics, Eq.(10), relates the rate of change of mass flow rate in the duct to the group C-ΔP. It means that as soon as a difference between C and ΔP is present, the equation returns a change in mass flow; if the difference is positive it will increase, otherwise it will decrease if negative. When these two terms assume equal values, there is no more change in mass flow rate and a steady-state condition is reached.

$$\frac{d\dot{m}_c}{dt} = (C - \Delta p)\frac{A_c}{L_c} \quad \textbf{(10)}$$

Where:

$\dot{m}_c$:	mass flow rate through compressor	[kg/s]
C :	pressure rise across the compressor	[Pa]
$\Delta p = p_p - p_1$:	pressure difference across the equivalent duct	[Pa]
A_c :	compressor section, area of the annulus at the intake of compressor (impeller eye)	[m^2]
L_c :	compressor effective length of equivalent duct	[m]

During the transient operation, the value of C is not constant, therefore its rate of change is defined adopting a simple, first order transient response model, Eq.(11).

$$\tau \frac{dC}{dt} = (C_{ss} - C) \quad \textbf{(11)}$$

Where:

C_{ss} :	is the new steady state pressure rise from compressor map	[Pa]
τ:	delay time, it depends on the rotational speed and the type of machine.	[s]

The compressor model contains a function able to read the machine performance maps and, thanks to an interpolation procedure, define the current steady-state pressure rise (C_{ss}).

Since efficiency maps are difficult to derive outside the normal operation range, a different approach, described in paragraph 4.3 is adopted to compute the absorbed power by the compressor; in practice, a power versus mass flow rate map has been created and implemented in the compressor model.

4.2.2. Plenum

Figure 10: Plenum dynamic model developed in Simulink for T-RIG1

Compressor discharge is connected to a plenum that represents the volume of the system, where fluid has no kinetic energy and the potential energy is associated with the gas pressure.

In this early configuration of the test rig, the volume contained in the pipe before compressor has been estimated in 0.0012 m^3 while discharge tube volume is 0.0038 m^3, for a total considered volume V_p equal to 0.005 m^3. The implemented continuity equation for the plenum is

$$\frac{dp_p}{dt} = (\dot{m}_c - \dot{m}_T)\frac{kP_p}{\rho V_p} \quad \textbf{(12)}$$

where:

dp_p/dt :rate of change of plenum pressure over the time

$\dot{m}_c$:	inlet mass flow (coming from compressor)	[kg/s]
$\dot{m}_T$:	outlet mass flow (going through the throttle)	[kg/s]
p_p :	instantaneous pressure inside the plenum	[Pa]
k :	specific heat ratio	
ρ :	flow density	[kg/m^3]
V_p :	plenum volume	[m^3]

4.2.3. Valve

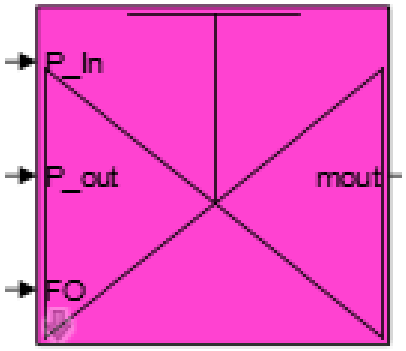

Figure 11: Valve dynamic model developed in Simulink for T-RIG1

Throttle valve is placed at compressor discharge pipeline and it is modeled by coupling an actuator disk and a constant area duct with equivalent length. Therefore, the set of equations for this component can be written as it follows:

$$\frac{d\dot{m}_T}{dt} = (\Delta p - Z)\frac{A_{T_{FO}}}{L_T} \quad \textbf{(13)}$$

$$Z = \frac{\dot{m}_T^2}{2\rho A_{T_{FO}}^2} \quad \textbf{(14)}$$

$$A_{T_{FO}} = A_T\, FO \quad \textbf{(15)}$$

Where:

$\dot{m}_T$:	throttle mass flow	[kg/s]
Δp :	pressure difference across the equivalent duct	[Pa]
Z :	throttle pressure drop	[Pa]
L_T :	equivalent throttle duct length	[m]
ρ :	fluid density	[kg/m^3]
A_T :	flow-through throttle area	[m^2]
FO :	valve fractional opening	[-]

For a given turbine inlet condition, the discharge valve is used to modify the compression system operating point. For example, by decreasing the valve fractional opening the

compressor operates at lower mass flow values, thus reducing its surge margin. The throttle valve proposed in this study presents a quite linear flow characteristic.

4.2.4. Shaft

Figure 12: Shaft dynamic model developed in Simulink for T-RIG1

Since in T-RIG1 model the turbine drives directly the compressor and no generator is present, a shaft component able to compute the balance of power between turbine and compressor is required:

$$\frac{d\omega^2}{dt} = \frac{2}{J}\left(Pow_{turb} - Pow_{compr} - Pow_{loss}\right) \quad \textbf{(16)}$$

where:

ω :	rotor angular velocity	[rad/s]
J :	rotor mechanical inertia	[kgm^2]
Pow_{turb} :	turbine power	[W]
Pow_{compr} :	compressor power	[W]
Pow_{loss} :	losses	[W]

Rotor mechanical inertia given by the turbocharger supplier has been validated with experimental tests, applying a linear change in air mass flow rate through turbine from one stable set point to another one. This made the compression system react with an increasing velocity ramp that was compared to the simulated one: by comparing the measured and simulated shaft accelerations, the rotor mechanical inertia could be inferred.

Moreover, an investigation on the impact of different rotor mechanical inertias has been performed, results have been then compared with experimental data. The tested different mechanical inertias are:

- J_{shaft} = 1.5x5.2x10E-08 [kgm^2]
- J_{shaft} = 2x5.2x10E-08 [kgm^2]

- J_{shaft} = 5x5.2x10E-08 [kgm^2]
- J_{shaft} = 10x5.2x10E-08 [kgm^2]

During these simulations a linear change in air mass flow rate through turbine disturbs the system's equilibrium, the compression system then reacts with a velocity ramp.

Figure 13 shows the calculated velocity ramps carried out with the Simulink model using the rotor mechanical inertias listed before. Basically, the higher the inertia and the longer it takes to complete the transient.

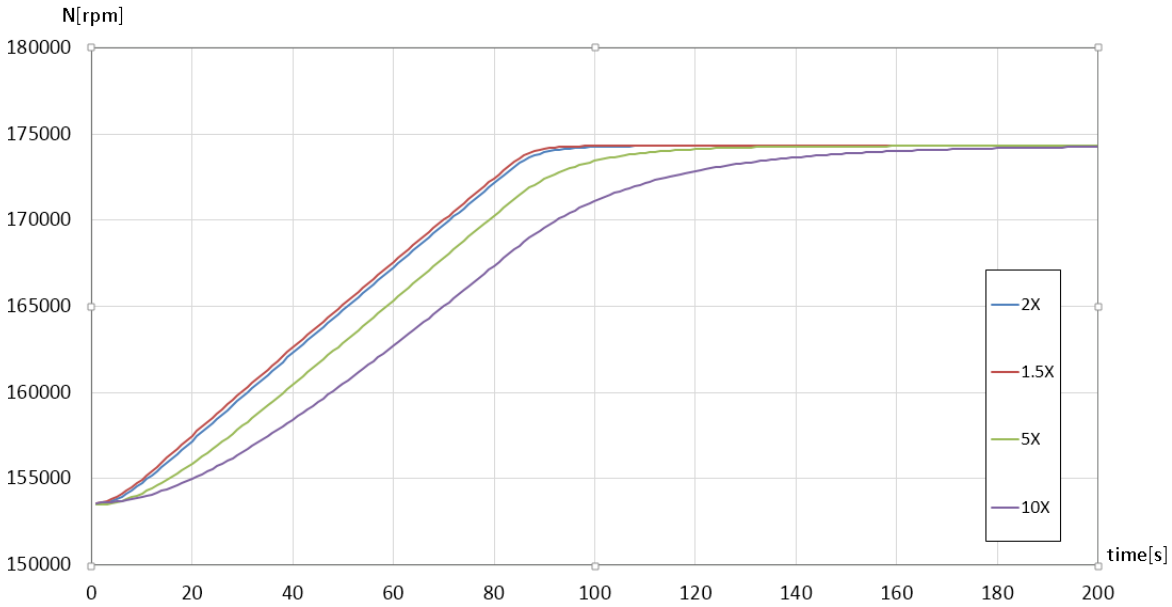

Figure 13: Velocity ramps with different values of rotor mechanical inertia

Here below is reported only the comparison between the verified simulation and experimental data. The initial stable condition for the test is defined as follows:

- m_t = 21.99 g/s
- FO = 1
- Turbine Inlet Temperature (TIT) = 800 °C = 1073.15 K
- J_{shaft} = 5,2 x 10^{-8} kg m^2
- N ~ 183000 rpm

shows the rise in turbine inlet mass flow air that disturbs the initial state and the resulting system's acceleration.

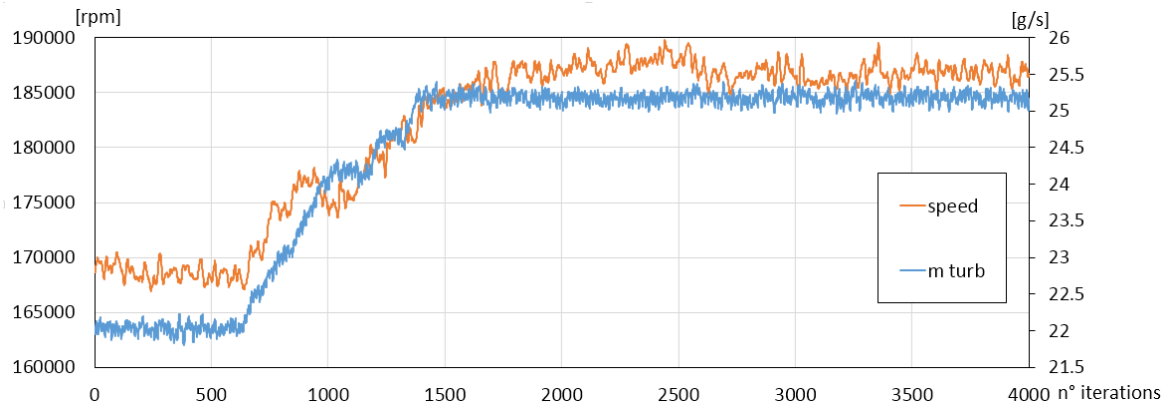

Figure 14: Reference acceleration trend obtained from experiment

As seen in figure, turbine elaborates an increasing mass flow rate (blue line) from 21.99 g/s to 25.127 g/s, the entire rap requires 83.1s, while the orange trend represents the system's response in terms of rotational speed. The rise in mechanical power produced by the turbine, drives compressor to a higher speed which absorbs more energy restoring a new stable operating point.

Figure 15 depicts TIT trend and velocity ramp. Clearly, turbine inlet temperature has a-reduced variability range near 800 °C, this fact allows to assume it constant along the entire test.

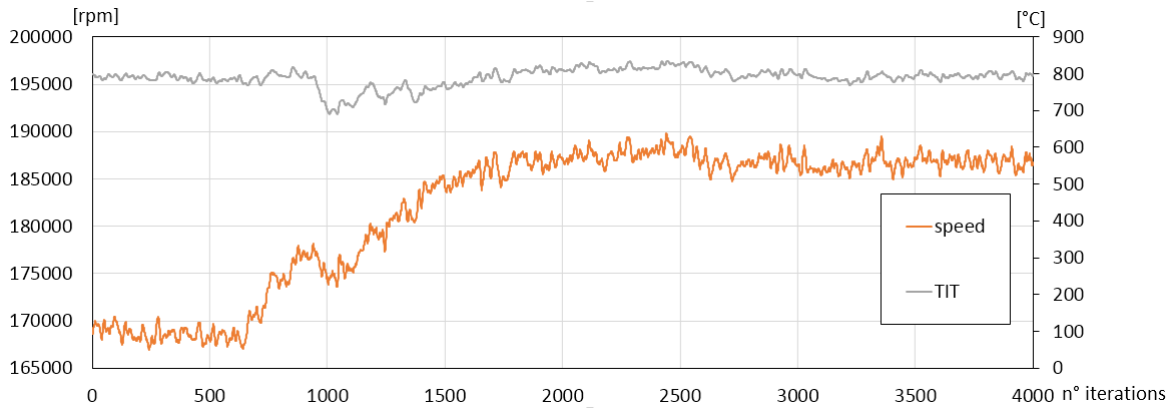

Figure 15: TIT transient during experiment

The T-RIG1 model is equipped with an input block from which the turbine inlet condition can be changed, in this case the same type of mass flow rate ramp as for the test is passed to the modelled system. Test returns as output the velocity ramp Figure 16, compared with the measured system's response, validate the used rotor mechanical inertia.

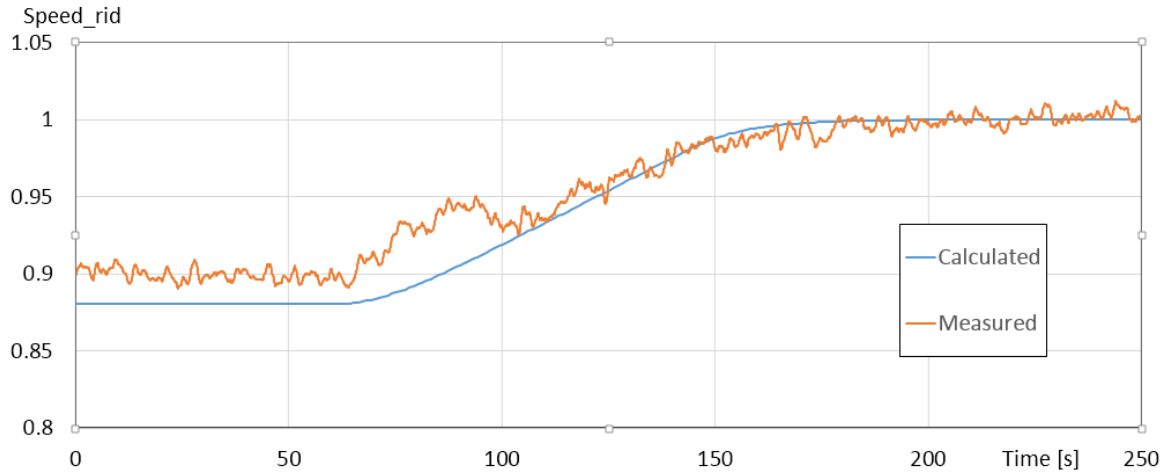

Figure 16: Comparison between simulated rotational speed and acquired signal from experiment

This and other tests have shown the good accuracy reached by the T-RIG1 model in performing dynamic simulations. By considering the level of detail of the model, Figure 16 also shows that the model has a good level of prediction of the steady state conditions compared to the real system. This is clear especially closer to the nominal condition (right side of the plot) where the error between simulated and real data is minimized.

4.2.5. Turbine

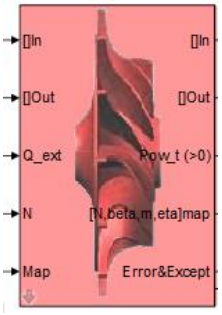

Figure 17: Turbine model developed in Simulink for T-RIG1

A centripetal turbine is coupled with the compressor in the current turbocharger layout. Table 2 lists the main available turbine data used in this study.

Table 2: Basic turbine technical data

Number of impeller blades	12
Outlet blade radius	0.015 [m]

The turbine is modeled as an actuator disk where operating steady state maps are used for expansion ratio and efficiency. The model performs an interpolation of maps in order to obtain the actual pressure ratio by knowing the mass flow rate and rotational speed.

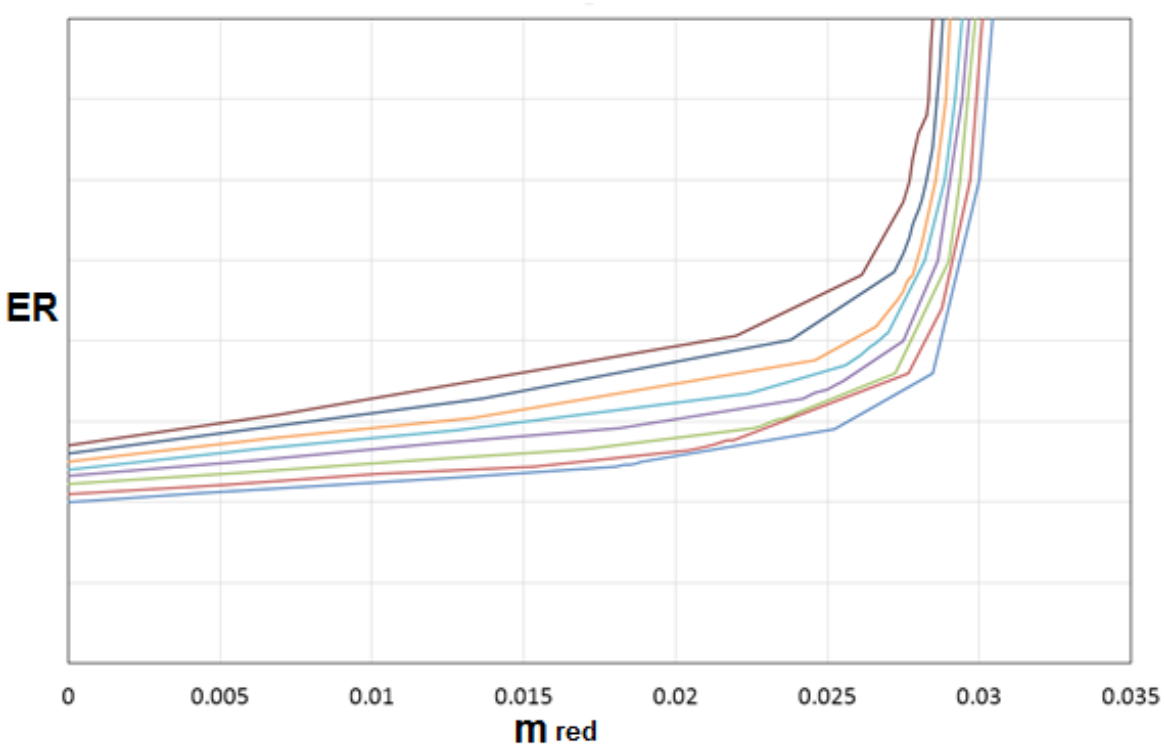

Figure 18: Turbine performance map 1, expansion ratio versus mass flow

Afterwards, an iteration is performed to derive the efficiency from an additional map by using the expansion ratio previously obtained and the rotational speed. This is necessary to obtain the power produced by the turbine, which represents an input for the shaft.

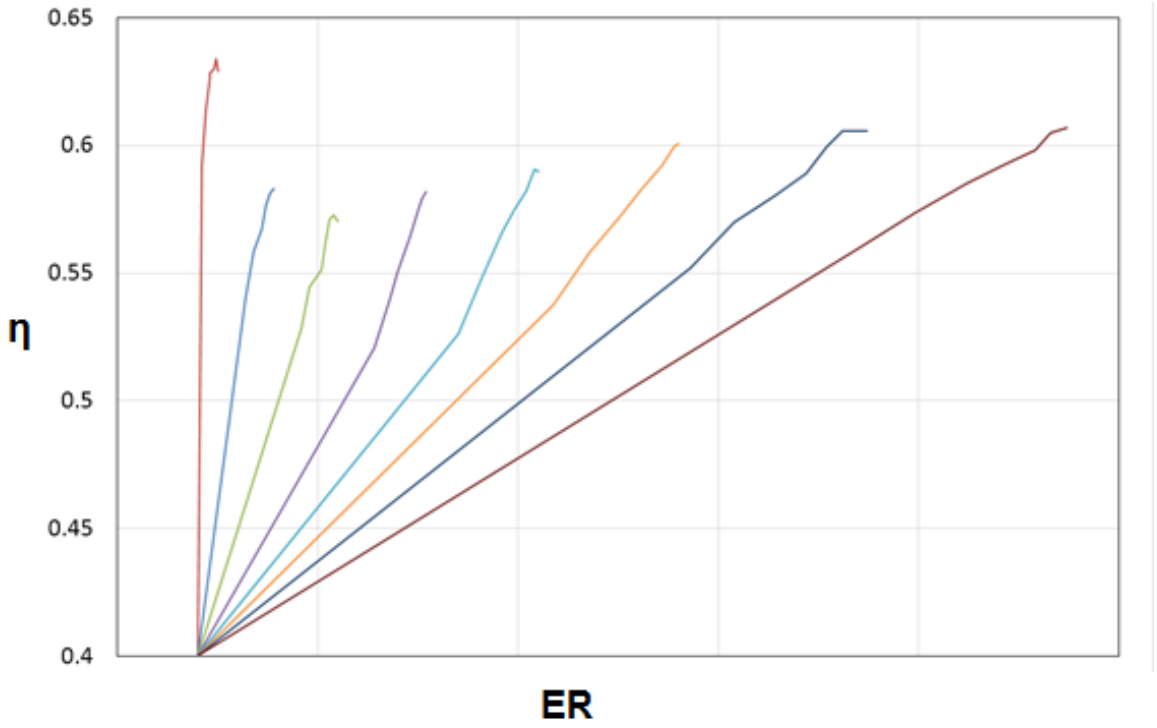

Figure 19: Turbine performance map 2, efficiency versus expansion ration

4.3. Equivalent flow time constants approach

In order to consider all the flow dynamic delays due to pipes and compressor, an analysis based on equivalent flow time constants has been performed. One representative flow characteristic time is calculated for each pipeline (upstream and downstream of the compressor). After that, the equivalent pipe was derived as it follows. Once the pipe cross section area is fixed as equal to the compressor intake, an equivalent length (L_c) is calculated; this must give a flow time, due to the momentum equation, equal to the sum of all the other contributes previously calculated. An example of characteristic flow time formula for pipes from [13] is reported in Eq.(17). The flow time constant represents the time for a duct to change its mass flow rate after a differential pressure variation (pressure step at inlet or outlet).

$$\tau_{flow} = 1.49 \frac{L\sqrt{\rho}}{\sqrt{2\,F}} \qquad \textbf{(17)}$$

Where:

L : actual length of the pipe [m]

ρ : density of fluid [kg/m^3]

F : force term depending on pressure drop across the pipe

For instance, assuming to have different pipe sections in series as shown by Figure 20, following this procedure it is possible to obtain the length of an equivalent pipe which, starting from the estimation of time constant of each single section, returns a flow delay time corresponding to the entire original pipeline.

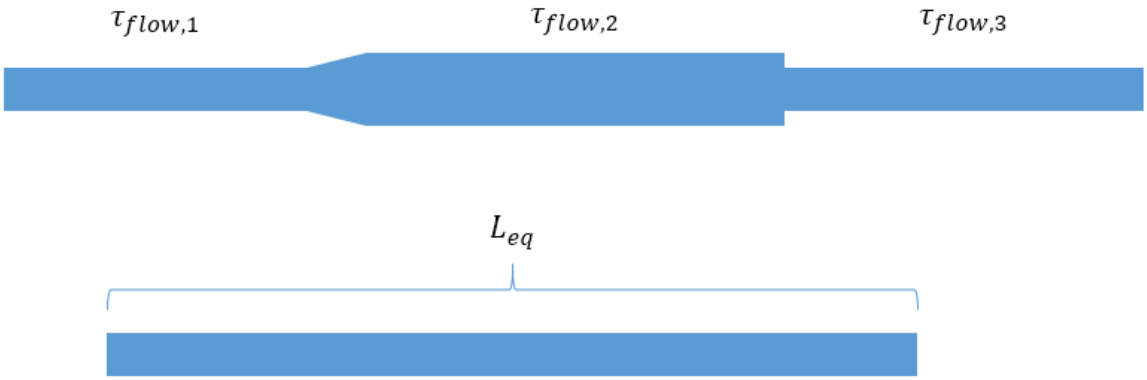

Figure 20: Example of equivalent length calculation procedure

The total flow time constant is calculated as sum of contributes from each section.

$$\tau_{flow\ tot} = \sum_{i=1}^{n} \tau_{flow,i} \tag{18}$$

Then, the length of the equivalent duct can be derived introducing the time constant calculated with Eq.(18) in the definition reported in Eq.(17).

$$\tau_{flow\ tot} = 1.49\ \frac{L_{eq}\sqrt{\rho}}{\sqrt{2\ F}} \tag{19}$$

4.4. Compressor map extension procedure

This section focuses on the assumptions and boundary conditions applied to extend the compressor map from the normal operating field to the negative mass flow condition through the no-flow operating point, when limited experimental data is available.

Usually compressor maps are provided only for the stable working condition, between the surge line and choking region. The dynamic model developed in this work is based on the

compressor map to replicate the surge cycles, this means that data beyond surge line are needed.

According to previous works [26], [27], [28], [29], [30], there are different approaches to extend the characteristic curves and obtain a wider working field for a compressor. This work focuses on centrifugal compressors, and it starts with the idea to divide the map into three different zones: Zone I, Zone II and Zone III or Normal Operation, as reported in Figure 21 (speed line values are normalized).

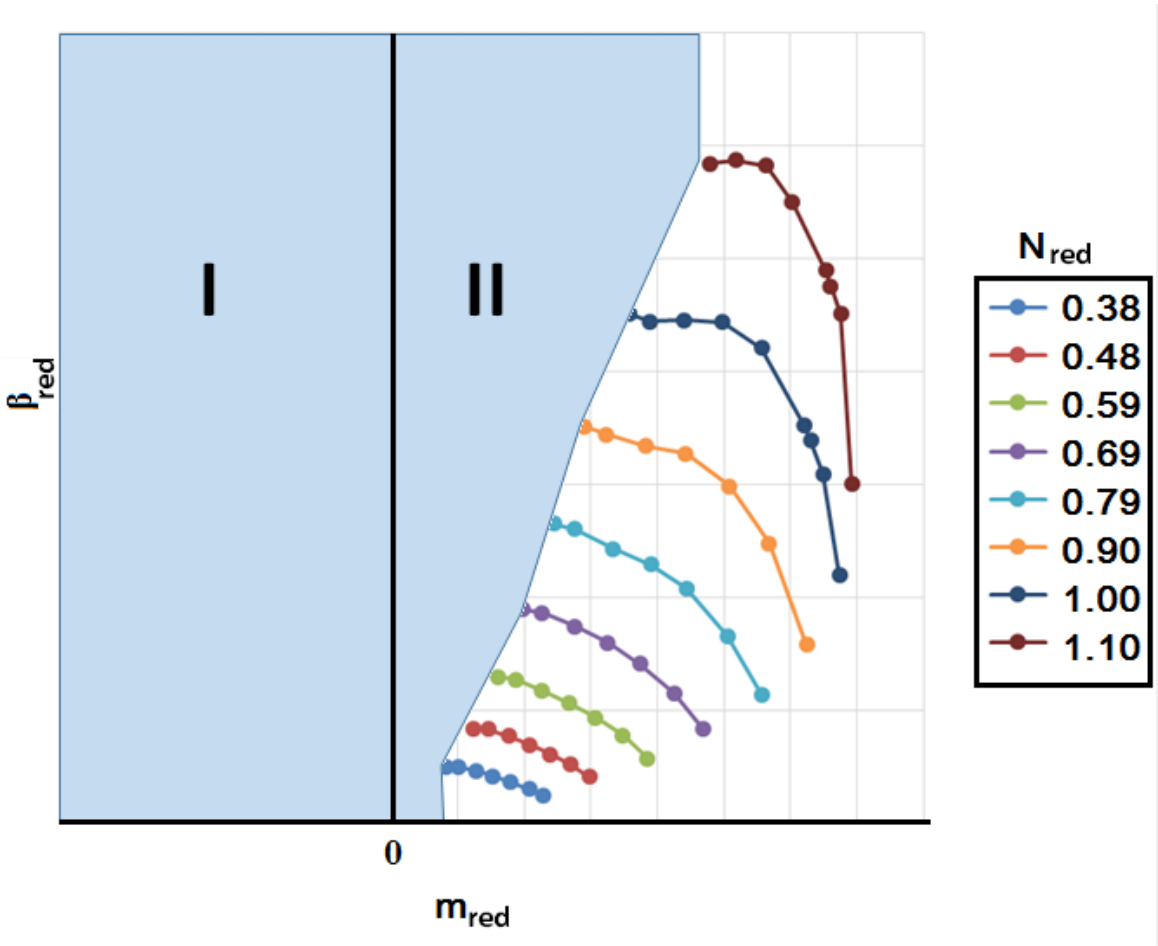

Figure 21: Identification of different working regions on compressor map

Zone III: Normal Operating zone

The turbocharger manufacturer (Garrett) has provided data contained in this region of the compressor map. shows the map expressed in terms of reduced pressure ratio versus reduced mass flow. Each line corresponds to an iso-speed condition (normalized). This data represents the starting point for the entire extension procedure. In the present work the assumption on these data are: the extreme left point on each iso-speed line represents the limit between stable and unstable condition on the steady state map; while the last points on the right indicate the limit for the choking condition region.

(20)

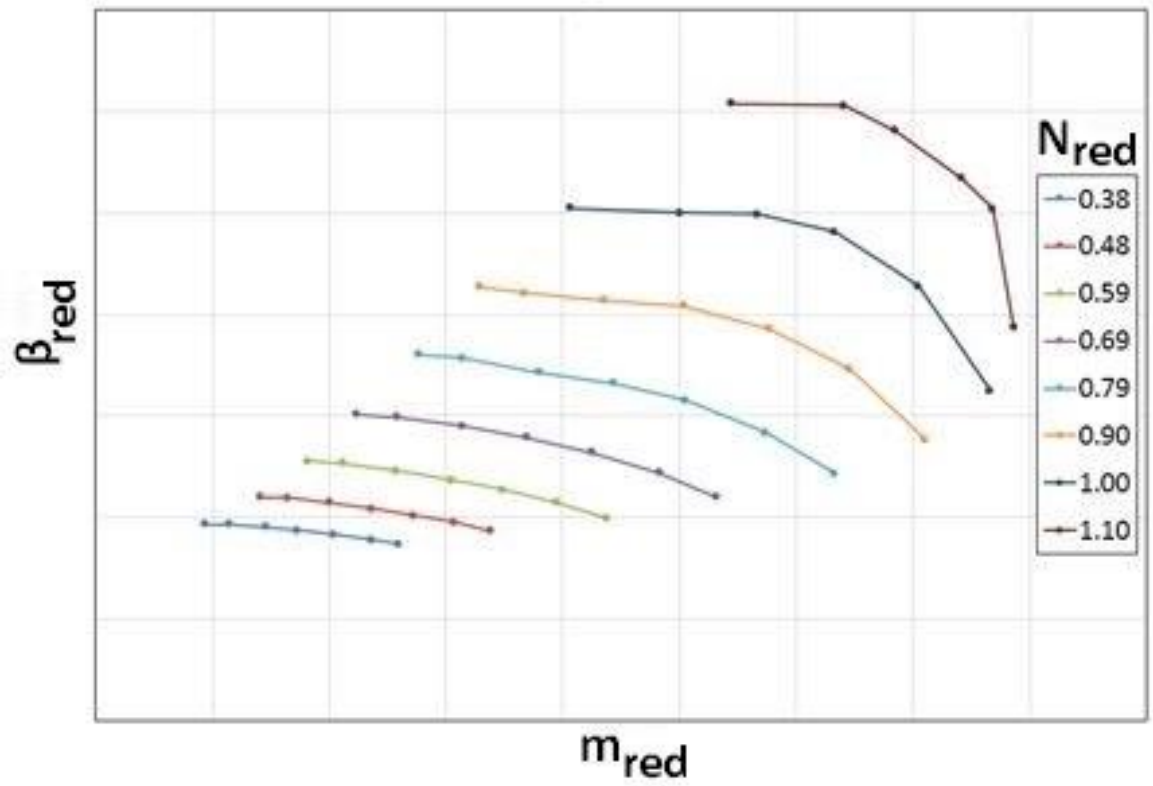

Figure 22: Compressor performance map provided by the manufacturer

Zone II

This zone which includes the operating points between no mass flow condition and surge line, has been developed following two different approaches. The first approach assumes a cubic trend of the iso-speed lines in this region, while the second method utilizes a quadratic one.

As introduced in the first approach the assumed trend is cubic, this means that each iso-speed curve is represented by the general Eq.(20).

$$f(x) = ax^3 + bx^2 + cx + d \qquad \textbf{(20)}$$

The polynomial function degree sets the number of boundary conditions required to derive the equation. In this case, the cubic polynomial has four coefficients to be found, each of these needs a boundary condition, so in total the number of conditions is four. There are two points per characteristic curve where such information can be obtained. The first is located at the left limit of each iso-speed in the normal operation field, while the other one is at zero flow condition.

In the first point, on the surge line, the actual coordinates for the polynomial are known because they are considered equal to the last data coming from the normal operating zone (see Figure 23 point (x_1,y_1)). Whereas, at the zero mass flow rate condition (point (x_0,y_0) in

Figure 23), data is obtained by merging information from experiments and the derivation of the load coefficient, which calculation is shown in a dedicated paragraph.

$$f(x_0) = y_0 \quad \textbf{(21)}$$

$$f(x_1) = y_1 \quad \textbf{(22)}$$

The third and fourth boundary conditions are the zero-slope condition in both starting and ending points, which implies that the first derivatives of the polynomial function, calculated at these specific abscissas, must be equal to zero.

$$\frac{df}{dx}(x = x_0) = 0 \quad \textbf{(23)}$$

$$\frac{df}{dx}(x = x_1) = 0 \quad \textbf{(24)}$$

The solution of the system of equations returns the value of the polynomial coefficients, the explicit formula for each coefficient is reported in Eq. (25) to Eq. (28):

$$a = \frac{-2(y_1 - y_0)}{x_1^3} \quad \textbf{(25)}$$

$$b = \frac{3(y_1 - y_0)}{x_1^2} \quad \textbf{(26)}$$

$$c = 0 \quad \textbf{(27)}$$

$$d = y_0 \quad \textbf{(28)}$$

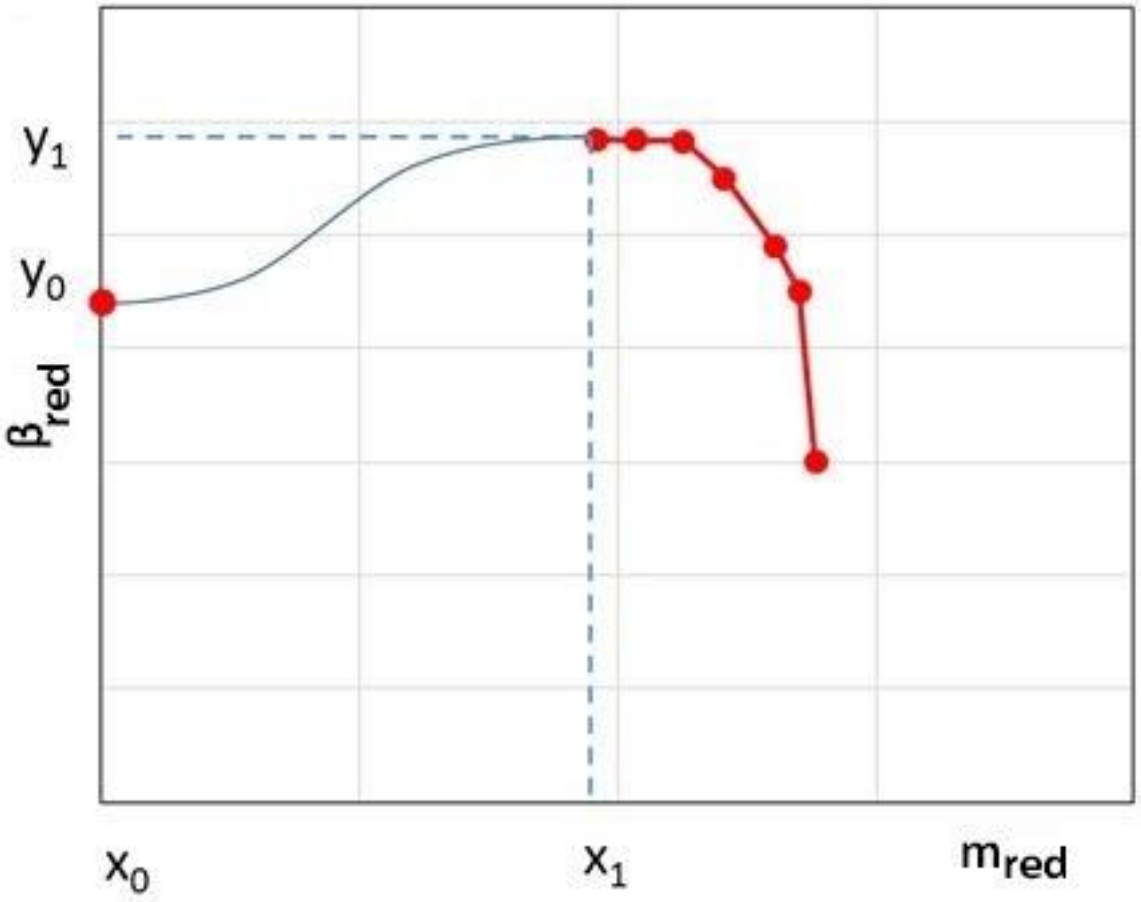

Figure 23: Example of extended iso-speed using the cubic approach for Zone II

In the second approach, the polynomial function has a quadratic structure; this means that the problem needs one boundary condition less compared to the cubic case.

Starting from the polynomial definition of Eq. (29), the system of equations to solve is now constituted by Eq. (30), (31) and (32):

$$f(x) = ax^2 + bx + c \quad \textbf{(29)}$$

$$f(x_0) = y_0 \quad \textbf{(30)}$$

$$\frac{df}{dx}(x = x_1) = 0 \quad \textbf{(31)}$$

$$f(x_1) = y_1 \quad \textbf{(32)}$$

where the assumptions on boundary conditions are the same as for the cubic case. The explicit solution of polynomial coefficients provides:

$$a = \frac{-(y_1 - y_0)}{x_1^2} \quad \textbf{(33)}$$

$$b = \frac{2(y_1 - y_0)}{x_1} \quad \textbf{(34)}$$

$$c = y_0 \quad \textbf{(35)}$$

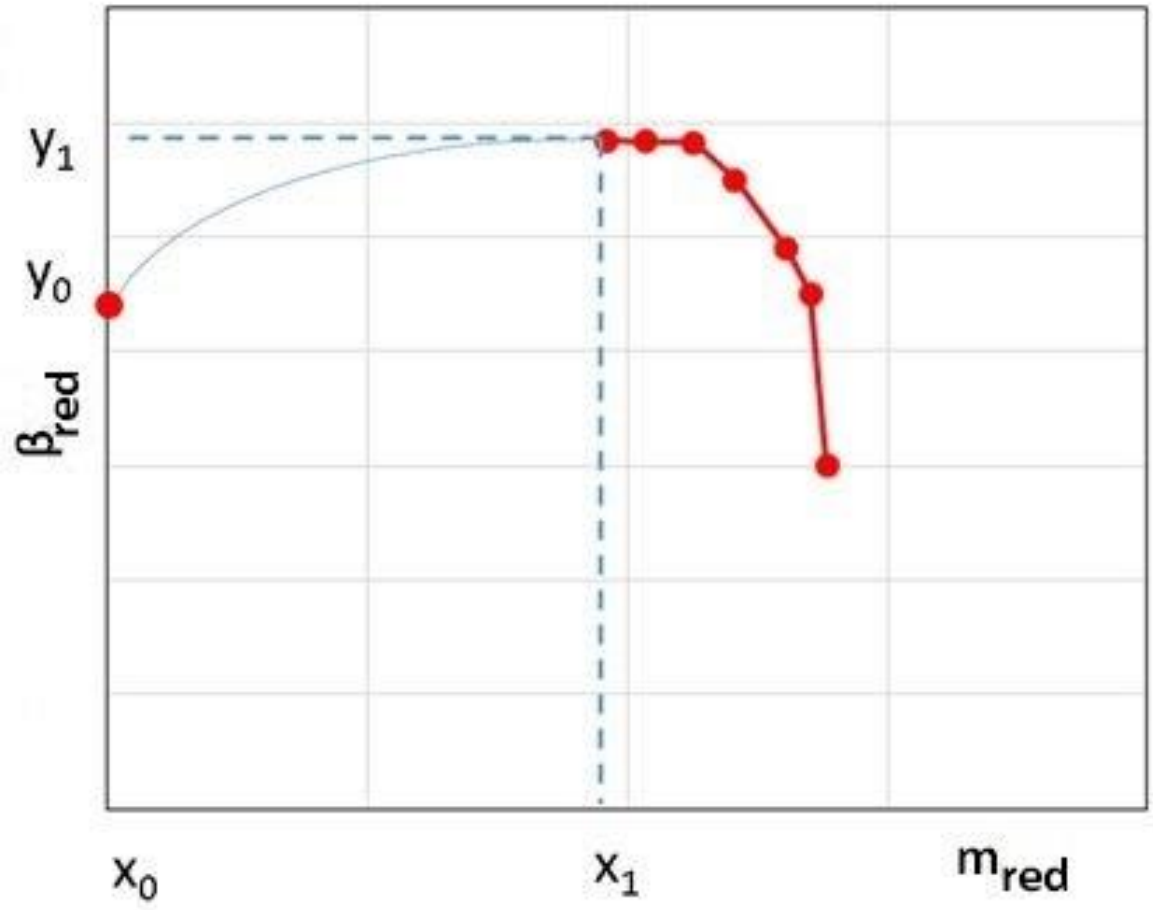

Figure 24: Example of extended iso-speed using the quadratic approach for Zone II

Zone I

The trend associated to this region is parabolic: in fact, the compressor operating in backflow condition is thought as a pressure drop. Boundary conditions on the y-axis corresponding to

the no-flow points are the same introduced before. The system to solve is now (Eq. (37), (38), (39)):

$$f(x) = ax^2 + bx + c \quad \textbf{(36)}$$

$$f(x_0) = y_0 \quad \textbf{(37)}$$

$$\frac{df}{dx}(x = x_0) = 0 \quad \textbf{(38)}$$

$$f(-x_1) = y_1 \quad \textbf{(39)}$$

As the polynomial coefficients are three (a, b, c) and flow is not measured during backflow, an auxiliary equation is needed.

To fix the last condition, a point with the same pressure ratio of Zone II but negative flow is chosen. According to Figure 25, this means that points with abscissa $m=\pm x_1$ have the same ordinate, where x1 was chosen as the mass flow rate of the last stable operating point divided by 5 (x_{minNO} /5). This method is similar to what has been done in [31]. Figure 25 presents the result of the extension starting from one iso-speed in normal operation zone, adopting the cubic approach for Zone II and quadratic approach in Zone I.

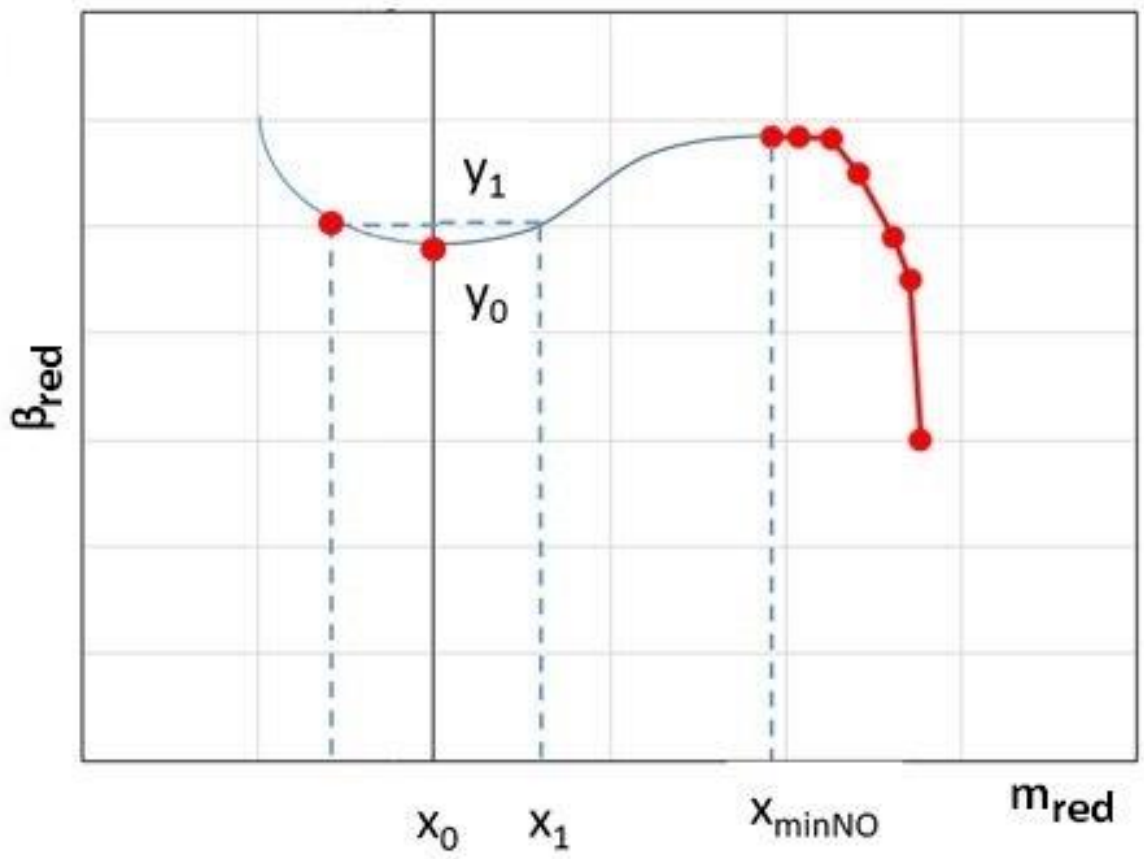

Figure 25: Example of extended iso-speed using the quadratic approach for Zone I

Polynomial coefficients can be derived in the following form:

$$a = \frac{y_1 - y_0}{x_1^2} \quad \textbf{(40)}$$

$$b = 0 \quad \textbf{(41)}$$

$$c = y_0 \quad \textbf{(42)}$$

According to [31], there is some uncertainty related to the choice of x_1 but a variation in this assumption was found to have minimal influence on simulated results.

4.4.1. Definition of boundary conditions

Boundary conditions are needed to extend the characteristic map in both Zone I and Zone II. For Zone I it is important to develop a strategy to extrapolate accurately all the points at zero mass flow rate condition, for different compressor speeds lines. Three different approaches

are here proposed and compared to experimental references, carried out from two separate experimental campaigns:

- approach 1 consists in the extrapolation of every value of pressure ratio at zero mass flow rate using a unique load coefficient obtained from a single test point;
- approach 2 utilizes a single load coefficient calculated as average among different experimental points;
- approach 3 makes use of an empirical correlation between load coefficient and rotational speed to vary the load coefficient depending on the speed.

During the first test, as shown in Figure 26 an entire iso-speed curve has been acquired. This was possible acting on the compressor discharge valve and the turbine mass flow controller simultaneously to pass from one stable operating condition to another. Thanks to this test, it was possible to obtain a constant speed curve and compare it to the map provided by the manufacturer.

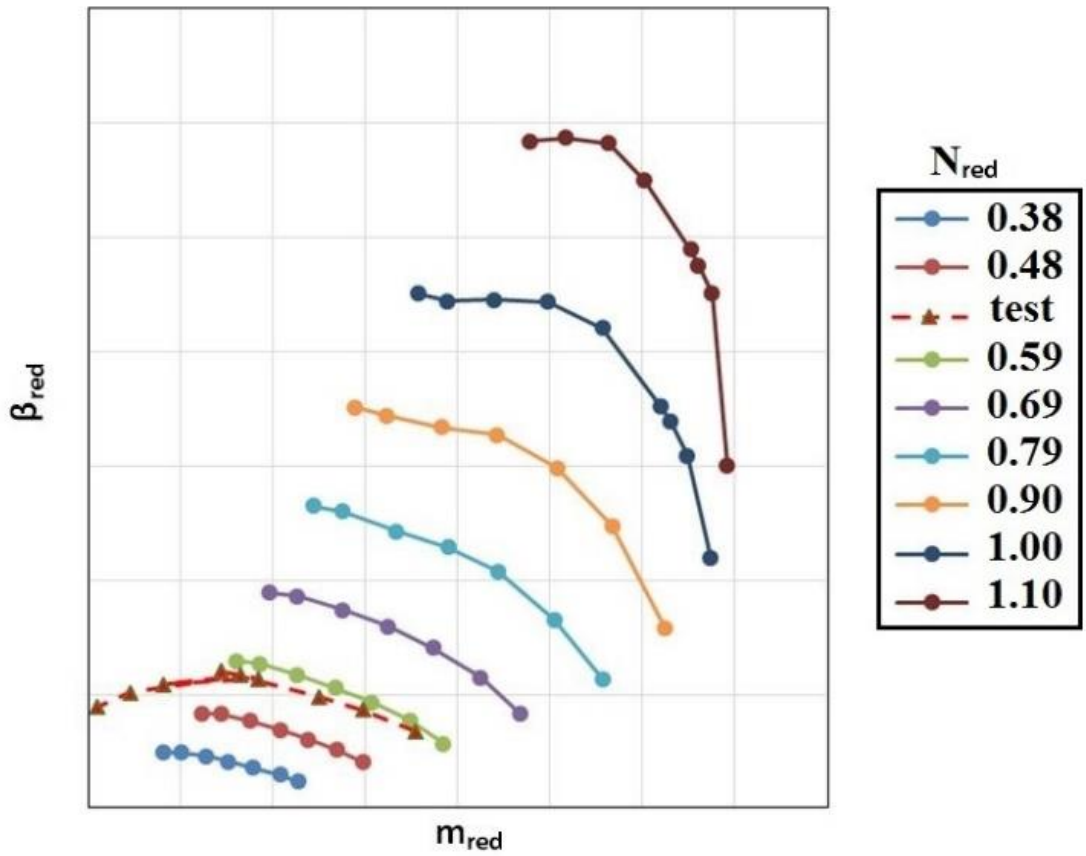

Figure 26: Test results: the acquired N_{red}=0.55 iso-speed curve on compressor map

In addition, by completely closing the compressor discharge valve and acting on turbine power to keep the compressor in rotation, it was possible to acquire the pressure rise produced by the compressor in a zero-mass flow rate condition (this condition could be tested for a limited time, to avoid compressor wheel over-heating).

This last point has been used as a reference for approach 1 to calculate the load coefficient reported in Eq.(43). By considering the value of this coefficient as a constant, the pressure rise at the other zero mass flow conditions at different rotational speeds may be extrapolated as in Eq. (44).

$$\Psi_{known} = \frac{L_{1,2is}}{U^2} = \frac{c_p T_{in}\left[(\beta_{known})^{\frac{k-1}{k}} - 1\right]}{U_{known}^2} \quad \textbf{(43)}$$

$$\beta_N = \left(\frac{\psi_{known}\, U_N^2}{c_p T_{in}} + 1\right)^{\frac{k}{k-1}} \quad \textbf{(44)}$$

To validate the presented extrapolation method a second test was performed. This time the turbine was fed with different mass flow rates. For each condition, the compressor discharge valve was initially kept closed in order to measure the compression ratio value when no mass flow passes across the compressor vane. After each measurement, the compressor valve was gradually opened, the turbine fed with additional air in order to accelerate the rotor and then the valve was closed again to acquire a different point.

Experimental results have been compared with data calculated at similar speed values using approach 1, as shown in Figure 27.

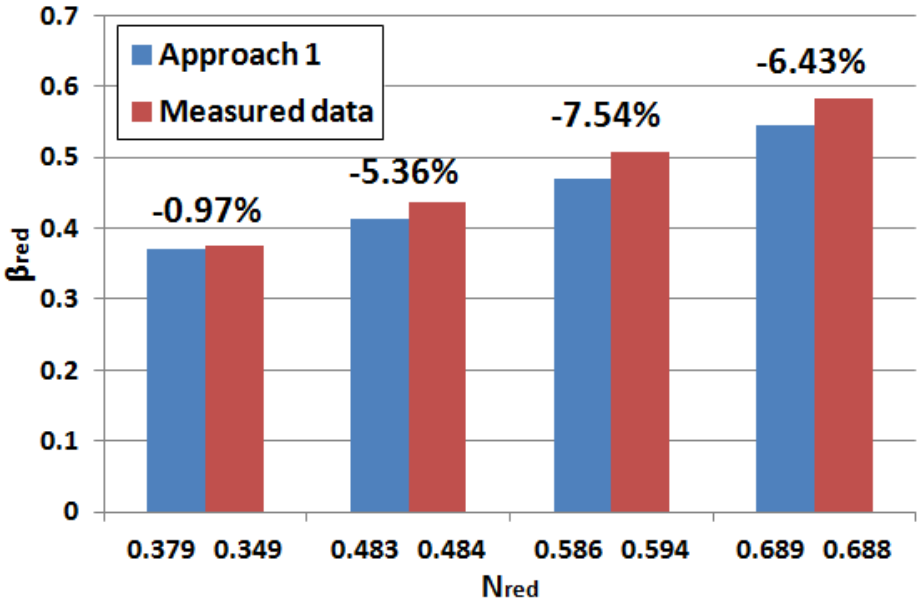

Figure 27: Comparison between test data and calculated points with percentage error (approach 1)

The difference between each measurement and the analytical calculation defines the accuracy of the extension process.

As this first approach seems not to be accurate enough, a work coefficient has been calculated from each data point collected during the second test, Table 3. The average value of these calculated coefficients is taken as known coefficient to extrapolate data in the *approach 2* using Eq.(45).

Table 3: Work coefficient for different rotational speeds

	ψ_{known}
meas1	0.432427
meas2	0.445697
meas3	0.455045
meas4	0.473965
meas5	0.475653

$\psi_{known\ average}$
0.456557267

$$\beta_N = \left(\frac{\psi_{known\ average}\ U_N^2}{c_p T_{in}} + 1 \right)^{\frac{k}{k-1}} \quad \textbf{(45)}$$

Figure 28 shows that also approach 2 does not seem to yield satisfactory results. The percentage errors between measurements and calculated results are still consistent.

The *approach 3* starts from the analysis of working coefficients calculated with data from tests, searching for possible trends. As the rotational speed increases, a decreasing trend on the loading coefficient can be observed (Figure 29).

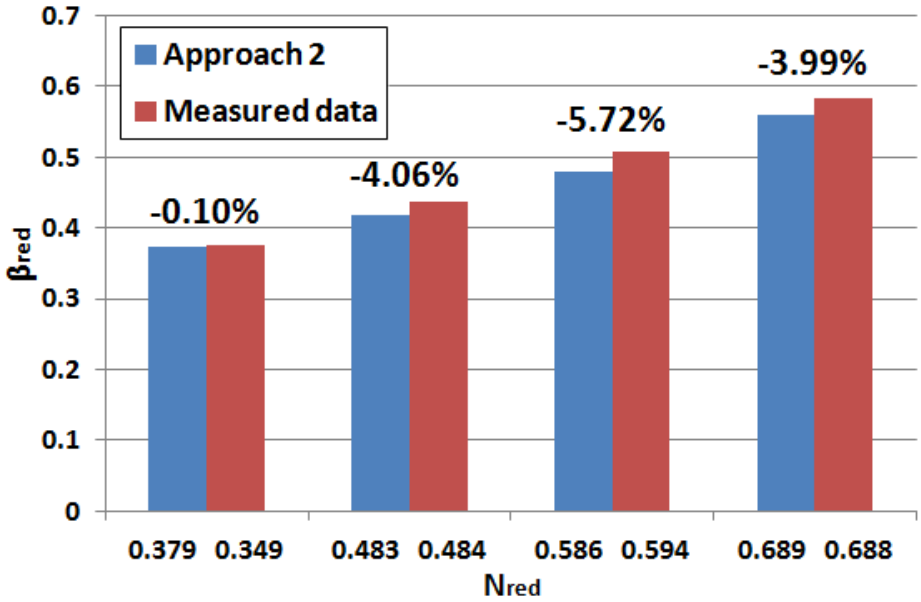

Figure 28: Comparison between test data and calculated points with percentage error (approach 2)

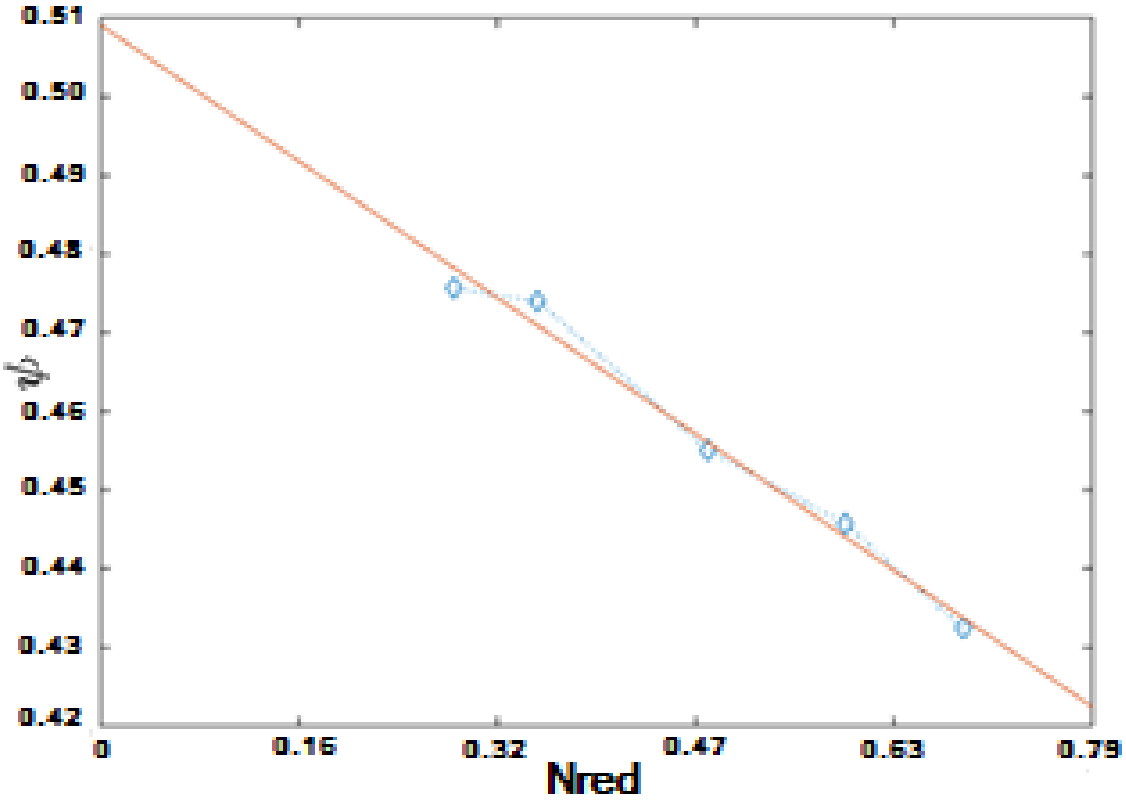

Figure 29: Experimental points (light blue) and best linear fir (orange)

This behavior is well captured with a linear law and introduced in the formula for the map extension using Eq. (46)

$$\beta_N = \left(\frac{\psi(N)U_N^2}{c_p T_{in}} + 1\right)^{\frac{k}{k-1}} \quad \textbf{(46)}$$

In comparison to previous approaches, the outcomes of the last method show a better match with experimental data (Figure 30).

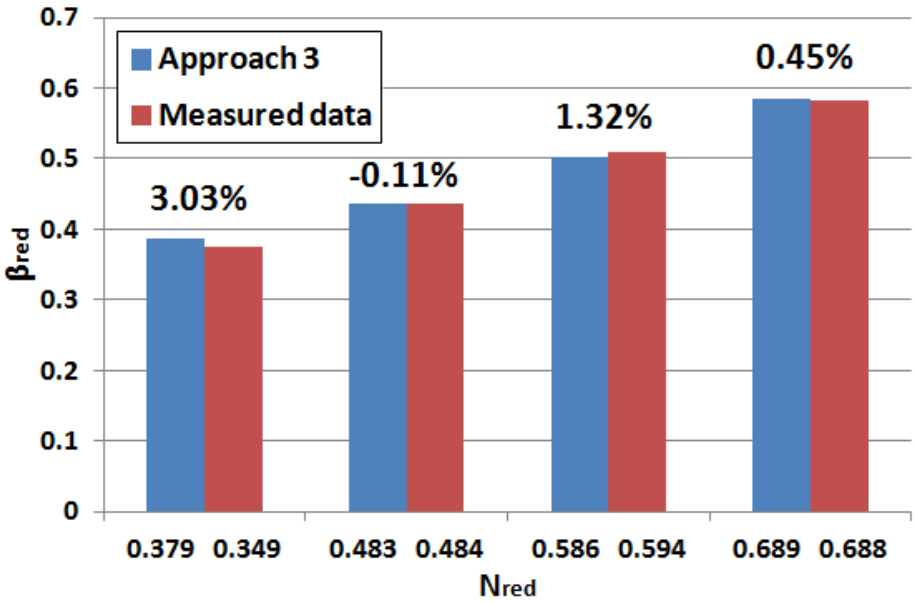

Figure 30: Comparison between test data and calculated points with percentage error (approach 3)

The next step was to obtain boundary conditions to extrapolate the compressor characteristics in Zone I. Figure 25 shows a single representative complete iso-speed: however, it should be remarked that a different (x_1,y_1) point can be used for each speed line as reference point for extrapolation.

The problem is to choose these (x_1,y_1) points avoiding collisions of the extended iso-speeds in Zone I. Because of this aspect, only one point on the maximum iso-speed is mirrored from the positive Zone II to Zone I and the corresponding non-dimensional work coefficient is calculated from it. All the others are extrapolated using the same work coefficient versus rotational speed dependency law presented in Figure 29, thus the entire set of compression ratios is derived for fixed negative mass flow.

Extended compressor characteristics obtained with both cubic and quadratic approaches (for Zone II) are shown in Figure 31 and Figure 32.

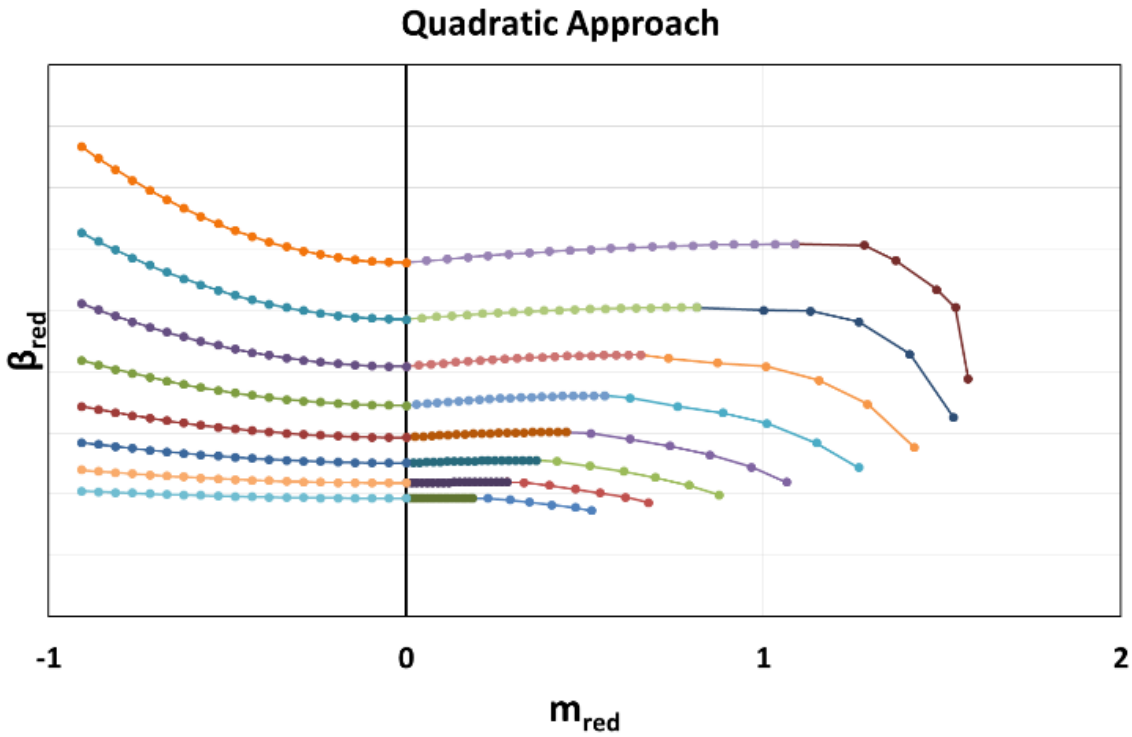

Figure 31: Extended map with parabolic approach

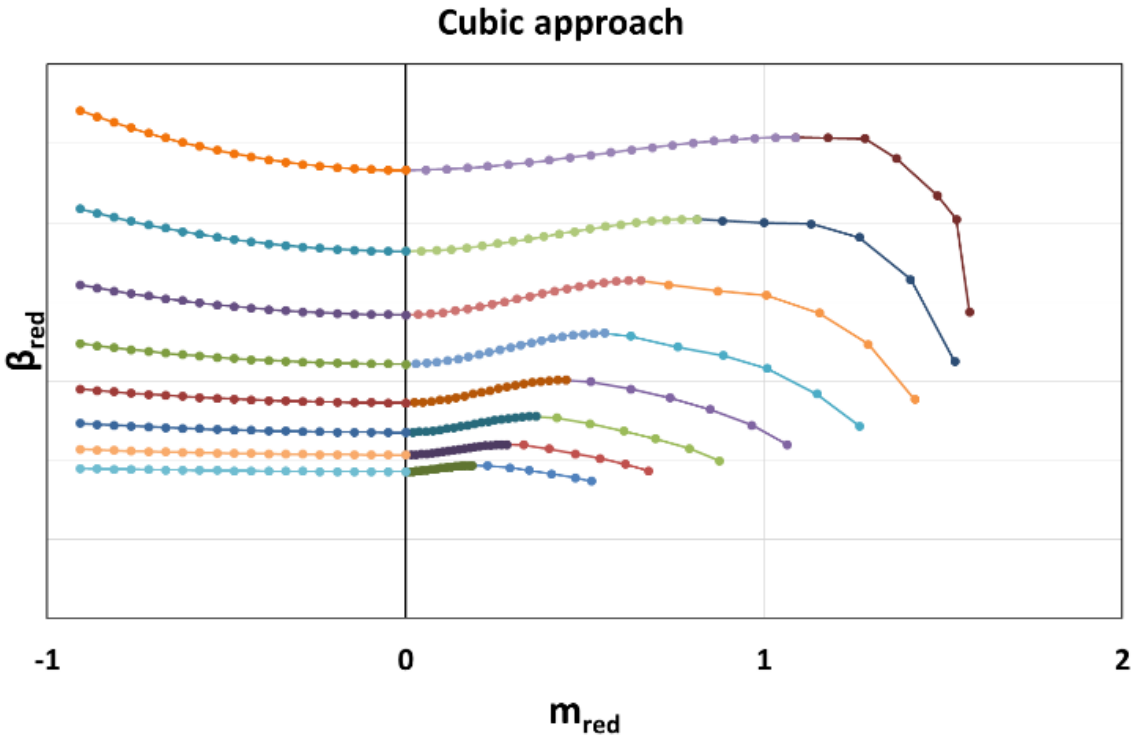

Figure 32: Extended map with cubic approach

Basing on Figure 26, since experimental results seem to indicate a quadratic trend for data acquired in Zone II, the parabolic (or quadratic) approach is used to represent the compressor map inside the model.

4.4.2. Power derivation

Obtaining an efficiency map for compressor in Zone I and Zone II is not obvious. For this reason, a function that relates the power to the mass flow rate and rpm has been studied in order to be able to estimate the compressor power consumption at every operating condition. A literature review has been conducted and it was decided to obtain non-dimensional information starting from characteristics that belong to a large centrifugal fan, illustrated in, which power data was available until zero flow.

Combining this information with an approximated approach from similitude theory, it was possible to obtain a curve in terms of non-dimensional parameters. This method provided a non-dimensional mass flow (flow coefficient φ) versus power (power coefficient τ) diagram, which is introduced in the compressor dynamic model. Centrifugal fan characteristics at design conditions are:

- N=1210 rpm
- Static pressure= 150 mmH2O
- Flow rate=18000 Nm^3/h
- Absorbed power=13 kW

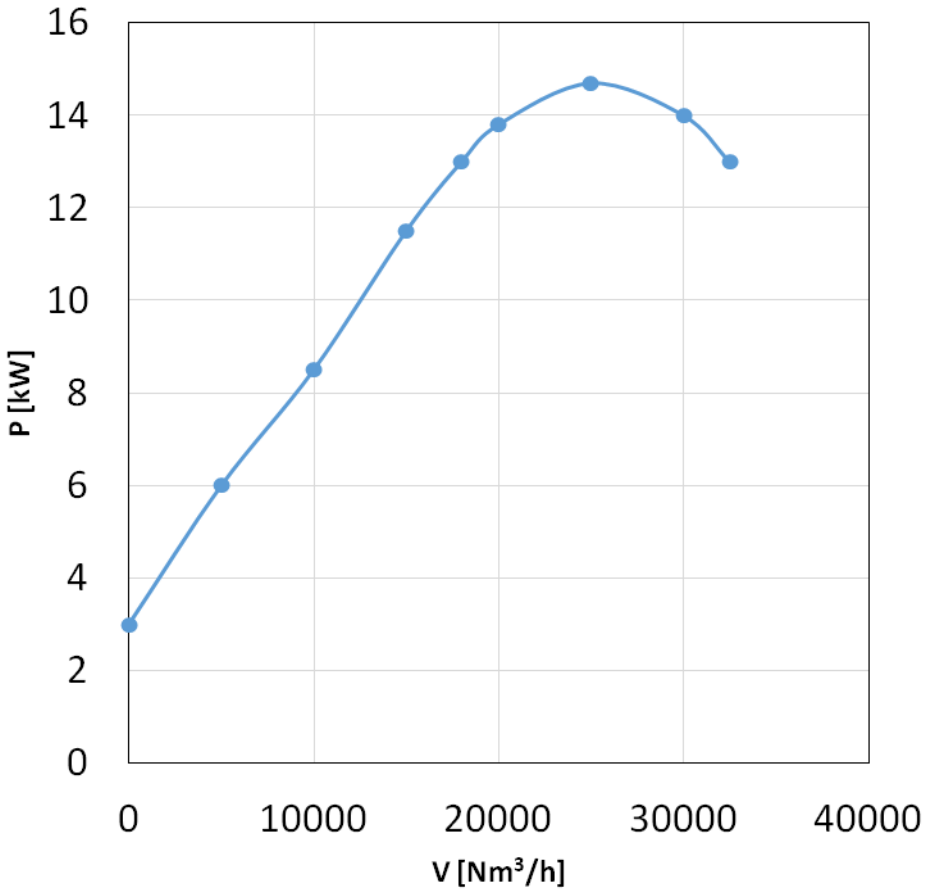

Figure 33: Absorbed power for the reference fan

The available trend has been traduced in terms of flow coefficient φ and power coefficient τ:

$$\varphi = \frac{\dot{V}}{\omega D_2^3} \tag{47}$$

$$\tau = \frac{P_a}{\rho \omega^3 D_2^5} \tag{48}$$

Assuming that compressor absorbs almost the same amount of power working in normal flow conditions and during backflow [7], a symmetric behavior for the power coefficient has been assumed Figure 34 depicts the curve trend. Simulink compressor model contains this data inside a lookup table that receives φ as input from mass flow signal and returns τ. Then, this quantity is converted into the actual absorbed power by the compressor, at every mass flow rate, negative values included.

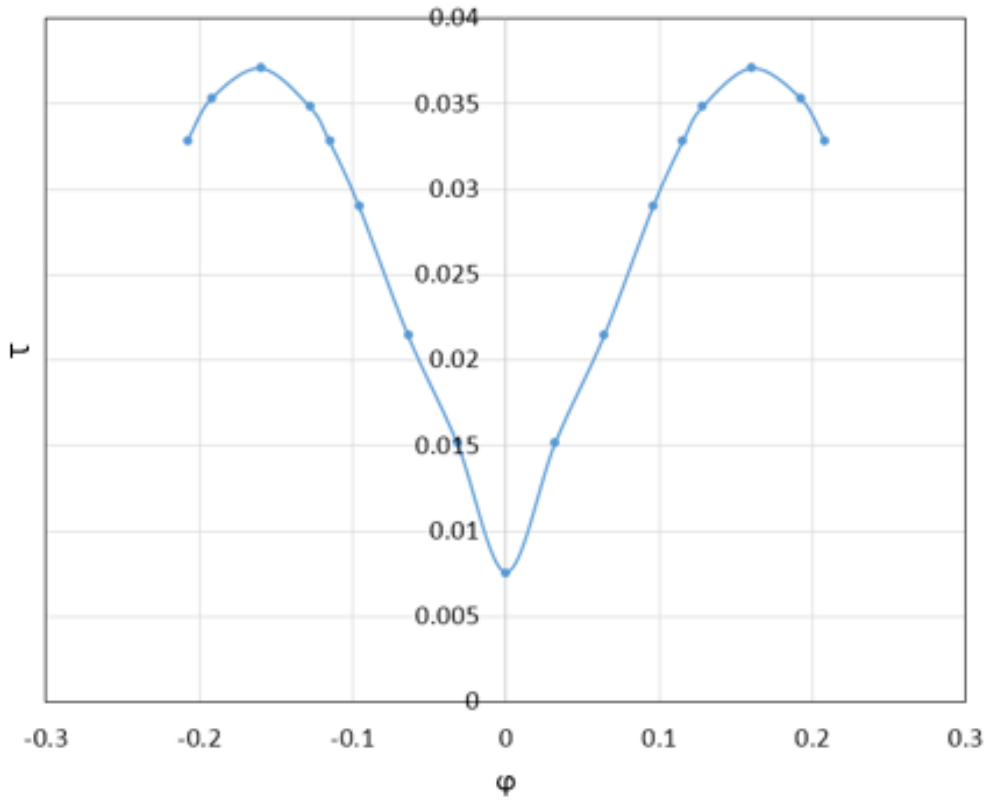

Figure 34: Power coefficient versus flow coefficient in the extended characteristic

4.5. Experimental results

The experimental investigation was performed on the facility at TPG laboratory in Savona. Figure 35 shows the rig used for these tests; the flow path through the turbocharger is also indicated.

Several tests for turbocharger characterization have been performed during:

- Steady-state operating conditions
- Speed ramps
- Compressor instability

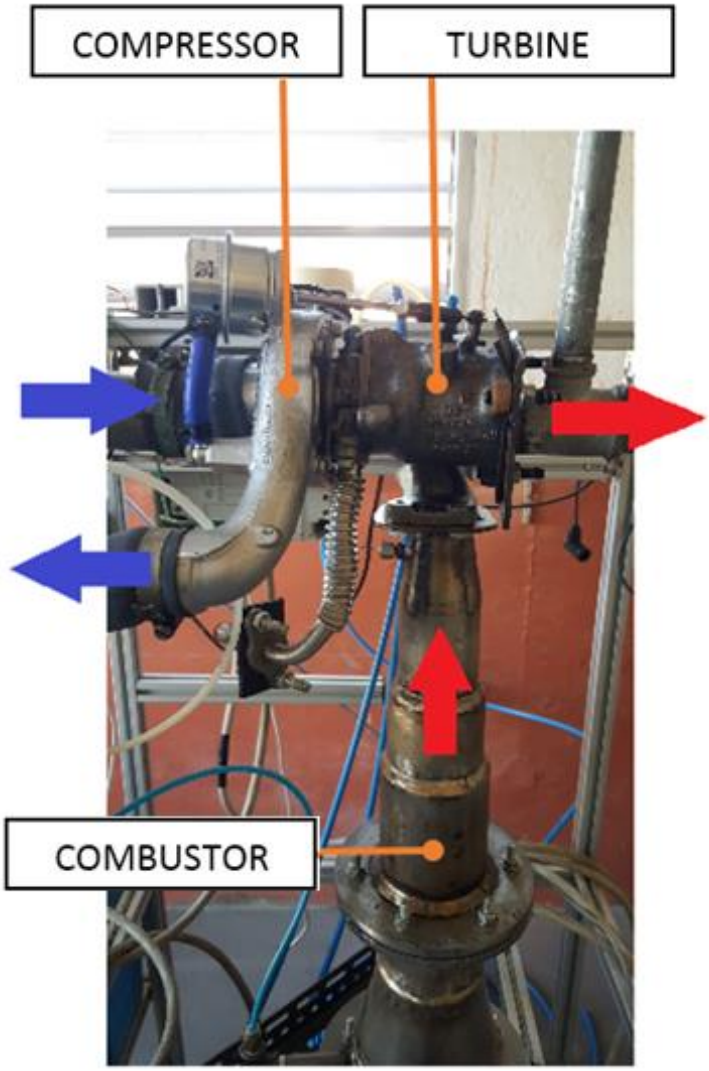

Figure 35: Turbocharger test rig 1 for hot tests (T-RIG1)

Figure 36 shows a hot test when surge events were studied at different working conditions. The blue line reports the mass flow fed into turbine while the orange one shows the rotational speed. The test was divided in four runs where the turbine inlet condition was changed mainly in terms of inlet mass flow rate supplied to the turbine. Spikes on rotational speed signal indicate when compressor was driven in an unstable region, gradually closing the discharge valve. As it is visible from this figure, compressor was driven in surge twice per run.

Acoustic emissions and vibrations were monitored during these tests.

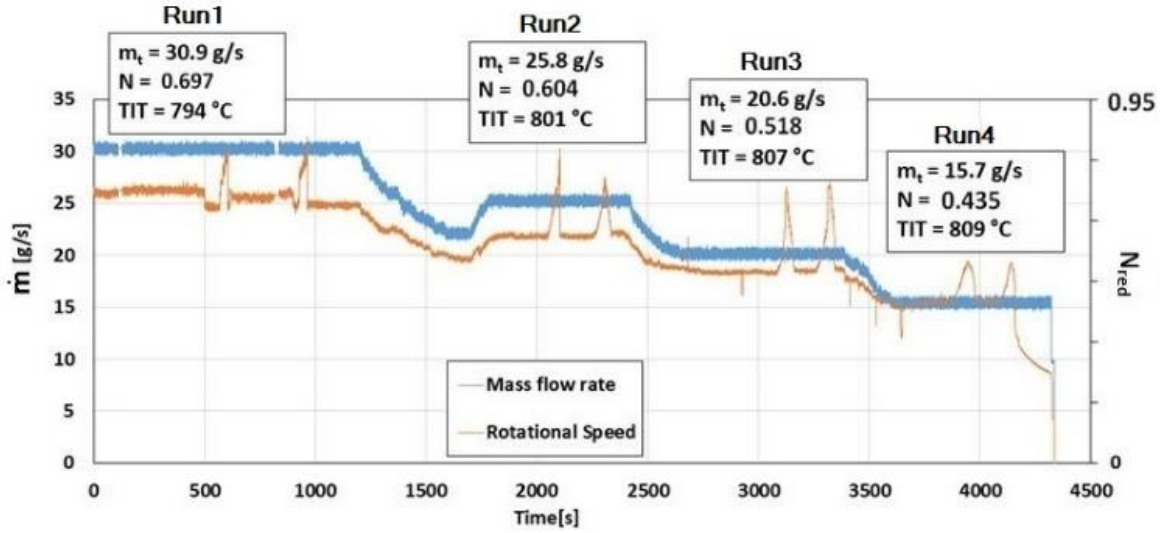

Figure 36: Turbine mass flow rate and rotor speed during experimental test (hot conditions)

Figure 37, Figure 38, Figure 39 and Figure 40 show color maps of the signal recorded by accelerometers set on compressor volute.

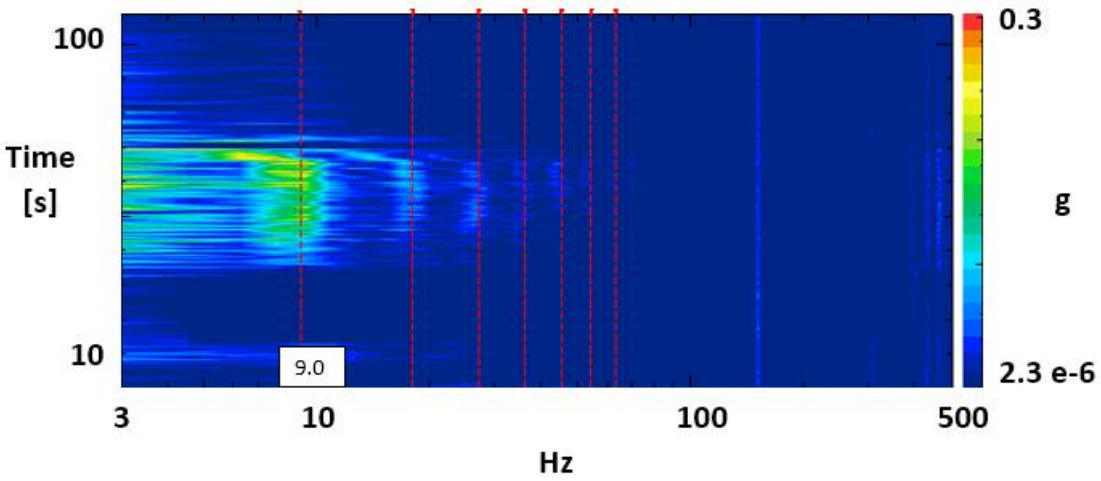

Figure 37: Waterfall diagram – Run1

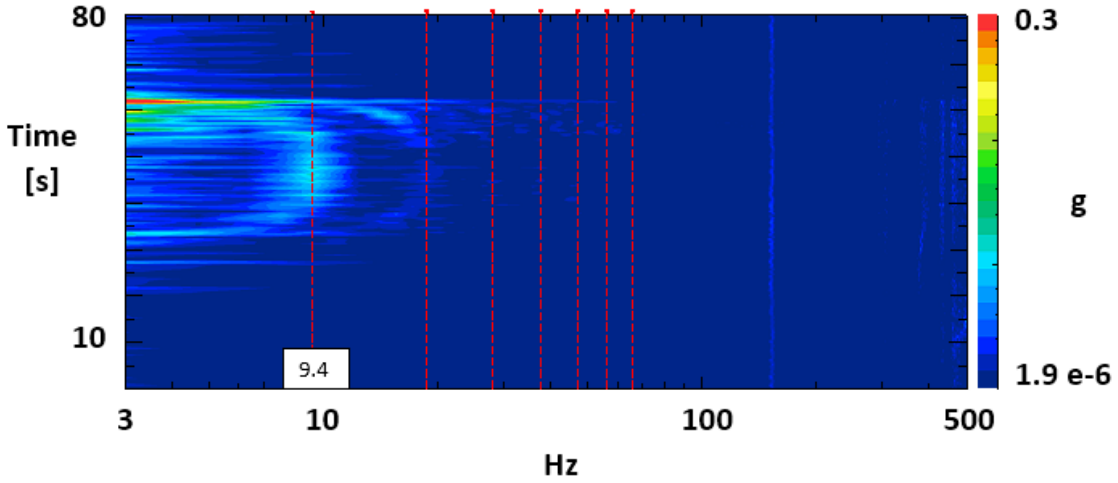

Figure 38: Waterfall diagram – Run2

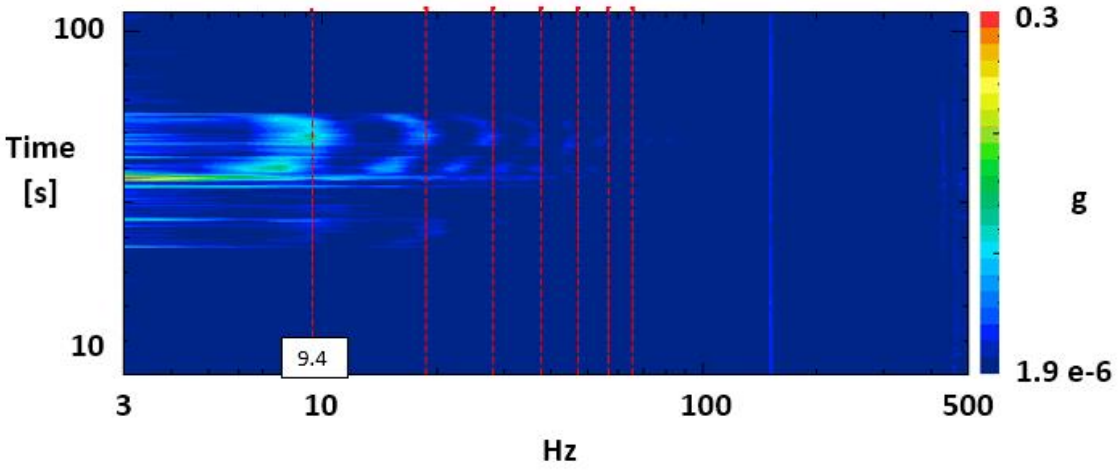

Figure 39: Waterfall diagram – Run3

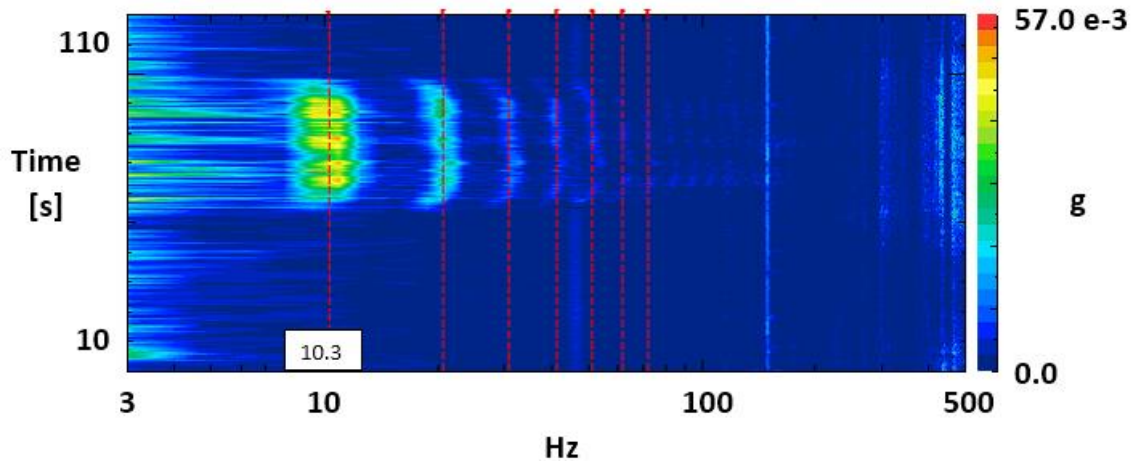

Figure 40: Waterfall diagram – Run4

The main frequency component of surge is highlighted by white boxes reporting the corresponding value. Red dashed lines indicate the main components and its multiples visible on these spectra.

The main surge frequency due to flow oscillations across the compressor, measured on the T-RIG1 during this test, is around 9-10 Hz, despite the quite different rotational speeds. The measurements from the acoustic sensor agree with these results. Data from this sensor are shown in Figure 41.

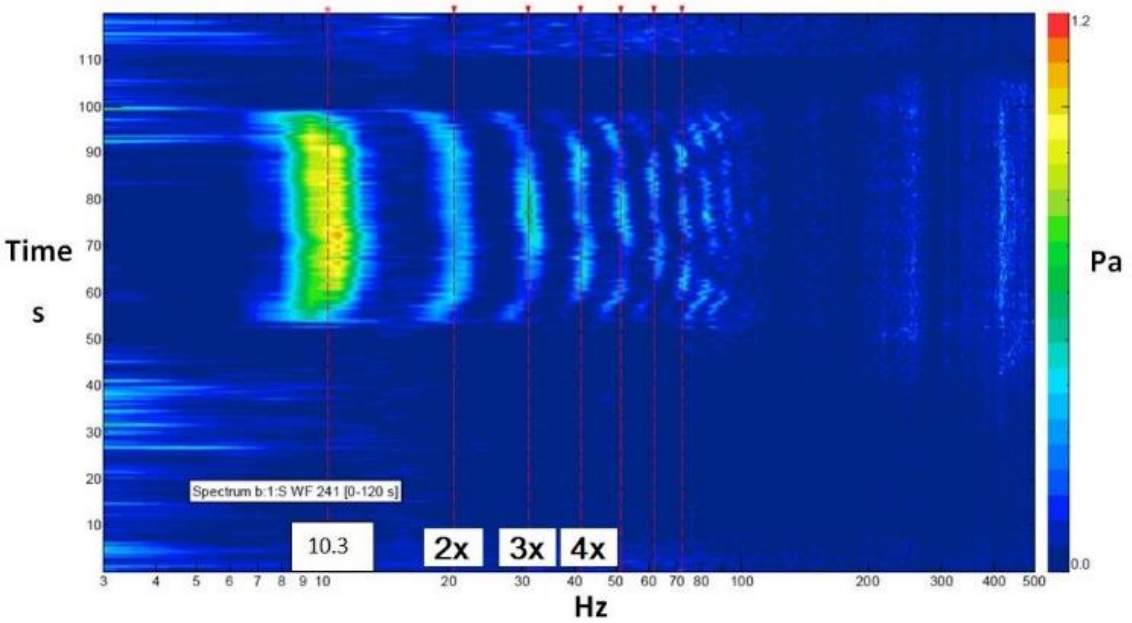

Figure 41: Surge frequency acquired using microphone during the hot test at turbine flow $\dot{m}$=15.7g/s

4.6. Simulation results

As explained, the main focus of this work was the development of a model able to replicate the surge events recorded on the real machine. In order to obtain this result, a simulation with the same boundary conditions of the test reported in Figure 36 has been performed, the case of a turbine mass flow rate of 15.7g/s was considered. The simulated surge cycle visualized on the compressor map is shown in Figure 42: only the initial point and the stabilized cycle are here reported for a clearer visualization.

The B parameter for this system calculated with Eq. (5) is estimated to be approximately 0.54.

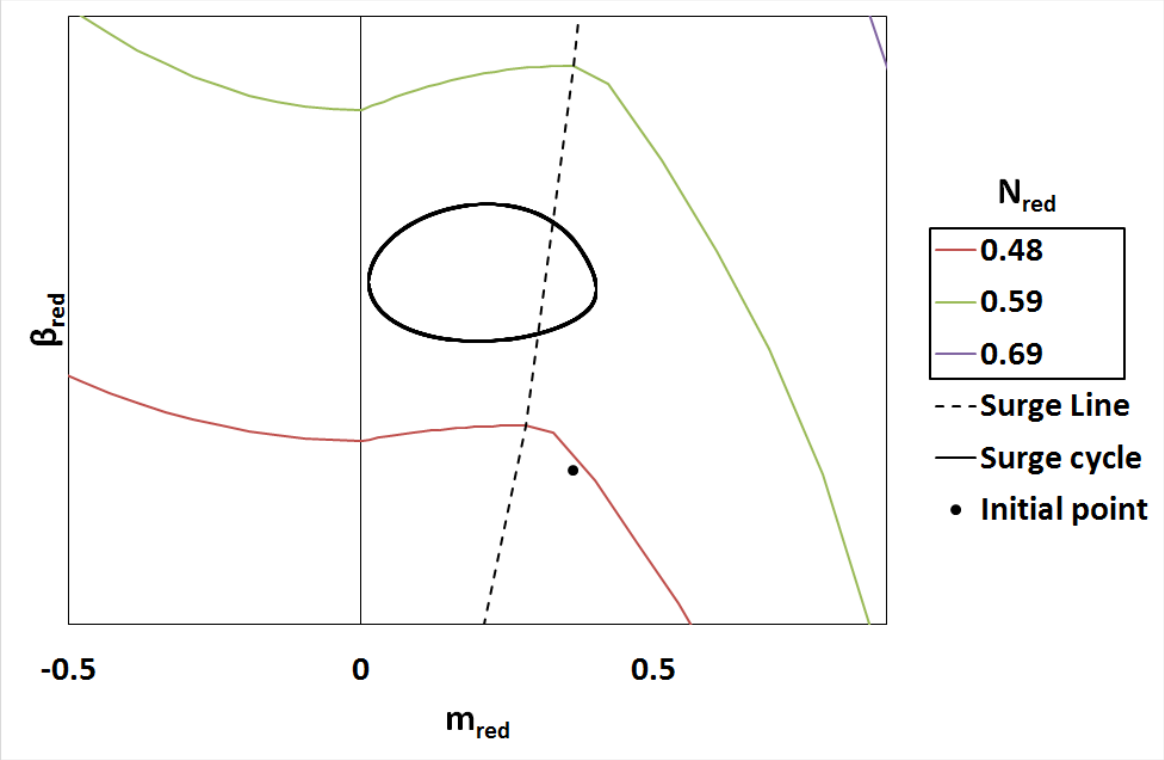

Figure 42: Surge cycle simulated with T-RIG1 model

As introduced in the Experimental Results paragraph, the surge condition was reached starting from a stable operating point and gradually closing the discharge valve.

This specific result from simulation were treated with a Fast Fourier Transform analysis (FFT). Figure 43 shows the calculated frequency for compressor mass flow oscillations during a simulation of surge. The main component and its harmonics are visible as spikes on this diagram.

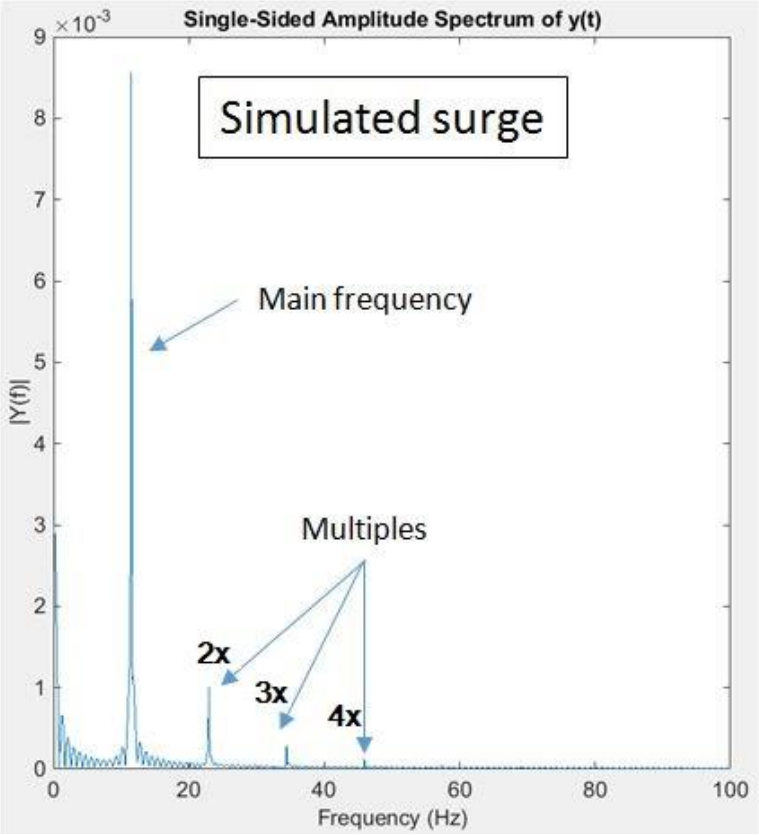

Figure 43: Surge frequency simulated with T-RIG1 model (fundamental and harmonics)

Simulated results have been validated against test data, the color map from the test used as reference is shown in Figure 41. This image shows the acquisition from the acoustic sensor (microphone) during the last part of the same hot test reported in the "Experimental Results" paragraph.

Simulated results, in terms of frequency domain, show a good accuracy compared with experimental ones. In this case, an error of less than 12% was obtained on frequency calculation. The comparison between measured and simulated frequencies is reported in Table 4.

Table 4: Measured and calculated frequencies

Measured frequency	Simulated frequency
10.3 Hz	11.5 Hz

4.6.1. Impact of volume size on surge frequency

A parametric analysis has been performed on the T-RIG1 model, in this first investigation two different volume sizes have been tested: V_p equal to 0.0042m^3 and V_p equal to 0.005m^3.

A comparison between Figure 44 and Figure 45 shows as a small increase in plenum size determines a sensible variation in frequency of oscillation.

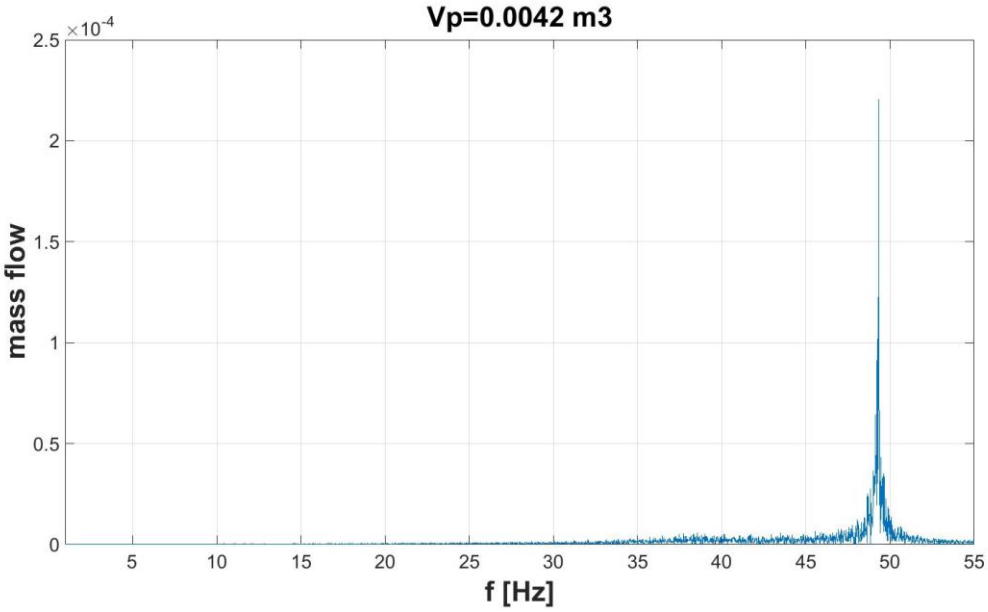

Figure 44: FFT analysis of mass oscillation when Vp=0.0042m^3

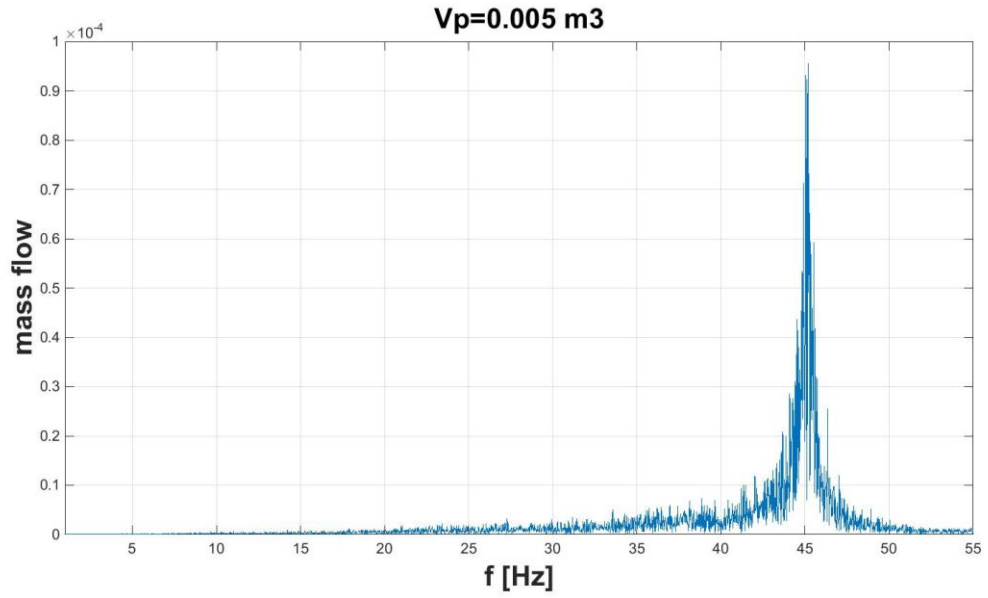

Figure 45: FFT analysis of mass oscillation when Vp=0.005m3

The shift of the peak on frequency axis obtained from FFT analysis is linked to the fact that an enlargement in plenum size determines bigger inertia of system, the time needed for the volume to change its pressure level is longer, consequently the mass oscillations are slower, and each surge cycle takes more time to be completed.

4.6.2. Impact of rotor mechanical inertia on surge frequency

A second study has been developed in order to define how the inertia of the shaft could affect the frequency result. In this case the comparison has been performed with J equal to $5*10^{-7}$ kgm^2 and J equal to $3.5*10^{-7}$ kgm^2.

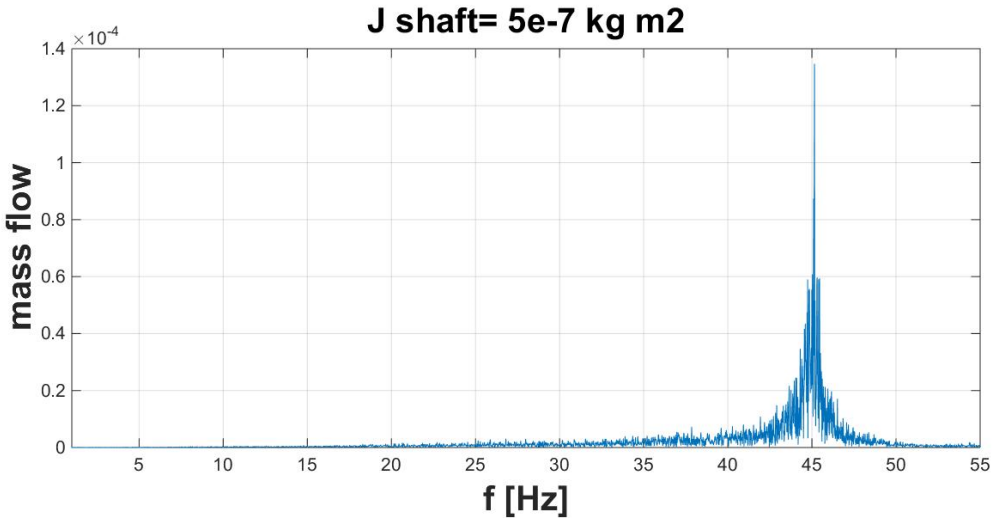

Figure 46: FFT analysis of mass flow oscillation when rotor mechanical inertia is $5x10^{-7}$ kgm^2

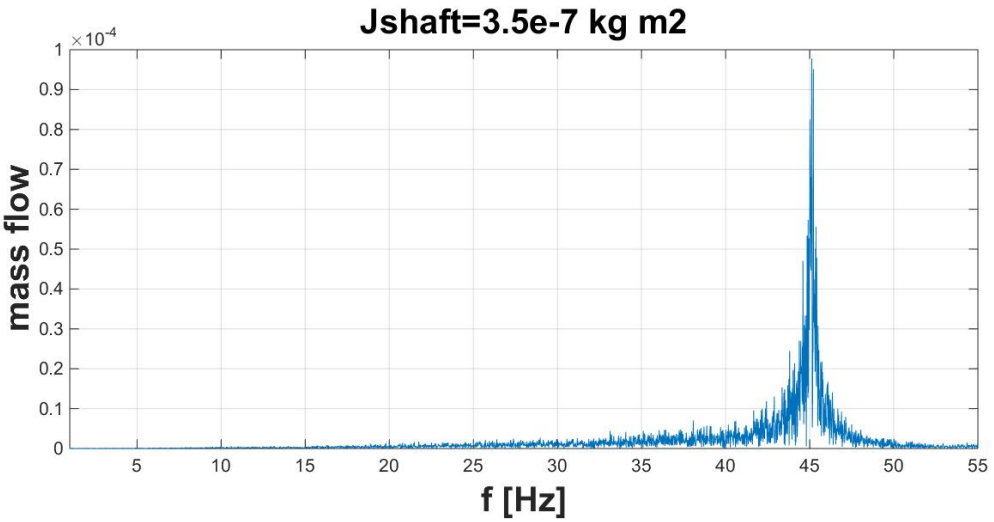

Figure 47: FFT analysis of mass flow oscillation when rotor mechanical inertia is $3.5x10^{-7}kgm^2$

The comparison between Figure 46 and Figure 47 shows that a small change in mechanical inertia of the shaft has almost no influence on the surge frequency of the system studied here. This aspect suggests that other are the parameter on which to act to have appreciable changes in dynamic response of the system when surge occurs.

4.6.1. Impact of equivalent lengths on surge frequency

In the T-RIG1 model two momentum equations are used to simulate the real system, one in the compressor component and one in the discharge valve. This means that two main equivalent lengths are present here, L_c for the compressor and L_t for the throttle. The first investigation focused on the valve equivalent length, in this study this parameter was changed from 0.2m to 3.8m without any significant different in the FFT plot which is in both cases very similar to Figure 48.

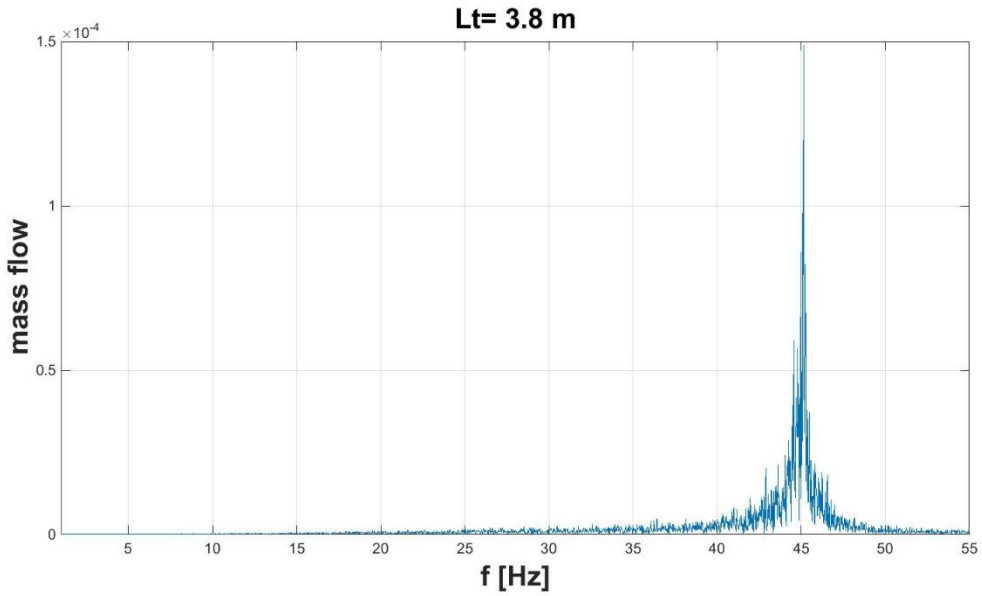

Figure 48: FFT analysis of mass flow oscillation with L_t = 3.8m

Established that L_t does not significantly affect the surge frequency result, a parallel investigation has been conducted to define the influence of compressor effective length Figure 49 shows the resulted obtained changing compressor effective length from the previous value of 0.2m to 1.2m, which is the length of the suction duct.

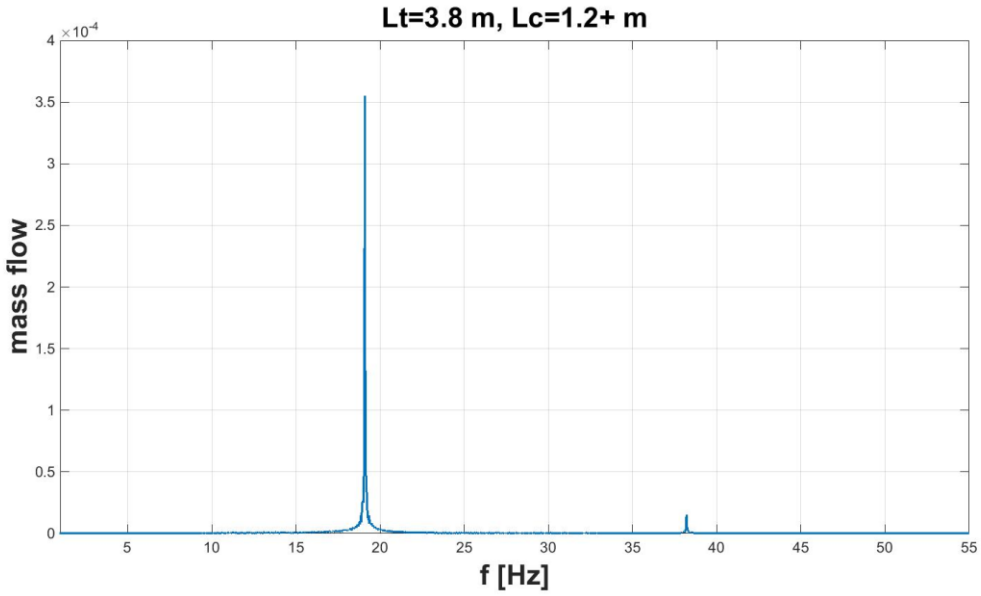

Figure 49: FFT analysis of mass flow oscillation with L_t = 3.8m and L_c = 1.2m

According to Figure 49, mass flow oscillation is subjected to a significant decrease. The fundamental frequency change from 45Hz to 19Hz. The last calculation reported in this section has been developed on turbocharger model considering that the whole test rig duct length is included in the compressor equivalent length and only the last part, close to the discharge valve is effectively contained into the throttle equivalent length. The values used for the model's equivalent lengths are: L_c = 3.66m and L_t =1.5m.

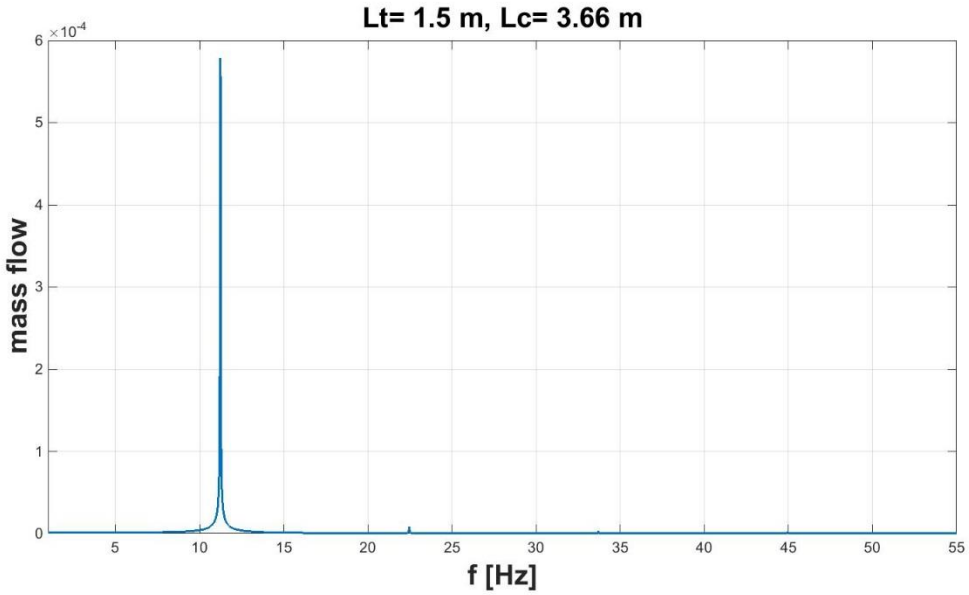

Figure 50: FFT analysis of mass flow oscillation with L_t = 1.5m and L_c = 3.66m

A frequency of 11.7Hz was calculated in this configuration. Even if the model at this stage did not fully represented (as it was in the first part of *simulation results* paragraph) the real test rig the obtained value better fits to the mechanical and fluid dynamical oscillation measured on the real compression system.

The model represents in a realistic way all the stable and instable phenomenon that rise in the system dynamic and returns a frequency value comparable to the measured one.

4.7. Conclusions

The T-RIG1 layout, comprising a turbocharger with the compressor operating on ambient air and the turbine being fed by hot exhausts, with independent flow lines, was studied and modeled during this study. The main goal was to build and validate a model able to replicate surge phenomenon of a centrifugal compressor in free spool configuration, in view of its application to turbocharged fuel cell systems. The system has been characterized with different experimental tests and data, towards its validation. In particular, the validation on the frequency domain based on experimental data allowed to provide a first confirmation of the goodness of (i) compressor map extension towards negative flows, (ii) model representation of piping and volumes upstream and downstream of the compressor, (iii) expected surge frequencies, which may be later used for early detection. Further investigation will focus on the coupling of the turbomachinery with larger volumes, representative of actual hybrid systems: first on a simulation level and then, as soon as the turbocharged hybrid system emulator will be commissioned at the University laboratory, also at experimental level. On the other hand, the results and methods proposed in this paper provide the reader with a useful approach to model, in a simplified but accurate way, the dynamic behavior of a centrifugal compressor from steady condition to surge. Therefore, the impact of the study is not limited to the simulation of hybrid systems but to all the turbomachinery community operating with centrifugal compressors.

Moreover, on the experimental side of this study, test acquisitions show that, for the supplied machine, curve composed by series of operating point between surge line and no mass flow condition (Zone II) for a constant reference rotational speed of 171000rpm, well shape a parabolic trend.

The T-RIG1 dynamic model permitted to perform a first investigation on the effect of different parameters such as volume size, shaft inertia and equivalent lengths, on the surge cycles characteristics.

5. A Hybrid System dynamic model for compressor instability investigations based on Hyper facility

5.1. Facility description

The Hybrid Performance (Hyper) project at NETL makes use of hardware simulation of a 200kW to 700kW solid oxide fuel cell (SOFC) system coupled to a 120kW turbine [32]. The use of a robust hardware-in-the-loop simulation (HiLS) facilitates the evaluation of dynamic performance during transient operation, avoiding the destruction of expensive fuel cell equipment and mitigating financial risk. The pressure vessels and a natural gas burner, driven by real time models, are used to simulate the fuel cell and gasifier in the system. The balance of plant hardware is composed of turbomachinery, a synchronous power generator, a continuously variable load bank, exhaust gas recuperators, and the associated valves needed to control the system airflow. The air intake from the test cell is compressed and guided around the turbine scroll in the compressor plenum. The compressed air is either directed to the system exhaust manifold and stack or routed through system piping to the heat exchangers for recuperation of turbine exhaust gas heat. The compressed, preheated air exiting the heat exchangers is expanded into a pressure vessel with a volume representative of the cathode volume of a solid oxide fuel cell and the associated air distribution manifold.

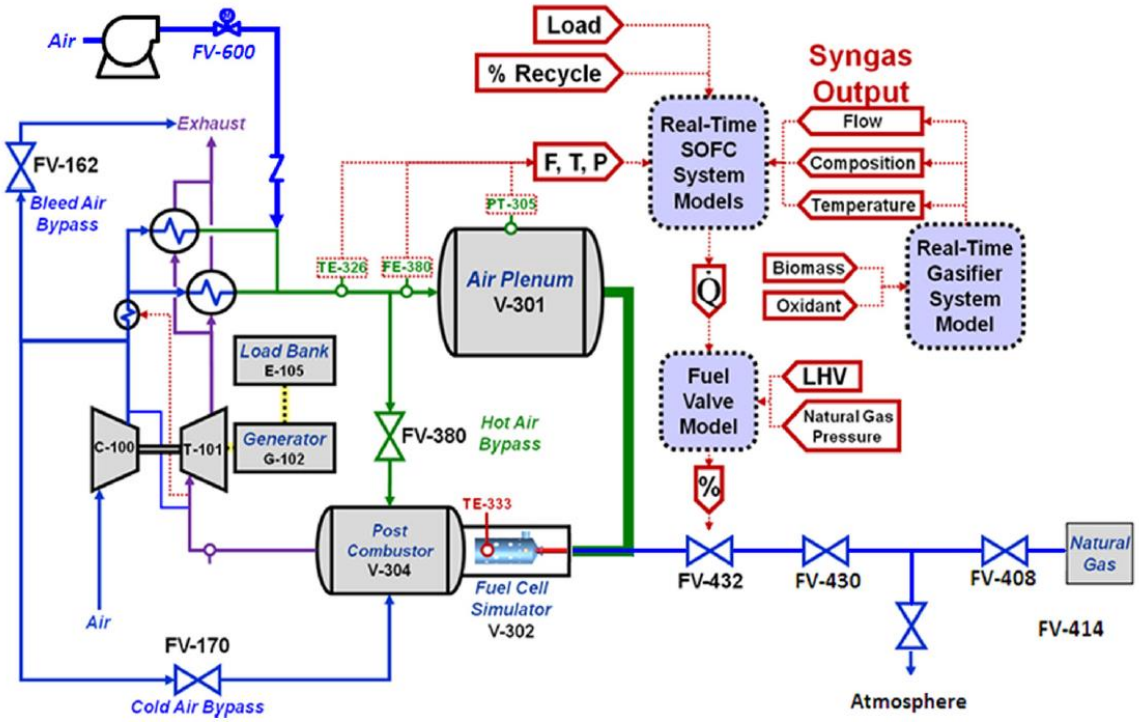

Figure 51: Flow diagram for the hybrid performance simulation facility at NETL.

Gas Turbine (C-100, T-101, G-102). A 120 kW Garrett Series 85 auxiliary power unit (APU) is used for the turbine and compressor system and consists of single shaft, direct-coupled turbine (T-101) operating at a nominal 40,500 rpm, a two-stage radial compressor (C-100)

and gear-driven synchronous (400 Hz) generator (G-102). The electrical generator is loaded by an isolated 120 kW resistor bank (E-105). The compressor is designed to deliver approximately 2 kg/s at a pressure ratio of about four. The compressor discharge temperature is typically 475 K for an inlet temperature of 298 K.

This turbo-machinery Figure 52, in its many variants is a ubiquitous engine, used as airborne APU in many famous aircraft such as the Boeing 737, KC135, Breguet Atlantic, Transall to name just a few. Moreover, it has been utilized in several ground power-support units, some also providing heating/cooling functions for field hospitals or the like.

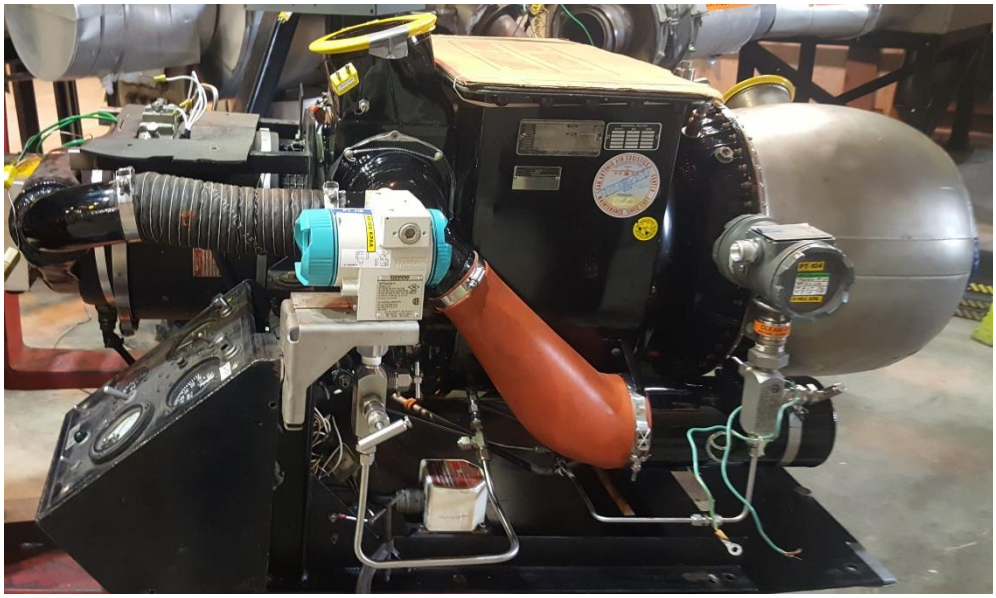

Figure 52: GTCP85 micro gas turbine at Hyper facility.

The power available at the shaft of most units is in the region of 150kW at a rotational speed slightly above 40000 RPM. Garrett AiResearch started design of this engine in the early 1950s but later on, several improvements have been added. The basic design of the GTCP85 is similar on all the versions, featuring a two-stage radial compressor, a single stage radial turbine and a single, reverse flow, can-type, tangentially mounted combustion chamber with a single duplex fuel nozzle to atomize the fuel, Figure 53.

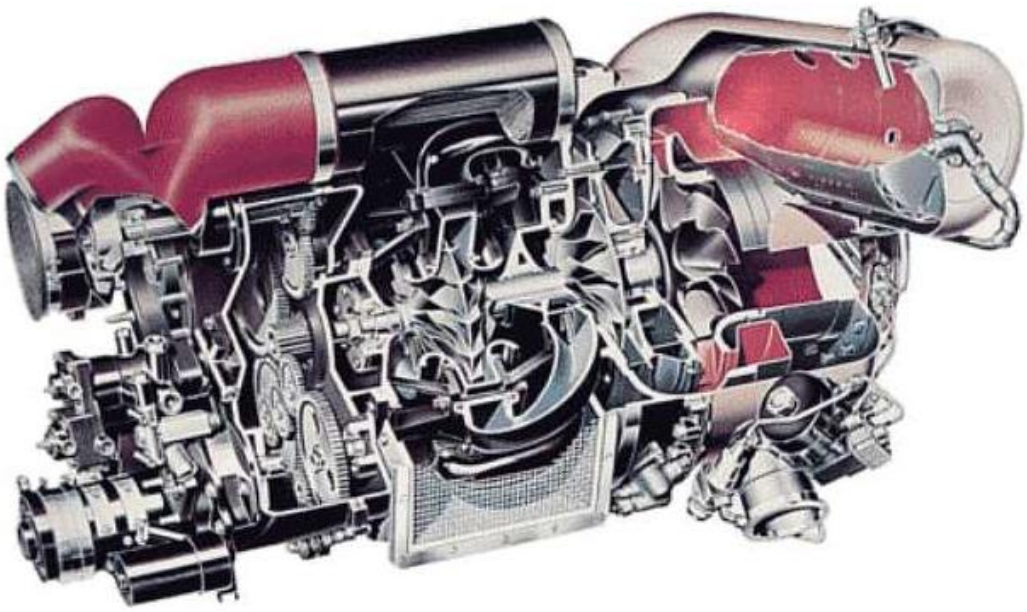

Figure 53: Sectioned drawing of the GTCP85 APU.

For this specific research application, the original configuration has been slightly changed, the external casing surrounding the entire machine has been modified in order to interface the pipe coming from the combustor chamber of the emulator directly with the turbine inlet. The combustor and original fuel system were removed. Referring to Figure 51 here are described some of the main features of the Hyper plant recalling nomenclature used in the diagram:

- Heat Exchangers (E-300 and E-305). The facility includes two counterflow primary surface recuperators (E-300 and E-305) in parallel with a nominal effectiveness of 89% to preheat the air fed to V-301;
- Pressure Vessels (V-301 and V-304). Pressure vessels represent the fuel cell cathode chamber and oxidant manifold volume (V-301), and the post combustion volume (V-304) of the fuel cell system.
- Fuel Cell Simulator (V-302). The thermal characteristic of the effluent exiting the post combustor of an SOFC system is simulated in hardware using a natural gas burner with an air-cooled diffusion flame.
- Cold-Air Bypass (FV-170). The cold-air bypass valve is used to bypass air from the compressor directly into the turbine inlet through the post combustor volume.
- Hot-Air Bypass (FV-380). The hot-air bypass valve is used to bypass air from the recuperators exit directly into the turbine inlet through the post-combustor volume.
- Bleed Air (FV-162). The bleed valve is used to discharge cold compressed air into the atmosphere. It is very effective in augmenting compressor surge margin, but it detrimentally affects system efficiency.
- Fuel Valves Line (FV-408, FV-430, FV-414). An industry standard double block (FV-408, FV-430) and bleed (FV-414) ON/OFF fuel valve are used to cut and vent the fuel from the line to the atmosphere.

5.2. Surge avoidance/recovery actions

As well know surge is a dangerous dynamic instability that may occur in compressors due to many reasons.

According to [6] and [7], when operating point overcomes the surge line on the characteristic map of compressor, and surge occurs, the overall annulus averaged mass flow varies with time, so that the entire compressor change more or less in phase from being unstalled to stalled and back again. As soon as the pressure of the volume connected to the compressor is higher than compressor outlet pressure, the fluid tends to reverse or even flow back in the compressor. Consequently, the plenum pressure will decrease, lower than compressor discharge and the flow reverses again.

Depending on the application many different actions have been proposed during the years to avoid compressor surge or to fully recover from it.

For those systems where a rotational speed control is applicable, the importance to choose an appropriate ramp rate during transients result crucial. For example, when a very fast maneuver such as an Emergency Shut Down (ESD) procedure must be performed on a turbomachinery coupled to a large volume there is a defined speed rate which identify the compromise between the possibility to quickly shut down the turbomachinery and to avoid surge phenomena at the same time.

In other similar cases when surge is detected, or the trend of the compressor operating condition is clearly driving the system to the unstable region, it is necessary to momentarily adjust the speed setpoint to restore a safe enough margin from the surge line.

Other authors focused more on the use of valves placed at different locations in the system layout, Bartolini et al. [8] address the problem of active surge control in compressor systems by using a Close-Coupled Valve (CCV) and a Throttle Valve (TV) as actuator devices simultaneously acting on the compressor.

Moreover, according to Simon et al. [9], an active compressor stabilization system conceptually consists of sensors to detect fluid disturbances within the compression system, actuators to introduce desired perturbations, and a suitable control law connecting the two. They suggest many methods to introduce unsteady fluid perturbation: varying throttle area, moving a plenum or duct wall, introducing or bleeding off mass flow, varying the heat addition in the plenum (when for instance there is a combustor), as well as introducing a variable throttle between the compressor and plenum.

Systems characterized by high complexity such as micro gas turbine-fuel cell hybrids have many constrains to respect. For example, the need to maintaining an optimal level of efficiency on the wider range for operability as possible must deal with fluid dynamic stability limits and temperature operability ranges of several components. To satisfy these constrains the impact of using by-passes or bleed valves to manage such kind of systems during both steady state and transient conditions has been studied.

Regarding the plant studied in this work, Pezzini et al. state in [11], that the cold-air bypass in a hybrid system is an innovative actuator in hybrid system, which has a strong coupling

on several parameters: cathode mass flow, turbine inlet temperature, turbine speed, and surge margin. Cold air in this plant is used to by-pass the air coming from compressor discharge directly to the turbine inlet, without crossing heat exchangers, the fuel cell emulator and the following combustor. This helps for example, to reduce the pressure drop of the system when required.

Moreover, with a cold air transient test in[3], they demonstrated that a significant valve opening increases the surge margin in the immediate few seconds after the movement. This approach could be helpful in an emergency shutdown procedure by moving the compressor transient operation just a little bit on the right of the operating map to increase the surge margin.

These and other considerations have provided an opportunity to start the study and development of the Hyper dynamic model described in this section in order to simulate both the dynamic behavior of the whole system in conditions of instability, and to study and test strategies of surge recovery in a secure virtual environment without risks for the plant and operators.

The activities have been focused in particular on: the impact of volume size on surge characteristics; the possibility to recover from surge acting on the cold by-pass; and on the analysis of possible interaction between control system and dynamic response of the system in stable and unstable conditions.

5.3. Model description

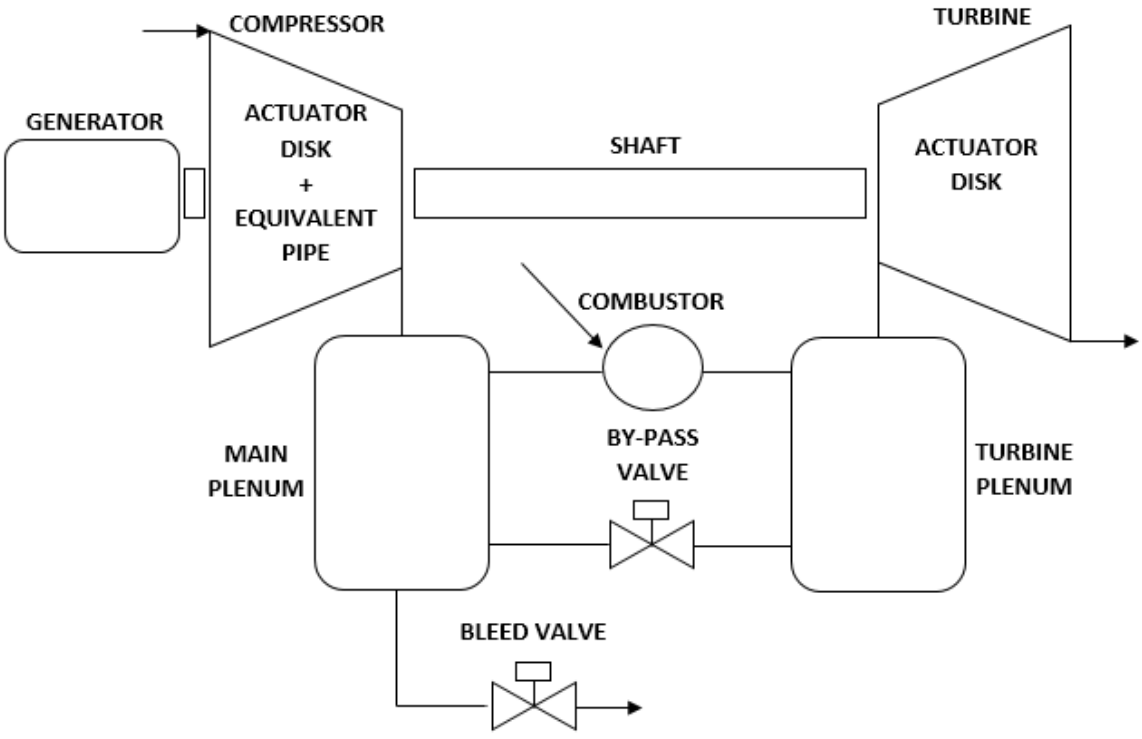

Figure 54: Model layout and simulated components

The modeling approach used for the Hyper facility starts from the work conducted by Greitzer in [12]. This paper, published in 1976, describes how to create a nonlinear model able to predict the response of a compressor system when the operating point moves from a stable to an instable zone. The compression system modeled by Greitzer consisted of a compressor, a duct, a volume and a throttle. As shown by Figure 54, the Hyper model includes additional components such as turbine, shaft and combustor to better replicate the facility layout and match its performance. Many of these components previously developed during the work reported in [33] have been enhanced in the present study.

The B parameter for this system calculated with Eq. (5) is estimated to be approximately 1.25.

5.3.1. Compressor model

The compressor has been modelled using the lumped-volume method; this approach couples an actuator disk and constant area pipe to have a superposition of effect able to replicate the dynamic behavior of a real component. The actuator disk consists in an interpolator-extrapolator developed in Matlab code by TPG able to return the source term *C* from compressor steady state map, which needed in the momentum differential equation; this equation, which can be written as in Eq (49), it is solved in the pipe model.

$$\frac{d\dot{m}_c}{dt} = (C - \Delta p)\frac{A_c}{L_c} \tag{49}$$

Where:

$\dot{m}_c$: mass flow rate across the compressor [kg/s]

C: source term of momentum equation, from steady state compressor characteristics [Pa]

Δp: current pressure difference between outlet and inlet of the compressor [Pa]

A_c: equivalent cross-sectional area of compressor [m^2]

L_c: compressor equivalent length [m]

Differently from the approach used in [33] where a first order delay has been adopted, the further rate of change of *C* term is not modeled.

The steady state map included in the compressor model expresses the pressure ratio as function of mass flow rate and rotational speed. The interpolator inside this component utilizes referred parameters to correctly consider the impact that variation in inlet pressure or temperature have on compressor performance.

$$\dot{m}_{ref} = \frac{\dot{m}\sqrt{\frac{T_{in}}{T_0}}}{\frac{p_{in}}{p_0}} \tag{50}$$

$$N_{ref} = \frac{N}{\sqrt{\frac{T_{in}}{T_0}}} \quad \textbf{(51)}$$

The source term *C* of Eq (49) is derived from the steady state characteristics (map) of the compressor at each step of simulation by the interpolation procedure; while the Δp is the difference between the pressure calculated by the downstream plenum and the compressor intake pressure. The difference between these quantities determines the instantaneous increment or decrement in mass flow rate. During transients, Δp is different from *C*.

The equivalent length has a double effect on model performance. On the one hand, it has a proportional influence on the time response of compressor mass flow evolution, on the other hand, the increase of this dimension helps to obtain a model computationally more stable, given the possibility to have a coarser simulation sample time with the result of faster model and leaner simulations.

Since during long and slow transients, the dynamic reaction of the compressor is often negligible compared to the overall system response, the equivalent length can be increased to speed up the simulations retaining numerical stability, without significantly affect the reliability of simulated results.

For quick transients, such as during the simulation of a surge event or a sudden valve opening, when the system response has a time scale comparable to compressor one, the actual equivalent compressor length should be restored to increase accuracy of results. It follows that, for stability reasons, in these cases a decrease of sample time is required, which, as introduced before, affects computational effort and time.

Figure 55, Figure 56 and Figure 57 show the influence of compressor equivalent length on results reported on the performance map. In these graphs, the instantaneous difference between the *C* and Δp terms is reported. The line called "*Trace* Δp*"* is the result obtained considering the actual Δp term only, while the so called "*Trace C"* is calculated considering the C term only. It is possible to observe how the two lines gradually get closer as the delay, purely due to the calculation process, decreases. When the two curves collapse on each other it is possible to assert that there is no influence of the calculation delay anymore (Figure 57). To obtain a computationally stable simulation for quick transients, a decrease of model integration time of one order of magnitude is then required.

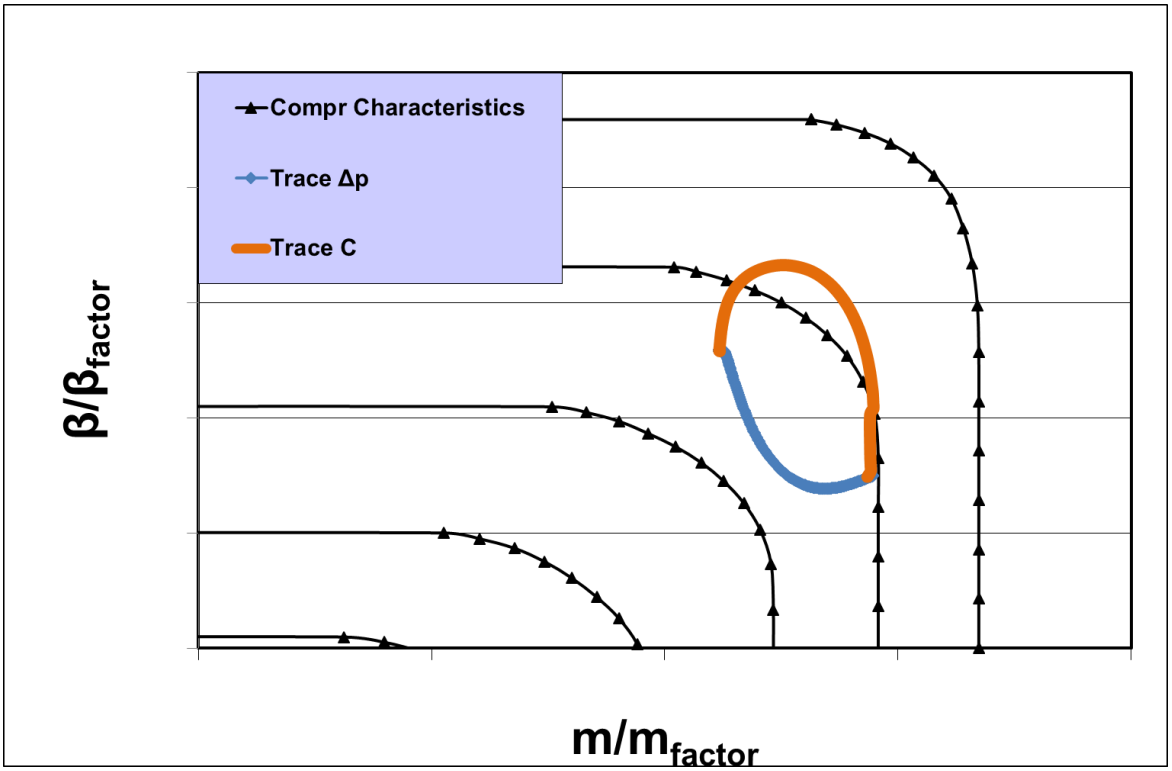

Figure 55: Example of compressor response with long L_c

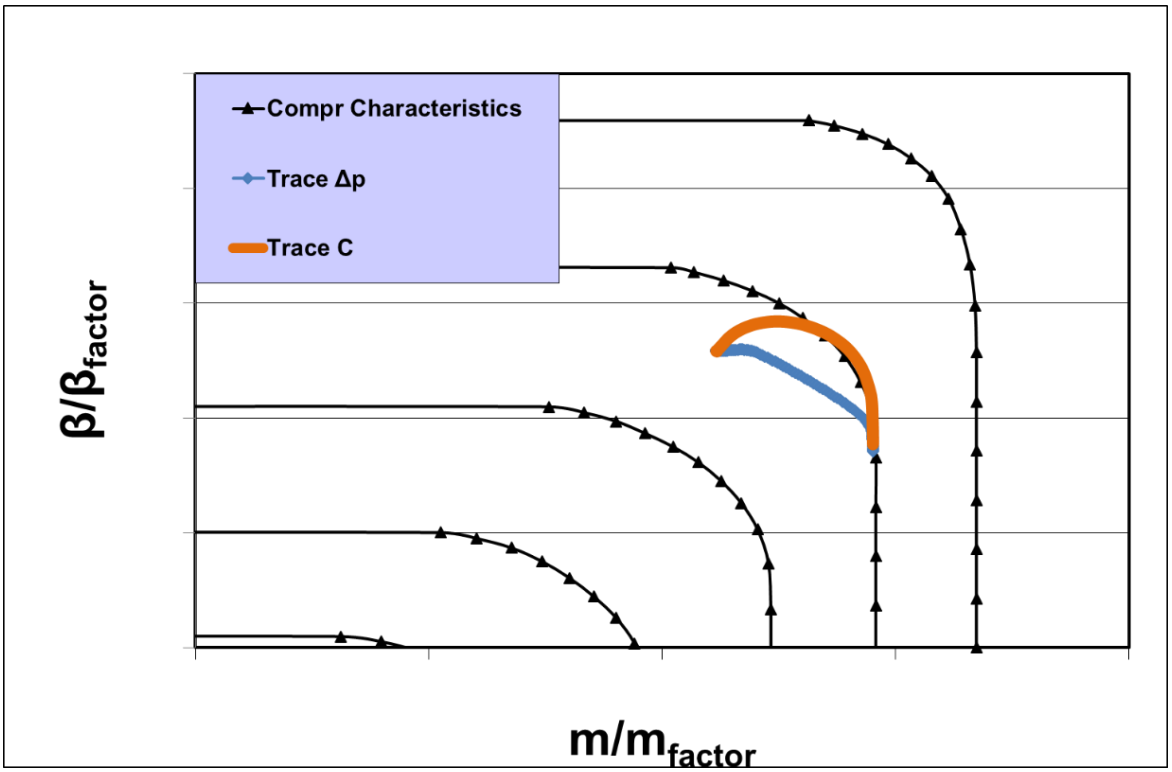

Figure 56: Example of compressor response with medium L_c

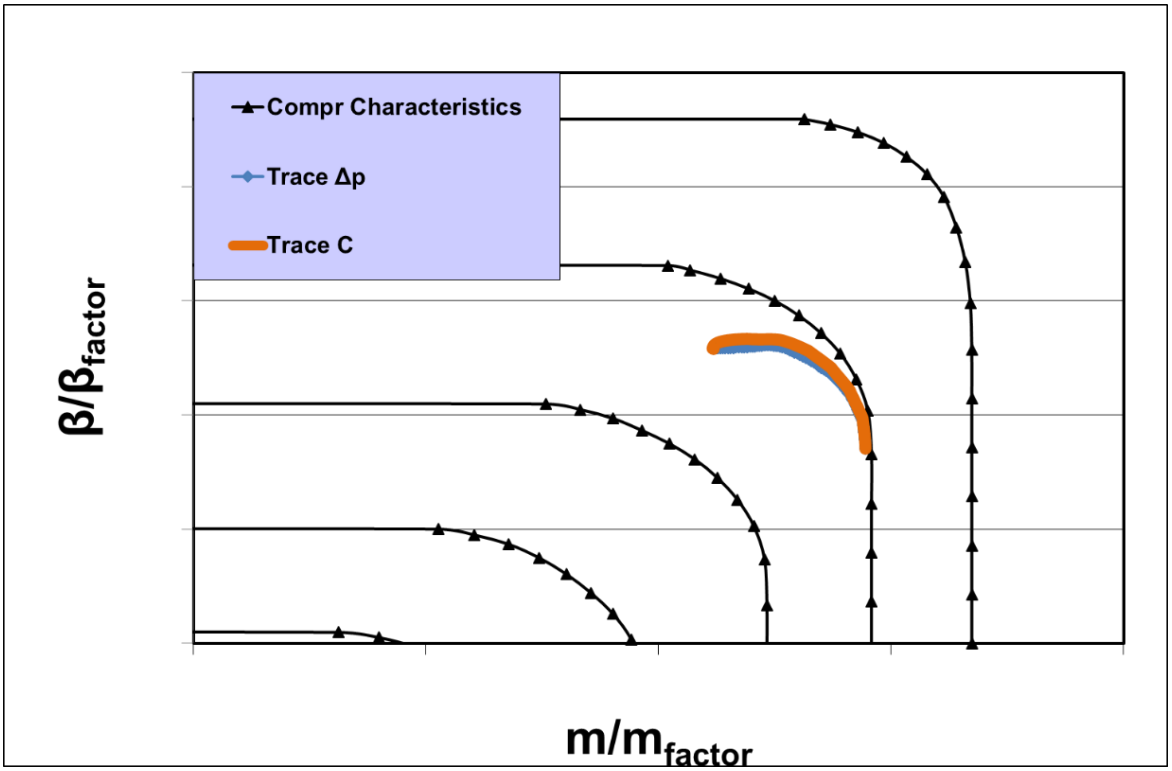

Figure 57: Example of compressor response with short L_c

Two other outputs of the compressor model are the surge margin and the required mechanical power.
The first one called K_p, is an online indicator of the distance between the current operating point and the surge line; this component evaluates the value of surge margin using Eq (52).

$$K_p = \frac{\beta / \dot{m}}{\beta_{surge\ line} / \dot{m}_{surge\ line}} \tag{52}$$

Regarding the mechanical power of the compressor, it is calculated starting by the torque definition.
Assuming no pre-whirl and knowing that for turbomachines the applied torque is equals to the change in angular momentum of the fluid, therefore equation for compressor torque can be expressed as

$$\tau_c^+ = \dot{m}\, r_2\, \sigma\, U_2 \qquad \dot{m} > 0 \tag{53}$$

This torque definition is valid for forward flow, however when deep surge occurs compressor instantly works in reverse flow, for this reason, an expression for the compressor torque at negative mass flow is needed. According to [34] an axial compressor in reversed flow can be viewed as a throttling device. In this work as for [31] it is assumed that a centrifugal compressor in backflow can be approximated with a turbine this allows for the use of Euler's turbine equation

$$\tau_c^- = -\dot{m}\, r_2\, \sigma\, U_2 \qquad \dot{m} < 0 \tag{54}$$

Combining Eq. (49) and (53) it possible to obtain a generalized form of compressor torque valid for every regime of mass flow rate.

$$\tau_c = |\dot{m}|\, r_2\, \sigma\, U_2 \qquad \forall \dot{m} \tag{55}$$

which is in accordance with the compressor torque used by [7].

The resulting torque is multiplied by the angular speed of the shaft, in this way in possible to obtain the mechanical power of the compressor.

$$P_c = \tau_c\, \omega \tag{56}$$

Since this turbomachinery is constituted of multiple impeller in series, it has been chosen to adopt a multiplicative factor to increase the calculated power.

The mask of this component contains the following editable input fields:

- Dimensions: the user can set here the flow-through area, the equivalent length and the impeller outlet diameter of the compressor which are utilized by the actuator disk and the following equivalent pipe.
- Power factor: this value represents the multiplicative factor which is used in the power calculation section of the model.
- Slip factor: this characteristic parameter for the compressor is needed for the power derivation.
- Sample Time: this is the current sample time used by the component to solve the implemented equations.
- Other information required by the compressor model are for example the name of the Matlab structure where the performance maps are saved, the fundamental map is the one expressed as function of pressure ratio versus mass flow rate, from which the C term of equation (49) is derived. In this component it is also available the possibility to utilize the compressor efficiency map to derive power and flow outlet temperature but for this specific application this option is disabled.
- Surge position: this value indicates the number of points on each iso-speed curve between the choke region and the unstable working field. It is used to identify

pressure ratio ad mass flow values on the surge line corresponding to current operating point and to calculate the surge margin.

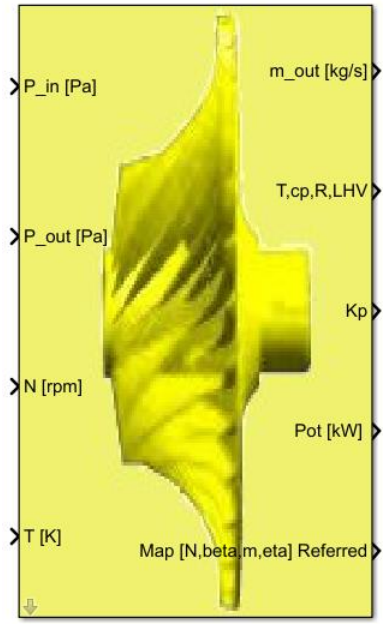

Figure 58: Compressor modelled in Matlab® Simulink

5.3.2. Valve model

Two different valves models are utilized in this work.

The first type used to simulate the fuel valve is a combination of an actuator disk plus two separate first order delays. In the actuator disk is implemented the following equation to obtain the fuel mass flow rate as function of the pressure drop across the fuel valve, valve rangeability and fractional opening:

$$\dot{m} = Cv_{max}\, R^{(FO-1)} \sqrt{\Delta p\, \rho} \qquad \textbf{(57)}$$

Where:

$\dot{m}$:	fuel mass flow rate	[kg/s]
$Cv_{,max}$:	maximum flow coefficient	
R :	valve rangeability	
FO :	fractional opening	[-]
Δp :	pressure drop across the valve	[Pa]
ρ :	flow density	[kg/m^3]

The pressure drop is calculated as percentage of the inlet pressure condition, pressure that is kept constant during the simulation considering a stable pressure level in the real fuel supply pipeline.

Since the response of the valve cannot be instantaneous a first order delay is implemented to describe the mechanical delay of the valve actuator and another one is representative of the dynamic delay of the fluid crossing the valve.

In the fuel valve mask, it is possible to insert information about the Cv_{max} and Rangeability, all the other parameters are set directly under the mask.

The second type of valve is used twice into this model to simulate both by-pass and bleed valves. The first is connected in between the two plena used to represent the system, while the bleed valve connects the main plenum directly to the ambient condition. In both cases the mass flow rate crossing the valve is function of the two pressure levels at the extreme of the valve and of the fractional opening. In this case the momentum equation is chosen to represent the dynamics of the valve and its source term F consists in the steady state pressure drop calculation at the current valve boundary conditions. Therefore, the set of equations for this component can be written as follow:

$$\frac{d\dot{m}_T}{dt} = (\Delta P - F)\frac{A_{T_{FO}}}{L_T} \quad \textbf{(58)}$$

$$F = \frac{\dot{m}_T^2}{2\rho A_{T_{FO}}^2} \quad \textbf{(59)}$$

$$A_{T_{FO}} = A_T\, FO \quad \textbf{(60)}$$

where:

$\dot{m}_T$:	throttle mass flow	[kg/s]
ΔP :	current pressure difference across the valve	[Pa]
F :	steady state throttle pressure drop	[Pa]
L_T :	quivalent throttle duct length	[m]
ρ :	fluid density	[kg/m^3]
A_T :	flow-through throttle area	[m^2]
FO :	fractional opening	[-]

For a given turbine speed condition, the main valve can be used to modify the compression system operating point. For example, by decreasing the valve fractional opening the compressor operates at lower mass flow values, thus reducing its surge margin. In this valve a dead time and a first order delay are implemented on the fractional opening signal, this

because a real valve always shows a delay between the opening/closing command and the actual response of the valve actuator.

The user can set the following parameters in the component mask:

- Throttle Dimensions: in this field the valve flow through area and the equivalent length of the downstream pipe are required
- Flow Density: here the user must insert an estimation of the flow density at the point of the system where the valve is placed.
- Deadtime delay: it represents the deadtime expressed in seconds required from the valve actuator to reacts, it is applied between inlet port for the fractional opening signal and the real value ridden by the model.
- First order delay: it is applied in series to the valve deadtime and it is the time constant for a first order delay applied to the fractional opening signal.
- Sample Time: this is the current sample time used by the component to solve the implemented equations.

5.3.3. Plenum models

Compressor discharge is connected to the main plenum that represents most of the volume contained into the system, where fluid has no kinetic energy and all the potential energy is associated with the compression of the gas.

Considering the dimensions of the facility the volume contained inside the pipes and components between compressor and combustor (Figure 51) is estimated around 2.9m^3. The time dependent continuity equation implemented in the plenum model is:

$$\frac{dp_p}{dt} = (\dot{m}_c - \dot{m}_T)\frac{kp}{\rho V_p} \qquad \textbf{(61)}$$

where:

$\frac{dp_p}{dt}$: rate of change of plenum pressure

$\dot{m}_c$: inlet mass flow (coming from compressor) [kg/s]

$\dot{m}_T$: outlet mass flow (sum of outlet streams) [kg/s]

k : specific heat ratio [-]

ρ : flow density [kg/s]

V_p : plenum volume [m^3]

The information required by the plenum mask are:

- Volume: the size of the volume expressed in cubic meters.
- Fluid characteristics: approximated local fluid density and specific heat ratio are the quantities needed.

- Sample Time: this is the current sample time used by the component to solve the implemented equations.

The second type of plenum used in this model is placed downstream to a merging point where hot gasses coming from the combustor meet the colder bypass air, in this case the impact of temperature on the energy content of the resulting stream is significant. In order to take into account the temperature difference effect, the continuity equation has been coupled together with the energy one. The set of equation chosen for this version of the plenum model are the following:

$$\frac{d(M)}{dt} = \sum \dot{m}_{in} - \sum \dot{m}_{out} \quad \textbf{(62)}$$

$$\frac{d(M\,T)}{dt} = \frac{c_{p,out}}{c_v}\left[\sum (\dot{m}_{in}\,T_{in}) - \sum (\dot{m}_{out}\,T_{out})\right] \quad \textbf{(63)}$$

Where:

$M = \rho\,V$: represents the mass stored in the plenum [kg]

T : temperature of the plenum itself which corresponds to the outlet temperature T_{out} [K]

The perfect gas state law is then used to calculate the plenum pressure p once temperature T and density ρ are known.

$$p = \rho\,R\,T \quad \textbf{(64)}$$

As shown by Figure 59, the plenum mask contains the following editable fields:

- Number of input streams: a popup menu permits to the user to select the number of input streams connected to the volume.
- Number of output streams: a popup menu permits to the user to select the number of output streams connected to the volume.
- Volume: amount of volume contained in this component expressed in cubic meters
- dtSampleTime: this is the current sample time used by the component to solve the implemented equations.

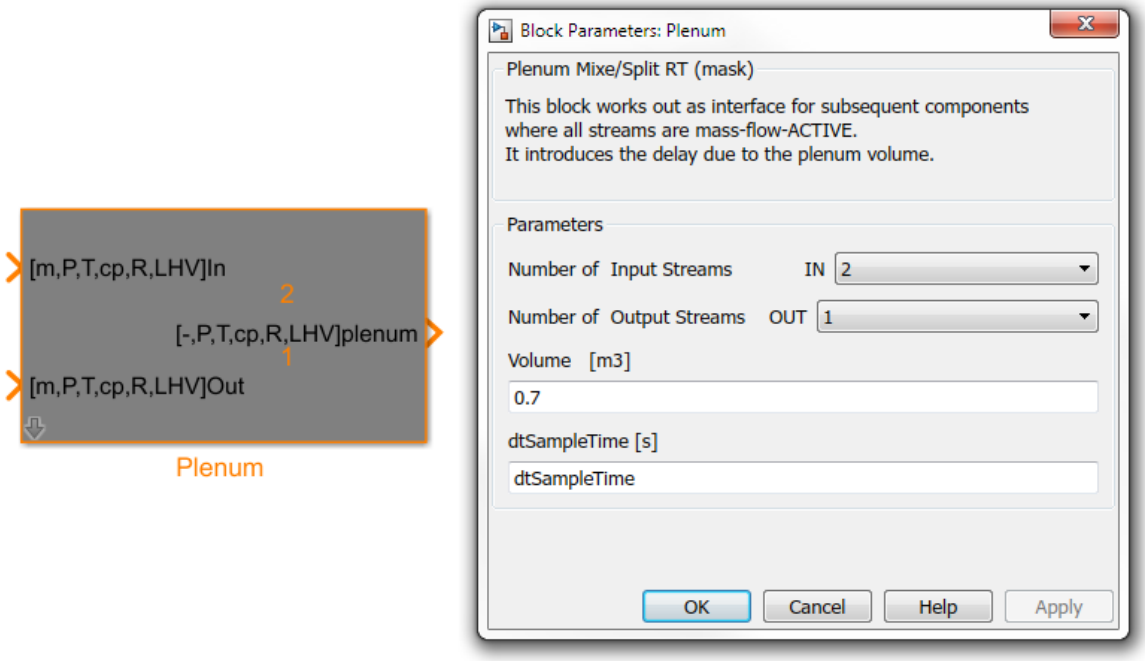

Figure 59: Plenum model and its user interface (mask)

5.3.4. Shaft model

Since in APU configuration the turbine drives the compressor and the generator, a shaft component able to compute the balance of power between these three components is required:

$$\frac{d\omega^2}{dt} = \frac{2}{J}\left(P_{turb} + P_{compr} + P_{loss} + P_{gen}\right) \quad \textbf{(65)}$$

where:

ω : rotor angular velocity [rad/s]

J : rotor mechanical inertia [kgm^2]

P_{turb} : turbine power [W]

P_{compr} : compressor power [W]

P_{loss} : losses [W]

P_{gen}: generator mechanical power [W]

As visible in Figure 60, this component receives information on the current powers delivered from or required for the other rotating component which are connected to the input ports and it computes and returns the rotational speed as feedback for the same simulated modules.

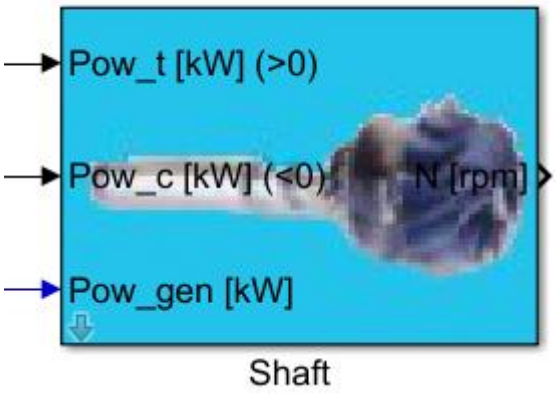

Figure 60: Shaft model implemented in Simulink

There is also the possibility to enable the losses calculation for such a component. In particular, a quadratic relationship between mechanical losses and rotational speed is available in this form:

$$P_{loss} = P_{loss,o.d.}\left(\frac{N}{N_{o.d.}}\right)^2 \quad \textbf{(66)}$$

where:

$P_{loss,o.d.}$:	is the amount of power lost at on design condition	[kW]
$N_{loss,o.d.}$:	is the corresponding value for the on design rotational speed	[rpm]

The information required from the mask fields are:

- Rotor mechanical inertia: here the user can insert the overall value of mechanical inertia considering all the rotating mass connected to the shaft.
- Power losses On-Design: this field is dedicated to the value of the amount of power lost at on-design condition.
- Speed On-Design: on design value of shaft rotational speed.
- Sample Time: this is the current sample time used by the component to solve the implemented equations.

5.3.5. Turbine model

In previous studies authors have investigated compressor systems in free spool configuration, often approximating the turbine to a valve with a constant throttle gain and a power derivation obtained only from current mass flow rate and rotational speed conditions. In this work, an innovative aspect can be identified in the introduction of real turbine maps (mass flow rate-ER and efficiency-ER) inside the system model. This implementation allows to the possibility to simulate the temperature effect due to the presence of a hot stream coming from the combustor.

Knowing the inlet and outlet pressure information and the current rotational speed the turbine map interpolator returns the value of updated mass flow rate, furthermore, with the same calculation routine the turbine efficiency is interpolated. Figure 61 and Figure 62 report the performance map implemented in the Hyper model to represent the turbine behavior.

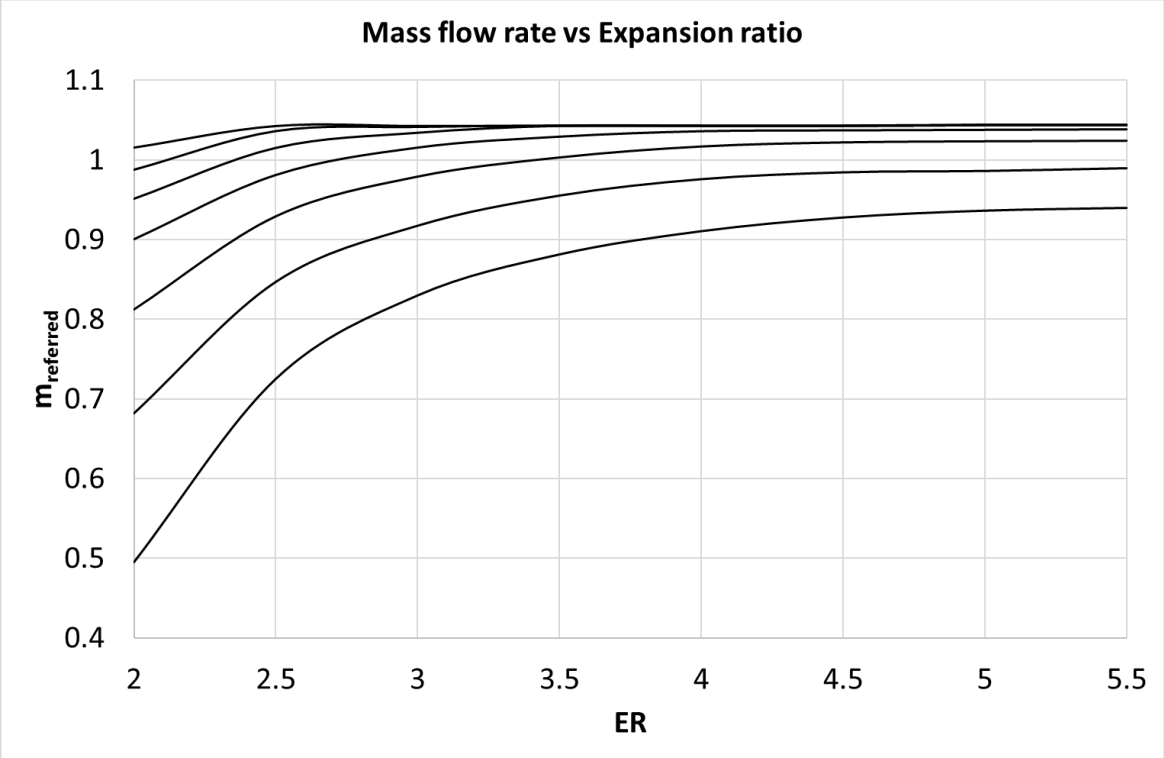

Figure 61: Turbine map from Hyper facility, referred mass flow rate versus expansion ratio

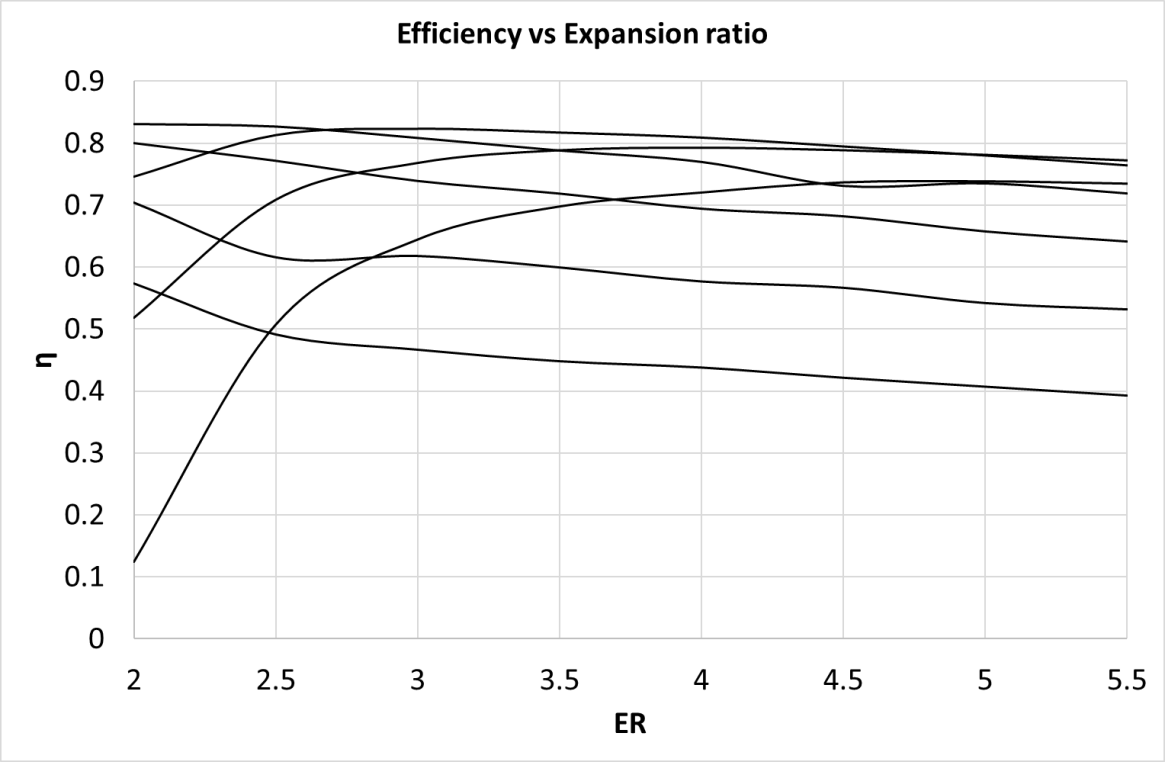

Figure 62: Turbine map from Hyper facility, efficiency versus expansion ratio

As introduced before, the turbine map interpolator can define the current turbine efficiency, therefore including such information into the isentropic efficiency definition, is it possible to calculate the turbine outlet temperature and the turbine power accordingly. In Eq. (67), (68) and (69) the power derivation procedure is reported.

$$T_{out,is} = T_{in} \left(\frac{1}{ER}\right)^{\frac{k-1}{k}} \quad \textbf{(67)}$$

$$T_{out} = T_{in} - \eta \left(T_{out,is} - T_{in}\right) \quad \textbf{(68)}$$

$$P_{turb} = \dot{m}\, c_p \left(T_{in} - T_{out}\right) \quad \textbf{(69)}$$

5.3.6. Combustor model

This component simply integrates a function able to calculate the combustor outlet temperature starting from the energy content of the inlet streams. Considering the two input steams, air and fuel respectively, the steady state energy balance and continuity equation for this component can be written as follows:

$$\dot{m}_{out}\, c_{p,out}\, T_{out} = \dot{m}_f\, \eta_{comb}\, LHV_f + \dot{m}_f\, c_{p,f}\, T_{f,in} + \dot{m}_a\, c_{p,a}\, T_{a,in} \quad \textbf{(70)}$$

$$\dot{m}_{out} = \dot{m}_f + \dot{m}_a \quad \textbf{(71)}$$

It is therefore possible to reformulate these equations making the combustor outlet temperature explicit.

$$T_{out} = \frac{\dot{m}_f \, \eta_{comb} \, LHV_f + \dot{m}_f \, c_{p,f} \, T_{f,in} + \dot{m}_a \, c_{p,a} \, T_{a,in}}{\left(\dot{m}_f + \dot{m}_a\right) c_{p,out}} \quad \textbf{(72)}$$

The combustor block has two input ports, one for the air stream and one for the fuel and on the other side one single output for the exhausts. Each single stream is constituted by six signals, which identify the main flow properties useful for the component calculation. These six signals are:

- Mass flow rate [kg/s]
- Pressure [Pa]
- Temperature [K]
- Specific heat [J/kg K]
- Gas constant [J/kg K]
- Lower Heating Value [J/kg]

5.3.7. Generator model

The Generator block can simulate both a motor or a generator depending if the power is taken from or supplied to the machine. In this study a constant efficiency model is utilized to simulate the generator.

As shown by the subsystem reported in Figure 63 the component has one input port and two outputs. It receives as input the electrical power requested, Pel_R. It is positive when the model works as a generator, negative when as motor. The first output, Pel_R, simply transfers the information of electrical power across the component for monitoring reasons. The second and last output port, Pmech_R contains the signal of mechanical power requested to satisfy the electrical power demand. The mechanical power is therefore only function of the electrical power request and electrical efficiency of the generator.

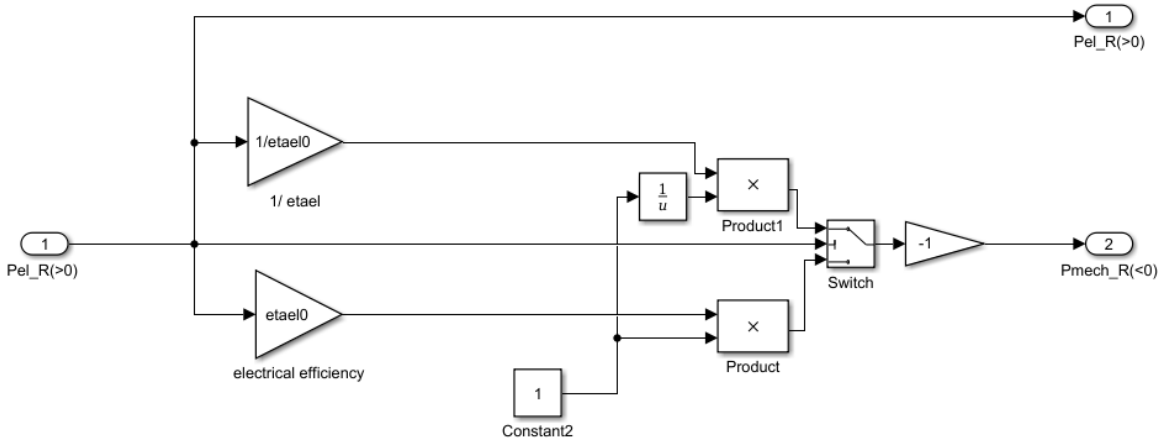

Figure 63: Subsystem view of the Generator model

5.4. Compressor map extension for surge modelling

In this section, the calculation process to extrapolate compressor characteristics beyond the compressor surge line and in the reverse flow region is reported. This approach was thought for those cases when the stable region of the compressor map is known, in other worlds when it is possible to have a complete set of iso-speed curves to describe the compressor steady state stable working conditions like in Figure 66.

As shown by Figure 64, the compressor map ideally can be divided in three separated zones, respectively:

- Zone I: the reverse flow zone, it is the unstable operating field characterized by negative mass flow rate conditions
- Zone II: it is unstable region between the surge line and the no-flow condition
- Zone III: the stable flow field or normal operating region.

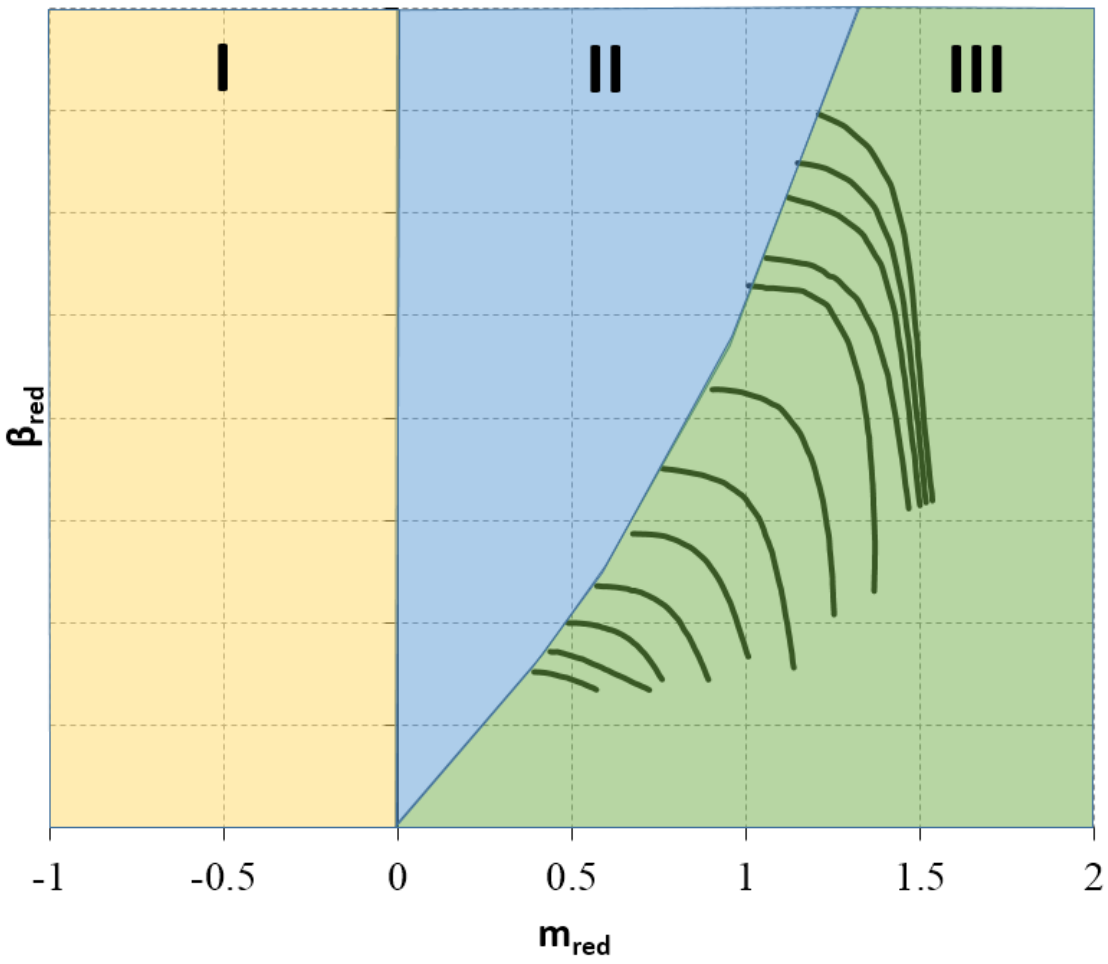

Figure 64: Compressor map zones.

This approach starts from the assumption that on a diagram like the one shown by Figure 64, the first points on the left of each characteristic defines the limit of the compressor stability region, therefore, the connecting line between these points determines the surge line.

A quadratic trend of the characteristics in both Zone I and Zone II is thought, respectively with positive and negative curvature. To define the parabolic speed lines in Zone II three boundary conditions are required, so the starting and ending points must be previously defined and the null derivative imposed on the surge line.

Regarding the null flow condition, the idea is to have a value of pressure ratio for each iso-speed. In order to obtain this information experimental data from system runs are necessary. A low temperature test or "Cold Test" has been scheduled; first thing, the compressor intake was sealed with a proper metal blind then the startup blower supplied air to the turbine to make the compressor spinning. The pressure increase across the compressor due to the impeller rotation has been acquired obtaining an experimentally derived point used as starting information to extrapolate points from the original compressor map. Since running the MGT with the compressor intake blocked can damage the turbo-machinery especially at

elevated load conditions, it was decided to do not ignite the turbine burner but to let the system running with the only energy input of the auxiliary blower. On the one hand, to perform the test in this way helped to preserve the system and especially the MGT from possible damages but on the other, it was possible to achieve only a low value of the rotational speed, reaching a partial running condition around the 27% of the design speed.

The work coefficient has been calculated from the measured pressure ratio at zero flow, and then thanks to this information, together with the linear trend between work condition and rotational speed carried out from previous tests on a turbocharger (Figure 65), it was possible to extrapolate the values of pressure ratio for the entire rotational speed field.

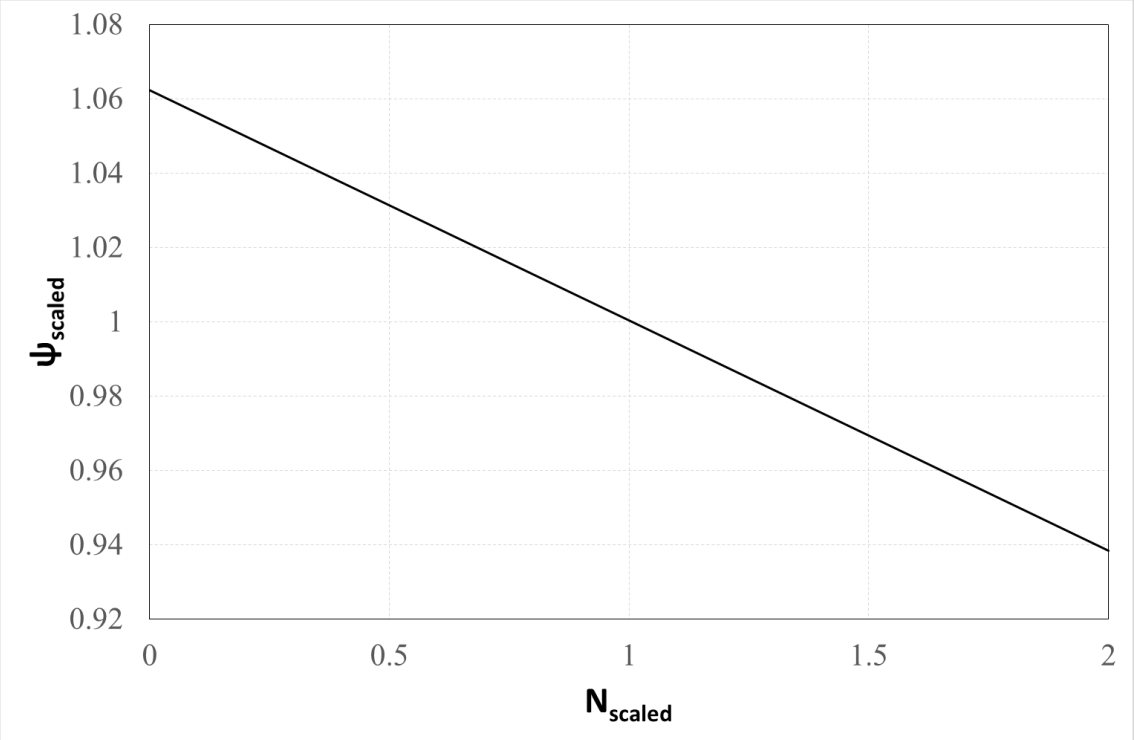

Figure 65: Experimental correlation between compressor work coefficient and rotational speed at zero flow condition (scaled with the values at 27% of rotational speed).

Here below all the calculation steps are reported.

Initially the pressure ratio and the corresponding rotational speed acquired from the "Cold Test" are known: β_{meas}, N_{meas}.

The work coefficient is derived as follow

$$\psi_{known} = \frac{c_p \, T_{in} \left(\beta_{meas}^{\frac{k-1}{k}} - 1 \right)}{U^2} \qquad \textbf{(73)}$$

At this point, it is possible to scale the values of rotational speed from the original map using the measured value from the "Cold Test",

$$N_{i,scaled} = \frac{N_i}{N_{meas}} \tag{74}$$

carry out the scaled work coefficient from the map in Figure 65 and obtain the actual work coefficient for each different iso-speed (Eq. (75)) and the corresponding pressure ratio at zero mass flow rate condition (Eq. (76)).

$$\psi_i = \psi_{i,scaled}\, \psi_{meas} \tag{75}$$

$$\beta_{i,0} = \left(\frac{\psi_i\, U^2}{c_p\, T_{in}} + 1\right)^{\frac{k}{k-1}} \tag{76}$$

All the required boundary conditions are now available to extrapolate the complete set of iso-speed in Zone II.

Regarding Zone I in the compressor working field, the assumption for the curve calculation are the following: a quadratic trend with positive concavity, fixed points at zero flow and at a predefined negative flow condition and null derivative again when no air flows across the compressor. It means that when the backflow occurs inside the compressor, this component is modeled as a duct with its pressure loss function of mass flow and the current impeller rotational speed. In order to fix the boundary condition at negative flow the first point of the lower iso-speed line is mirrored from Zone III to Zone I and then, using the correlation in Figure 65, has been applied the same extrapolation process used for the points at no-flow condition.

The entire extrapolation process has been written in Matlab code in order to have a simple way replicate the procedure with different compressor maps or to easily test different extrapolation settings on the same case study.

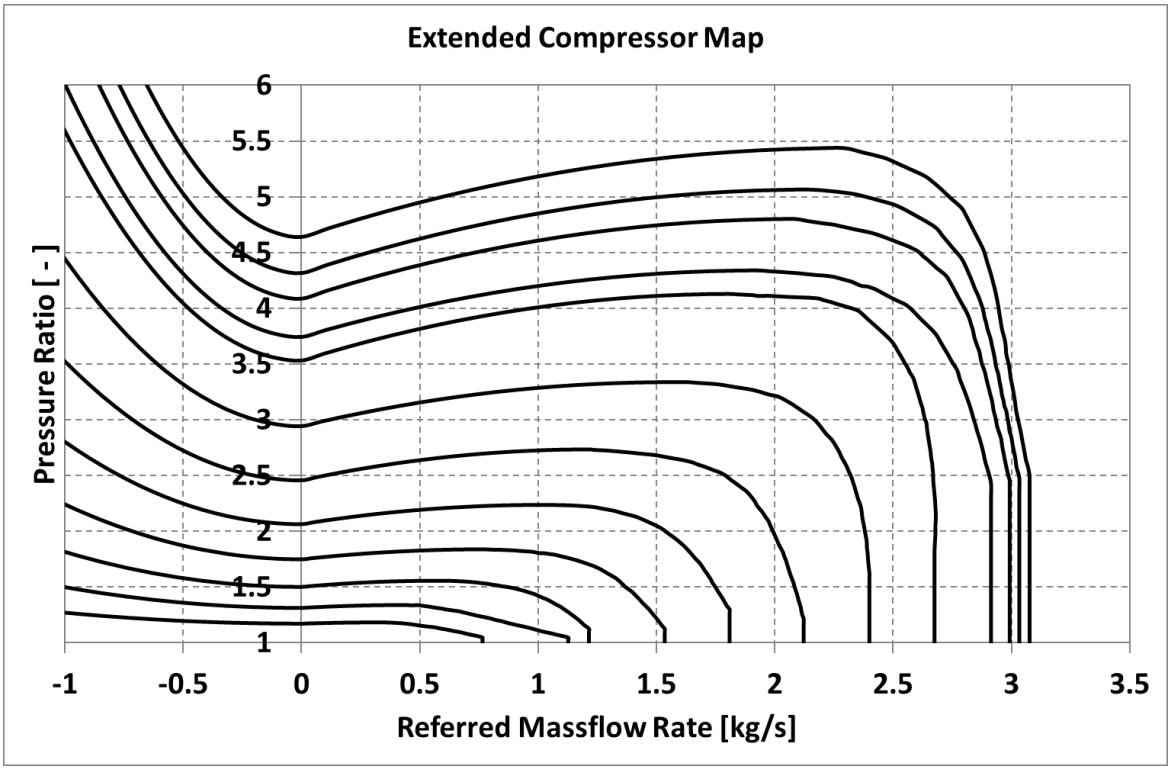

Figure 66: Final extended compressor map.

5.5. Rotational speed controller setup.

As in the real plant, also in the model there is the possibility to control the MGT rotational speed acting on the fuel valve fractional opening. A proportional-integrative controller able to react to a change in rotational speed set point has been developed.

In order to setup the PI controller the Reaction Curve tuning method is adopted. The case study is commonly identified as SISO control loop, where the error *E* between the system output *Y* and the set point *S* is used by the controller to calculate the control output *U* and drive the plant. In this case, instead of having a real plant, the model is the entity to be controlled but the control chain is the same as in Figure 67.

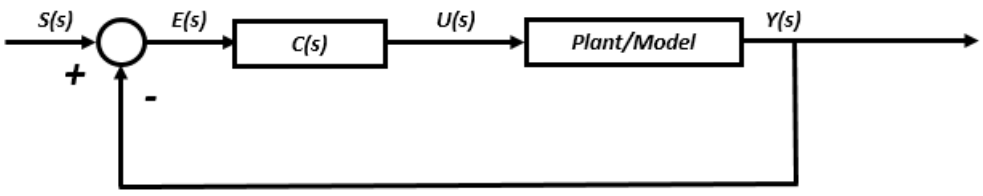

Figure 67: Basic feedback control loop.

Depending by the type of the required controller a different transfer function can be derived, the equation for proportional Eq. (77), proportional-integrative Eq. (78), proportional-derivative Eq. (79) and proportional-integrative-derivative Eq. (80) are reported.

$$C_P(s) = K_p \quad \textbf{(77)}$$

$$C_{PI}(s) = K_p \left(1 + \frac{1}{T_r\, s}\right) \quad \textbf{(78)}$$

$$C_{PD}(s) = K_p \left(1 + \frac{T_d\, s}{\tau_D\, s + 1}\right) \quad \textbf{(79)}$$

$$C_{PID}(s) = K_p \left(1 + \frac{1}{T_r\, s} + \frac{T_d\, s}{\tau_D\, s + 1}\right) \quad \textbf{(80)}$$

Where K_p, T_r and T_d are respectively called proportional gain, reset time and derivative time.

As introduced before a Reaction Curve based method has been utilized to develop the rotational speed controller for the Hyper model. A linearized quantitative version of the system response has been obtained with the open loop experiment as follows:

A constant input $u(t) = u_0$ is used to drive the model to a stable operating point with output $y(t) = y_0$. At time t_0 a step change to the model input is applied, from u_0 to u_∞. The model output is recorded until a new stable operating point y_∞ is reached. Figure 68 reports the step in fuel valve fractional opening, which is the forcing quantity in this analysis and the rotational speed as model response.

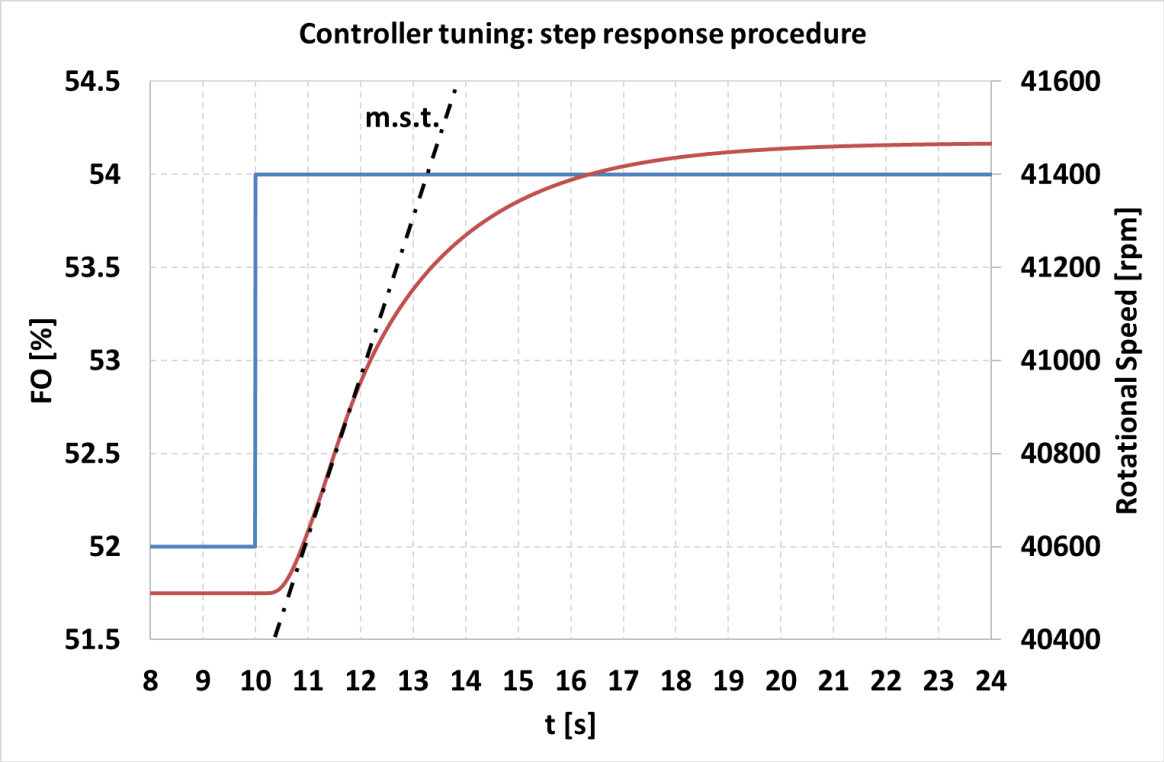

Figure 68: Model input (solid blue line), process reaction curve (solid red line) and maximum slope tangent (dashed-dot black line).

From Figure 68 it is possible to obtain preparatory information for the PI gains such as:

$$K_0 = \frac{y_\infty - y_0}{u_\infty - u_0}; \qquad \tau_0 = t_1 - t_0; \qquad \nu_0 = t_2 - t_1 \tag{81}$$

Where u_0, u_∞ and y_0, y_∞ are the initial and final values that input and output respectively assume before and after the transitory. While t_0 is the instant when the step change of the input occurs, t_1 is when the output parameter starts to react to the input perturbation and t_2 is the first instant when the m.s.t. curve intercepts the steady state value of the output after the transitory.

Thanks to these considerations, it is possible to derive the controller gains; it was decided to utilize the Cohen-Coon tuning method summarized in Table 5.

Table 5: Cohen-Coon tuning by using the reaction curve.

	K_p	T_r	T_d
P	$\frac{\nu_0}{K_0\,\tau_0}\left[1+\frac{\tau_0}{3\,\nu_0}\right]$		
PI	$\frac{\nu_0}{K_0\,\tau_0}\left[0.9+\frac{\tau_0}{12\,\nu_0}\right]$	$\frac{\tau_0\,[30\,\nu_0+3\,\tau_0]}{9\,\nu_0+20\,\tau_0}$	
PID	$\frac{\nu_0}{K_0\,\tau_0}\left[\frac{4}{3}+\frac{\tau_0}{4\,\nu_0}\right]$	$\frac{\tau_0\,[32\,\nu_0+6\,\tau_0]}{13\,\nu_0+8\,\tau_0}$	$\frac{4\,\tau_0\,\nu_0}{11\,\nu_0+2\,\tau_0}$

The initial gains setup calculated by this empirical tuning method is reported in Table 6.

Table 6: PI gains calculated by Cohen-Coon tuning method.

	K_p	T_r
PI	$-1.664 \cdot 10^{-4}$	0.943

From a first test, the controller seemed not able to guarantee a stable response of the controlled plant. Switching the model from manually driven with fixed fuel valve fractional opening to automatic control configuration enabling the PI controller operation, the system starts to oscillate. Looking at the increasing amplitude of the oscillations in system output it is easy to conclude that this controller is not optimized yet.

According to the tuning map reported in Figure 69, in this case, to improve the stability of a PI controller, either decrease the proportional gain in absolute terms or increase the reset time can be a solution. As the gains are adjusted, either doubled or halved, the process can be seen to respond quite differently from one case to the other.

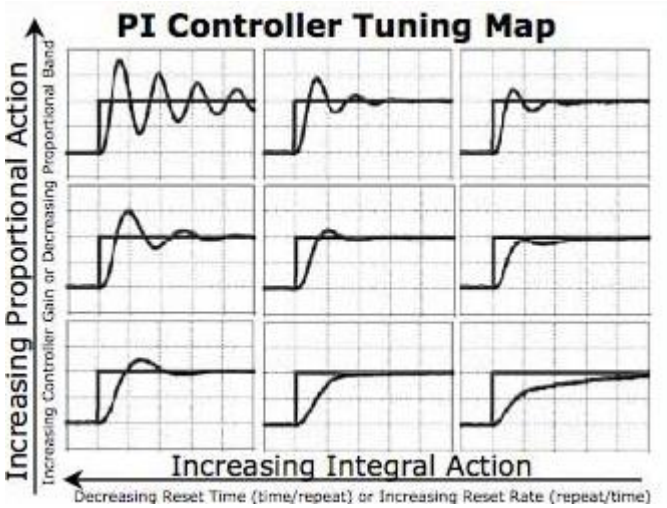

Figure 69: Example of tuning guidelines map for PI controllers.

Gradually decreasing the proportional gain, it is possible to obtain a better controller behavior, this is reflected by the fact that the oscillations in the rotational speed signal decrease as a different K_p is utilized. Figure 70 shows three different choices of proportional gains, starting from the original derived by the Cohen-Coon formulas, which has returned the green line as result, K_p has been decreased by two and ten times and results are shown respectively with red and blue lines. To better appreciate the differences in system responses behavior a very small scale has been chosen on the rotational speed axis. While the red and especially the green line show an increasing oscillation, the blue one reports the result of a constant controlled output because of accurate and stable controller action.

Table 7: Different PI controller setups

	K_p	T_r	
PI	$\frac{-1.664 \cdot 10^{-4}}{10}$	0.943	**K_p LOW**
PI	$\frac{-1.664 \cdot 10^{-4}}{2}$	0.943	**K_p MEDIUM**
PI	$-1.664 \cdot 10^{-4}$	0.943	**K_p HIGH**

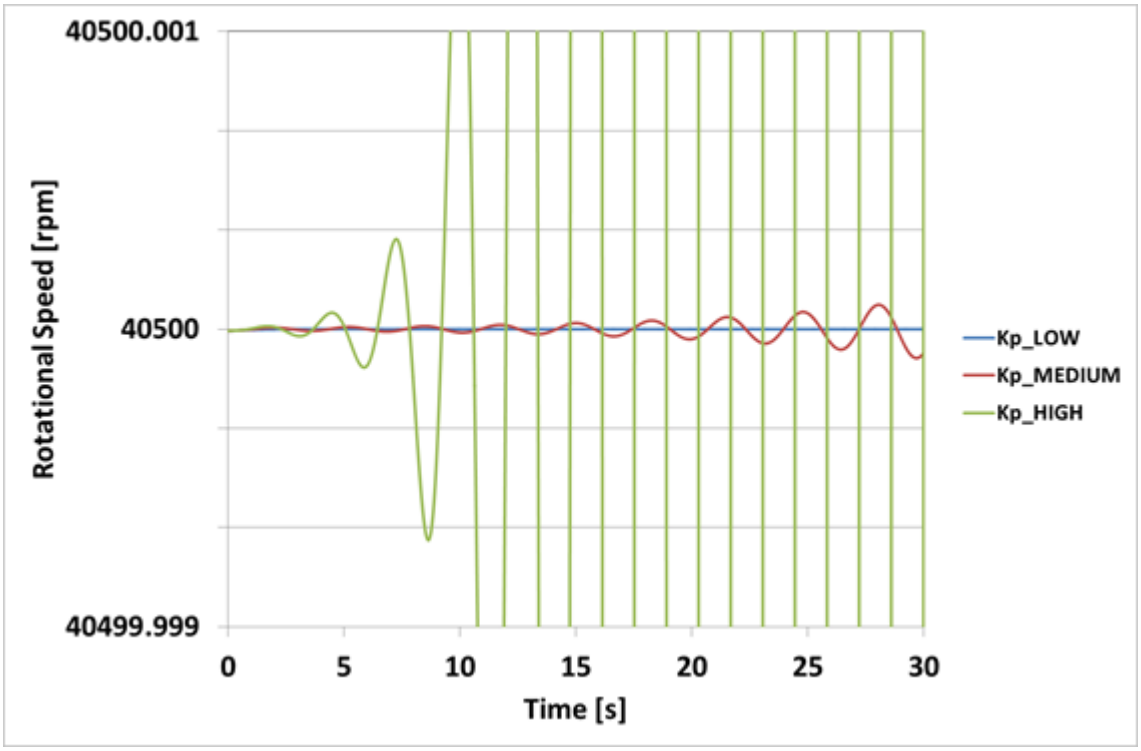

Figure 70: Effect of proportional gain K_p on the system stability.

At the end of the tuning procedure a good compromise seems reached thanks to settings for proportional and integrative gains shown in Table 8.

Table 8: Final PI gains for rotational speed controller

	K_p	T_r
PI	$\frac{-1.664 \cdot 10^{-4}}{5}$	0.943

5.6. Results

5.6.1. Surge Test1

The same simulation is conducted for two different sizes of the main plenum, called “Vp case” and “Vpx10 case” respectively with volume equal to 2.9 m^3 and 29 m^3.

Starting point.

Table 9: Initial condition of the simulation

Compressor mass flow rate	1.852	kg/s
Pressure ratio	4.083	-
Electric power	70	kW
Fuel mass flow rate	0.018	kg/s
Surge margin	1.03	-

Test description.

The starting point, which is the same for every test to be consistent in results, is chosen very close to the surge line to minimize the path in the stable region before the surge triggering. During this simulation named “Surge Test1” a step reduction of the bypass valve fractional opening has been performed, this maneuver increases the pressure drop along the system and moves the operating point toward the region of instability of the compressor. All the other model inputs, such as fuel valve fractional opening and electrical load are kept constant. The model has been driven in “open loop” configuration, it means that all the controllers are kept deactivated for the entire simulation.

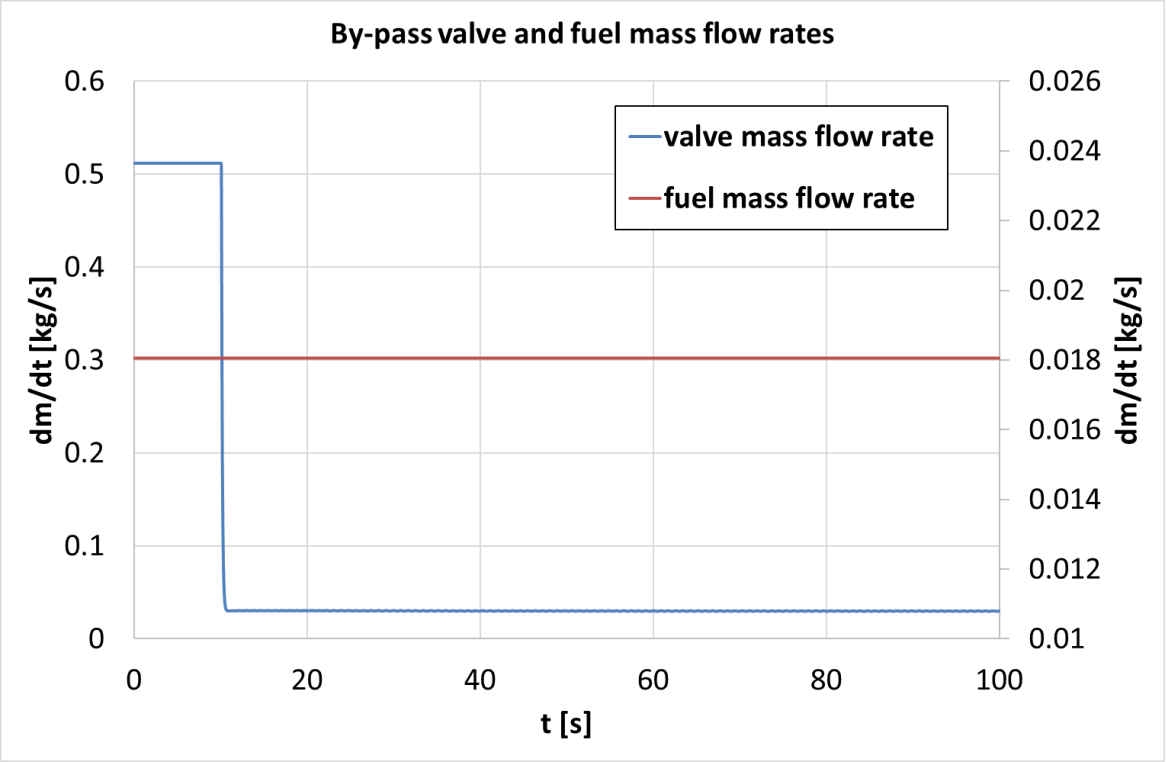

Figure 71: By-pass and fuel mass flow rate trends during Surge Test1 simulation.

Analysis of results.

When the valve is partially closed at the 10th second of simulation, there is a sudden reduction in the flow exiting the compressor. The same reaction can be observed in both studied cases but, as expected, the dynamic response of the system is influenced by the amount of volume considered.

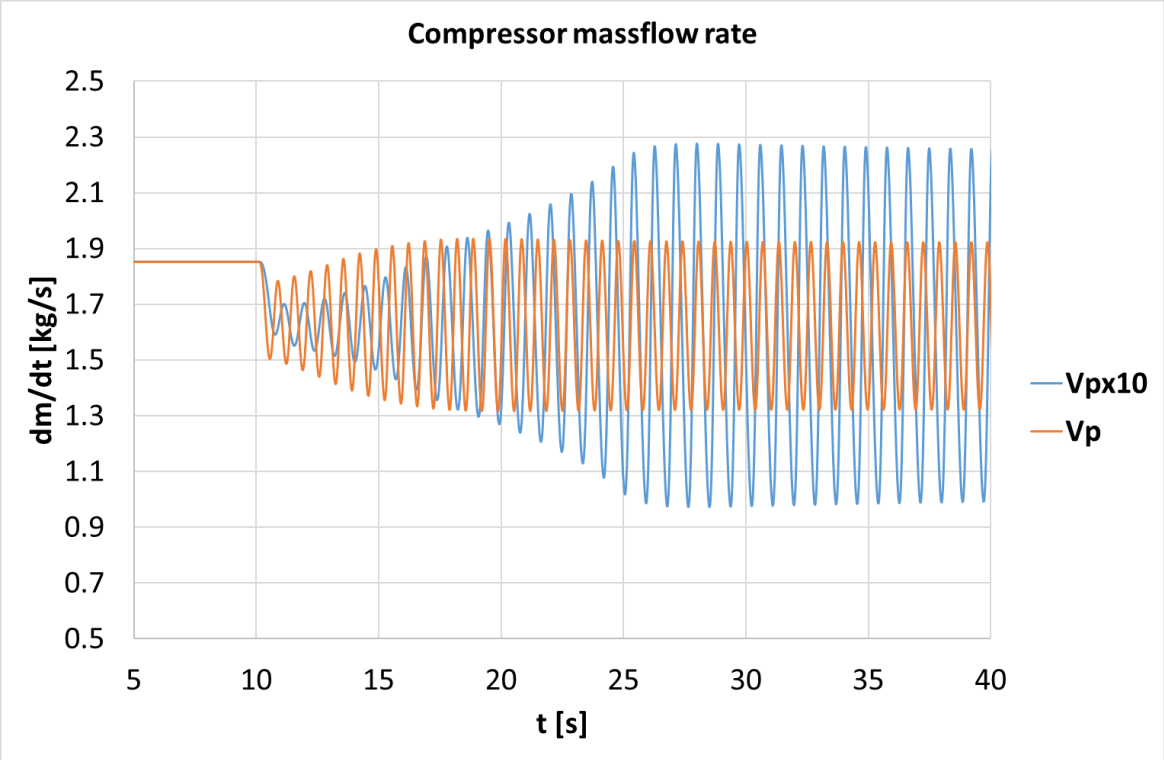

Figure 72: Compressor mass flow rate trends during the simulations with large volume (blue line) and small volume (orange line).

The faster reaction to the valve closure and the higher frequency shown by the small volume case shown in Figure 72, confirm the lower rigidity of a system with a smaller volume.

Referring again to Figure 72, the large volume (Vpx10 case) seems to behave as a buffer, which damps the quick flow fluctuations extending the duration of the instability development interval. On the other hand, when the surge is fully developed, and the amplitude of oscillation is constant, the instability is characterized by a larger width due to the increase in potential energy stored in a bigger volume. It is interesting to observe how the average value of the mass flow rate during surge is very similar, the mean calculation of signals returns values around 1.6kg/s in both cases (1.62kg/s for the Vp case and 1.60kg/s for the Vpx10 case). These results seem to indicate that the mean value of the surge oscillation obtained by the model in open loop configuration is not influenced by the size of the volume considered.

The Fast Fourier Transform (FFT) performed on the mass flow rate signal confirms and highlights the same considerations on the amplitude and the frequency of oscillations. For this type of investigation, the fully developed surge signal is taken, reduced by its average value and analyzed with the Fast Fourier Transform tool available on Matlab®. With this approach the resulting diagram reported in Figure 73, shows information about the amplitude of the simulated oscillation and about the characteristic frequencies for the monitored phenomenon. The results of the FFT returns the main frequency (fundamental) of the surge event and its multiples (harmonics). Both simulated results, at 2.9m^3 and 29m^3, are shown

and compared in Figure 73. It is evident as a system with a large volume (red line) is characterized by a lower characteristic surge frequency and a bigger amplitude in terms of mass flow oscillation compared to the lower volume case.

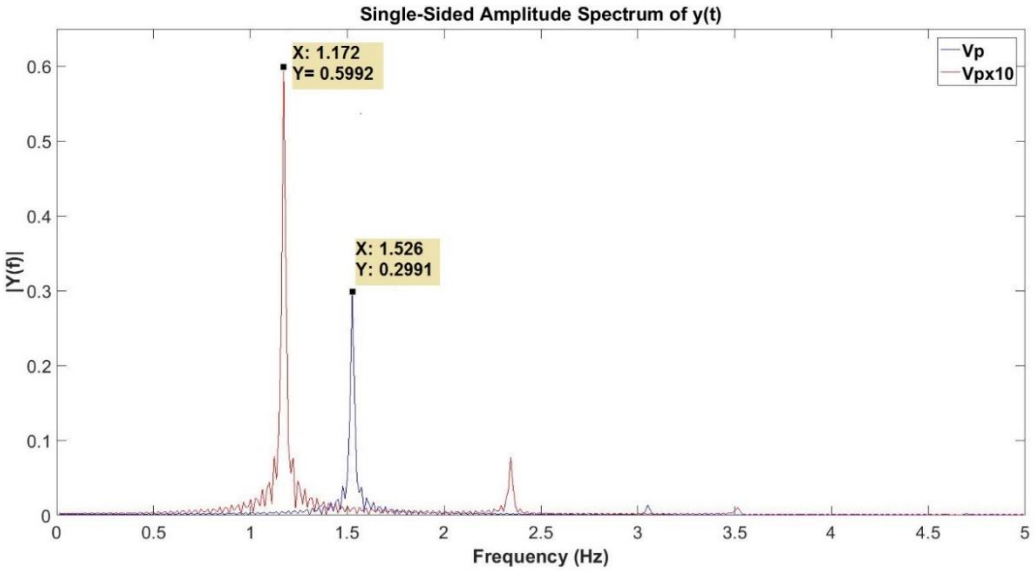

Figure 73: Fast Fourier Transform of the compressor mass flow rate signals during surge simulation, comparison between two different volume size cases.

Compressor discharge pressure is monitored at the outlet of the equivalent duct, this signal, together to the mass flow rate gives important information on the system dynamics and on the surge cycle development. The trend of compressor outlet pressure during the Surge Test1 is reported in Figure 74. As the valve is partially closed there is a sudden increase in the main vessel pressure that, together to the reduction in mass flow rate, bring the compressor operating point to cross the surge line triggering the instability process. It is evident that the smaller volume case is the quicker to respond to the forcing input, the orange line (Vp case) in Figure 74 shows a sharper underdamped behavior characterized by faster transition between a stable working condition to a fully developed surge oscillation. Two main characteristics can be identified in the pressure signal acquired during the simulation of a system with a bigger volume (blue line): on the one hand, compared to the Vp case, there is a smaller deviation from the initial pressure value during the first instants of simulation; on the other hand a longer settling time is needed to reach the final average pressure level for this case.

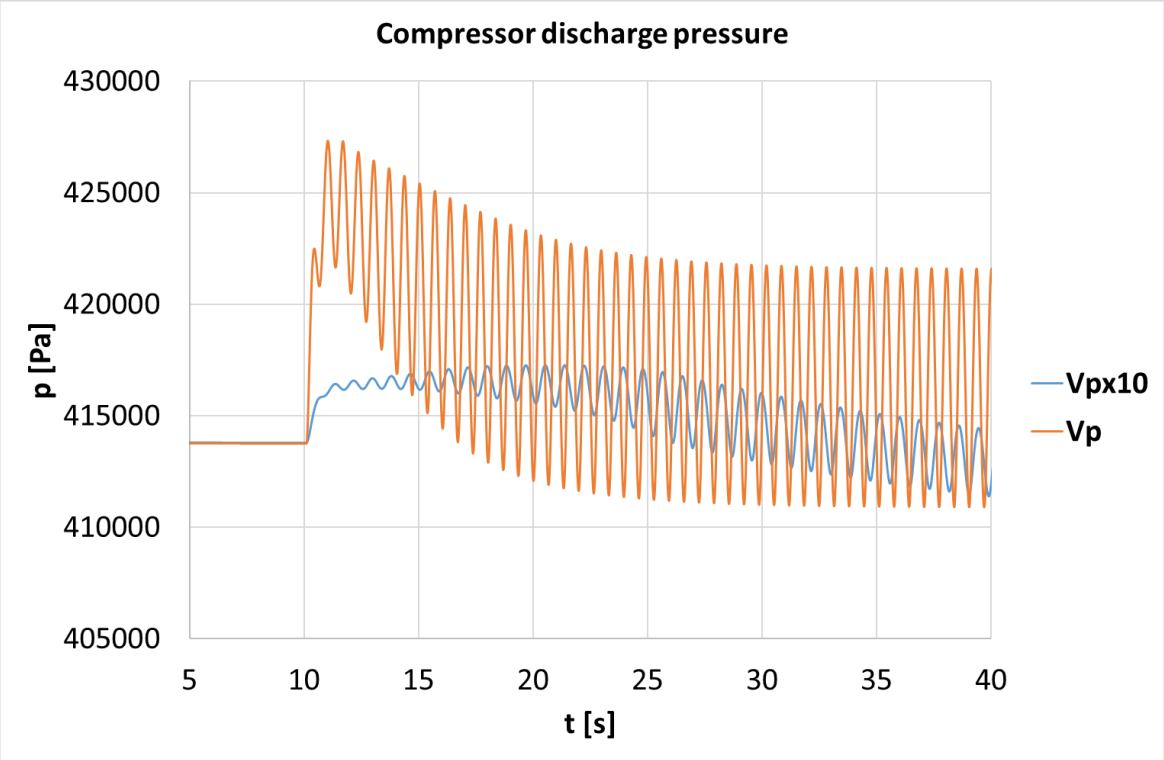

Figure 74: Compressor discharge pressure trends during the simulations with large volume (blue line) and small volume (orange line).

Again, the FFT analysis of the signal is an effective methodology to underline the main aspects that differentiate the two studied cases during fully developed surge cycles.

As it happens for the mass flow rate signal, also for the pressure, the fundamental frequency of a system with a bigger volume is lower than the small volume case, but on the contrary the amplitude of the pressure oscillations is larger when the size of the system is reduced.

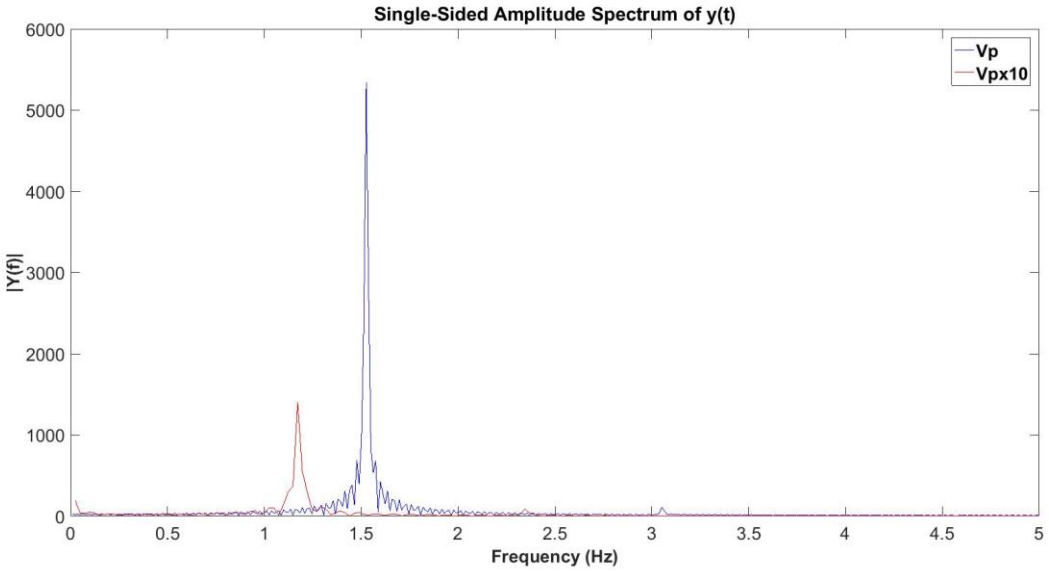

Figure 75: Fast Fourier Transform of the compressor discharge pressure signals during surge simulation, comparison between two different volume size cases.

Plotting the data on compressor map gives a clearer overall idea of system behavior under surge conditions. Figure 76 shows the compressor operating point moving on its steady state performance map for the entire duration of the simulation. The first observation that can emerge regards the different shape of the surge cycles when the system is characterized by a larger or a smaller volume. This shape is defined by the combination of mass flow rate and pressure oscillations and it is strongly affected by the volume size. Simulations seem to indicate that with a bigger volume, during each surge cycle, the mass flow oscillation is predominant compared to the pressure oscillation. This probably happens because the big volume let the mass flow to change in a wider range without to significantly affect the average pressure level in the system.

In both simulated cases, when the valve is partially closed the compressor operating point quickly moves to the left side of the graph, it crosses the surge line with a sudden increase in pressure and rotational speed but decreasing its mass flow rate. After entering the unstable region of the map, both mass flow and pressure start their fluctuations establishing the surge cycle development. These cycles start with limited variation in both pressure and mass flow quantities, to gradually extend their amplitude creating at the end of this phase well defined surge cycles. Once surge is developed the operating unstable operating point moves toward lower values of pressure and rotational speed, this is visible from the evident downward movement of the cycles on compressor map in Figure 76.

Open loop simulations like these, indicate that size of the volume contained between compressor and turbine strongly affects the dynamic of the Hybrid System response; in particular, even the surge instability is characterized by different behavior, for example a bigger volume seems to be critical for those component which can be damaged by fast and wide change in mass flow rate, while a smaller volume seems to be more dangerous for those element sensitive to wider change in pressure.

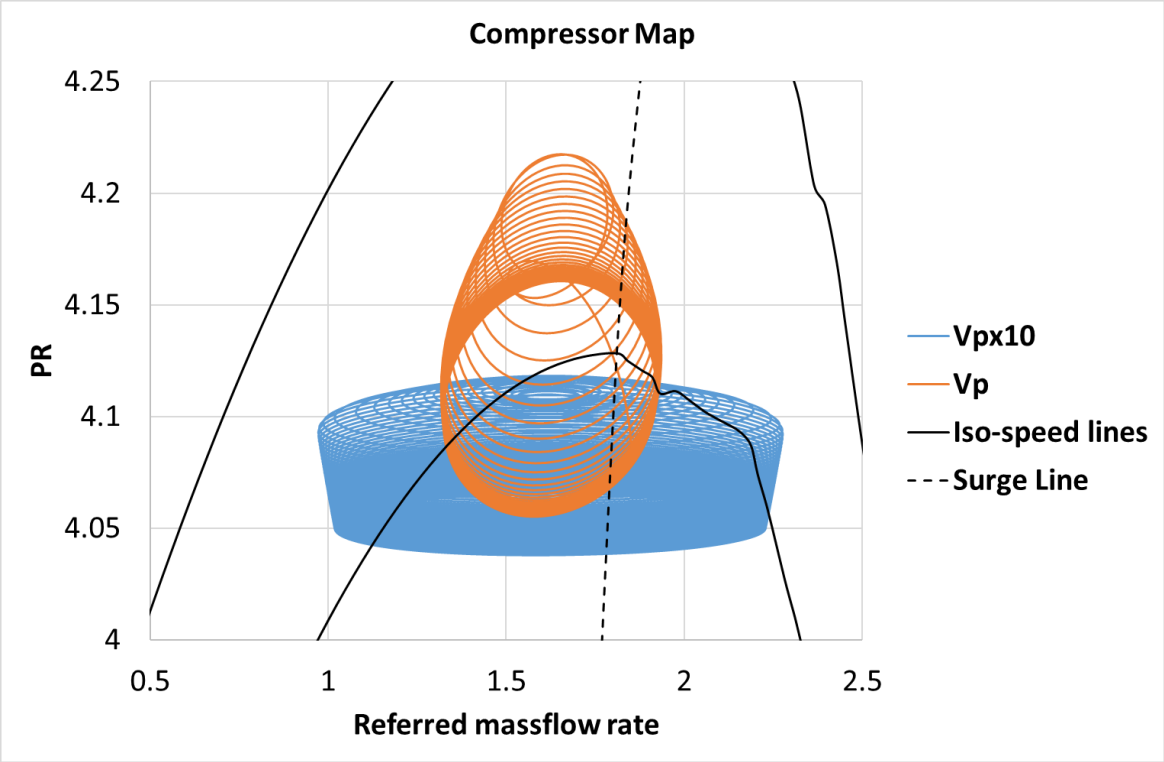

Figure 76: Trace on compressor map during the simulations with large volume (blue line) and small volume (orange line).

It is possible to state that Figure 76 shows a system which seems to be more reactive in term of change in pressure level if characterized by a smaller volume rather than a big one. It is remarkable how the shape of surge cycle is really volume depending, in this system configuration when a smaller volume is simulated an almost circular cycle is created by the compressor operating point on its map, while when a bigger volume is simulated the shape becomes more elliptical due to the predominance of flow oscillation compared to the pressure ones. As already introduced, this might be an important aspect for those components that suffer damage due to strong pressure fluctuations rather than flow oscillations or vice versa.

One information that is missing on the compressor map diagram is the temporal progression of the phenomenon, it is therefore advisable to combine this type of graph with diagrams where the time evolution of the reported parameters is shown. For this reason, compressor mass flow rate and discharge pressure trends over the time have been previously introduced in Figure 72 and Figure 74, and the rotational speed of the micro gas turbine is reported in Figure 77.

Regarding the amplitude of speed oscillation, the larger volume case shows a wider range of velocity variations and a lower frequency of the oscillation as expected. Figure 77 also reports the moving average of the speed signals, these lines give indications on the general trend of the speed and help to explain the direction of surge cycles shown on the previous compressor map. The moving averages underline the difference in terms of dynamic characteristic time of the response of a system when its volume size changes. Once again, a

slower and smoother trend of the average speed value is shown in the larger volume case, but on the other hand phenomenon shows a more intense fluctuation which could be more unsafe in terms of mechanical stress on shaft, bearings and other rotating parts of the machine.

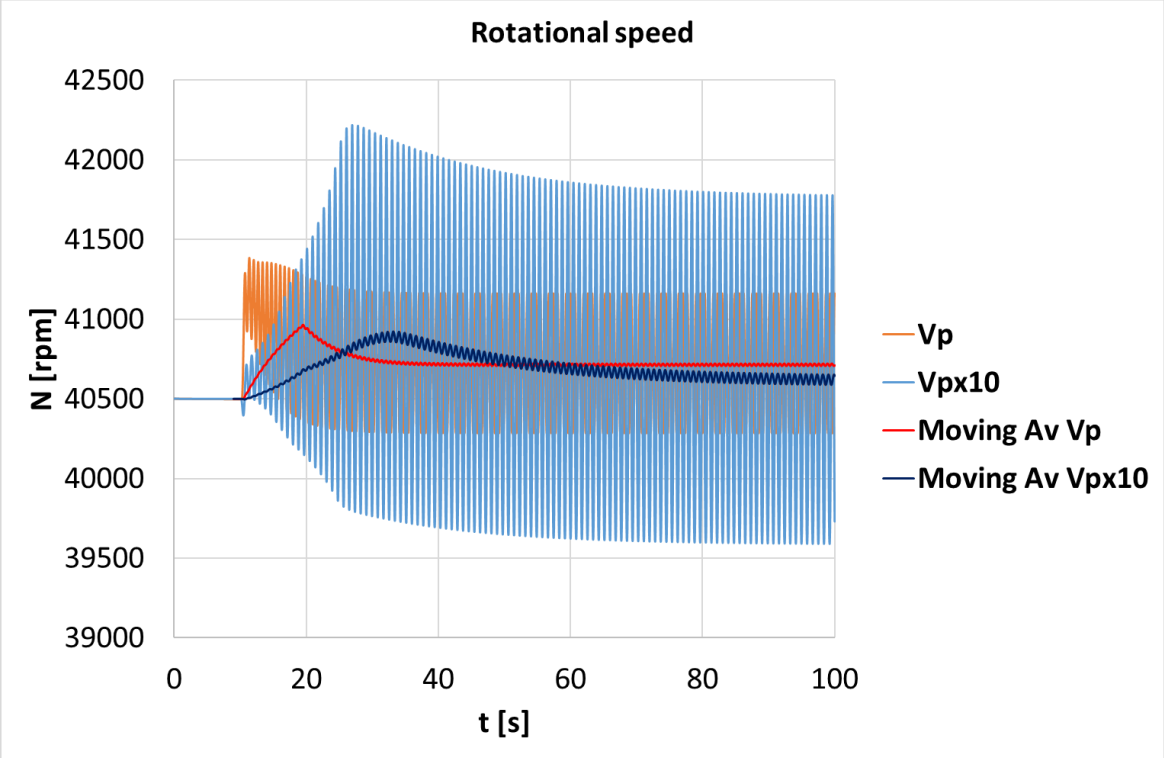

Figure 77: Dynamic fluctuations of the rotational speed during surge and moving averages of signals.

5.6.2. Surge Test2

The same simulation is conducted for two different sizes of the main plenum, called “Vp case” and “Vpx10 case” respectively with volume equal to 2.9 m^3 and 29 m^3.

Starting point.

Table 10: Initial condition of the simulation

Compressor mass flow rate	1.852	kg/s
Pressure ratio	4.083	-
Electric power	70	kW
Fuel mass flow rate	0.018	kg/s
Surge margin	1.03	-

Test description.

During this simulation named "Surge Test2" as well as during "Surge Test1" a step reduction of the bypass valve fractional opening has been performed, once again the aim is to increase the pressure drop along the system and to move the operating point toward the compressor instability region. Among the model inputs, only electrical load and bleed valve fractional opening are kept constant. This time, the rotational speed controller has been enabled so the model is driven in "closed loop" configuration. This means that the control system is free to adjust the fuel valve fractional opening trying follow the imposed constant speed setpoint.

Analysis of results.

Solid blue lines in Figure 78 and Figure 79 show the mass flow rate across the by-pass valve during the simulations for smaller volume case and the bigger volume case respectively. While red lines show the fuel mass flow rate behavior.

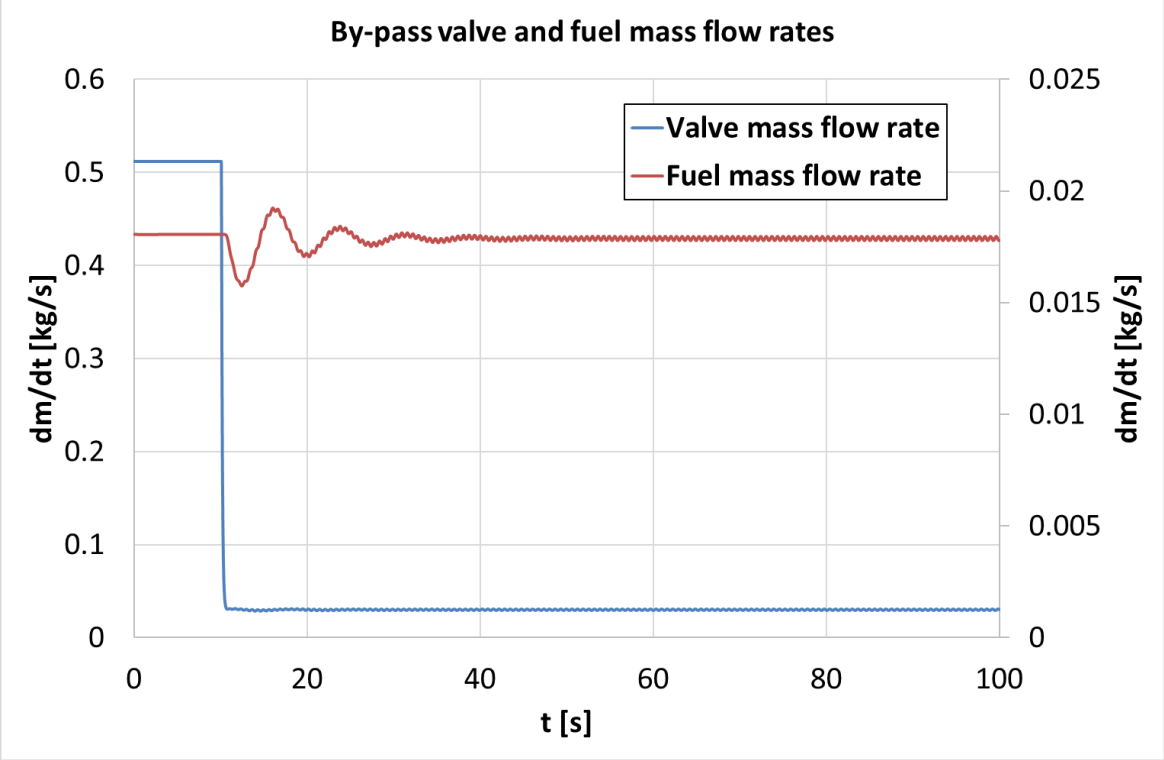

Figure 78: By-pass and fuel mass flow rate trends during Surge Test2 simulation, "Vp" case study.

Comparing the two figures, controller behaves in a very different way when different sizes are considered in the system. While with a small volume, after a transition of about 30 seconds controller seems to restore the fuel value around a precise mean value, with a larger volume there is more instable reaction of the system instead. In this last case controller response alternates high frequency and small amplitude oscillations with low frequency and wide amplitude fluctuations.

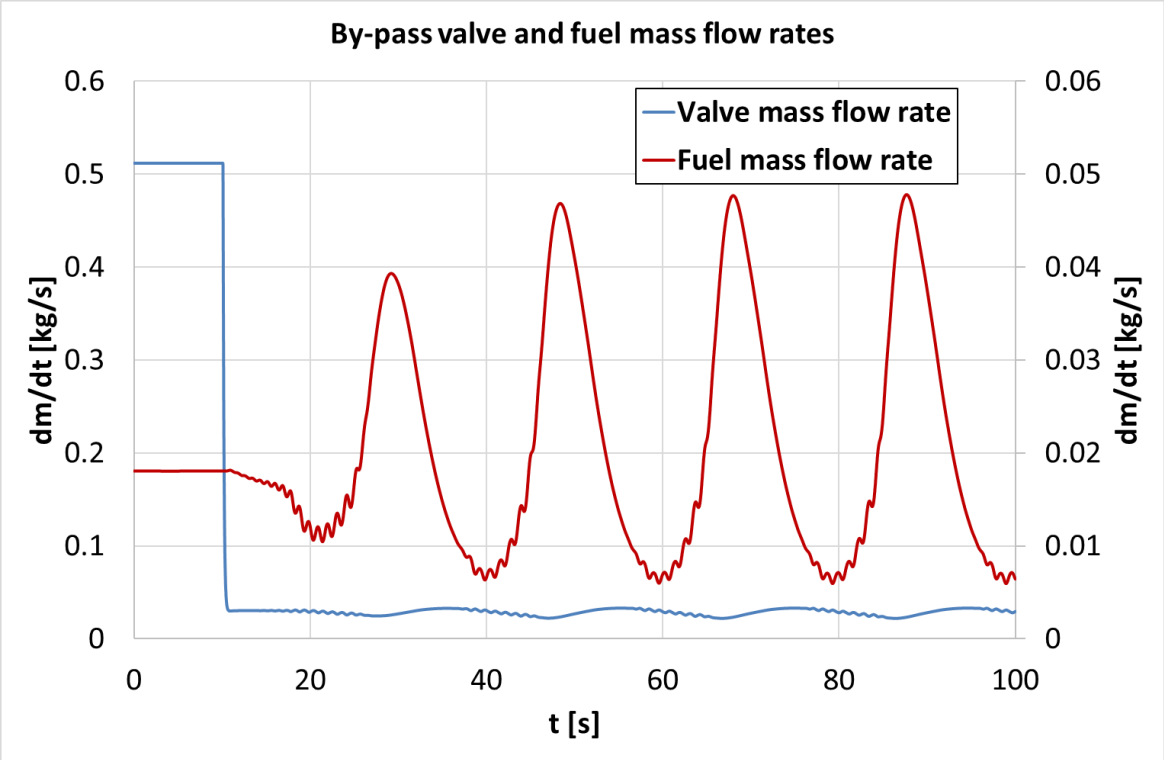

Figure 79: By-pass and fuel mass flow rate trends during Surge Test2 simulation, "Vpx10" case study.

Figure 80 shows the compressor mass flow trends, the smaller volume case (orange line) reports the same transition seen for the fuel mass flow rate signal, this occurs in the interval between the surge triggering and the full development of the phenomenon. Once surge event reaches stable periodic oscillations it is characterized by amplitude and frequency very similar to the open loop case, the main difference between open loop and closed loop simulation stays in the surge "stabilization" time for the smaller volume case.

When the speed controller is enabled, the bigger volume case, labelled Vpx10, shows a completely different behavior. In closed loop, all the quantities acquired during the simulation show a combination of higher and lower frequency oscillations, the firsts are attributable to the effect of surge cycles, while the seconds seem be linked to the gradual and periodic process of decrease and restore of the overall pressure level in the system.

Comparing Figure 79 and Figure 80, it is evident there is a match in the time the high frequency oscillation in fuel mass flow signal and surge fluctuation in compressor mass flow occur.

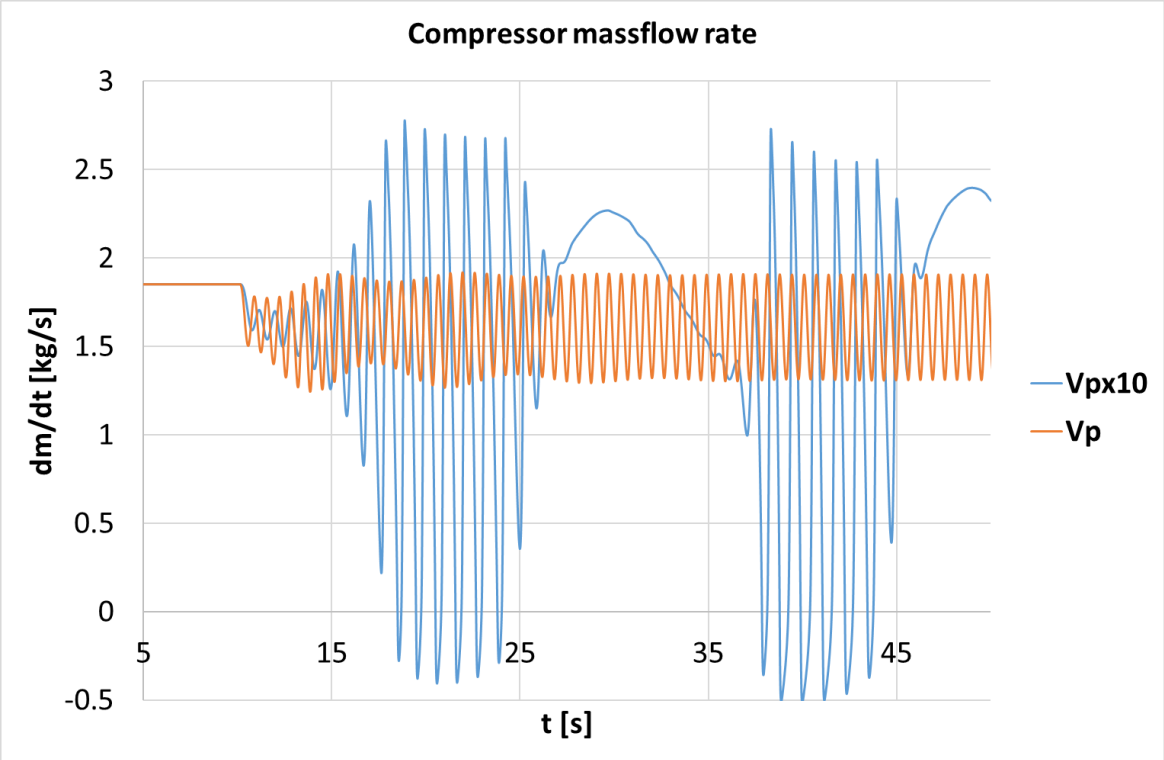

Figure 80: Compressor mass flow rate trends during the simulations with large volume (blue line) and small volume (orange line).

It is interesting to observe that, while for the smaller volume case the FFT analysis returns very similar results in open and closed loop configuration (see Figure 73 and Figure 81) with just a smaller amplitude of the oscillation in the second, for the Vpx10 case instead, there are differences both in terms of amplitude and frequency of the surge event. In particular, the speed controller action seems to move the peak of the fundamental toward lower frequency levels, the main frequency of the surge oscillations changes from 1.172Hz in the open loop simulation to 0.8789Hz in closed loop. The use of the control system has a strong effect on the amplitude of the mass flow rate fluctuations, this amplitude changes from a value of 0.6kg/s to one close to 1.5kg/s affecting the type and intensity of surge event.

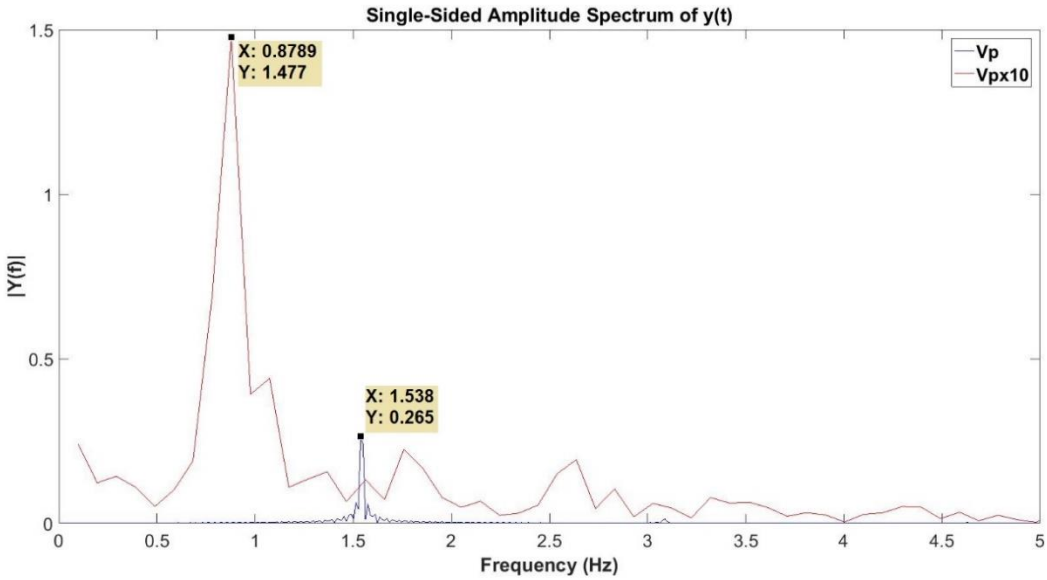

Figure 81: Fast Fourier Transform of the compressor mass flow rate signals during surge simulation, comparison between two different volume size cases.

Figure 82 clearly highlight the different model response considering a smaller or bigger volume in the system. The orange line (Vp) shows an initial overshot and a fast transient before the establishment of a constant frequency oscillation. The bigger volume case depicted with blue line, shows a longer and weaker pressure transient before surge begins. In parallel to the fast surge fluctuations, a low frequency oscillation in the pressure is developed. The superposition of these two phenomena creates a wave in the pressure acquired signal characterized by jagged shape in the descending phase when surge occurs and a smooth climb when the operating point exits from the unstable region and the control system force the model back to desired speed setpoint. Therefore, the bigger volume case operated in closed loop is characterized by two main phases, a strong surge event and a restore phase when for a short interval of time compressor is recovered from surge. However, the stable transient ends with a significant overshot in pressure and, as shown by Figure 83, also in rotational speed. This overshot brings the operating point beyond the surge line and the instability is triggered again creating a process which alternates safe and potentially destructive working conditions.

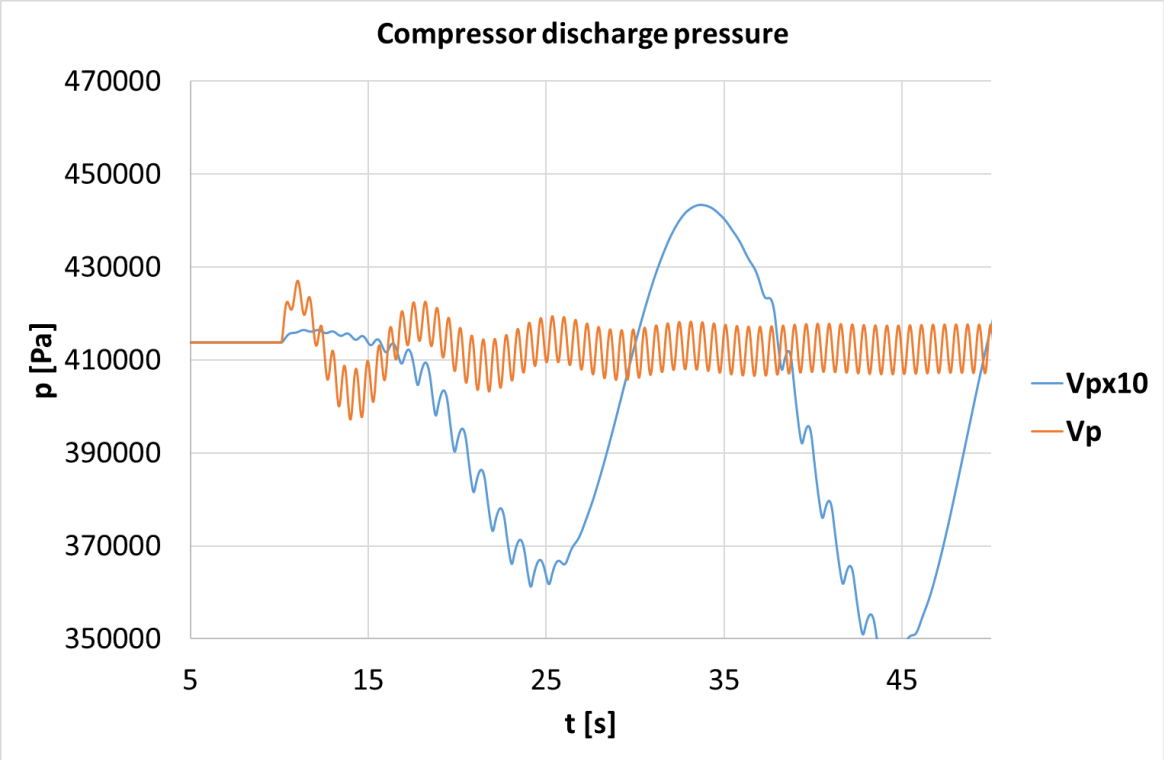

Figure 82: Compressor discharge pressure trends during the simulations with large volume (blue line) and small volume (orange line).

Figure 83 gives a qualitative impression of the difference in intensity of surge in the two configurations reported. The starting point described in Table 10 is the same for both simulations but the dynamic response of compressor mass flow and discharge pressure are significantly different and combined on the compressor map they return a totally different characterization of surge event.

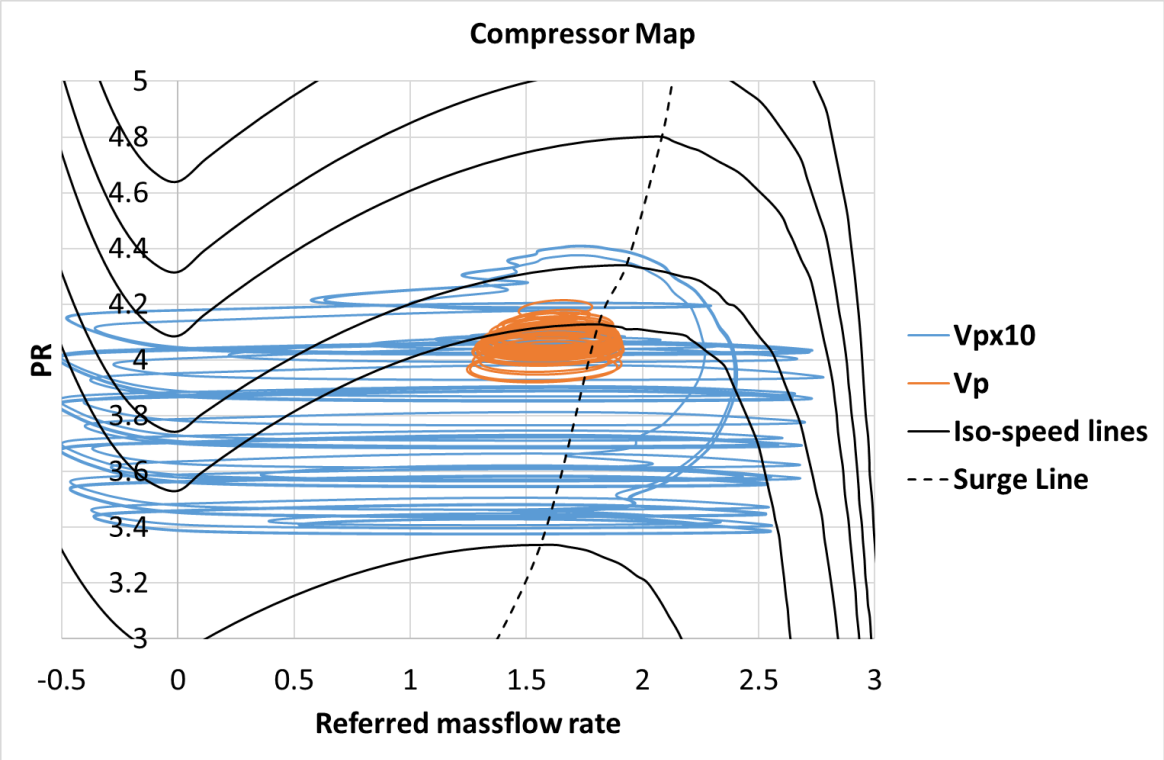

Figure 83: Comparison of system responses on compressor map, orange line represents the Vp case and blue line the Vpx0 one.

The surge margin, defined in Eq. (52), is a model output used to estimate current compressor operating point on the compressor map. Considering that it assumes values greater than 1 when compressor operates in the stable working region and lower than one if it operates beyond the surge line, this parameter can give information about the way the system approaches the surge event, or it can be used as surge risk indicator.

From the analysis of the blue line in Figure 84, when the valve gets closed at time 10s, as the surge margin becomes lower than one the model simulated results show an increasing instability. But when the compressor operating point is restored back from surge, the overshot seen in other parameters is transformed here in a constant decreasing trend of surge margin and surge is triggered at a lower value of this quantity. This can be addressed to the type and the intensity of the maneuver which brings the compressor operating point beyond the surge line. In these simulations two type of forcing phenomena can be identified, the first is the valve closure which is the cause of the first surge initiator at time 10s, while the second is the combination between the controller action and system response, which seems the predominant reason why surge event presents a delay before its second occurrence at time 35s.

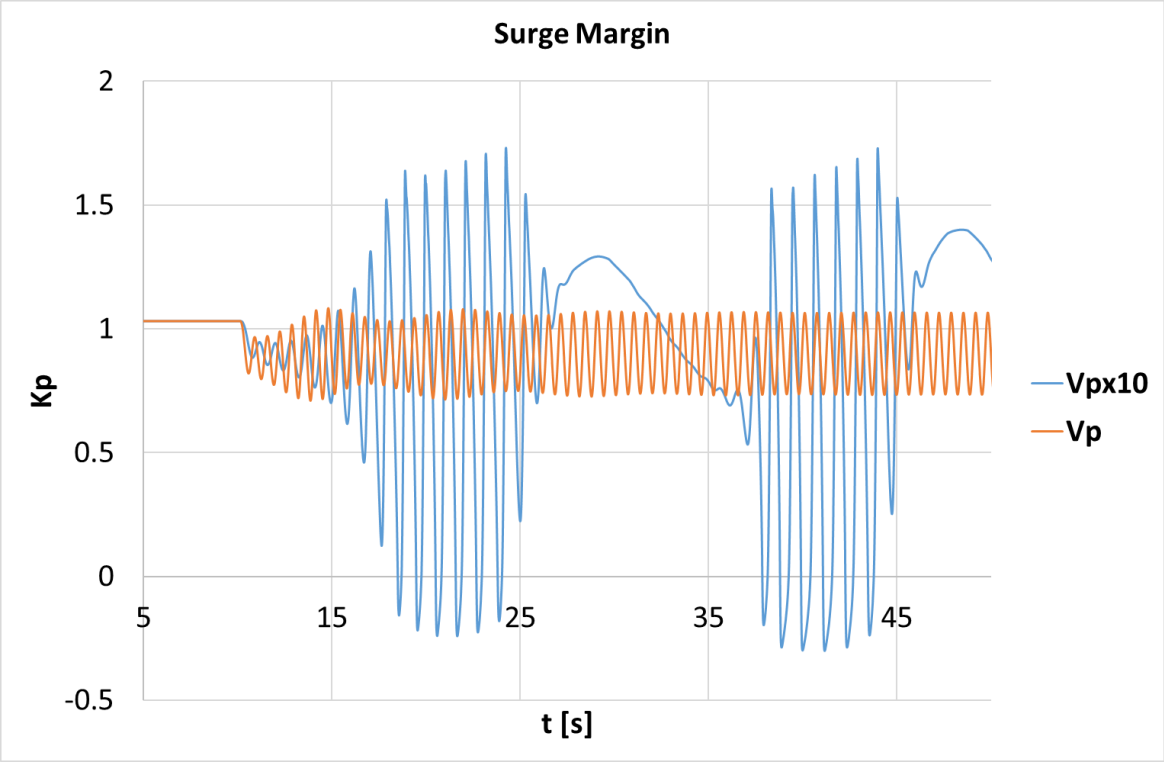

Figure 84: Compressor surge margin monitored during Surge Test2

5.6.3. Surge recovery Test1

The initial condition of this test is the same as for the previous simulations (see Table 9, Table 10). The aim of this specific simulation is to investigate the possibility to perform a surge recovery maneuver using the by-pass valve in open loop configuration. It means that the speed controller is kept disabled for the entire duration of the simulated test and a fixed fuel valve fractional opening is adopted. As for the other in simulation, also in this case two different sizes of the volume are studied, a smaller case labelled as Vp with approximately 2.9m^3 contained into the main volume and a bigger case called Vpx10 where this volume is increased by ten times. During this test compressor operating point is driven into surge condition closing the by-pass valve after ten seconds of simulation, and the same condition as for Surge Test1 is reached. Once the surge oscillation is fully developed the valve fractional opening is restored back to the initial value. The aim of this maneuver is to bring the compressor operating point back to a stable region on its map recovering from surge.

The impact of cold by pass was previously investigated in[11], while an operation on cold air by pass for surge avoidance, similar to the one studied here, has been experimentally demonstrated on the real plant in the work published in [3].

The blue line in Figure 85 reports the mass flow rate across the by-pass valve as consequence of the two steps in fractional opening while the red signal is the fuel mass flow rate kept constant during the entire simulation and fed to the combustor. A small difference between the two volume cases is already visible in the by-pass mass flow after the increasing in its fractional opening.

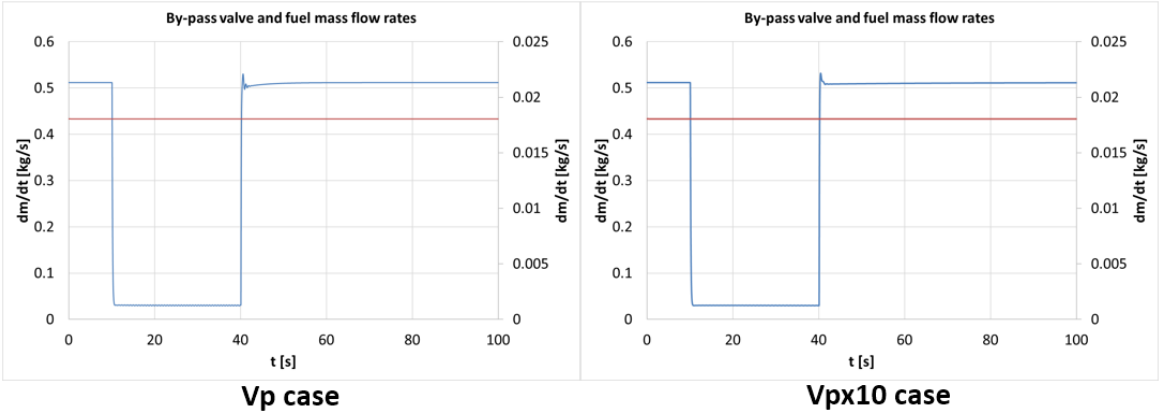

Figure 85: By-pass and fuel mass flow rates during Surge RecoveryTest1

Up to 40 seconds of simulation all the signals simulated have the same trend as for the Surge Test1 case, looking at Figure 86, as the by bass valve is opened the mass flow oscillation starts to decrease in amplitude and the average value shifts to an higher value, this is a clear sign that compressor operating point is reaching a position on the right side of the surge line. The mass flow recovery time, thought as the time needed by the mass flow rate to completely dampen its fluctuation, is longer in the bigger volume case then for the smaller volume one.

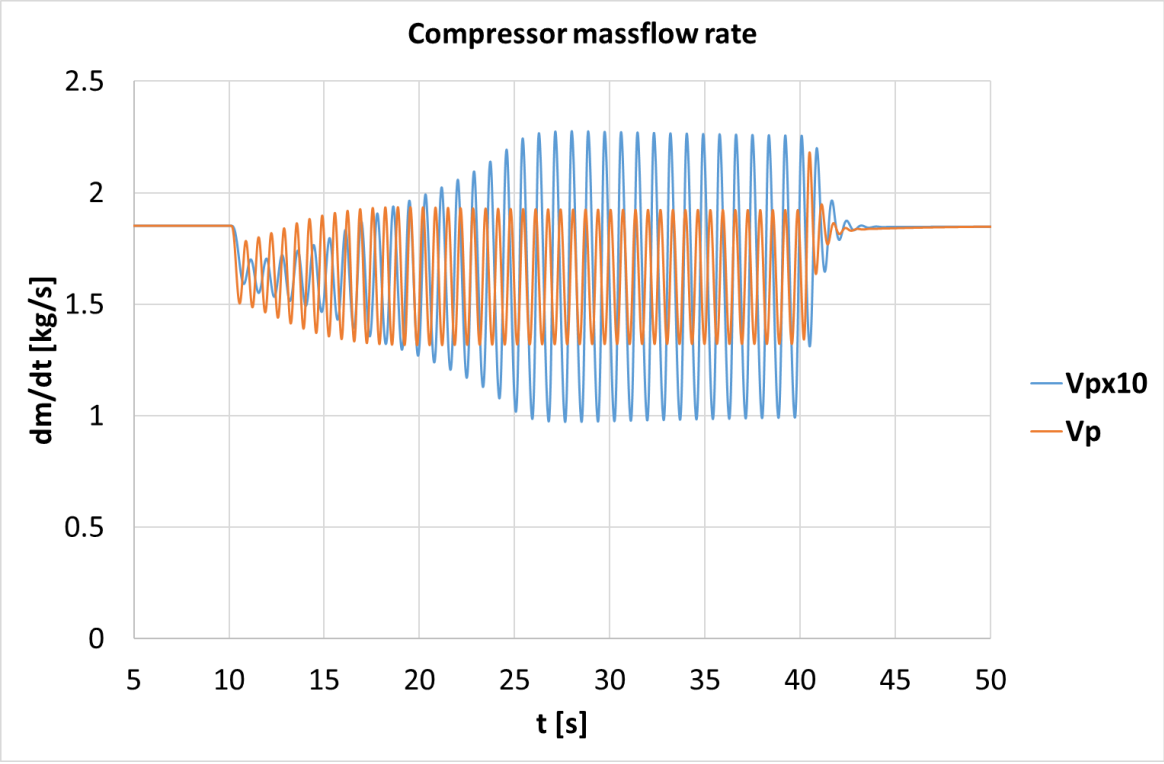

Figure 86: Compressor mass flow rate trends during Surge Recovery Test1 simulations with large volume (blue line) and small volume (orange line).

Regarding the pressure trend during the surge recovery simulation, a sudden decrease at compressor outlet occurs. This behavior is particularly evident in the smaller volume case that is then characterized by a long period during which the compressor outlet pressure

slowly rises again. Contrary to the mass flow signal, this pressure seems to need more time to be restore to the original value in the smaller volume case then in the bigger. This could be a consequence of the wider range of pressure amplitude oscillations that a smaller volume system has shown in all these simulated tests until now.

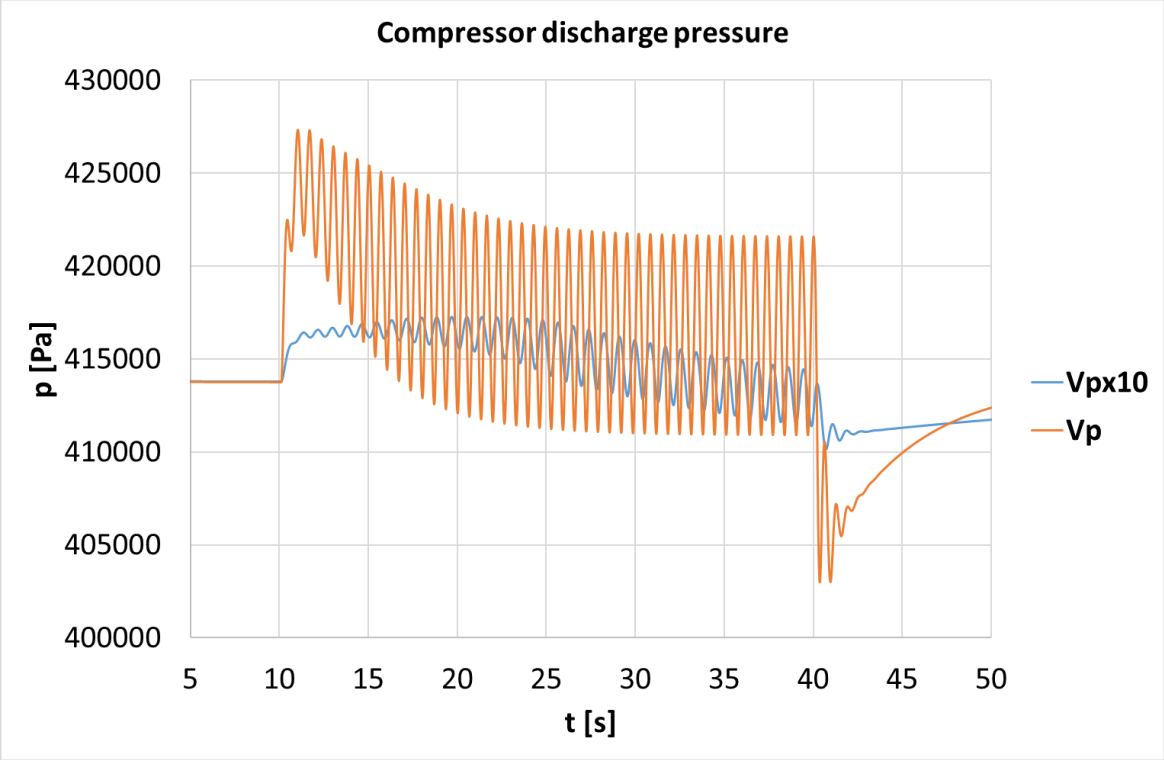

Figure 87: Compressor discharge pressure signals simulated during Surge Recovery Test1

From the analysis of the two previous simulated quantities, when the by-pass valve is opened both different volume size cases show it is possible to move the compressor operating point out of the unstable region with this maneuver. Moreover, the smaller volume case shows how after a reduced number of damped oscillations it is possible to have a transient condition where the mass flow is very close to constant while the pressure needs time to be restored.

This aspect is clear also looking at the operating points reported on the compressor map (Figure 88), the orange line moves from the stable surge cycles down towards lower pressure ratios and then with a spiral movement it shifts to the right, once mass flow fluctuations are terminated a vertical ascending trend is visible until the original pressure level is achieved. Once again, when the system is operated in open loop there is a wider movement of the compressor operating point in terms of mass flow rate if a bigger volume is considered, but a smaller amplitude in pressure fluctuation. It seems possible to state that a system with a bigger volume allows wider mass flow variation rather than pressure, it tends to keep its pressure condition longer than a smaller volume case. This aspect is helpful for those application where fast pressure transients must be avoided.

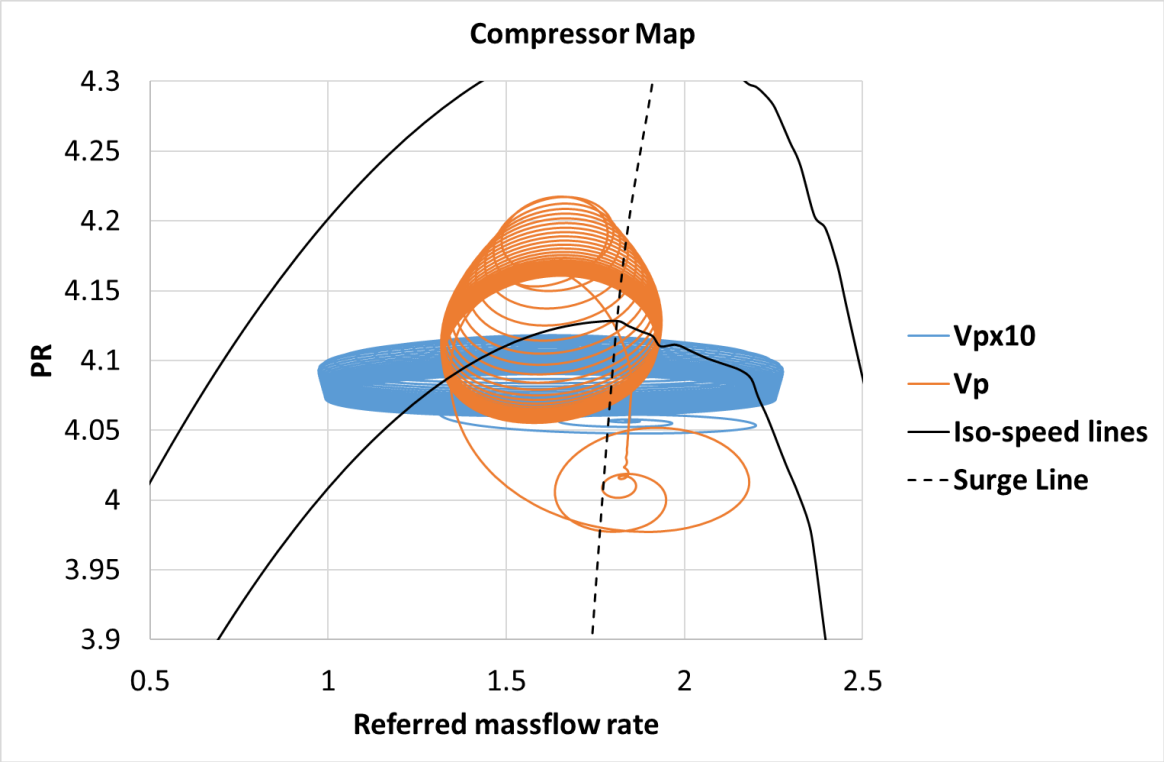

Figure 88: Operating point trends during Surge Recovery Test1 reported on compressor map

5.6.4. Surge Recovery Test2

This simulation aims to investigate what could be the impact of a control system on compressor instability, in particular, since in the previous simulated case it has been demonstrated that surge recovery is feasible acting on the by-pass opening, it is interesting to analyze what are the positive or negative interactions between a closed loop operated system and a surge recovery action like the one proposed here.

Figure 89 shows with red line the fuel mass flow rate governed by the speed controller and with a blue solid line the mass flow evolving through the by-pass valve. A significant difference emerges already by analyzing these signals coming from the two volume size configurations.

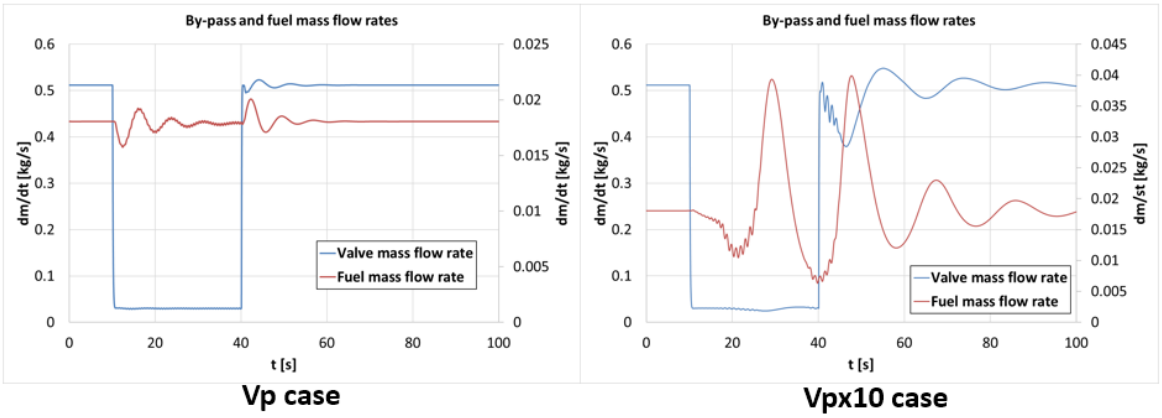

Figure 89: By-pass and fuel mass flow rates during Surge RecoveryTest2, closed loop configuration

Compared to the open loop case (Surge Recovery Test1), the system response needs a longer time to restore from signal fluctuations. It happens in both volume configurations, but it is highly evident in the bigger case as reported in Figure 90 with the blue solid line. When the original by-pass fractional opening is restored at second 40 of simulation there is an initial phase where the mass flow oscillations suddenly start to decrease their amplitude and surge event is gradually mitigated. At the end of this phase there is a slower transition until a stable working condition is recovered. The duration of this last transition phase in a closed loop configuration is highly affected by the size of the volume coupled to the turbomachinery, in fact in the Vpx10 case a transition phase is still present at the end of the simulation (t=100s) when a perfectly stable steady state condition is not reached yet.

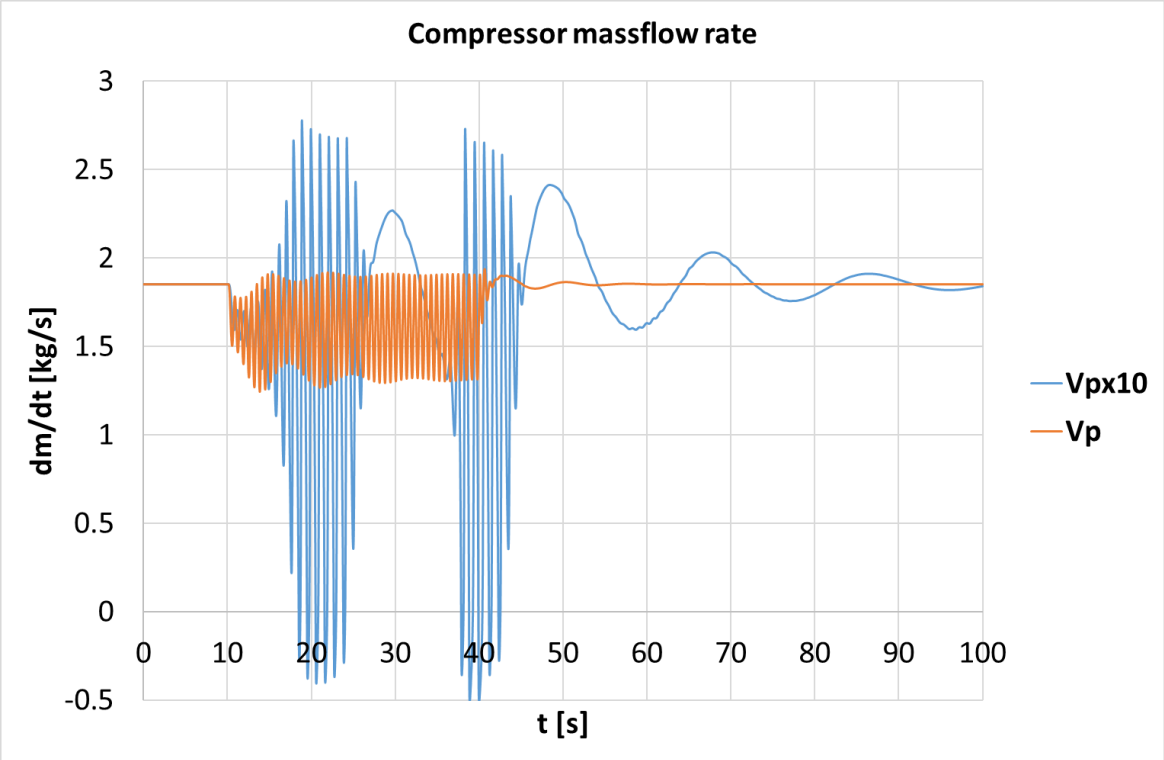

Figure 90: Compressor mass flow rate trends during Surge Recovery Test2 simulations with large volume (blue line) and small volume (orange line).

Similar considerations emerge from the analysis of pressure trends in Figure 91, here is probably easier to distinguish from the phase where surge is still present, but it is reducing its intensity and the transition phase where the fast pressure fluctuation terminate and a slower alternate progression proceeds.

It is important to underline that in the Vpx10 case, during surge event, there is a superposition of two main oscillating trends, one characterized by high frequency and the other one by a longer period. The presence of this second periodic behavior can strongly affect the recovery time just because the compressor operating point is moved farther from the original working condition; this doesn't happen in the Vp case for example. Even if each surge cycle presents a lower pressure variation in the Vpx10 case rather than in the Vp one, the overall pressure variation over the time is wider in the first case, Figure 91. This fact, as introduced in Surge Test2 description, is a peculiarity only for a large volume system subject to an automatic speed control, and together with the higher inertia of the system, seem to be the prime reasons of a longer recovery time.

Also from Figure 91 as was for Figure 90, it is clear how the transition between surge event and a recovered condition is longer in closed loop simulation then for the open loop case, and especially for the bigger volume configuration a stable condition is not completely reached at the end of the 100 seconds of simulation.

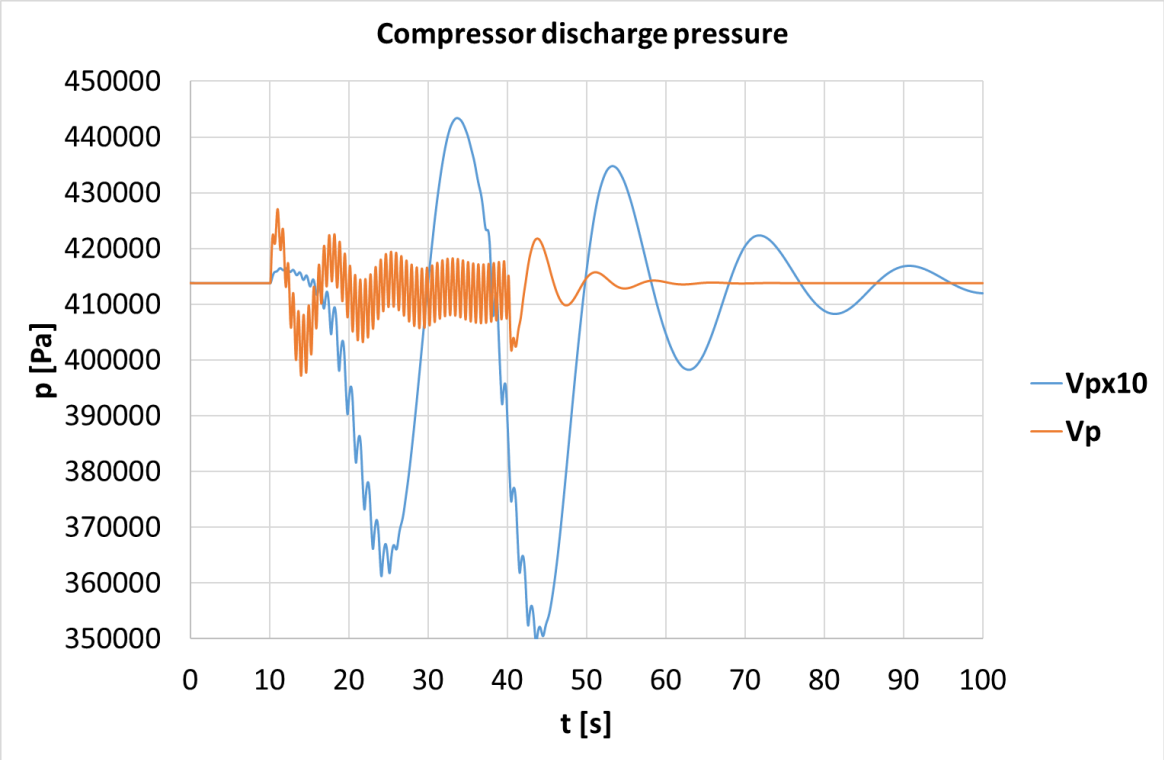

Figure 91: Compressor discharge pressure signals simulated during Surge Recovery Test2

Mass flow rate and compressor discharge pressure signals are combined and reported on compressor map. The complete simulation is reported in Figure 92. The differences between the bigger and smaller volume are highlighted by a significant difference between the two paths that operating points assume on this type of diagram.

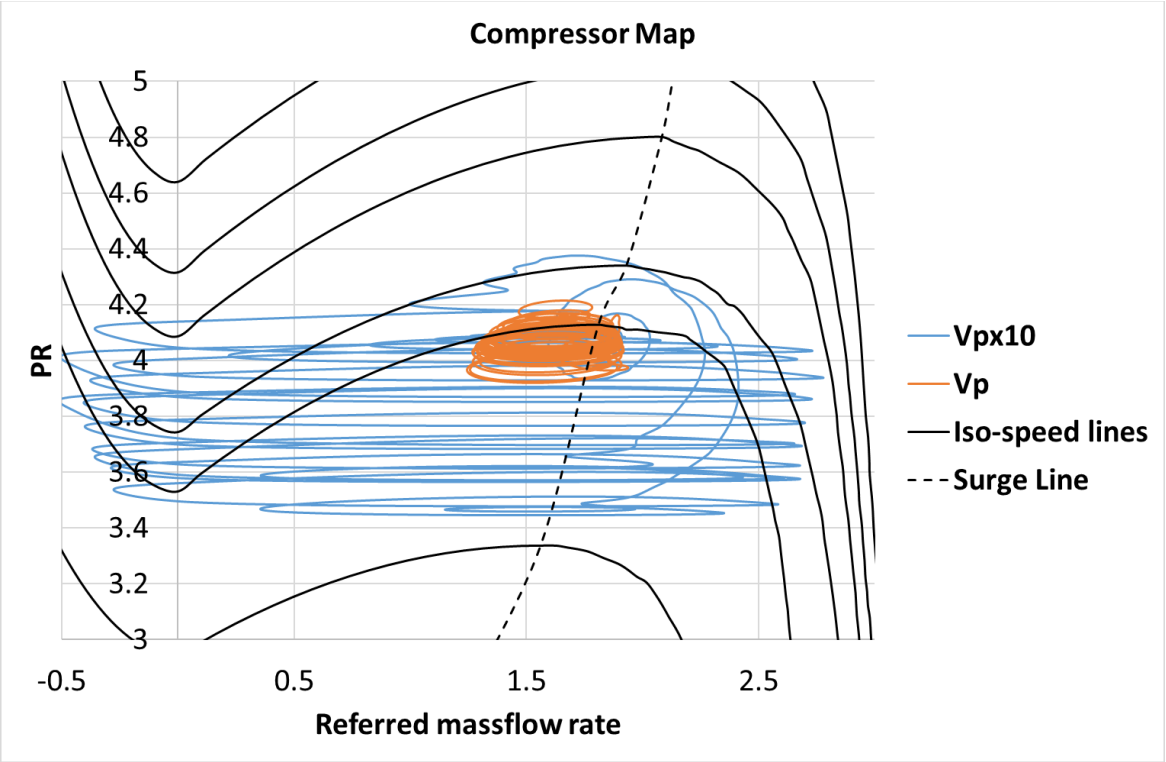

Figure 92: Operating point trends during Surge Recovery Test2 reported on compressor map

5.7. Compressor performance maps validation

Honeywell provided a complete set of characteristic curves of both compressor and turbine for the GTCP85-91C engine. Further investigations have shown that those maps were not specifically referred to the turbo-machinery installed at NETL laboratories, but they contained precious performance information about the series to which the machine belong.

Thus, to realize a dynamic model able to better match the actual working behavior of the entire system, an elaboration of the original maps was carried out.

Several tests were performed to collect data and characterize the MGT performance close to the design working point. During these tests, the emulator has been warmed up and driven to the system nominal point; starting from this state different load conditions have been reached, for example modifying the electrical load to the generator, or using different set points for the valve fractional openings of the bypasses. The main goal of this experimental campaign was to collect as many points as possible at constant rotational speed to create a reference iso-speed for the comparison of both compressor and turbine maps provided by the MGT supplier.

All the acquired set of data have been reduced and non-dimensionalized to be compared with the original maps. The reduction/non-dimensionalization process used in this analysis is reported from equation (82) to (87).

$$\dot{m}_{red} = \frac{\dot{m}_{dim}}{\dot{m}_{factor}} \quad \textbf{(82)}$$

$$\beta_{red} = \frac{\beta_{dim}}{\beta_{factor}} \quad \textbf{(83)}$$

$$N_{red} = \frac{N_{dim}}{N_{factor}} \quad \textbf{(84)}$$

Where:

$$\dot{m}_{factor} = \dot{m}_{d.p.} \sqrt{\frac{T_0}{T_{in}}} \frac{p_{in}}{p_0} \quad \textbf{(85)}$$

$$\beta_{factor} = \beta_{d.p.} \quad \textbf{(86)}$$

$$N_{factor} = \frac{N_{d.p.}}{\sqrt{\frac{T_0}{T_{in}}}} \quad \textbf{(87)}$$

Figure 93 shows the comparison between the original compressor map (orange solid line) and the post-processed characteristics (black solid line). The red points are the experimental points acquired during the hot test, which have been used as references to shift the original curves. The assumption at the base of this process is that all the curves are only translated in terms of mass flow rate and pressure ration keeping unaltered their shape. This means that only additive factors have been utilized to tune the iso-speed lines.

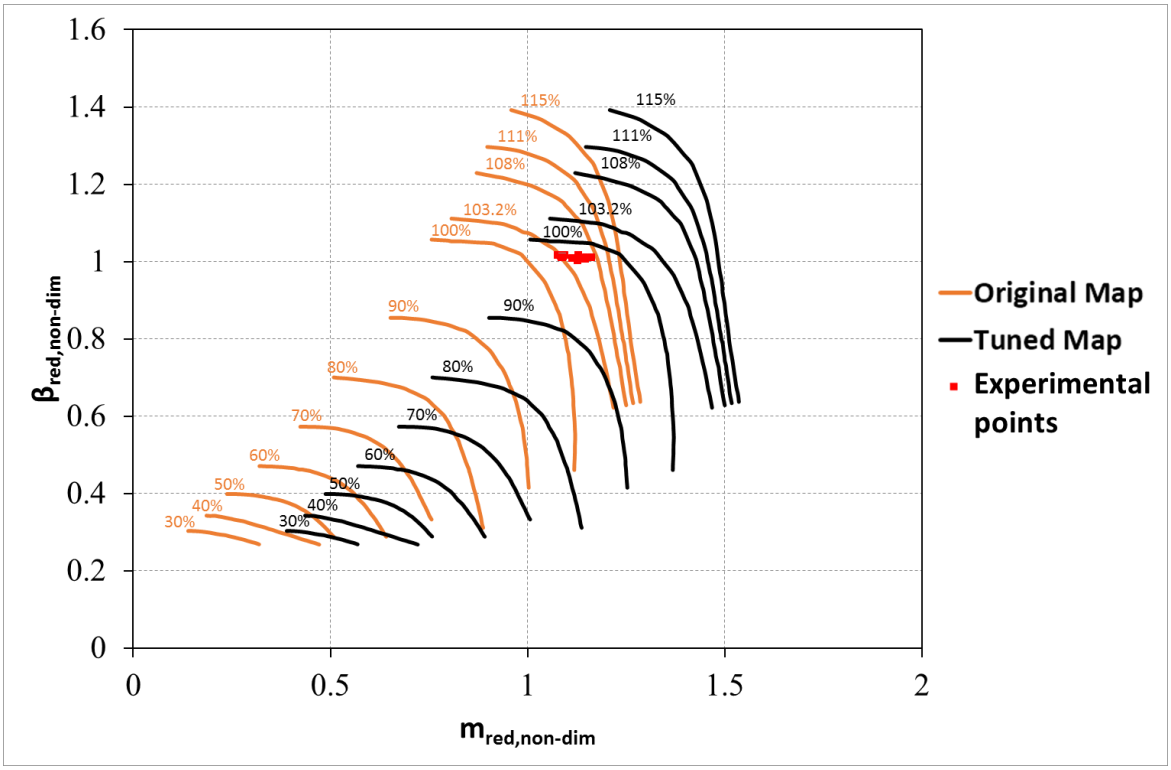

Figure 93: Compressor characteristics: comparison between experimental points, original map and tuned one.

The same procedure has been followed to tune the turbine map, obtaining the references for the curve shifting from the experimental data.

5.8. Conclusions

A novel dynamic model for the simulation of turbomachinery in Hybrid System configuration subject to unstable working condition has been developed basing on Hyper facility. A rotational speed control acting on fuel valve opening has been implemented and tuned. In this way both open loop and closed loop setups can be investigated on this layout.

The impact of the size of the volume between compressor and turbine on the system stability was studied thanks to two different configurations: Vp and Vpx10 case.

Generally, the model confirms that as the volume is increased the fundamental surge frequency decreases. It is remarkable how the shape of surge cycle is really volume depending, when a smaller volume is simulated an almost circular cycle is created by the compressor operating point on its map, while when a bigger volume is simulated the shape becomes more elliptical due to the predominance of flow oscillation compared to the pressure ones. As already introduced in the previous sections, this might be an important aspect for those components that suffer damage due to strong pressure fluctuations rather than flow oscillations or vice versa.

Once the compressor type is fixed the surge phenomenon is influenced by the system characteristic with which it is coupled. For example, the model response suggests that as different by-pass fractional openings identify different working conditions in the stable compressor field, similarly they imply different surge types with different intensity in the compressor unstable operating field.

The possibility to study the impact of the interaction between the control system and the volume size on the compressor dynamic stability is one of the novelties of this model. This suggested that in closed loop configuration it is possible that due to the establishment of several oscillating phenomena at different frequencies, a sort of superposition of effects generates a more complex oscillating motion in systems like the one object of this study. Many other studies can be performed with this simulation tool, maneuvers such as ESD and other transients will be object of future works.

6. A Hybrid System dynamic model for compressor instability investigations based on TPG facility

6.1. Facility description

The test rig facility object of this study is located at the university campus of University of Genoa in Savona, Italy, it is part of the Innovative Energy Systems laboratory operated by the Thermoelectric Power Group – TPG. The test rig is based on a commercial 100 kW recuperated MGT (Ansaldo/Turbec AE-T100) modified to be connected to a modular volume designed for physical emulation of fuel cell stack influence. As shown by Figure 94, it is designed for hybrid system emulation; the volume is located between the recuperator outlet and the combustion chamber inlet and can be isolated acting on VR and VO valves.

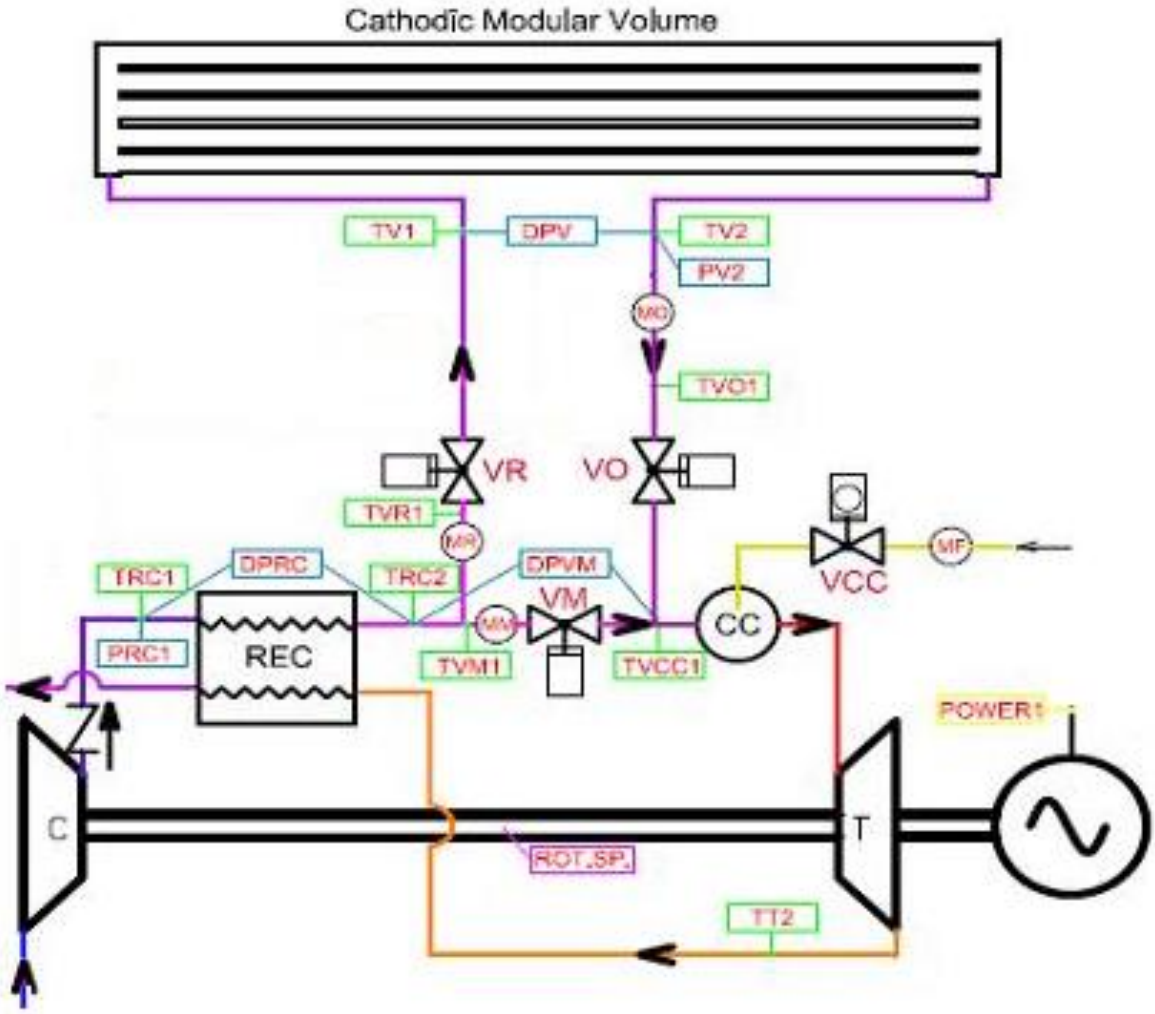

Figure 94: Layout of the AE-T100 based Hybrid System emulator

The test rig designed for hybrid system emulation is also equipped with a set of pipes designed for measurement reasons and to widen the operative range of the machine with a bleed, five valves to control the flow rates during start-up phases and a high temperature modular volume for the fuel cell stack physical simulation.

The fuel cell physical emulator, designed and presented in previous works such as[35] and [36], is a thermally insulated modular vessel connected between the recuperator outlet and the combustor inlet, as in a real pressurized hybrid system. This vessel, designed for a maximum temperature of about 630°C (903.15 K), is composed of two collector pipes, connected to the recuperator outlet and the combustor inlet respectively, and five module pipes connected to both collectors. These last pipes are mounted on seams for easy removal, i.e. easy volume dimension change. Both collectors and module pipes have a nominal diameter of 350 millimeters and their total length is around 43 meters for a maximum volume of about 4 m^3.

Figure 95 shows the AE-T100 based Hybrid System at IES lab, in this picture the main components are indicated with numbers:

- 1-4 Cathode emulation pipes
- 5 Anode emulation pipe
- 6 Connection pipes
- 7 AE-T100 micro gas turbine

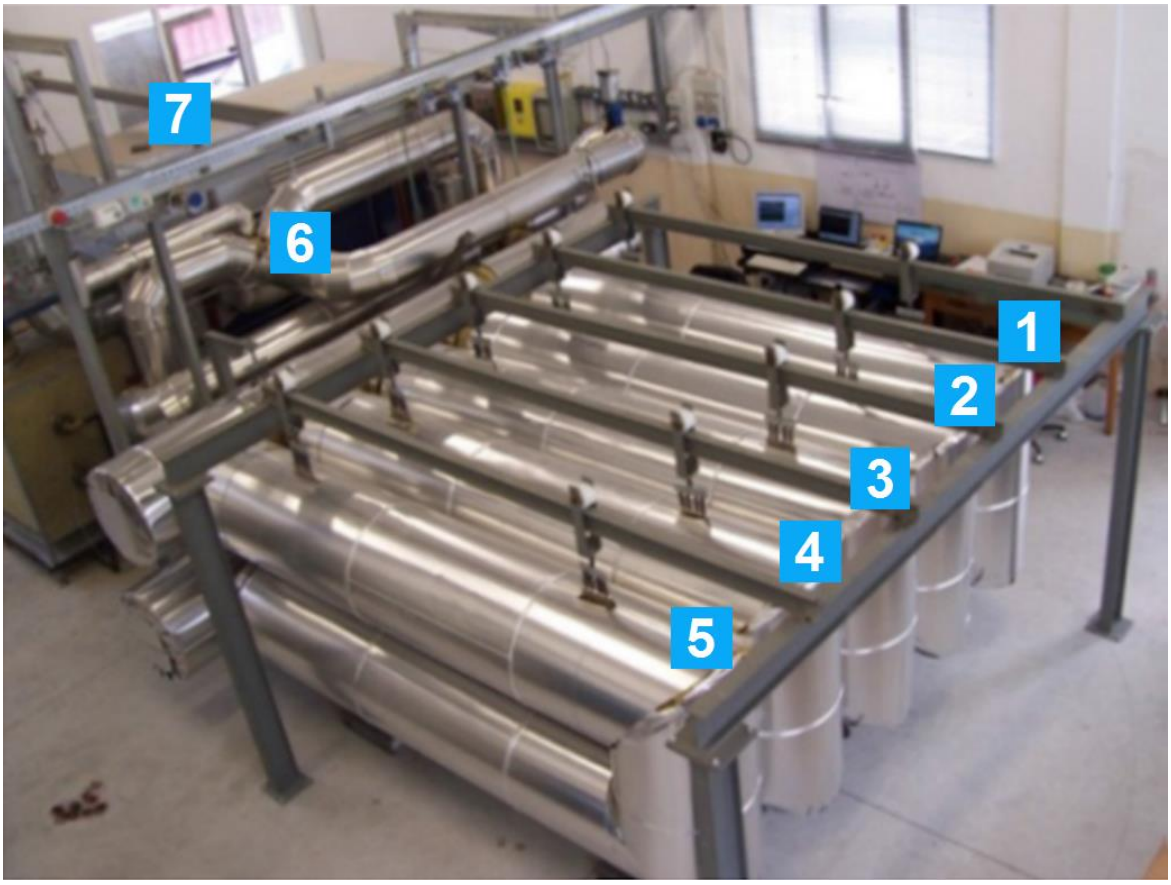

Figure 95: Picture from IES laboratory: the AE-T100 based Hybrid System emulator

6.1.1. The commercial machine

Ansaldo Energia manufactures AE-T100 micro turbines in a dedicated facility located inside its headquarter in Genova (Italy). AE-T100 new units and relevant service are commercialized worldwide through dedicated Distributors / Partners, but also through direct selling of micro turbines and spare parts to the final Customer. The machine is a Turbec AE-T100 PHS Series 3 [37] operating at stand-alone configuration or connected to the electrical grid with an apt safety interconnection panel. It is constituted of a complete module for power generation (100 kW at nominal conditions), a heat exchanger located downstream of the recuperator outlet (hot side) for cogenerative applications, and two battery packages for the start-up phase when the machine operates at the stand-alone configuration. The power module includes: a single shaft radial machine (compressor and turbine) operating at a nominal rotational speed of 70000 rpm (PR = 4.5) with a turbine inlet temperature (TIT) of 950°C; a natural gas fed combustor; a cross flow recuperator; a high speed generator; a power electronic group (rectifier, converter, filters, and main circuit breaker); an automatic control system; and the auxiliaries.

Figure 96: Microturbine equipped with direct connections

6.1.2. Connection pipes

Since the machine is not designed for connection with additional components, such as external pipes and volumes, the connection pipes have been designed with the objective of having the lowest possible pressure losses between the recuperator outlet and the combustor inlet. This is necessary to not to reduce the surge margin of the compressor and the overall machine performance too much. For this reason, gate valves have been chosen for this layout, except for the bleed line, and the pipes have been designed with a wide theoretical support. Table 11 lists the dimension of the connection pipes system illustrated in Figure 97.

Table 11: Dimension of the connection pipes system

	L [m]	**R [m]**	**V [m^3]**
1	4.575	0.05	0.0587
2	1.224	0.05	0.0096
3	2.400	0.05	0.0188
4	2.244	0.05	0.0176
5	0.917	0.05	0.0072
6	1.631	0.05	0.0128
7	2.200	0.05	0.0366
8	2.240	0.05	0.0248

9	1.224	0.05	0.0096
10	1.581	0.05	0.0124
11	7.315	0.07	0.1121

The redundant number in this figure represent the identical parallel paths that air coming from or going to the recuperator can cross. Parallel loops for the same path are all considered for the volume estimation in the model but taken into account only once for the equivalent length calculation.

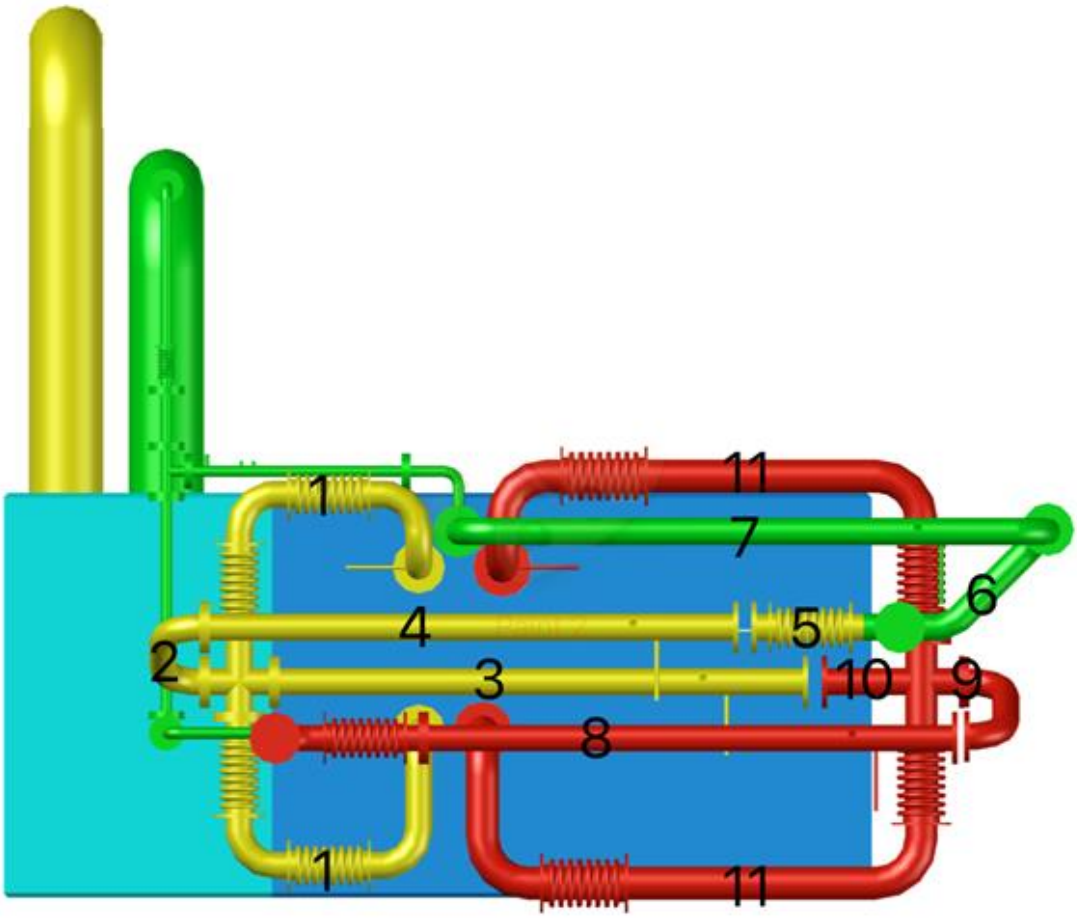

Figure 97: Scheme of the connection pipes between the MGT and the fuel cell emulator

6.1.3. Fuel cell emulator

The fuel cell physical emulator is a thermally insulated modular volume connected between the recuperator outlet and the combustor inlet, as in a real hybrid system. Even if the real fuel cell stack is not present in the rig, a volume coupled with the machine combustion chamber can be used, as demonstrated in previous works by the TPG [35], to generate both pressure and thermal effects typical of a high temperature fuel cell. The absence of a real

fuel cell allows to perform tests looking for new operative conditions, preventing expensive damages caused by surge events, excessive differential pressure between anode and cathode, unsustainable thermal gradients, or too low steam-to-carbon ratio problems. This volume is composed of two collector pipes, connected at the recuperator outlet and at the combustor inlet, respectively, and five module pipes connected to both collectors. Both collector and module pipes have a nominal diameter of 350 mm and their total length is around 43m to have a maximum volume of about 4 m^3. The modular approach used to design this system permits to emulate different fuel cell sizes and technologies simply connecting or disconnecting the parallel U shape sections.

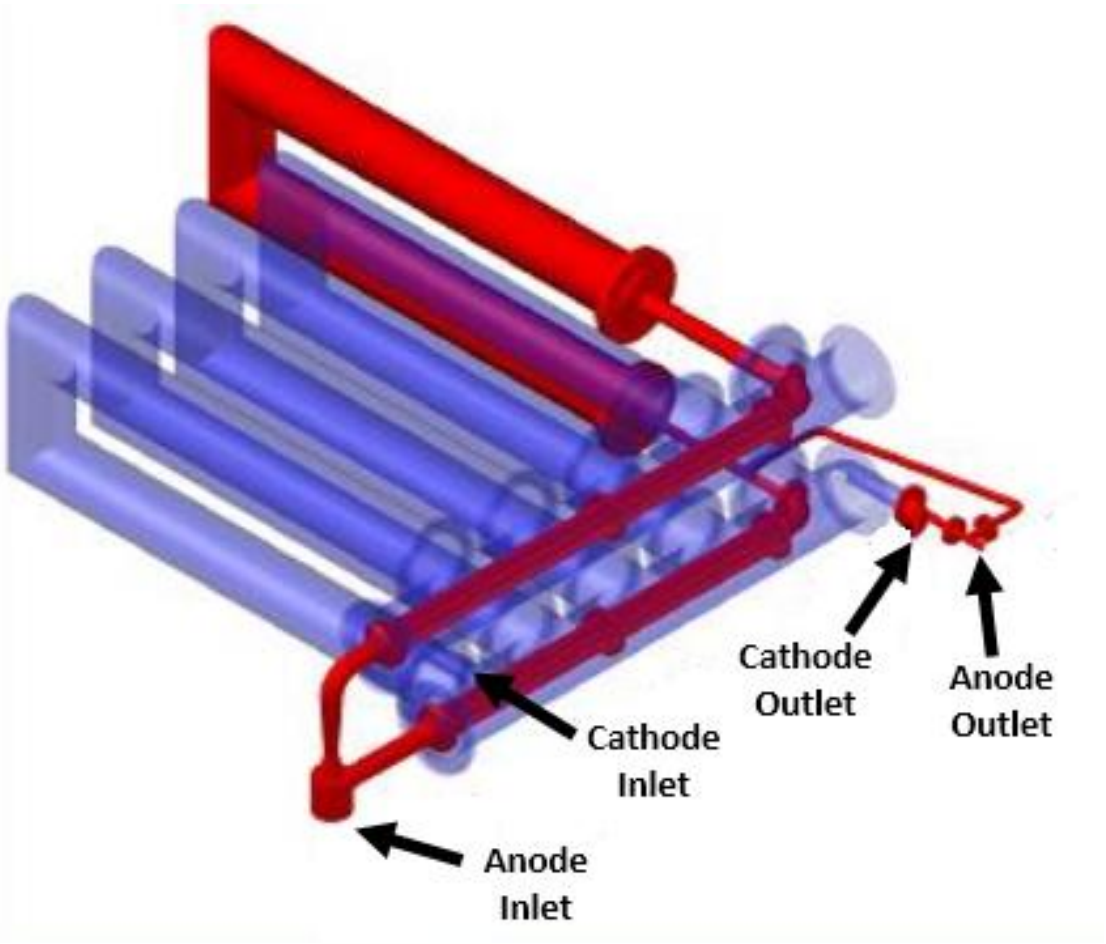

Figure 98: Fuel cell emulator modular volume

6.1.4. Data acquisition system

The commercial machine is equipped with the essential probes for control (rotational speed, TOT, intake temperature, and heating water temperature meters) and diagnostic reasons (vibration sensor, filter differential pressure, and other thermocouples), further instruments are installed on the test rig to measure the largest number of properties. All the additional transducers are connected to a PC through a FieldPointTM device, and their signals are acquired via LAN using the LabVIEW TM software. Table 12 shows a complete list of all the properties acquired.

Table 12: List of instrumentation installed on the AE-T100 based Hybrid System emulator

Mass flow rates		
Name	**Location**	**Probe type**
MM	Main line	Pitot tube
ME	Plant outlet	Thermal meter
MF	Fuel inlet	Thermal meter
MR	Volume inlet from recuperator	Pitot tube
MO	Volume outlet	Pitot tube
MC	Volume inlet from compressor	Pitot tube
MB	Bleed outlet	Pitot tube
Pressures		
Name	**Location**	**Probe type**
PA1	Ambient	Ambient sensor
PRC1	Recuperator inlet	Absolute
DPRC	Recuperator loss	Differential
DPVM	Main line loss	Differential
DPV	Volume loss	Differential
PV1	Volume	Absolute
Temperatures		
Name	**Location**	**Probe type**
TA1	Ambient	Ambient sensor
TRC1	Recuperator inlet	Thermocouple
TRC2	Recuperator outlet	Thermocouple
TVM1	Main line pitot	Thermocouple
TVCC1	Combustor inlet	Thermocouple
TT2	Turbine outlet	Thermocouple
TE1	Plant outlet	Thermocouple
TVR1	From recuperator pitot	Thermocouple
TV1	Volume inlet	Thermocouple
TV2	Volume outlet	Thermocouple
TVO1	From volume pitot	Thermocouple
TVC1	From compressor pitot	Thermocouple
TVB1	Bleed valve inlet	Thermocouple
TVB2	Bleed valve outlet	Thermocouple
TCHP1	Heating water inlet	Thermocouple
TCHP2	Heating water outlet	Thermocouple

6.2. Compressor map

The centrifugal compressor consists of an impeller, in which the gas is accelerated and an annular disc, named diffuser which decelerate the gas (kinetic energy) but increases the static pressure. The compressors performance can be analyzed on the so-called compressor map, here different information is available, for example it shows the relationship between the

pressure ratio β or PR (outlet pressure divided by the inlet one), the mass flow and rotational speed. Or it provides details on efficiency of the compressor. As introduced in the previous chapters, to obtain a model able to simulate compressor surge event an extended version of the compressor operating map is necessary.

In accordance with the definition in Chapter 0 three different zones can be defined on the compressor map.

- The first area is where the fluid reverses and compressor works unsteadily in backflow condition.
- The second area called Zone II identifies the conditions when the operating point has crossed the surge line, and the compressor operates in the zone between the zero-mass flow and surge line. This field is typically characterized by an unstable flow condition.
- The third area labelled Zone III contains the normal and steady operating area.

The complete working field can be derived from experimental data, calculated with energy transfer and energy losses balance or with a mix of experimental and calculated results.

In this work a mix of analytical and experimental approach is used. The compressor map obtained for the normal operating region with experimental acquisition performed by the compressor provider is utilized as starting point for the extension, moreover geometrical data and boundary working conditions such as the different values assumed by rotational speed are utilized to derive pressure ratios in the unstable regions.

The complete extended compressor map for the AE-T100 machine is reported in Figure 99.

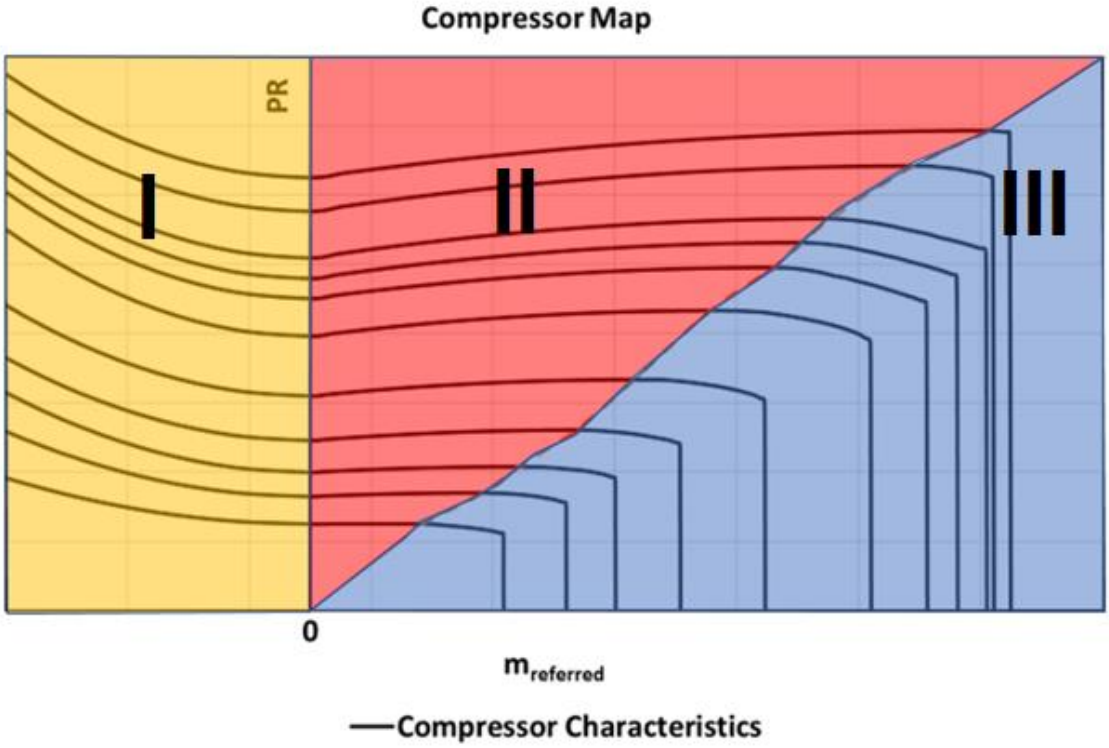

Figure 99: Extended compressor map for AE-T100 machine

6.2.1. Compressor map: Zone III

The data for the compressor characteristic is provided by Ansaldo, a leading international player in the power generation industry based in the city of Genova. In this study, the data required to start the map extension are the values of pressure ratio and mass flow rate for each iso-speed line in the normal operating region of the compressor map (Zone III).

It is important to underline that it is usually particularly difficult to obtain such information from the turbomachinery manufacturer, for this reason we thank the microturbine division of Ansaldo Energia that during this study and previous collaborations showed great willingness to provide valuable data and information.

The manufacturer has supplied the complete set of compressor (and turbine) performance maps, this are two diagram, the first one shows pressure ratio as function of mass flow and rotational speed of the compressor while the second reports the efficiency for different pressure ratios and speeds; only the first one is used in the present work.

Figure 100 reports the compressor characteristic map of an AE-T100 machine Series 2. Some considerations can be outline from main details in this map: first, the curves have a not very marked concavity in the central part, which, contrary to the axial machines is typical for a centrifugal compressor as the one installed on the AE-T100; there is a sudden change of slope in correspondence of the choke region, which suggests that the trend of the curves is not purely physical in this area; by following some of the curves referred to the low

rotation speeds from right to left (from the choke condition towards the surge line), it is possible to see that they have a progressively increasing and then decreasing trend.

In this work, only the points where the curves assume a decreasing trend as the flow rate increases are considered as belonging to the Zone III map, in fact, it was decided to place the surge line exactly at the maximum point of each compressor iso-speed line.

Figure 100 shows the on-design operating point recommended by the manufacturer when the machine operates in standard configuration (red point) and the corresponding nominal operating curve (dashed line).

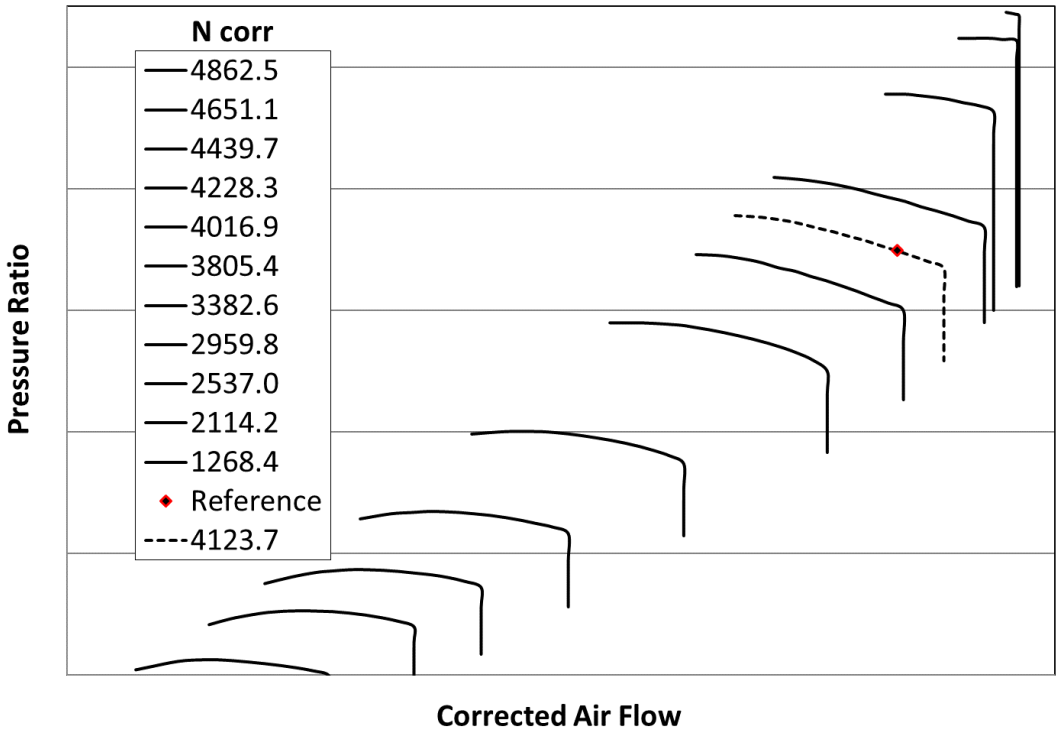

Figure 100:AE-T100 compressor map (Zone III)

In order to be accepted by the model, this map has been reorganized in one table where values of pressure ratios (Y) and mass flows (X) are alternatively reported in columns. Each set of two columns (Y, X) is representative of one specific iso-speed line.

6.2.2. Compressor map: Zone II

To determine the shape of the characteristic curves in this area of the compressor map, a mixed procedure was adopted combining the experimental data provided with Zone III, the geometric parameters provided by the manufacturer and an analytical approach that will be described below.

During this working phase, the characteristic curves of the compressor were analytically obtained following the approach used by other authors such as Gravdahl [31], once the complete set of iso-speeds is obtained the calculated compressor map is adjusted using corrective factors to align them to the compressor map in Zone III.

Starting from the definition of compressor total to static isentropic efficiency and thanks to the perfect gas assumption with constant c_p, it is possible to substitute the enthalpies with h = c_p T, obtaining the efficiency formulation reported in Eq.(88).

$$\eta(\dot{m}, U) = \frac{h_{2s} - h_{01}}{h_{02} - h_{01}} = \frac{T_{2s} - T_{01}}{T_{02} - T_{01}} \quad \textbf{(88)}$$

Knowing that for an isentropic compression relation (89) is valid

$$\frac{T_0}{T} = \left(\frac{p}{p_0}\right)^{\frac{k-1}{k}} \quad \textbf{(89)}$$

and for a radially vaned impeller the ideal enthalpy difference can be written as

$$\Delta h_{oc,ideal} = c_p\,(T_{02} - T_{01}) \quad \textbf{(90)}$$

the efficiency formulation of Eq.(88) can be rearranged to obtain the pressure ratio definition reported in Eq.(128)

$$\beta(U_1, \dot{m}) = \left(1 + \frac{\eta_i(m, U_1)\Delta h_{0c,ideal}}{T_{01} C_p}\right)^{\frac{k}{k-1}} \quad \textbf{(91)}$$

Starting from the Euler's equation where the power delivered to the fluid from the compressor can be calculated as

$$P_{c,ideal} = \dot{m}\,(U_2 C_{\theta 2} - U_1 C_{\theta 1}) = \dot{m}\,\Delta h_{0c,ideal} \quad \textbf{(92)}$$

Assuming there is no pre-whirl at the impeller inlet ($\alpha_1 = 90°$) which implies $C_{\theta 1} = 0$; the ideal specific enthalpy delivered to the fluid can also be expressed as function of the tangential outlet velocity and slip factor

$$\Delta h_{0c,ideal} = \frac{P_{c,ideal}}{\dot{m}} = \sigma U_2^2 \quad \textbf{(93)}$$

Where σ is the slip factor and the tangential velocity is derived with Eq. (94).

$$U_2 = \omega\, r_2 = D_2\, \pi\, n \quad \textbf{(94)}$$

Contrary to what this relationship (93) would suggest, the energy transferred to the fluid is not constant when the mass flow varies. In fact, different types of losses that play a fundamental role in this type of calculation must be taken into account, which as introduced they vary with changing operating conditions.

According to Watson and Janota [38], Ferguson [39], Nisenfeld [40], and other authors the two major losses expressed as specific enthalpies are: incidence losses in impeller and diffuser Δh_{ii} and Δh_{id}; and fluid friction losses in impeller and diffuser Δh_{fi} and Δh_{fd}.

The Stainz's formulation is used for slip factor definition (for more detail on slip factor see Appendix 9.1), here the approximation for radial tip is reported where *i* is the number of compressor blades.

$$\sigma \cong 1 - \frac{2}{i} \tag{95}$$

The isentropic definition used for this calculation includes all the correction contributes due to losses in the volute or clearance and back-flow introduced by many authors such as Gravdahl.

$$\eta_i(\dot{m}, U_1) = \frac{\Delta h_{0c,ideal}}{\Delta h_{0c,ideal} + \Delta h_{loss}} - \Delta\eta_{bf} - \Delta\eta_c - \Delta\eta_v - \Delta\eta_d \tag{96}$$

Where Δh_{loss} term considers incidence and friction losses both in impeller and diffuser.

$$\Delta h_{loss} = \Delta h_{ii} + \Delta h_{if} + \Delta h_{di} + \Delta h_{df} \tag{97}$$

Each individual loss contribution is now briefly introduced, for the complete discussion about each single part and to see all the calculation steps, please refer to the work presented in [31].

The first contribute of Eq. (97) is due to the incidence losses in the impeller, these can be calculated using the following equation:

$$\Delta h_{ii} = \frac{1}{2}\left(U_1 - \frac{cot\beta_{1b}\,\dot{m}}{\rho_{01}\mathrm{A}_1}\right)^2 \tag{98}$$

Where:

- β_{1b} is the fixed blade angle;
- ρ_{01} is the constant stagnation inlet density;
- A_1 called the impeller eye is calculated as:

$$A_1 = \frac{D_1^2\,\pi}{4} \quad \textbf{(99)}$$

Knowing that the mean quadratic diameter D_1 is calculated from the inducer diameter at tip D_{t1} and at hub D_{h1}.

The incidence losses for diffuser instead, are only present in the case of vaned diffuser and they can be evaluated using Eq. (100).

$$\Delta h_{di} = \frac{1}{2}\left(\frac{\sigma\, D_2\, U_1}{D_1} - \frac{cot\alpha_{2b}\,\dot{m}}{\rho_{01}\mathrm{A}_1}\right)^2 \quad \textbf{(100)}$$

Where:

- α_{2b} is the fixed diffuser angle;
- D_2 is the outer diameter;

The viscous friction constitutes a further loss contribution both in the impeller and in the diffuser. For those located in the impeller, it is possible to adopt the following formula introduced by Ferguson [39]

$$\Delta h_{if} = \frac{C_h l}{2D\rho_1^2 A_1^2 sin^2\beta_{1b}} m^2 = k_{fi} m^2 \quad \textbf{(101)}$$

Where:

- l is the mean channel length
- C_h is the surface friction loss coefficient defined by Watson and Janota in [38]
- D is the mean hydraulic channel diameter calculated using the mean values of the cross-section area and perimeter for the passage

In the same way the friction losses in the diffuser can be calculated similarly thanks to Eq.

$$\Delta h_{df} = k_{df}\dot{m}^2 \quad \textbf{(102)}$$

As anticipated further contributions to the losses may be considered, a possible modeling of these consists in estimating the corresponding drop in efficiency points and then to subtract them from the calculated efficiency. For instance, according to Pampreen [41], knowing the axial clearance l_{cl} and the impeller tip width b, it is possible to estimate the clearance loss of a centrifugal compressor.

$$\Delta\eta_c = \frac{0{,}3 l_{cl}}{b} \quad \textbf{(103)}$$

For other types of losses, due to the lack of correlations in the literature, different authors have suggested a loss of points of efficiency, according to Gravdhal back-flow loss occurs because the compressor has to reprocess the fluid that has been reinjected into the impeller due to pressure gradients existing in the impeller tip region, and it can be estimated as:

$$\Delta\eta_{bf} = 0.03 \quad \textbf{(104)}$$

Or again, according to Cumptsy, in the volute a loss will take place mainly due to the inability of the volute to use the radial kinetic energy out of the diffuser.

$$0.02 \leq \Delta\eta_v \leq 0.05 \quad \textbf{(105)}$$

As expected the resulting compressor map does not perfectly meet the shape of the original curves, it happens because even if the method is quite accurate, the result still remains a mathematical approximation of the performance in a real machine. Therefore, at the end of this calculation process the compressor map obtained is slightly modified in order to better match the first point of the iso-speed lines acquired experimentally and provided by the manufacturer. In particular, the curve corresponding to the nominal rotational speed is taken as reference during this passage.

The result of the previous mathematical steps did not deviate excessively from the expected results and guaranteed an excellent starting point for the extension, the final result, subsequent to the further correction phase, is proposed in Figure 101.

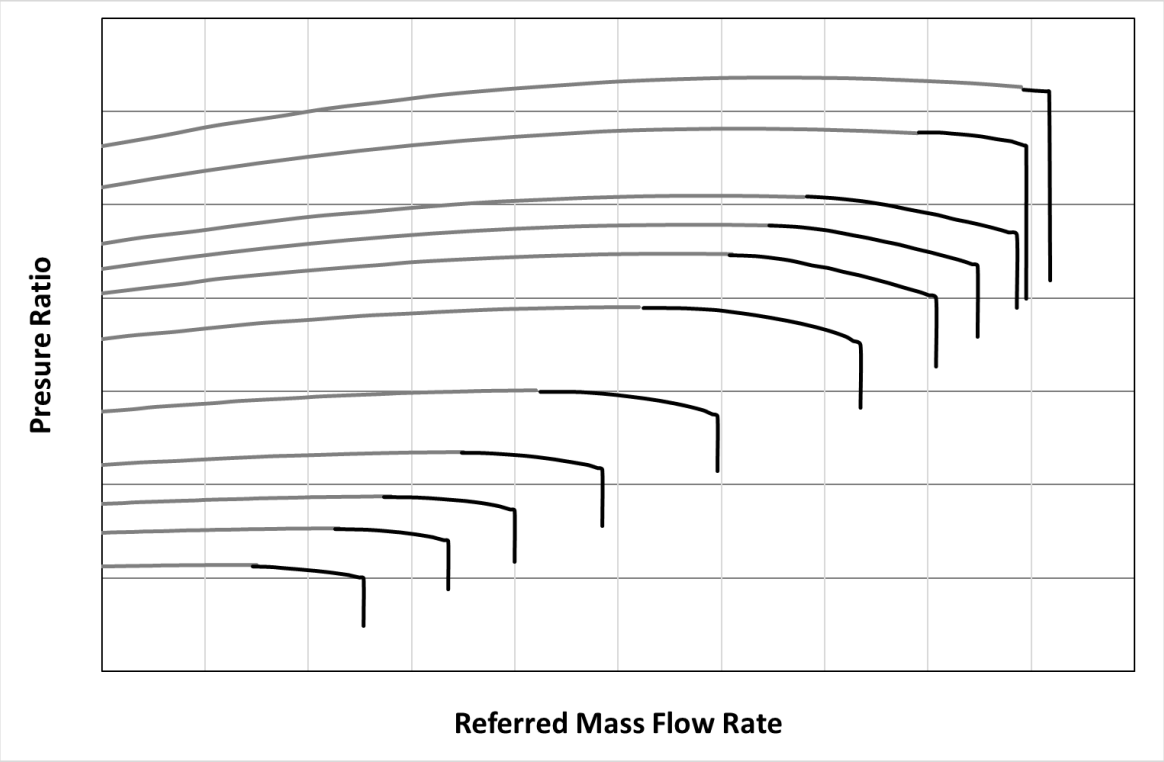

Figure 101: Compressor map extension in unstable region (Zone II)

The result obtained with this method, for the extension of the compressor operating points within Zone II of its own map, has been considered coherent with previous works by other authors and with the anticipated results from this thesis.

However, as can be seen in Figure 101, this approach does not guarantee perfect continuity between the calculated and experimentally acquired curves for each speed level. Consequently, in order to avoid discontinuities that could affect the correct operation of the code used to interpolate the compressor maps, it was decided to keep the points calculated in correspondence with the zero-flow condition and analytically connect them using quadratic curves to the extreme left points of the compressor stability region. It is possible to obtain such an extension applying the same boundary conditions used in the previous chapters of this thesis, where the zero derivative in correspondence of the points on the surge line is applied and the starting and ending points of each curves are defined.

The final result obtained after this further passage is reported in Figure 102.

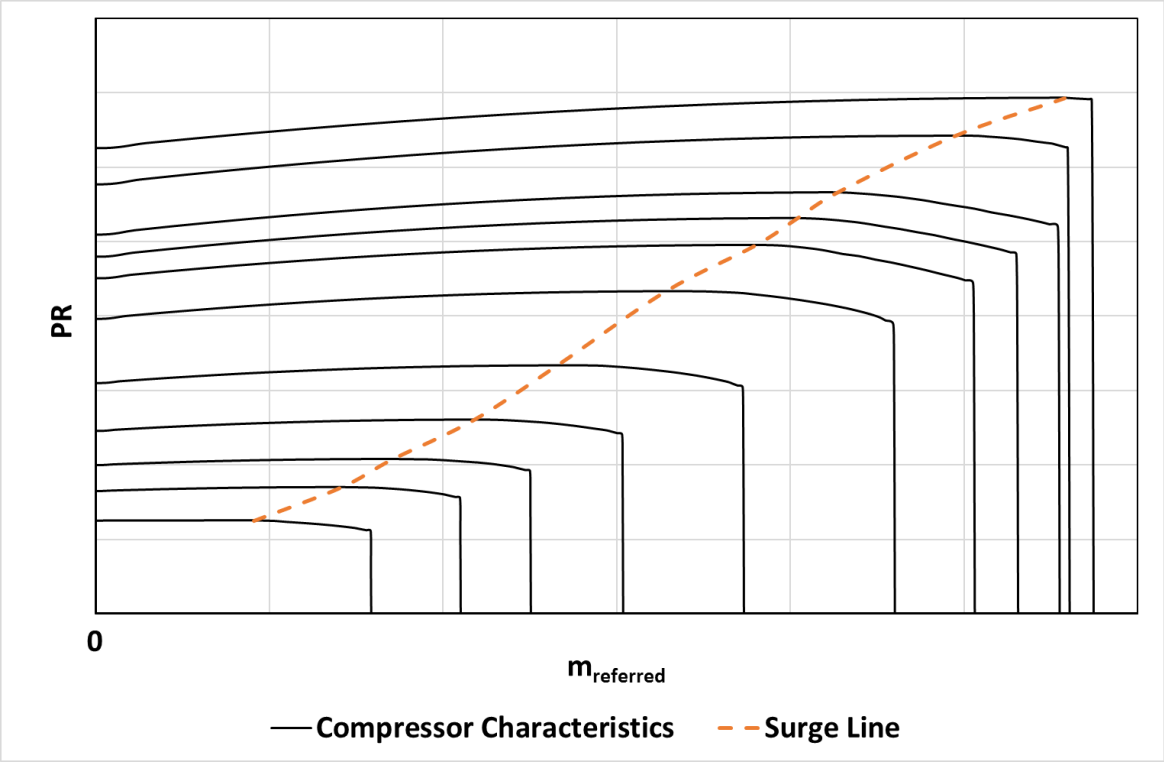

Figure 102: Final version of compressor map extension, Zone II and Zone III

6.2.3. Compressor map: Zone I

The same procedure used during the analyzes reported in the previous chapters was also used in this case to obtain the extension of the compressor map in the reverse flow zone (Zone I).

For the complete steps, refer to the previous chapters and in particular to paragraph 4.4.

The process has been automated thanks to the development of several codes in Matlab language, as for the values of Zone II, also in this case the code is able to create the extension of the map starting from the insertion of the necessary data. The following inputs are required: the rotation speed vector for which to calculate the iso-speed; the upper and lower limits of the range of flow within which to carry out the extension; the resolution required to identify the spacing between the points to be calculated.

The final result of the compressor map extension process is shown in Figure 102, for reasons of confidentiality the values on the axes have been removed.

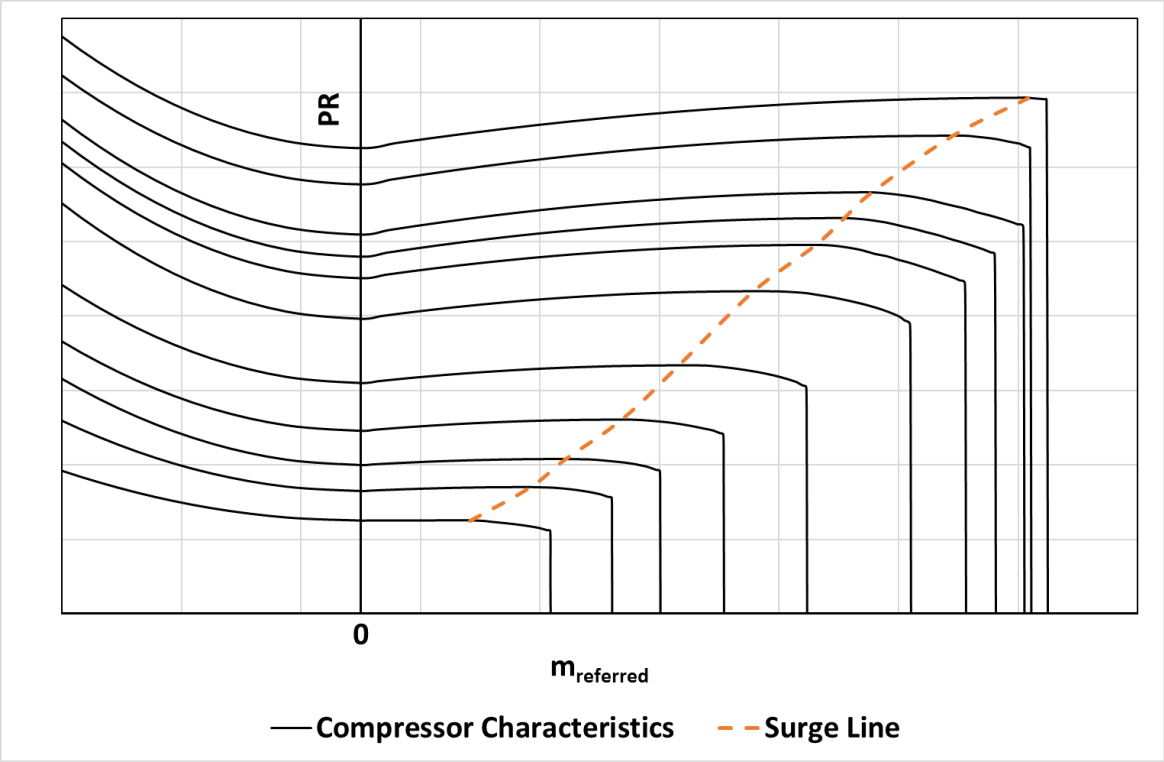

Figure 103: Final version of the complete extended compressor map for AE-T100 machine, Zone I, Zone II, Zone III

6.3. AE-T100 emulator model layout

The dynamic model represents the MGT-based hybrid system emulator test rig at the IES lab of University of Genoa located inside the Savona Campus.

The model shown schematically in the figure, has been assembled in a modular way connecting different models of dynamic components. these blocks, developed during the three years of study, were designed to be able to represent the single real components to which they are inspired, or to be connected together to create a more complex system layout. Over the years, a library of components has been created from which to draw on to create different layouts of the system.

To obtain a correct approximation of the real system through the lumped volume approach used in this study the following components are necessary: the compressor with the momentum equation (Eq.(106)) and the extended-map interpolator which acts as an actuator disk implemented under it mask; the main plenum that for this specific application is modelled using the only transient continuity equation (Eq.(107)); three different valves that share the same code scheme presented in paragraph 5.3.2 (Eq.(108)) but they differ in terms of equivalent lengths and sections depending on the portion of the system they are supposed to simulate; the combustor that simulates the increase in temperature due to the combustion of methane; the turbine block which, in this case, is purely assimilated to an actuator disk able to interpolate the maps in terms of flow rate, expansion ratio and efficiency; the generator which transform the electric power demand in to a mechanical power to extract

from the turbomachinery; and the shaft which deals with managing the balance of mechanical energy between turbine compressor and generator (Eq.(109)).

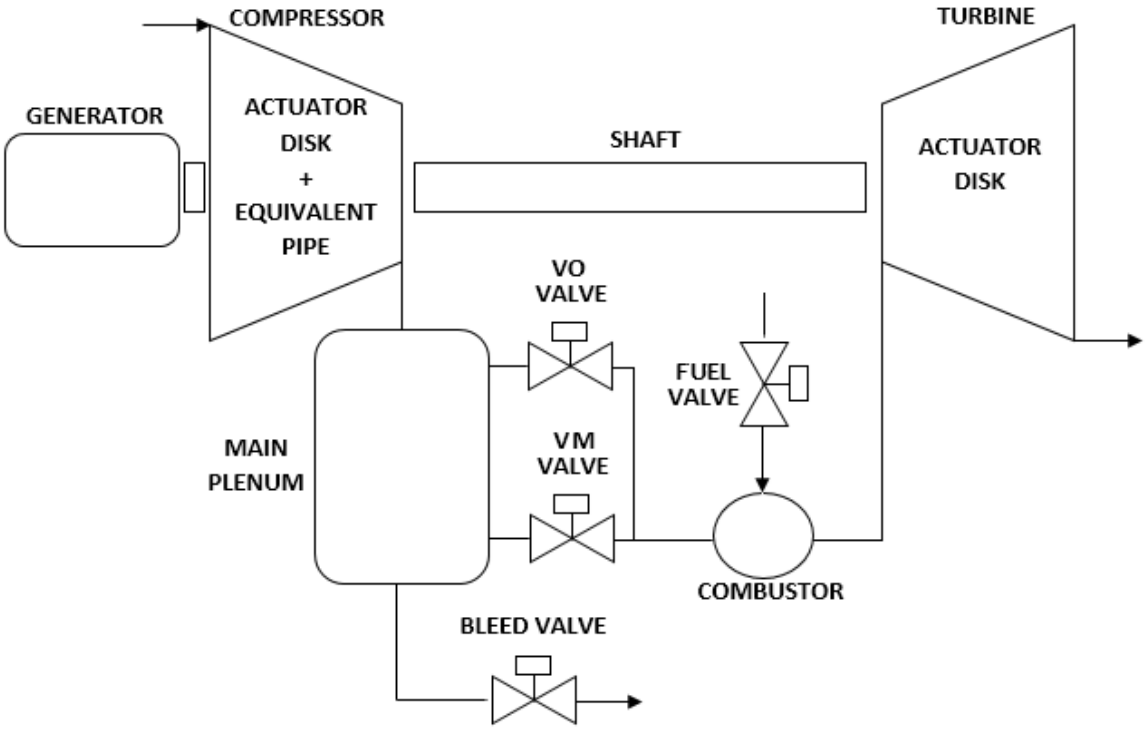

Figure 104: Model layout for the AE-T100 emulator

The set of main equations used to simulate the T100 based hybrid system emulator are merely listed here, the derivation and explanation for each one has already been introduced in the previous sections.

$$\frac{d\dot{m}_c}{dt} = (C - \Delta p)\frac{A_c}{L_c} \quad \textbf{(106)}$$

$$\frac{dp_p}{dt} = (\dot{m}_c - \dot{m}_T)\frac{kp}{\rho V_p} \quad \textbf{(107)}$$

$$\frac{d\dot{m}_T}{dt} = (\Delta P - F)\frac{A_{T_{FO}}}{L_T} \quad \textbf{(108)}$$

$$\frac{d\omega^2}{dt} = \frac{2}{J}\left(P_{turb} + P_{compr} + P_{loss} + P_{gen}\right) \quad \textbf{(109)}$$

Moreover, the model has been equipped with a control system that regulates the fuel through a PI controller in order to follow the imposed rotational speed setpoint. It must be specified

that this control strategy does not correspond to the system actually installed on the turbomachinery, but it allows to replicate a series of tests effectively without having to access the complex logic developed by AE company.

The B parameters for this system calculated with Eq. (5) are estimated to be approximately 2.65, 1.87, 0.73 with 4 m^3, 2 m^3 and 0.3 m^3 respectively.

6.4. Simulation results

This section presents the results obtained from four different simulations. The first three simulate the behavior of the system when it is driven in the zone of instability of the compressor, here the system is deliberately driven into surge by closing the valve that is located along the primary flow line, positioned immediately after exiting the main volume. The fourth simulation focuses on the risk to incur in dangerous flow oscillations during transients if the operating point is close to the surge line.

The first three simulations differ in the dimensions of the volume considered. As already mentioned in the previous system description, the real plant consists of a series of parallel U-shaped pipes that make the entire system modulable in terms of the volume contained between the compressor discharge and the turbine inlet.

The three different tests were carried out respectively with volumes equal to 4 m^3, 2 m^3 and 0.3 m^3, this was done to obtain results comparable to those reported in the work [42] published in 2018. In this specific work the same procedure that brings the system into surge acting on the valve placed in the main air flow path was experimentally tested on the AE-T100 based Hybrid System emulator. This experimental test is particularly interesting as it has been repeated several times with three different volume sizes considered.

6.4.1. Impact of volume size on surge event

The following three simulations reported in this section start from the same initial condition to better compare and study the three cases. They are called Surge Test 1, Surge Test 2 and Surge Test 3 passing from the biggest to the smallest volume respectively.

Table 13: Initial conditions for Surge Simulation 1, 2 and 3

Compressor mass flow rate [kg/s]	0.51
Electric Power demand [kW]	40
Shaft rotational speed [rpm]	62800
VM valve position	Fully closed
Bleed valve position	Fully closed
VO valve position	Fully open

Surge Test 1

The volume simulated in the first test is 4 cubic meters, which in the real HS emulator corresponds to the configuration with all the pipes connected to the turbomachinery. The simulation starts from the stable condition indicated in Table 13, after which the valve VO is partially closed at second 5 and kept constant for the rest of simulation. This operation increases the pressure drop in the main stream, consequently the mass flow rate across the VO valve is drastically reduced as shown by Figure 105, then the compressor operating point crosses the surge line and the instability arises.

The oscillation due to the surge propagates throughout the whole simulated system, for example fluctuations in the flow signal VO through the valve (black solid line), or in the shaft rotation speed (red solid line).

The flow oscillations monitored at the valve downstream of the volume are of modest amplitude even when the compressor is in deep surge as in this case (see Figure 106). This happens because a large volume behaves like an oscillation damper in this case.

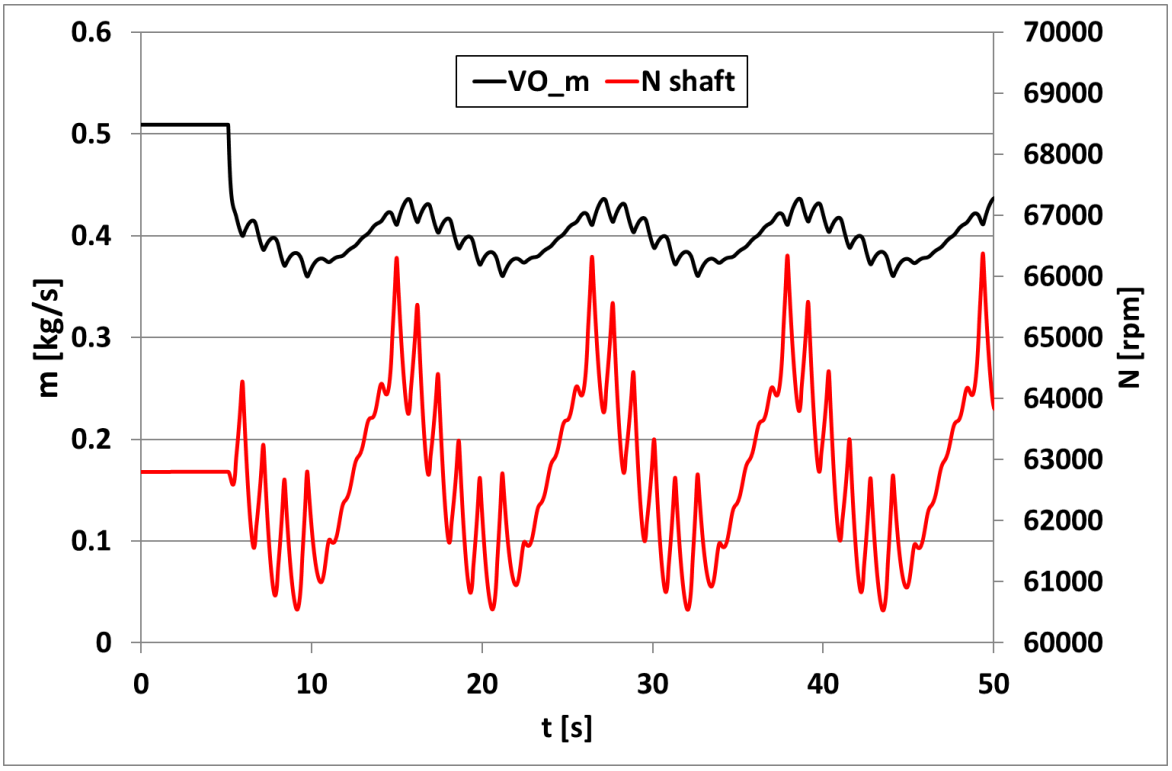

Figure 105: VO mass flow rate (black line) and shaft rotational speed (red line) during Surge Simulation 1

The Figure 106 shows the complete trend of the compressor operating point shown on its performance map. The chosen starting point is located in an area very close to the surge line to reduce the transient between stable and unstable operating conditions during all the simulations reported in this chapter.

During Surge Test 1 simulation it is possible to identify two distinct moments that alternate and repeat cyclically. There is a first phase in which the operating point of the compressor rapidly oscillates between the stability and instability zones, tracking large surge cycles on the map that extend their amplitude up to the backflow condition. As anticipated, this reverse flow condition is only present up to the vessel supply pipe and, under these test conditions, does not propagate downstream of the volume. During this first phase the surge cycles develop at lower and lower mean velocity levels until a partial stability condition is reached, here the operating point of the compressor is momentarily reported in an area to the right of the surge line.

The second phase begins when the minimum speed condition is reached, hence the control system tries to re-establish the starting point of operation. The Figure 106 shows how the operating point moves across the surge line increasing the rotation speed in an almost linear way (see figure 116).

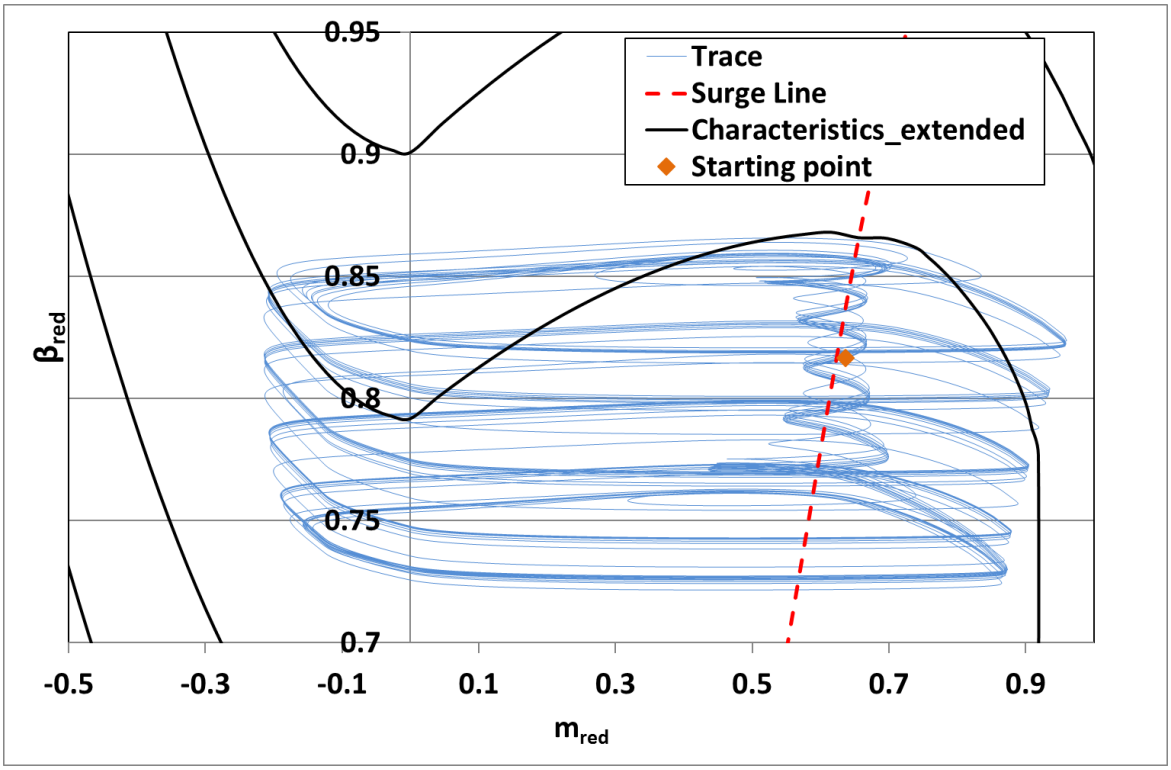

Figure 106: Compressor operating point on its map during Surge Simulation 1

During this rise on the compressor map, the compressor discharge pressure also increases linearly while the flow rate suffers from small amplitude fluctuations keeping its mean value almost constant. The mass flow rate and pressure trends at the outlet of the compressor are shown in Figure 107.

It is interesting to observe that both in Figure 105 in the Figure 106 as at the end of the second phase of ascent the compressor undergoes a kind of overshot in terms of rotation and

the discharge pressure as well (Figure 107). Due to this fact the operating point overcomes the stable starting condition.

For this specific test with a volume size equal to 4 m^3, the period of each surge cycle is approximately 1.2 s which therefore corresponds to a surge frequency of 0.8 Hz.

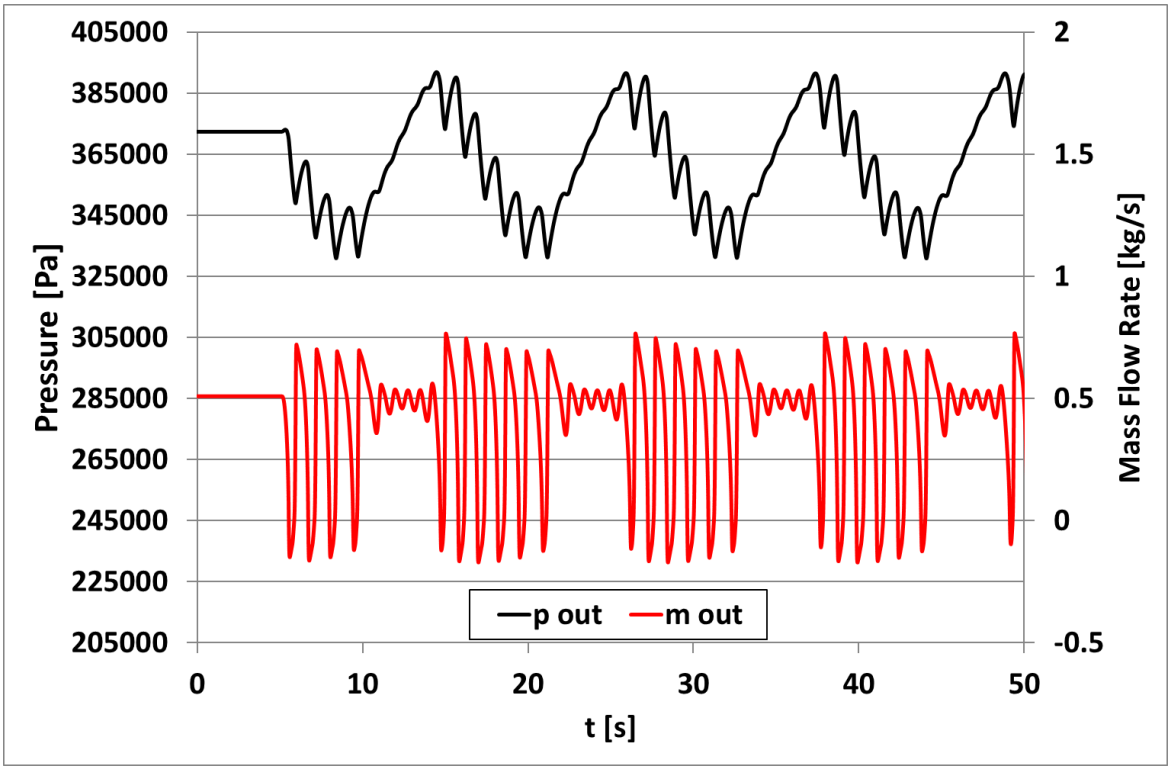

Figure 107: Compressor discharge pressure (black line) and mass flow rate (red line) during Surge Simulation 1

Surge Test 2

The second simulation discussed in this section follows the same control logic as the Surge Test 1. Moreover, also the maneuver performed during the test is the same, starting from the stable equilibrium condition described in Table 13, the same closing step of the valve VO placed in the main line of the system is carried out.

The difference compared to the previous test consists of the volume size considered inside the main planum, this time the volume is fixed to $2m^3$, which corresponds to a partial connection of the U pipes in the real emulator plant.

In this configuration the partial closing of the valve VO is followed by a phase lasting about 30 seconds at the end of which the surge cycles reach a stable oscillation condition. This transition is observable in all the monitored quantities, this is more evident for some observed parameters then others.

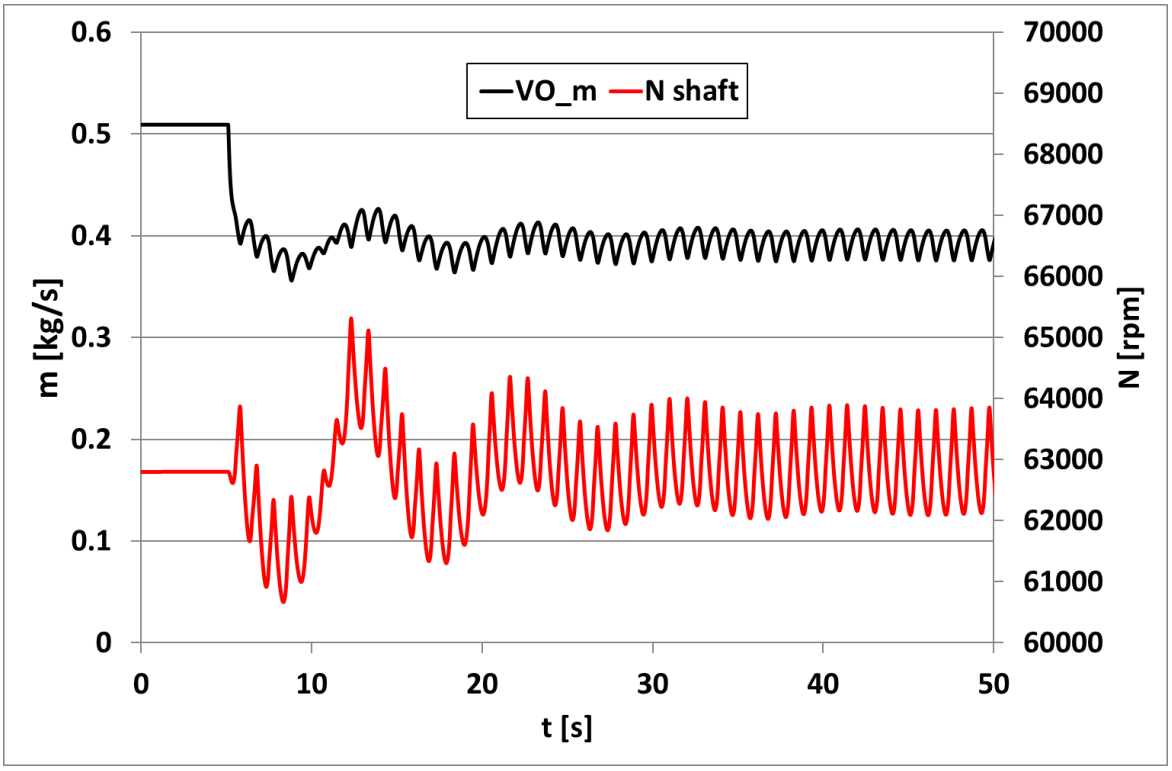

Figure 108: VO mass flow rate (black line) and shaft rotational speed (red line) during Surge Simulation 2

The results of this test show that after the first transition phase the surge cycles develop steadily with a period equal to about 1 second. The characteristic frequency of the surge in this case is therefore increased to 1 Hz. As expected the model shows that the surge frequency decreases as the system volume decreases.

The cyclic alternation of the two different phases described in Surge Test 1 are not present in this simulation. Here the rotational speed reaches a stable oscillation around a value slightly below the imposed setpoint of its controller (62800 rpm), therefore the cyclic behavior presented in Figure 105 is not triggered anymore.

A more marked trace on the map of the compressor in Figure 109 denotes a subsequent overlap of different surge cycles, this is an indication that the oscillation due to this phenomenon has stabilized.

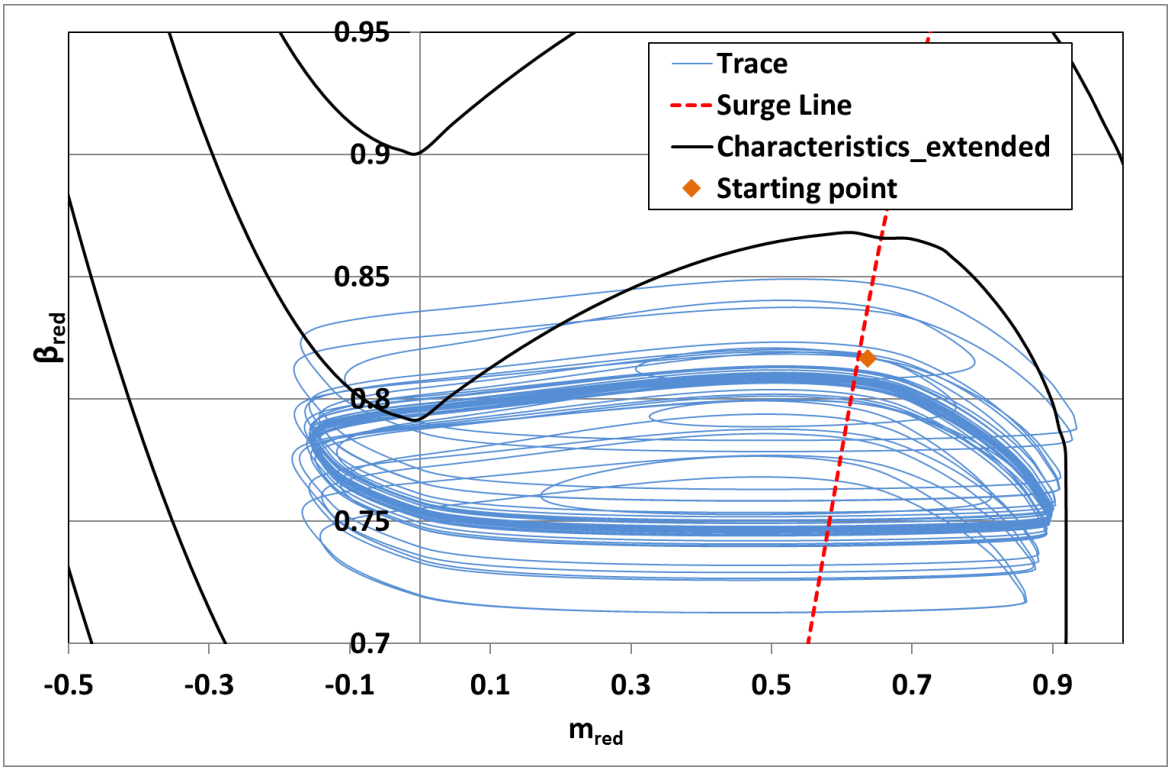

Figure 109: Compressor operating point on its map during Surge Simulation 2

Changing from a model with $4m^3$ to one with $2m^3$ it is noticeable how the single surge cycle surge has different characteristics. In particular, as the volume decreases, the cycle tends to shrink in the horizontal direction and to expand vertically on the compressor map. This means that the flow oscillations are characterized by a lower amplitude while the pressure fluctuations are characterized by a greater amplitude.

All these aspects can be found by observing Figure 110 where the flow and pressure signals, which combined reproduce the surge cycles, are shown.

Also interesting are the first moments of this simulation, immediately after the valve VO is closed, four successive surge cycles are established with amplitude similar to that will have once stabilized. Subsequently the average pressure level tends to rise towards the starting value, in this phase the surge cycles are partially mitigated temporarily and then re-developed around the 12s instant of the simulation.

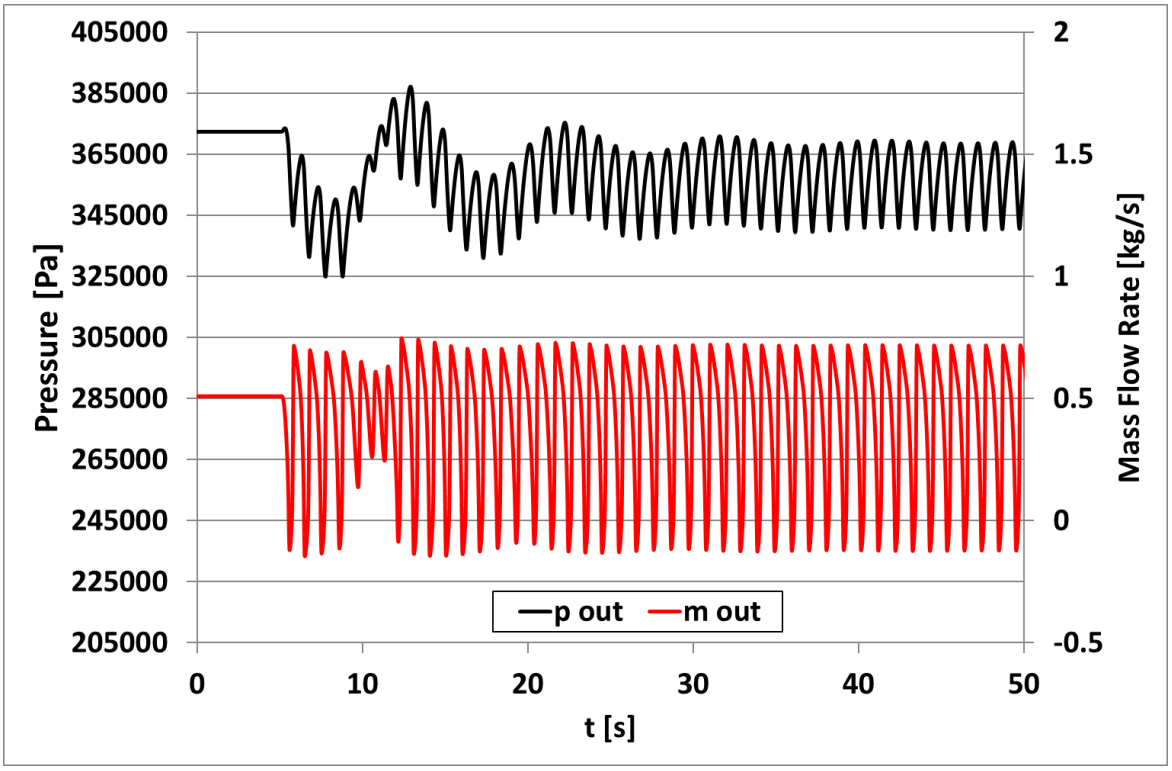

Figure 110: Compressor discharge pressure (black line) and mass flow rate (red line) during Surge Simulation 2

Surge Test 3

In this third test are reproduced the same maneuvers already presented in the two previous tests, in this case the volume contained in the main plenum was further reduced by imposing a value of $0.3m^3$.

It is evident how the transient between the instant in which the system is excited with the valve opening step and the achievement of the permanently developed surge cycle condition is much more contracted than the Surge Test 2. Both the flow rate at the VO valve and the shaft revolutions (Figure 111) are characterized by smaller amplitudes compared to the two previous cases. As expected also the frequency of oscillation of every signal has increased drastically.

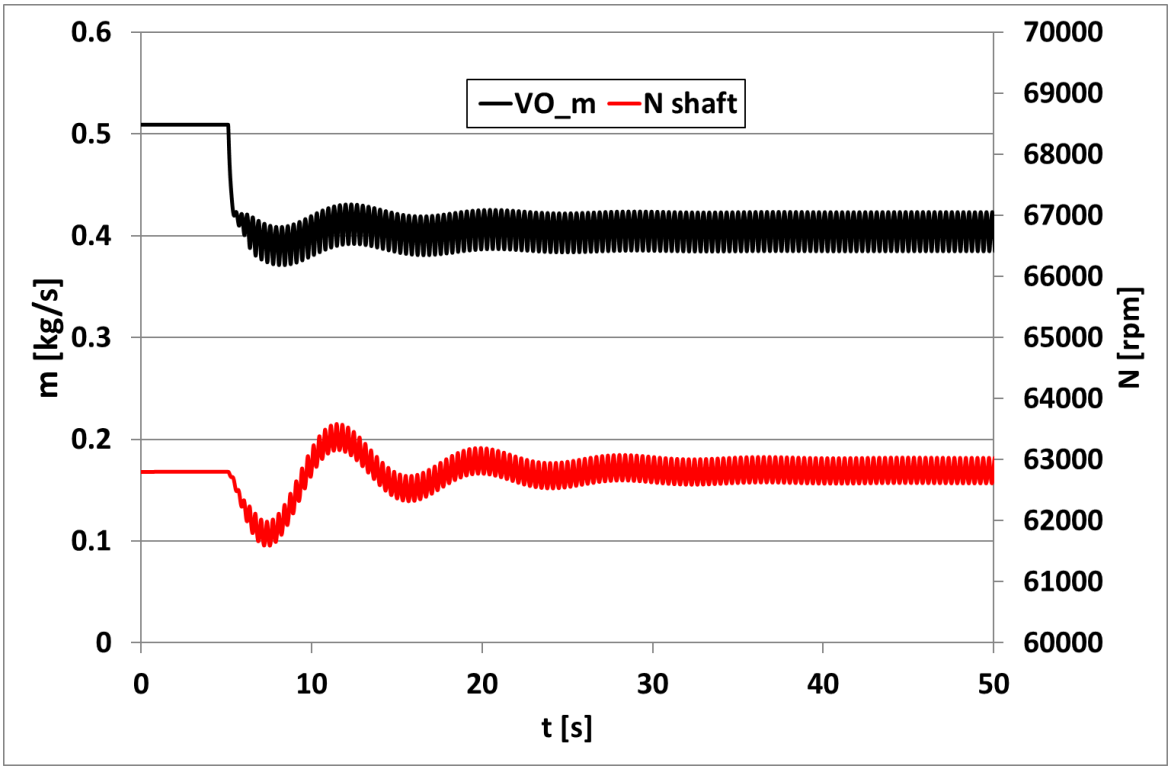

Figure 111: VO mass flow rate (black line) and shaft rotational speed (red line) during Surge Simulation 3

The reduced dispersion of the traces on the map of the compressor in Figure 112, shows how the transitory from the starting condition to establishment of a stable developed surge event covers a reduced zone, this is in agreement with the fact that a system characterized by a smaller volume has a lower inertia that speeds up its dynamics. Moreover, also the very first phase, in which the oscillations increase in amplitude until they reach dimensions comparable to those of the final condition, is shortened as the volume considered decreases. It is necessary to remember that in all the cases reported in this chapter the dynamics shown are the result of the interaction between the system response and the control system reaction, there are no open loop simulations discussed here.

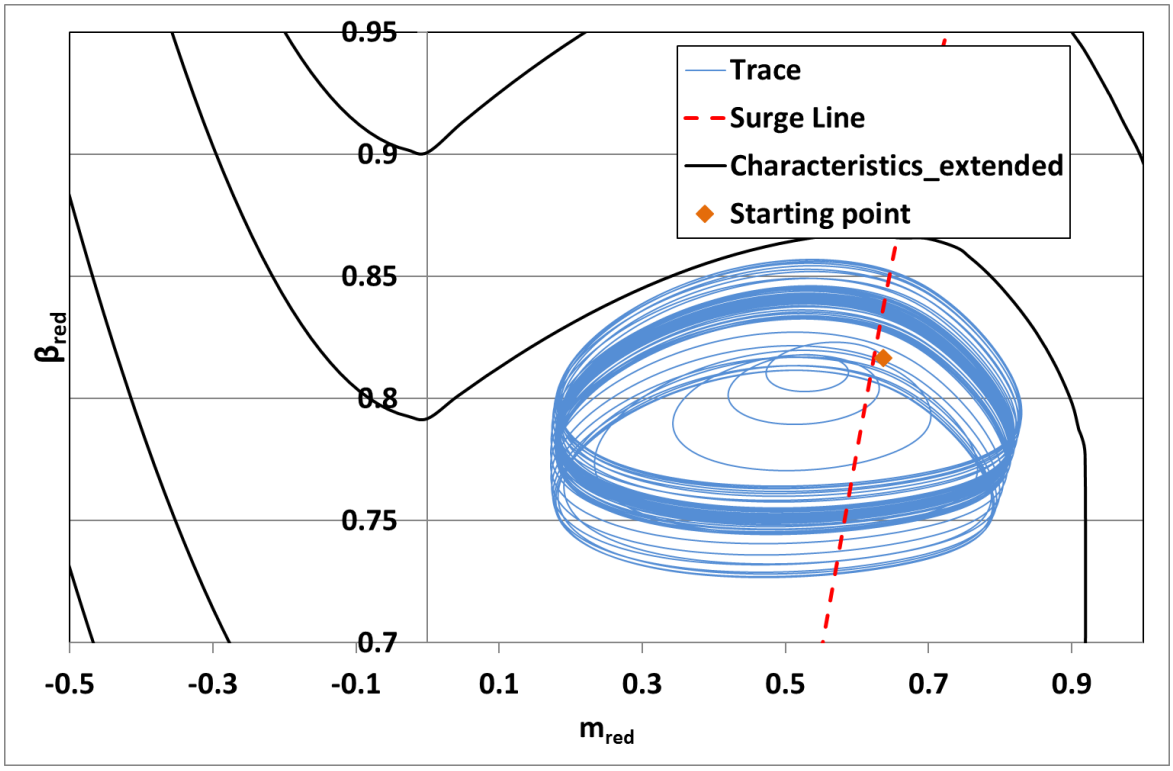

Figure 112: Compressor operating point on its map during Surge Simulation 3

Compared to the previous simulations the surge frequency increases up to 1.5Hz, surge cycles are faster and characterized by a more circular shape. The mass flow oscillations are characterized by a reduced amplitude while the pressure ones are wider as the volume is decreased, this is clear for example comparing Figure 110 and Figure 113.

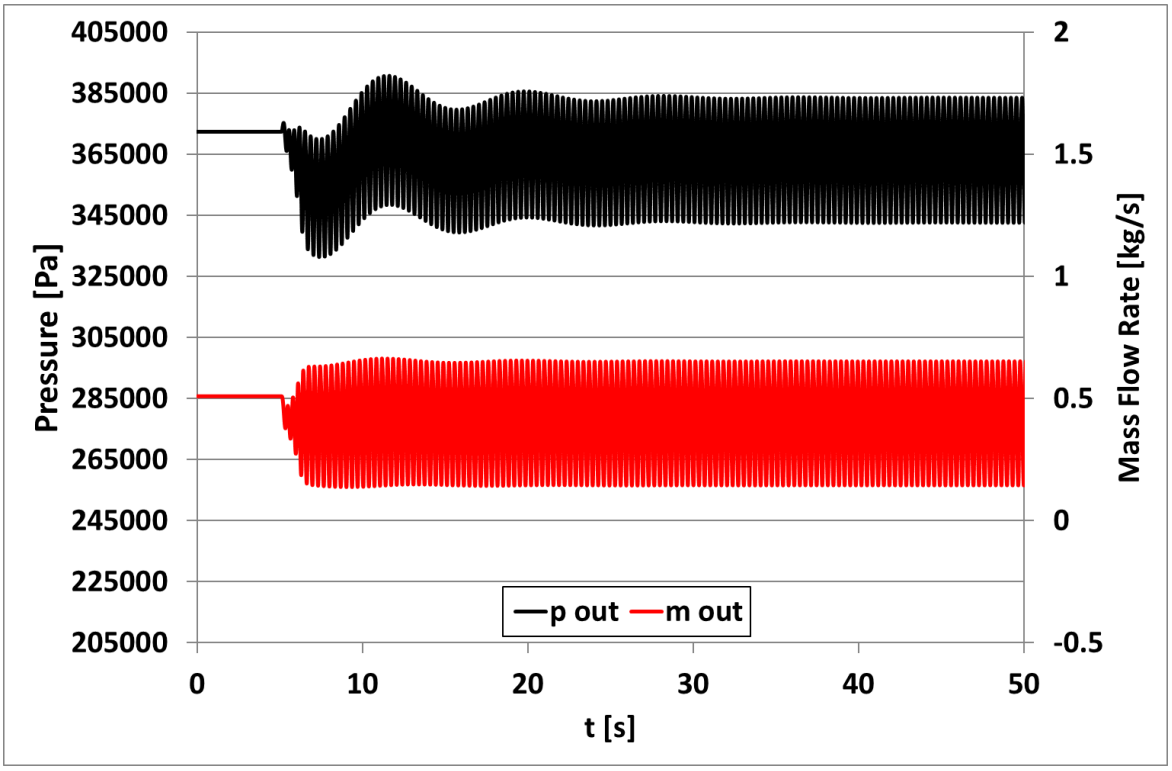

Figure 113: Compressor discharge pressure (black line) and mass flow rate (red line) during Surge Simulation 3

6.5. Comparison between simulated and experimental results

This section compares some results extracted from the simulations discussed in the previous paragraphs with the experimental results presented in the work [1], that were acquired experimentally on the same hybrid systems emulator based on the T100 machine. In both cases the impact of different volume sizes on the system dynamics is studied, and in particular on the surge phenomenon. The purpose of this discussion is to have data for a qualitative comparison between the performance obtainable from the model and the results obtained experimentally.

There are some substantial aspects to keep in mind during this comparison. In both cases the results derive from the same type of maneuver (closing of the VO valve in the main stream) but the openings at the end of the maneuver are different, during the experimental tests valve is completely closed but during the simulations this does not happen. Moreover, during the experiment performed on the real emulator, in the smaller volume case the flow path is completely different compared to the other cases because the volume composed by the U shape pipes is completely isolated. The reduction in the compressor pipe equivalent length due to this aspect is not considered in the model.

The two following figures show the simulated and experimental results respectively in terms of compressor mass flow rate considering different volume sizes. There is a short time interval in which the results can be compared, this interval includes at most two surge cycles per case study. After this period the control system installed on the real machine detects an abnormal behavior and it reacts by acting on its operation.

Both in Figure 114 and Figure 115 red dotted line indicates the bigger volume case, black solid line is used for the middle size volume and the yellow solid line for the smaller one.

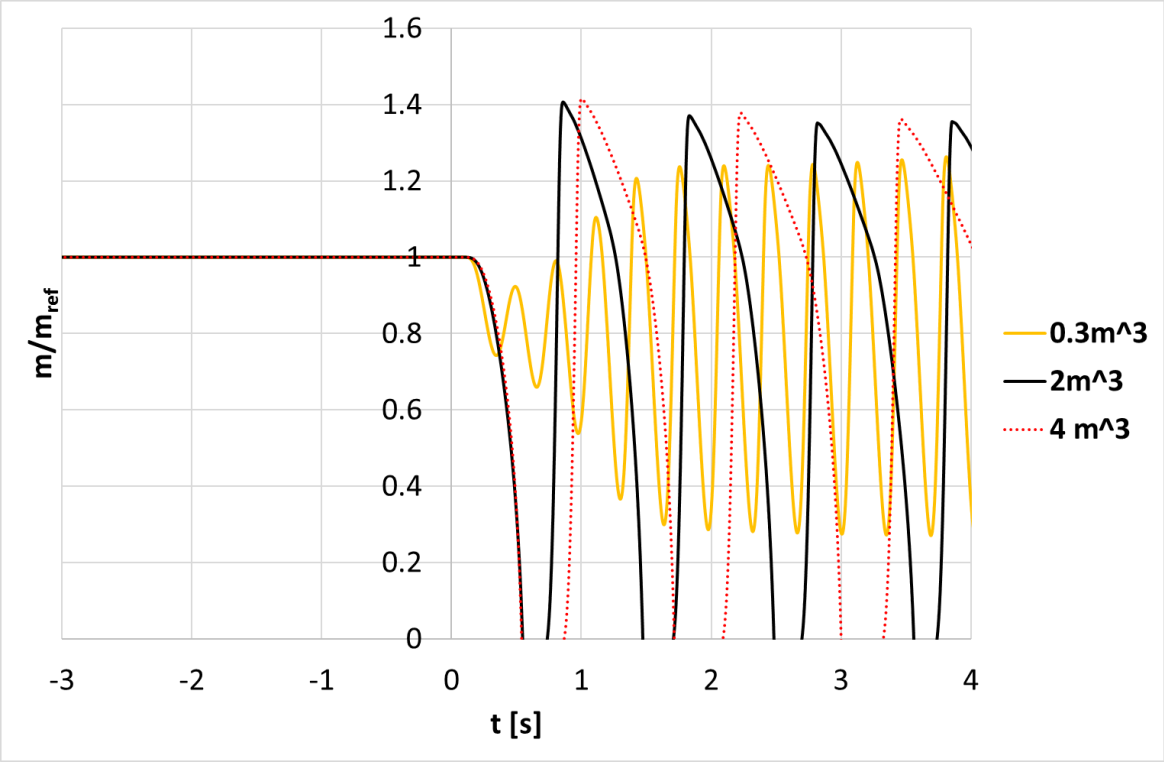

Figure 114: Simulated results, mass flow oscillations with different volume sizes

Observing the black and red lines it is possible to notice very similar shapes between the two figures, in both cases the serrated shape of the oscillations is very similar, with a very steep ascending phase and a more curved and less nervous.

The trend that connects surge frequency and volume size is present in both graphs, it is possible to notice how the frequency tends to decrease as volume increases.

The model is able to coherently replicate the instants immediately following the closure of the VO valve, both in Figure 114 and in Figure 115 a rapid decrease in the flow occurs which, in the case of 4 and 2 m^3, extends towards negative values index of compressor backflow. Another detail that can be found in both the experimental and the simulated data is the presence of a positive peak in the mass flow signal with a higher value compared to the initial stable condition, this is present for the two bigger volume sizes but not for the

smaller one. Thus, from the very first moments, the flow oscillation due to the surge phenomenon comprises a very large area of the compressor map when big volumes are present. It is expected that the stresses to which the compressor and the other components are subjected are immediately significant in these cases.

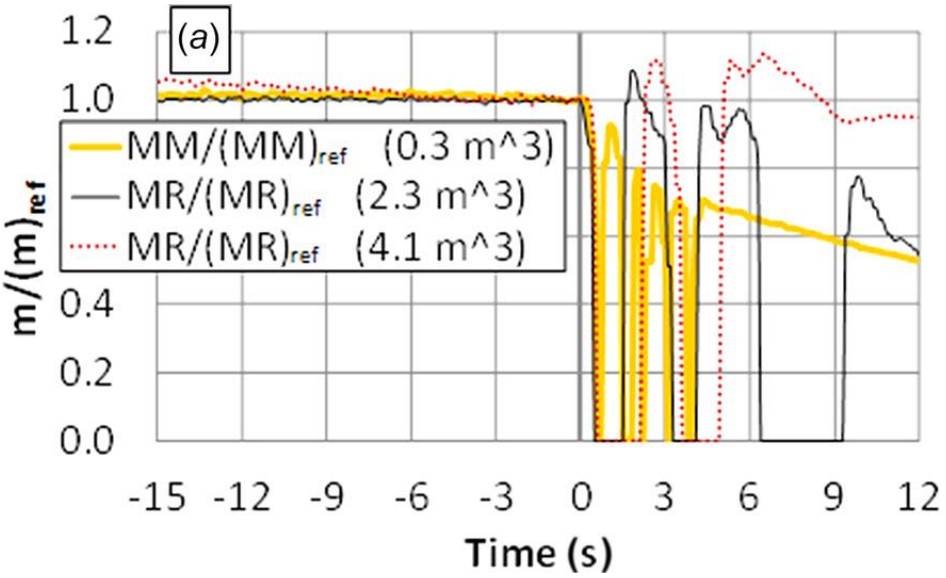

Figure 115: Experimental results, mass flow oscillations with different volume sizes

All the aspects in common between simulations and experimental acquisitions emerged from the analysis of the mass flow rate data can also be found by comparing the compressor discharge pressure graphs (Figure 116 and Figure 117). In all cases, it can be seen that the simulations return slightly higher surge frequency values than experimental acquisitions, this could be attributed to several causes including: impact of the different control system reactions between experiments an simulations, as demonstrated in Chapter 5 controller action can highly affect the surge dynamic response; underestimation of the whole system volume between compressor and turbine, larger volumes, for instance, can significantly extend the characteristic period of every single surge cycle; moreover, due to the complex geometry of the pipeline in the fuel cell emulator an error in the estimation of equivalent lengths may be present; or the estimation of the shaft mechanical inertia can also add further uncertainty in the surge dynamics simulation. The impact of many of these parameters on the surge frequency has been investigated in Chapter 4 and is not discussed in this session.

However, it is possible to conclude that the order of magnitude of the simulated frequencies match what carried out by experimental results; for example, the case with 4 m^3, which experimentally returns a frequency of 0.4 Hz, in simulation shows a frequency around 0.8 Hz, and in the case of 0.3 m^3, values of 1.3 Hz and 1.5 Hz are obtained during experiments and simulation respectively.

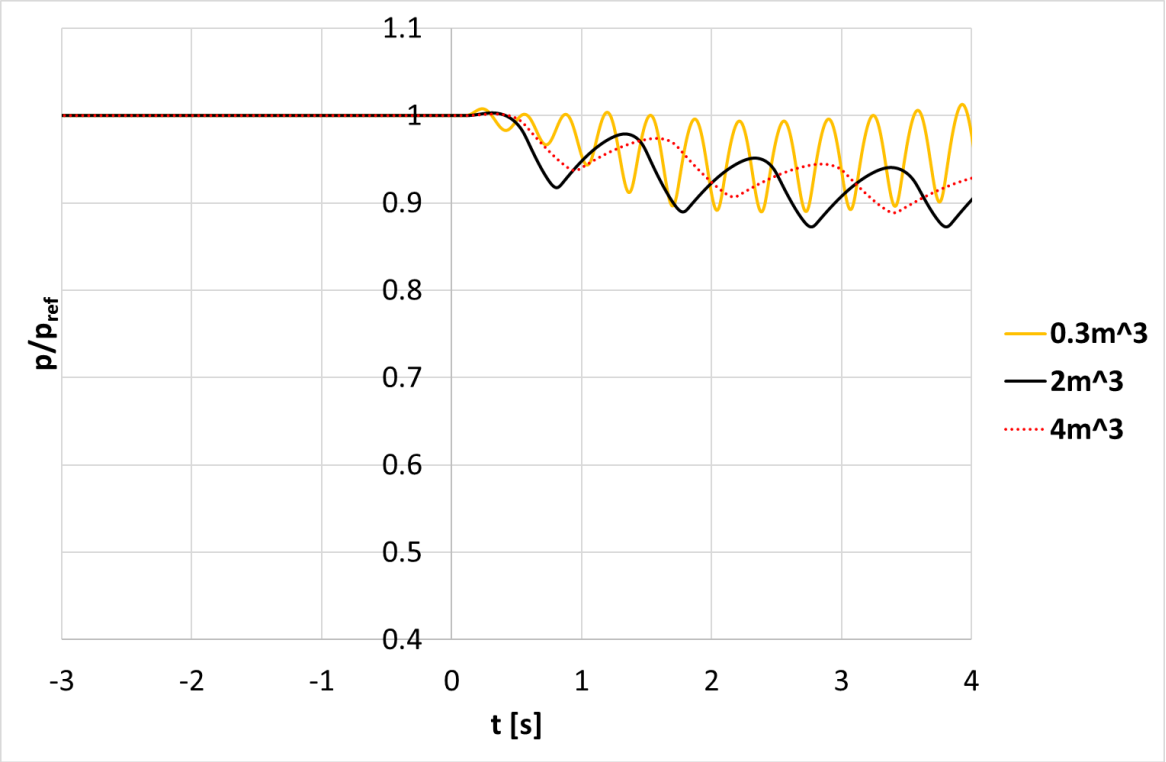

Figure 116: Simulated results, pressure oscillations with different volume sizes

Also in the comparison between the pressure signals the best correspondence between experimental data and simulations is obtained in the larger volumes cases. Observing the black solid lines and red dotted lines decreasing trends of the average levels of pressure during the oscillations are visible in both figures.

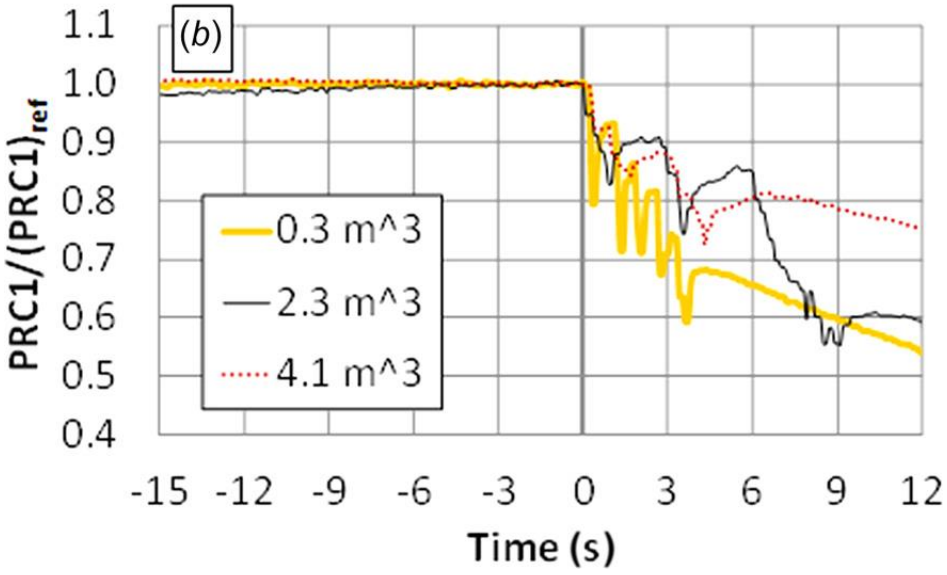

Figure 117: Experimental results, pressure oscillations with different volume sizes

7. Conclusions

This research work was immediately planned with the aim of developing a dynamic modeling method for the surge phenomenon representation applied to energy systems that foresee the coexistence of turbomachinery and energy production devices with medium-large volumes of evolving gases. Therefore, the impact of the study was not limited to the simulation of hybrid systems but to all the turbomachinery community operating with centrifugal compressors.

The intent was to study and develop an approach as lean as possible but able to guarantee the respect of physics at the base of the thermodynamic processes in real systems; for this reason, it was decided to implement the lumped-volume approach.

Depending on the case study analyzed, adaptations, integrations and dedicated extensions were necessary. However, there was a single coherent guideline divided into three phases on which the entire work was based. The three main steps that were propagated throughout the thesis work can be summarized as contributions:

- **Theoretical contribution:** use of formulas belonging to the consolidated scientific literature (i.e. Greitzer's approach etc.), with additions and extensions where necessary.

- **Experimental contribution:** experimental performance databases (ie performance maps for compressor and turbine), information on the fundamental physical quantities and geometrical characteristics of the analyzed systems (lengths, diameters, volumes etc.), references from experimental measurements (pressure drops, pressure distributions, etc.).

- **Validation:** comparison between simulated results and the experimental evidence available depending on the specific application (acoustic/vibrational acquisitions, measurements of physical quantities during steady state or transient etc.).

The layout of the thesis followed the chronological development of research activities, therefore the level of maturity of the used approach, the proposal and the development of alternative solutions and the structural complexity of the systems analyzed followed the order of the manuscript as well.

The entire work was organized on the description of the three main applications:

- T-RIG1 model (UNIGE)
- Hyper model (NETL)
- T-100 based HS Emulator model (UNIGE)

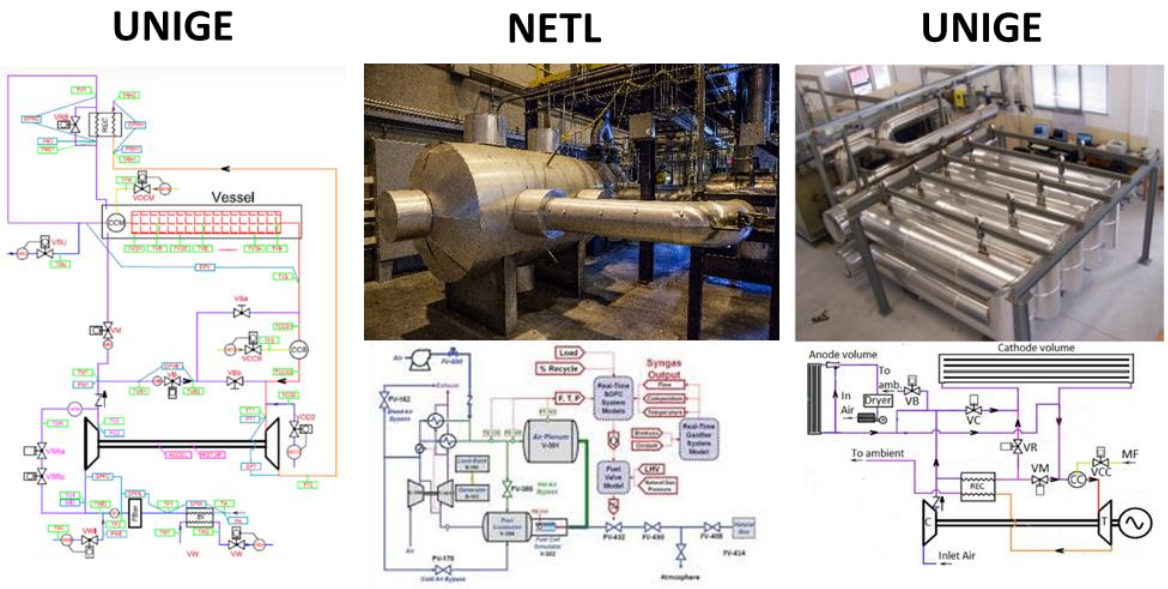

Figure 118: The three investigated emulator plants: T-RIG1 (UNIGE), Hyper (NETL), T-100 based HS Emulator (UNIGE)

The first analysis has been carried out on the T-RIG1 layout. It was constituted by a turbocharger operated in open loop, with the compressor bounded by ambient condition and the turbine being fed by hot exhausts. The two parts have independent flow paths and were not fluid-dynamically connected but their interactions were established only mechanically through the shaft. This layout was studied with the main goal to build and validate a model able to replicate surge phenomenon of a centrifugal compressor in free spool configuration.

The major outcomes from this first study can be summarized in:

- Model representation has been achieved for: compressor, turbine, shaft, discharge valve, piping and volumes. (Chapter 4.2).

- Compressor map extension towards negative flows (theoretical analysis): two different path type are proposed for Zone II; comparison between parabolic and cubic extension types. (Chapter 4.4).

- Compressor map extension towards negative flows (experimental analysis): mass flow rate and pressure acquisitions showed that, for the supplied machine, curve composed by series of operating point between surge line and no mass flow condition (Zone II) for a constant reference rotational speed of 171000rpm, well shape a parabolic trend. (Chapter 4.4.1).

- Surge frequency simulation model capability: replication of measured surge frequencies with high level of accuracy, a deviation of less than 12% could be achieved between simulation and reference measurement. (Chapter 4.6).

- Validation of the proposed time constants approach (τ-flow approach) for dynamic delays characterization of complex piping systems. (Chapter 4.3).

- Parametric study to investigate the effect of different parameters such as volume size, shaft inertia and equivalent lengths, on the surge cycles characteristics. (Chapter 4.6).

The second application was focused on a dynamic model for a Micro Gas Turbine (MGT), characterized by an intrinsic free-spool configuration, coupled to large volumes. This was inspired by an experimental facility at the National Energy Technology Laboratory (NETL) called Hyper, which emulates a hybrid MGT and Fuel Cell system. The experiment and model could simulate stable and unstable operating conditions. The model was used to investigate the effects of different volumes on surge events, and to test possible strategies to safely avoid or recover from unstable compressor working conditions. The modelling approach started from the Greitzer lumped parameter approach, and it has been improved with integration of empirical methods and simulated components to better match the real Hyper plant layout and performance. The possibility to study the impact of the interaction between the control system and the volume size on the compressor dynamic stability was one of the novelties of this model.

The main results carried out by this second application can be summarized in:

- Model representation of further components such as combustor, plenum with energy equation, by-pass valves. (Chapter 5.3).

- The impact of the size of the volume between compressor and turbine on the system stability was studied thanks to two different configurations: Vp and Vpx10 case. Generally, the model confirms that as the volume is increased the fundamental surge frequency decreases. It is remarkable how the shape of surge cycle is really volume depending, when a smaller volume was simulated an almost circular cycle is created by the compressor operating point on its map, while when a bigger volume was simulated the shape becomes more elliptical due to the predominance of flow oscillation compared to the pressure ones. This might be an important aspect for those components that suffer damage due to strong pressure fluctuations rather than flow oscillations or vice versa. (Chapter 5.6).

- Once the compressor type is fixed the surge phenomenon is influenced by the system characteristic with which it is coupled. For example, the model response suggested that as different by-pass fractional openings identified different working conditions in the stable compressor field, similarly they implied different surge types with different intensity in the compressor unstable operating field.

- Pressure, flow rate, and frequency plots during surge were analyzed comparing two different volume sizes, for cases where gas turbine shaft speed is uncontrolled (open loop) and controlled (closed loop). This suggested that in closed loop configuration it is possible that due to the establishment of several oscillating phenomena at

different frequencies, a sort of superposition of effects generates a more complex oscillating motion in systems like the one object of this study. (Chapter 5.6.1 and Chapter 5.6.2)

- The possibility to recover from a surge event acting on by pass valves was also presented both in open and closed loop configurations. (Chapter 5.6.3 and Chapter 5.6.4).

The last test rig facility object of this study was based on a commercial 100 kW recuperated MGT (Ansaldo/Turbec AE-T100) modified to be connected to a modular volume designed for physical emulation of fuel cell stack influence. The singular layout, of the plant makes its modelling particularly challenging. The presence of by-passes together with the modular arrangement of the pipes allow to operate the system in many possible different configurations. These aspects have been considered during the modelling activity in order to have a simulation tool able to capture the main features of the system.

The main activities and results obtain by this analysis are:

- As introduced, due to the modular arrangement of the system, this time constants approach (Tau flow approach) was adopted for a challenging layout, consisting of a dense network of pipes in series and parallel. (Chapter 6.1.2).

- A different method to determine the shape of the characteristic curves was proposed. A mixed procedure was adopted combining the experimental data provided by Ansaldo (performance maps) and an analytical approach used by other authors such as Gravdahl in [31]. Following the real compression equation and adding contribution due to other losses present in the real compressor stage a set of iso-speed was obtained for Zone I and Zone II. The detailed geometrical information provided by the manufacturer were integrated within this approach. Then resulting left side of the compressor map was refined to align it to the right side one (Zone III). (Chapter 6.2).

- A qualitative comparison was performed between simulations and the experimental results presented in the work [1]. The two dissertations are based on the same hardware (AE T-100 based HS Emulator). In both cases the impact of different volume sizes on the system dynamics was investigated, and in particular, the simulated and experimentally acquired system dynamic responses during surge were compared. Considering the modelling assumption and the slightly different boundary condition used during the comparison, the model confirms an exhaustive capability to faithfully represent dynamics of the real system. (Chapter 6.5.).

All the models and considerations developed in this thesis work were designed in the hope of being used, shared and improved within present and future research activities.

8. Appendix A

8.1. T-RIG1 measurement and acquisition systems

8.1.1. Mass flow measurement and control system

DELTAFLOW DF12: [14] (M1, MW, MSR, MB) is a Pitot tube, it measures the mass flow elaborated by the ducts according to the differential pressure law, Figure 119. Due to the special probe profile, the DELTAFLOW flow measurements can assure the highest level of precision and excellent process liability, even under extreme conditions. It is used to measure gas, steam and liquids in more or less all the operation conditions. This product is basically easy to be installed on the rig; it causes minimum pressure losses and is therefore highly energy efficient. The aerodynamic profile permits to obtain a constant resistance coefficient in the entire measure field.

Technical data of the two different models purchased by TPG are tabulated in Table 14.

Table 14: DELTAFLOW DF 12 technical data

Pipe size	DN20 to DN100
Connection type	Weld-in, flange stud, cutting rid stud, spool piece
Pressure range	0 to 160 bar
Temperature range	-200 to 1240 °C
Materials	1.0305, 1.4571, 1.4828, 1.4539, Hastelloy C4, Haynes Alloy, 1.5415

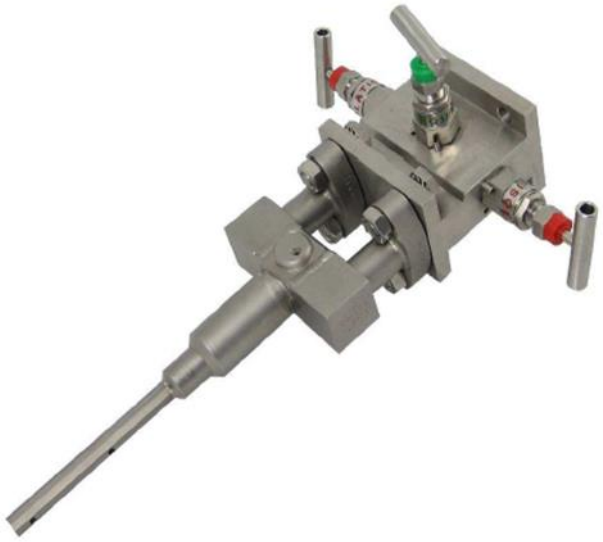

Figure 119: DELTAFLOW DF12

ROSEMOUNT 2051 DIFFERENTIAL FLOW TRANSMITTER: [15] it is a differential pressure flow transmitter designed to provide industry-standard performance to offer dependable differential pressure (DP) flow measurements. This product, matched with the previously introduced DF12, provide reliable differential, relative and absolute pressure measurement.

Table 15: ROSEMOUNT 2051 technical data

Measurement Type	Differential Pressure
Accuracy	Up to ±0.05% of span
Stability	Up to ±0.125% of Upper Range Limit (URL) for 5 years
Warranty	Up to 5-year limited warranty
Rangedown	Up To 100:1
Measurement Range	Up to 2000 psi (137.9 bar) differential
Output	Differential pressure, scaled variable
Diagnostic	Basic Diagnostic

Figure 120: ROSEMOUNT 2051 DIFFERENTIAL PRESSURE TRANSMITTER

BRONKHORST (VCCM, VCCS) EL-FLOW: is a thermal mass flow meter assembled with a modular approach. Control valves can be either integrally or separately mounted, to measure and control gas flow. This digital instrument from Bronkhorst High-Tech offer great flexibility thanks to the multi-bus concept.

Table 16: BRONKHORST EL FLOW technical data

Accuracy	Standard 0.5%Rd plus 0.1%FS
Rangeability	Digital mode up to 1:187.5
Response	Down to 500 msec
Optional Multi-gas/Multi-range functionality	Freely programmable ranges and gas types
Pressure ratings	64/100 bar (Multi-gas/Multi-range functionality up to 10 bar)
Repeatability	excellent

Figure 121: BRONKHORST EL FLOW

8.1.2. Pressure measurements

GE UNIK 5000: [16] is an incredibly flexible silicon pressure sensor solution incorporating a wide range of accuracies, outputs, temperature ranges and physical constructions. The T-RIG1 requires several of these elements differentiated for measurement field specifics, here below the number and type of sensors are listed:

Table 17: GE UNIK number of units

Pressure range [mbar]	Quantity
From 0 to 70	1 unit
From 0 to 3	1 unit
From 0 to 75	2 units
From 0 to 150	3 units

Figure 122: GE UNIK 5000

PIEZOTRONICS: This series of miniature dynamic pressure sensors is specifically designed for shock tubes and blast wave measurements and for other applications requiring very high frequency, near non-resonant response. These high frequency response time piezoelectric sensors are set at compressor inlet and outlet.

Table 18: PIEZOTRONICS technical data

Model Number	113B28	113B03
Measurement Range (+/- 5 Volt Output)	50 psi 345 kPa	15 kpsi 103,420 kPa
Useful Overrange (+/- 10 Volt Output)	100 psi [1] 690 kPa [1]	—
Sensitivity	100 mV/psi 14.5 mV/kPa	0.44 pC/psi 0.064 pC/kPa
Maximum Pressure	1 kpsi 6895 kPa	15 kpsi 103,420 kPa
Resolution	0.5 mpsi 0.0034 kPa	10 mpsi [3] 0.07 kPa [3]
Resonant Frequency	≥ 500k Hz	≥ 500k Hz
Rise Time (Reflected)	≤ 1 µsec	≤ 1 µsec
Low Frequency Response (-5 %)	0.5 Hz	—
Non-linearity	≤ 1 % [2]	≤ 1 % [2]
Acceleration Sensitivity	≤ 0.002 psi/g ≤ 0.0014 kPa/(m/s²)	≤ 0.002 psi/g ≤ 0.0014 kPa/(m/s²)
Temperature Range	-100 to +275 °F -73 to +135 °C	-400 to +400 °F -240 to +204 °C
Discharge Time Constant (at room temp)	≥ 1 sec	—
Electrical Connector	10-32 jack	10-32 jack
Housing Material	17-4 Stainless	17-4 Stainless
Diaphragm Material	Invar	Invar
Sealing	Welded Hermetic	Welded Hermetic

8.1.3. Temperature measurement

RS PRO Type K thermocouples: these sensors provide an economic solution for temperature measurement with many practical advantages for the user; moreover, these thermocouples are extremely robust, they have a fast response to temperature changes and are capable to measure over very wide temperature ranges, from cryogenics to engine exhaust. The thermocouple used in the shown test rig are K type (Chromel Alumel).

Table 19: RS PRO technical data

Accuracy	±2.5 °C
Temperature range	-40 °C to +1200 °C
L	150 [mm]

Lp	1000 [mm]
OD	3 [mm]

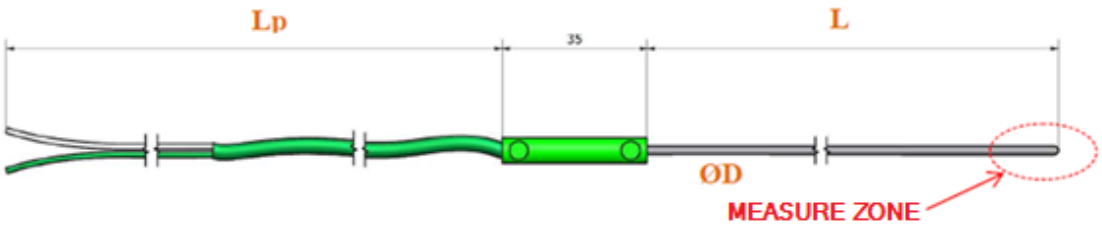

Figure 123: RS PRO thermocouple

8.1.4. Speed measurement

PICOTURN (ROT SP): [17] This instrument measures rotational speeds up to 400000rpm, it requires no modification of rotating parts, and it can sense the compressor wheel directly. It is compatible with single and two-stage turbocharger systems. It has a compact housing and a programmable number of vanes. The system has open architecture and works well stand-alone or fits easily into another measurement system.

This sensor is directly mounted rear the rotor of the compressor, it is made by a coil with ferritic center. The working principles is based on inductance: compressor rotation causes changes in the inductance of the coil; these variations are measured by the Time to Digital Converter (TDC).

Table 20: PICOTURN technical data

Rotational speed measurable	400000 [rpm]
Analog output	0.5-4.5 [V]
Digital output	TTL, 50% duty cycle
Number of programmable vanes	1-31
Compact housing	105x30x85 [mm^3]

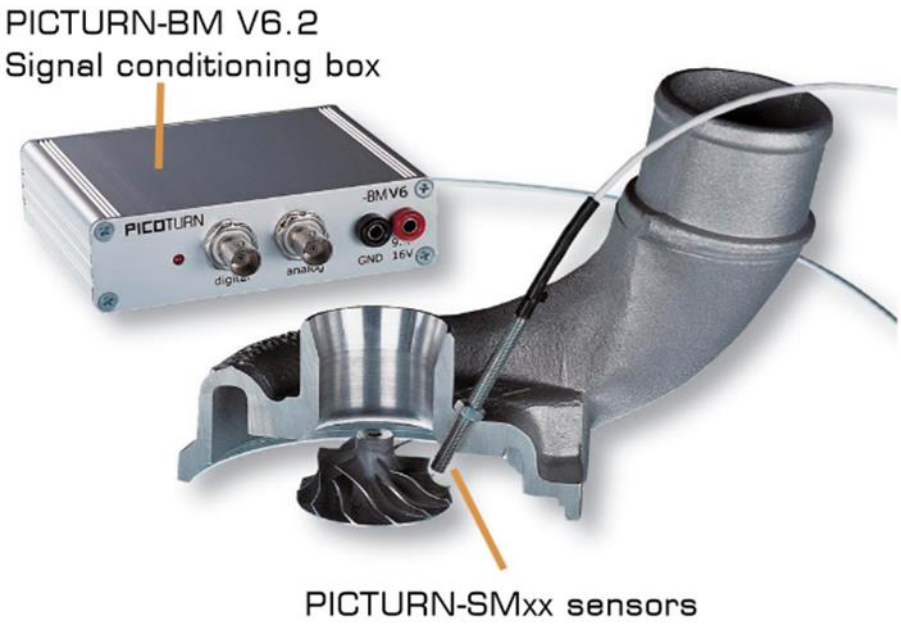

Figure 124: PICOTURN

8.1.5. Data acquisition and processing system

In order to monitor, control, record and post-elaborate the physical magnitude of interest, it is necessary to use a multi-channel data acquisition system. Starting from the sensor the processing system translates the physical quantities in electrical signals, it amplifies and perform the signal conditioning before to transfer the parameter to the software. The chosen system is CompactRIO (cRIO-9004), it is a real-time embedded industrial controller made by National Instruments for industrial control system. The Compact RIO system is a combination of a real-time controller chassis, reconfigurable IO Modules (RIO) an FPGA module and an Ethernet expansion chassis. CompactRIO controllers can be programmed with LabVIEW

Figure 125: NI cRIO – 9004 with chassis for I/O modules

8.1.6. Acoustic and vibration measurement

Vibration and acoustic measurements were conducted using a Siemens Scadas mobile data acquisition system Figure 126, which allows to acquire 8 different channels with frequencies up to 204.8 kHz sampling rate per channel, at the same time. It offers versatile signal-conditioning and data-acquisition capabilities. Designed for high measurement, this product is one of the most powerful system in its class. Siemens SCADAS Mobile becomes a dedicated modular front-end for vibration control applications.

Structural measurements were performed using mono and tri-axial accelerometers located on the compressor side of the turbocharger. Sensor dynamic characteristics allowed investigating the frequency signals up to 10 kHz.

Table 21: Siemens SCADAS Mobile technical data

Channels	8
Dynamic range	150 dB
Sampling rate per channels	Up to 204.8 kHz
Battery autonomy	2.5 hour

Figure 126: Siemens SCADAS Mobile data acquisition system

Different type of sensors are used for experimental investigation during this work, here is reported the list of their main technical characteristics.

PCB Piezotronics 356A15: [18] it is a triaxial accelerometer powered by simple constant-current signal conditioner, these sensors are easy to operate and interface with signal analysis, data acquisition and recording instruments. This particular sensor is a Platinum Stock Product with high sensitivity.

This accelerometer is mounted on compressor cochlea in order to acquire the vibration components on three directions:

- X=Tangential component
- Y=Radial component
- Z=Axial component

Table 22: PCB Piezotronics 356A15 technical data

Sensitivity	(±10%) 100 mV/g (10.2 mV/(m/s^2))
Measurement Range	±50 g pk (±490 m/s^2pk)
Broadband Resolution	0.0002 g rms (0.002 m/s^2rms)
Frequency Range	(±5%) 2 to 5000 Hz
Electrical Connector	1/4 -28 4-Pin

Figure 127: PCB Piezotronics 356A15

PCB Piezotronics 352C33 [19]

Table 23: PCB Piezotronics 352C33

Sensitivity	(±10%) 100mV/g (10.2 mV/(m/s^2))
Measurement Range	± 50 g pk (±490 m/s^2) pk
Broadband Resolution	0.00015 g rms (0.0015 m/s^2rms)
Frequency Range	(±5%) 0.5 to 10000 Hz
Weight	0.20 oz (5.8 g)

Figure 128: PCB Piezotronics 352C33

PCB Piezotronics 393B04 [20]

Table 24: PCB 393B04 technical data

Sensitivity	(±10%) 1000mV/g (102 mV/(m/s^2))
Broadband resolution	0.000003 g rms (0.00003 m/s^2rms)
Measurement range	± 5 g pk (±49 m/s^2) pk
Frequency range	(±5%) 0.06 to 450 Hz
Electrical connectors	10-32 Coaxial Jack

Figure 129: PCB Piezotronics 393B04

PCB Piezotronics 353B03 [21]

Table 25: PCB 353B03 technical data

Sensitivity	(±5%) 10mV/g (1.02 mV/(m/s^2))
Broadband resolution	0.003 g rms (0.03 m/s^2rms)
Measurement range	± 500 g pk (±4905 m/s^2) pk
Frequency range	(±5%) 1 to 7000 Hz
Weight	0.38 oz (10.5 g)

Figure 130: PCB Piezotronics 353B03

G.R.A.S. 25CA ½" CCP Standard Preamplifier with BNC Connector: [22] G.R.A.S 25CA preamplifier is a small, robust unit optimized for acoustical measurement with condenser microphone. The casing is made of stainless steel for maximum strength and durability with minimal sensitivity to vibrations.

Table 26: G.R.A.S. 25CA ½" technical data

Frequency range	2.5 Hz – 200 kHz
Noise	1.8 µV
Gain	-0.30 dB
Special feature	General purpose

Figure 131: G.R.A.S. 25CA ½"

Brüel & Kjær Piezoelectric Charge Accelerometer TYPE 4374: [23] 4374 is a subminiature planar shear accelerometer with extremely low weight and high resonance frequency. It features an integral side cable that terminates with a 10–32 UNF connector and is mounted on the test object with an adhesive. The housing material is titanium. Brüel &

Kjær Piezoelectric Charge Accelerometer TYPE 4374 is used for high-frequency vibration testing and analysis in confined spaces and on delicate structures.

Table 27: Brüel & Kjær TYPE 4374 Accelerometer technical data

Frequency range	2.5 Hz – 200 kHz
Noise	1.8 µV
Gain	-0.30 dB
Special feature	General purpose

Figure 132: Brüel & Kjær Piezoelectric Charge Accelerometer TYPE 4374

Brüel & Kjær Piezoelectric Charge Accelerometer TYPE 4393: [24] 4393 is a miniature accelerometer with a low weight and small size characterized by and high resonance frequency. Accelerometer 4393 has an M3 side connector and an M3 threaded hole for mounting. Brüel & Kjær Piezoelectric Charge Accelerometer TYPE 4393 is used for high-level and high-frequency measurements so that it is perfect for shock measurements on delicate structures.

Figure 133: Brüel & Kjær Piezoelectric Charge Accelerometer TYPE 4393

G.R.A.S SOUND AND VIBRATION.40AE ½": [25] it is a prepolarized free-field microphone for measuring medium sound pressure levels at medium frequencies. G.R.A.S

40AE is a high precision electret condenser microphone and it is optimized for free-field measurement with a 12 dB increase of the sensitivity. This instrument has been located near the compressor's inlet duct section

Table 28: G.R.A.S. SOUND AND VIBRATION 40 AE ½" technical data

Frequency range	3.15 Hz to 20 kHz
Dyn range	15 dB(A) to 148 dB
Sensitivity	50 mV/pa

Figure 134: G.R.A.S. SOUND AND VIBRATION 40 AE ½"

9. Appendix B

9.1. Helmholtz resonator

Helmholtz resonators are particular reverberant cavities created by Hermann von Helmholtz in 1860 for study sound and its perception. A Helmholtz resonator is a container of gas (usually air) with an open neck, the characteristic dimensions are, as depicted in Figure 135 the length of the neck L, the volume of the container V and the neck flow through area.

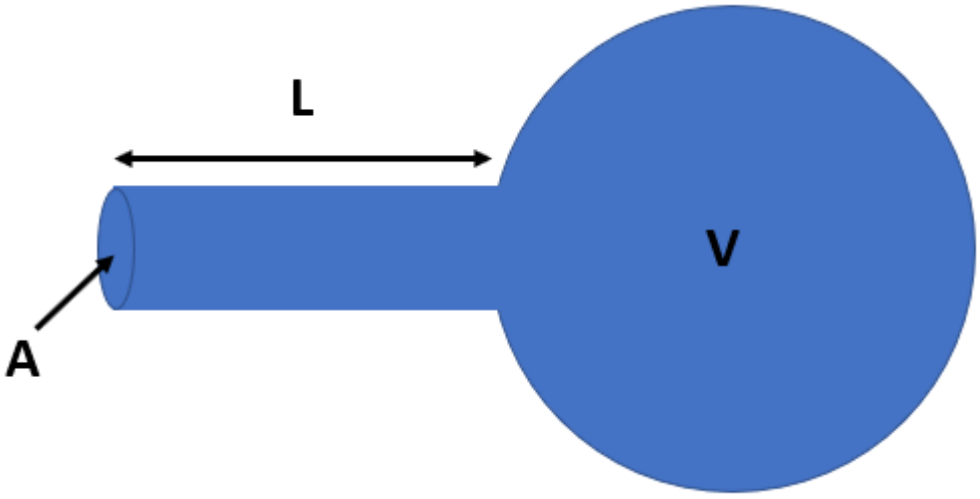

Figure 135: Helmholtz resonator

When an external air jet pulls the air contained in the resonator neck inside the volume, its pressure increases, and it tends to expand it back to its original volume, but, when air gets to its original position, its inertia takes it on outside the neck for a small distance. This rarifies the air inside the body, which then sucks the lump of air back in again. This phenomenon can be simply emulated by a mass-spring system where mass tally with mass of air contained in the neck and the spring constant is referable to system inertia dependent by the volume ratio between the container and the neck.

First of all, we assume that the wavelength of the sound produced is much longer than the dimensions of the resonator, in that way pressure drops inside volume are negligible and flow oscillation are described by a single frequency component. Therefore, the oscillation curve is a perfect sine curve.

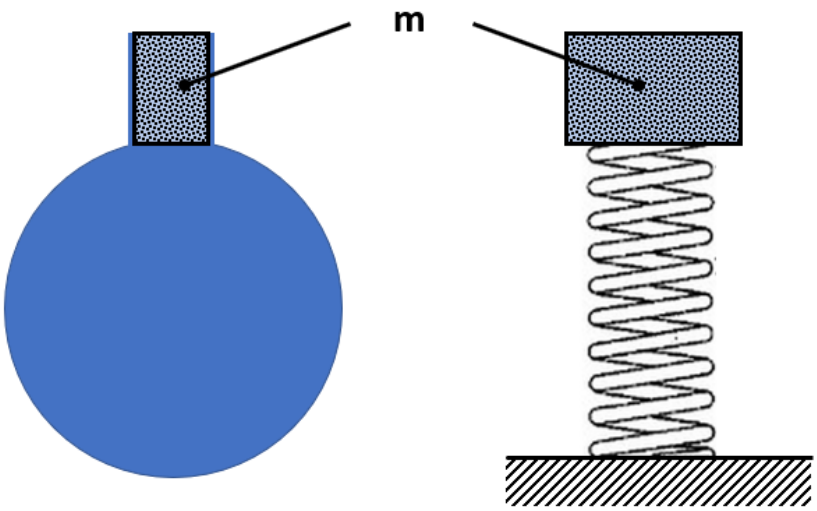

Figure 136: Helmholtz resonator dynamic model

In Figure 136 is described the dynamic model that emulates the Helmholtz resonator, resonator neck contains a quantity of air with an approximated mass equal to neck volume multiplied per air density.

$$m = v\,\rho = AL\rho \tag{110}$$

Where:

$\rho =$ air density

A = Neck flow through area

L = Neck length

Figure 137 helps to understand the physic behind the Helmholtz resonator operating and equations consequently listed.

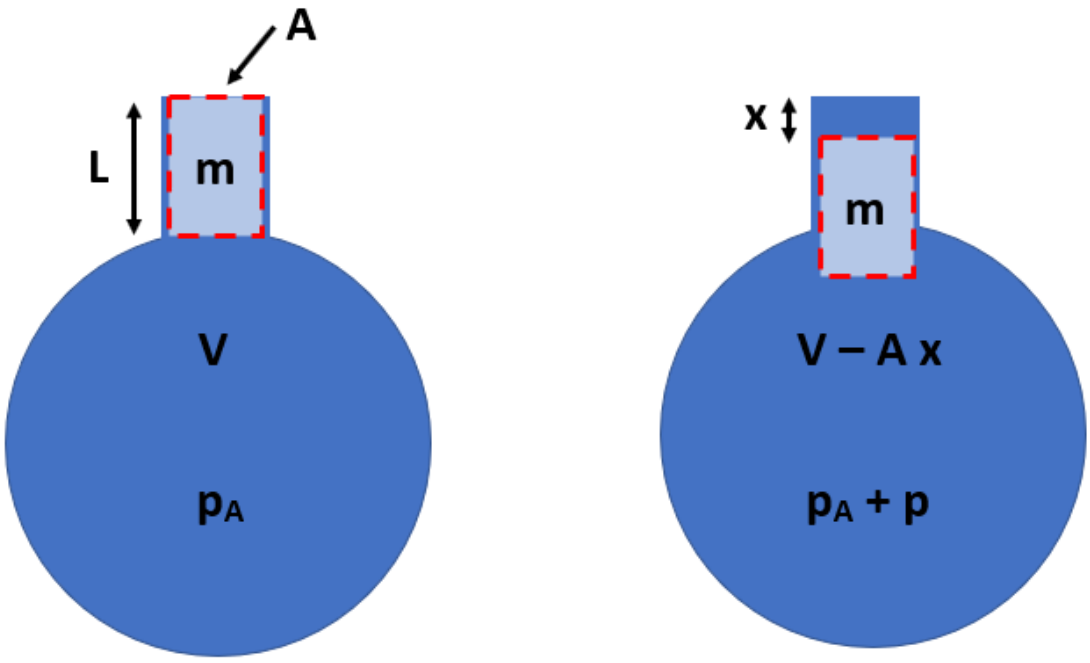

Figure 137: Helmholtz resonator operating

When this small quantity of air descends inside the volume for a x distance, it compresses the air that previously occupied the container volume producing an increase in its pressure that pass from an atmospheric magnitude to a $(p_a + p)$ value. Vibrations like the one that rises in Helmholtz resonator cause an increase in temperature, which determines a larger rise in pressure compering to the one bound to the volume reduction.

Pressure change p produced by a small volume change ΔV is:

$$\frac{p}{p_a} = -k\frac{\Delta V}{V} = -k\frac{A\,x}{V} \tag{111}$$

k is the specific heat ratio, as known as polytrophic exponent; since system is adiabatic, and heat has no time to move, its value is constant, and it is about 1.4 for air.

As air is moved by the difference of pressure between atmosphere and container volume, Newton law can be written in the form:

$$F = ma \tag{112}$$

$$F = \rho v\frac{d^2x}{dt^2} \tag{113}$$

$$\frac{p\,A}{\rho\,A\,L} = \frac{d^2x}{dt^2} \tag{114}$$

$$-k\frac{p_a A}{\rho\,V\,L}x = \frac{d^2x}{dt^2} \tag{115}$$

But, considering the spring physics, it is also true that:

$$-\frac{Kx}{m} = a = \frac{d^2x}{dt^2} = -k\frac{p_a\,A}{\rho\,V\,L}x \tag{116}$$

Helmholtz defines resonator frequency as below.

$$f = \frac{1}{2\pi}\omega_H = \frac{1}{2\pi}\sqrt{\frac{K}{m}} = \frac{a}{2\pi}\sqrt{\frac{A}{V\,L}} \tag{117}$$

9.2. Slip factor

In a dynamic compressor, typically a centrifugal one, the slip factor indicates the measurement of the fluid slip in the impeller. The fluid slip manifests itself as a variation of the angle at which the flow leaves the impeller with respect to the blade solid angle. If on the one hand this phenomenon is almost negligible in axial compressors, it is a rather important aspect in centrifugal machines. This parameter plays an important role in determining the work input to the flow, and more precisely it is widely used to estimate the energy transfer between machine and fluid.

Due to the difference in pressure and velocity between the trailing and leading faces of the impeller blades there is a reduction in the output whirl velocity, which is a measure of the compressor net power.

In literature there are many factors accounting for slip factor [43]:

- Relative eddy.
- Back eddy.
- Impeller design or geometry
- Mean blade loading.
- Thickness of blade.
- Finite number of blades.
- Fluid entry conditions.
- Working fluid's viscosity.
- Effect of boundary layer growth.
- Flow separation.
- Friction forces on the walls of flow packages.
- Boundary layer blockage.

Slip factors it is typically indicated with the symbol σ and defined as the ratio between the actual and ideal values of the whirl velocity components at the exit of impeller. The ideal values can be calculated by Eq. (118) using analytical approach shown in Figure 138.

$$\sigma = \frac{V'_{w2}}{V_{w2}} \tag{118}$$

where,

V'_{w2} : Actual Whirl Velocity Component ,

V_{w2} : Ideal Whirl Velocity Component

Usually, σ varies from 0-1 with an average ranging from 0.8-0.9.

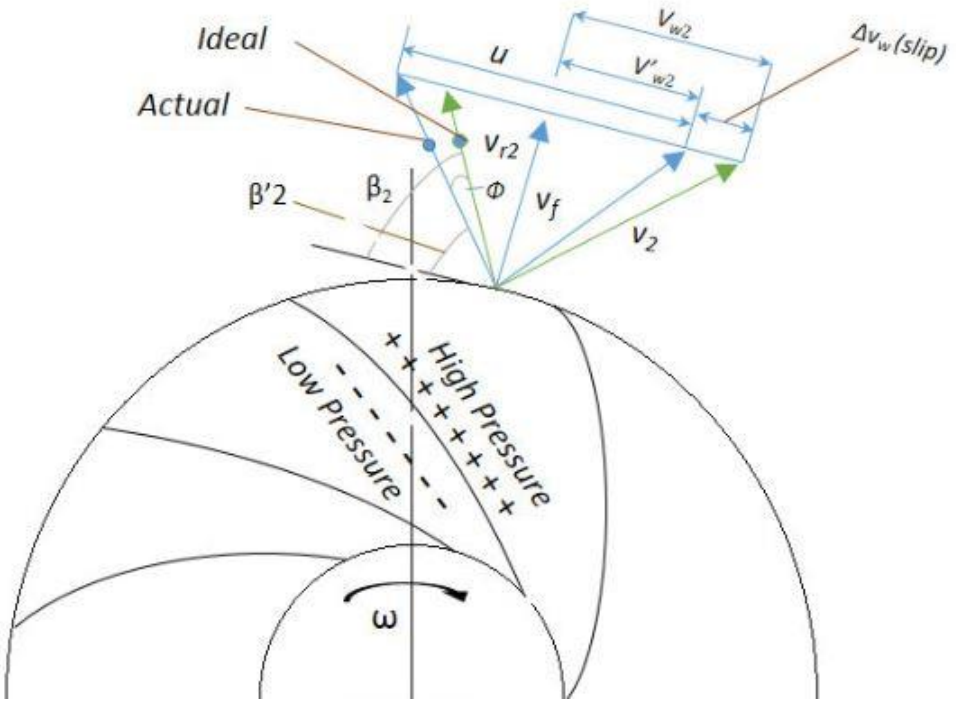

Figure 138: Velocity triangles at impeller exit, ideal and actual velocity components

Here below some of the most popular formulations used to define the slip factor are listed with reference to the authors who theorized them.

Stodola's Equation: According to Stodola, it is the relative eddy that fills the entire exit session of the impeller passage. For a given flow geometry, the slip factor increases with the increase in the number of impeller blades, thus, accounts for one of the important parameters for losses.

$$\sigma = 1 - \frac{\pi}{z} \frac{\sin \beta_2}{(1 - \phi_2 \cot \beta_2)} \tag{119}$$

where, z = number of blades and $\phi_2 = \frac{V_{r2}}{U_2}$, [44]

For Radial tip, $\beta_2 = 90°$

$$\sigma = 1 - \frac{\pi}{z} \tag{120}$$

Theoretically, In order to get the perfect ideal flow guidance, one can infinitesimally increase the number of thin vanes so that the flow should leave the impeller at an exact vane angle.

However, later experiments proved that beyond a particular value, further increase in number of blades results in reduction of slip factor due to increase in blockage area.

Stanitz's Equation: Stanitz found the slip velocity does not depend upon of the blade exit angle and hence, gave the following equation.

$$\sigma = 1 - \frac{1.98}{z\,(1 - \phi_2\ \cot\beta_2)} \tag{121}$$

where, z = number of blades,

β_2 varies from 45° to 90°.

For radial tip: β2 = 90°

$$\sigma = 1 - \frac{1.98}{z} \tag{122}$$

Balje's Equation: An approximate formula given by Balje for radial-tipped (β2=90°) blade impellers:

$$\sigma = \left(1 + \frac{6.2}{z\,n^{\frac{2}{3}}}\right)^{-1} \tag{123}$$

where, z = number of blades, and

$$n = \frac{D_{tip\ impeller}}{D_{tip\ eye}} \tag{124}$$

10. Appendix C

10.1. Bio-HyPP vessel: concept design and technical specifications

As already mentioned, various activities carried out during these three years of PhD are closely connected and integrated within the European Project Bio-HyPP, among them the candidate was involved supporting the activity of design and development of the hybrid system emulator based on turbocharger that the university of Genoa is called to realize at the university campus of Savona. A special focus is posed here to present details concerning the design of the pressure vessel realized for the containment and emulation of a SOFC type pressurized fuel cell.

10.1.1. Emulator test rig general test rig

The plant layout and other information can be found in the published paper [42].

This test rig was designed to obtain the coupling of a turbocharger (the GT1238Z machine) with a pressure vessel, as in the real SOFC bio-fuelled plant. In this introduction, abbreviations and nomenclature refer to Figure 139. For this reason, the tank designed to emulate the stack was located between the recuperator (REC) outlet duct (cold side) and the turbine inlet line. Moreover, to generate conditions similar to SOFC operations, the vessel is including a combustor (CCM) fed by natural gas and inert ceramic materials (20 mm diameter alumina spheres). So, the SOFC emulation is obtained considering the following solutions: (i) appropriate volume size to generate a similar fluid dynamic behavior, (ii) the CCM to release the electrochemical reaction heat, (iii) the inert ceramic materials for the thermal capacitance emulation. A further component, necessary for the cell system emulation, is the CCS burner fed by natural gas. Although it is the start-up combustor, it was designed also for emulating the off-gas burner (OGB) of the real plant. The rig layout (Figure 139) was designed to consider a cooling system for the external vessel zone with the air flow from the compressor. The rig will also include additional devices with the following specific functions: (i) CO2 injection line (managed by the VCO2 valve) to generate the effects of a biogas fuel on the turbine, (ii) a bleed line including recirculation at the compressor inlet duct (managed by VSRa and VSRb valves) for tests on surge prevention, (iii) a compressor/turbine bypass line with two different options (managed by VB, VBa and VBb valves) for turbocharger speed control reasons, (iv) a recuperator bypass line (managed by VRB) for fuel cell heating emulation, (v) a start-up line (managed by VSU valve) for injecting compressed air during the turbocharger start-up phase, (vi) a water injection line (managed by VWI valve) for humidification of compressor inlet flow, (vii) an air/water heat exchanger for compressor inlet temperature control and (viii) a check valve (optional) to prevent mass flow rate backflow in case of surge events.

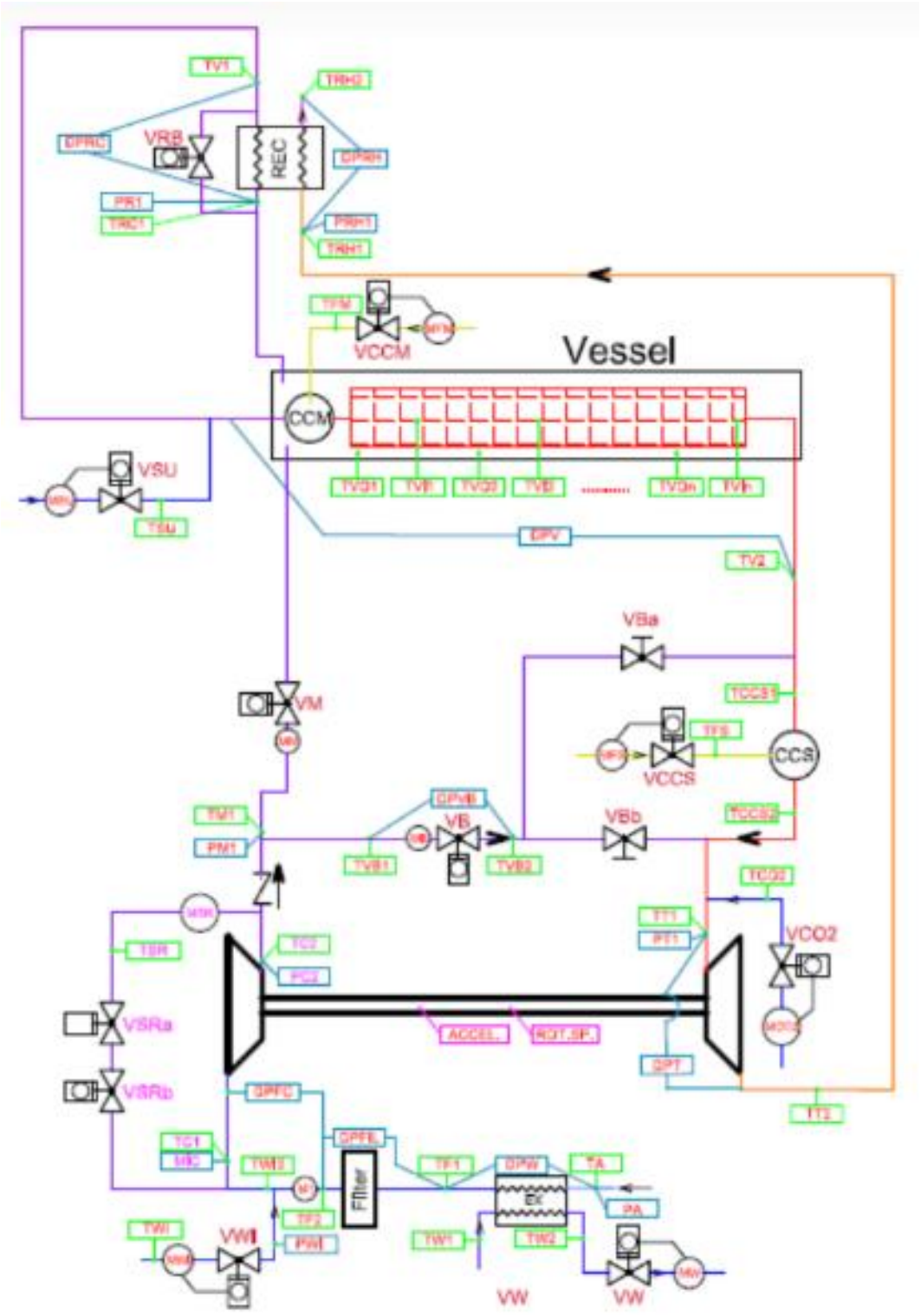

Figure 139: Emulator test rig layout

The pressure vessel was designed considering a three-skin layout Figure 140. This approach is essential to obtain a high temperature internal zone (about 860°C), including the ceramic material with is exposed to flow at low temperature conditions. This is a sort of insulation for avoiding the high costs of special alloys and for reducing the thermal loss.

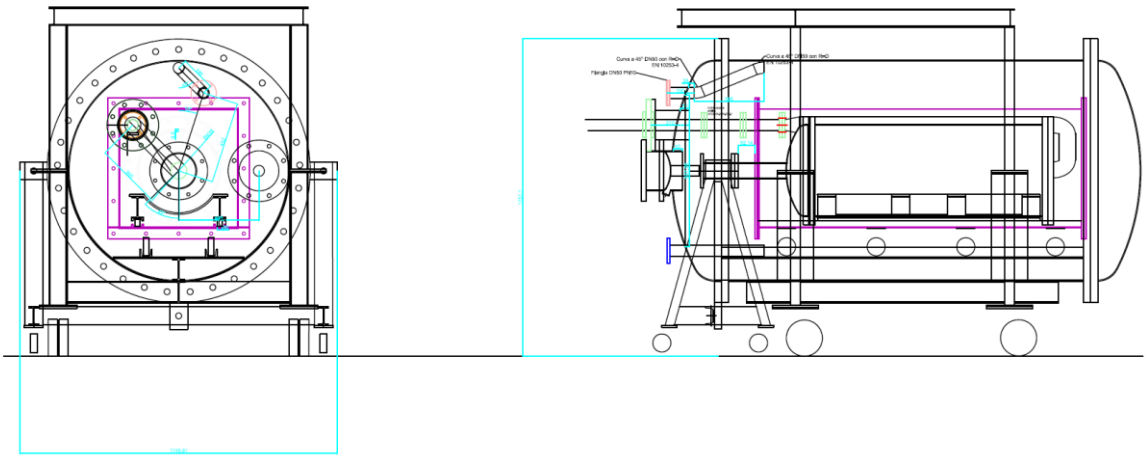

Figure 140: overall view of the three-skin pressure vessel

In this document are summarized the main steps that allowed the design of the pressure vessel and its internal components. It is important to underline that the temperature containment problem has been decoupled by the one for the pressure containment. The external case is designed to resist mainly to the working pressure while the internal components (squared pink vessel in Figure 140) address mainly the temperature containment.

10.1.2. Fuel cell emulator design

In this section the passages to obtain the final design for the fuel cell emulator are listed. It is thought as a horizontal pipe filled with approximately 530kg of ceramic spheres, each with a diameter of 2cm. This solution is chosen to emulate the thermal capacitance of a 24.5kW Solid Oxide Fuel Cell. The material taken into consideration is AISI 310 stainless steel, which is a steel suitable for high temperatures; as known, high temperatures significantly lower the value of the Young's module E, generating structural collapses for much more modest stress than those tolerable at ambient temperature.

The mechanical characteristics as a function of temperature are provided by Outokumpu Stainless Steel together with the performance tables, interpolating it is possible to obtain the value of E at a temperature of 860 ° C, the design temperature for this application.

It is necessary to proceed to the structural verification of the steel tube subjected to compression at high temperature condition; since the radius of the alumina spheres is much lower than the radius of the tube it is possible to approximate the problem using the Hertz theory.

The dimensions for the emulator pipe are:

- Inner diameter 438mm
- Thickness 9.5mm
- Length 1315mm

A standard pipe is chosen to keep the emulator as much cost effective as possible.

Assuming that the load has a uniform distribution on the entire lower half of the pipe, knowing the area of the semi-cylindrical surface projected on the plane orthogonal to the line of action of the weight of the structure it is possible to derive the contact pressure dividing the total load by this projected area.

This calculated stress must be lower than the corresponding creep rupture strength at 860°C. The reference values are reported in Table 29.

Table 29: Creep Rupture strength for 100000hours for different temperatures

Creep rupture strength, $R_{km,100\,000}$ MPa (mean values), according to EN 10095 — Table 5b

Steel grade	Temperature °C												
	500	550	600	650	700	750	800	850	900	950	1000	1050	1100
4948*	192	140	89	52	28	15							
4878			65	36	22	14	10						
153 MA™		160	88	55	35	22	14	8	5	3	1.7		
4833			65	35	16	10	7.5	5	3				
4828			65	35	16	10	7.5	5	3				
253 MA®		160	88	55	35	22	15	11	8	5.5	4	3	2.3
4845			80	33	18	11	7	4.5	3				
4841			80	33	18	11	7	4.5	3				

*values according to EN 10028-7

It is calculated a yield stress equal to 0.011MPa, which is way lower than the corresponding value reported in Table 29.

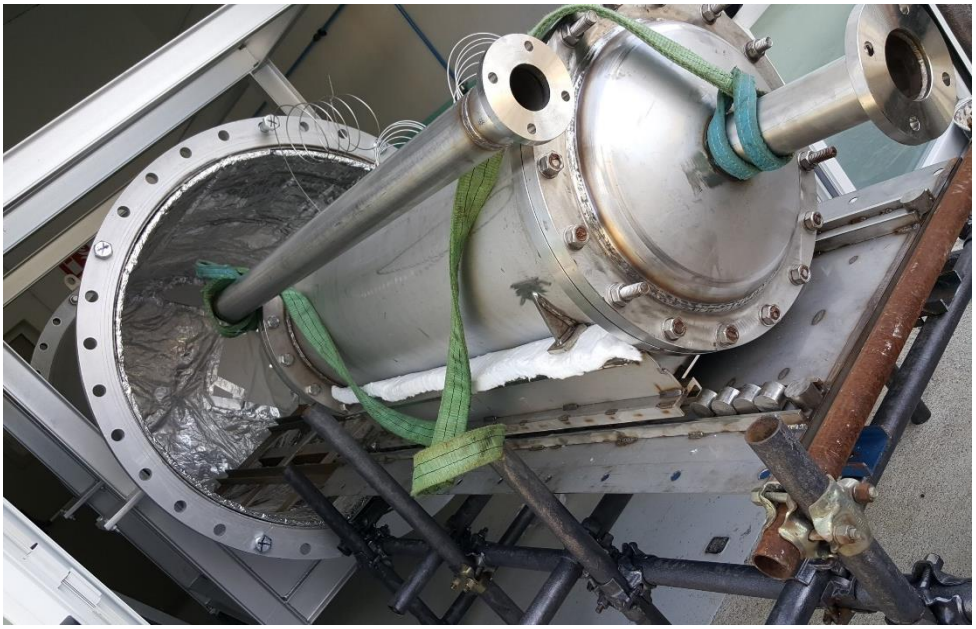

Figure 141: Pressure vessel, fuel cell emulator and thermal vessel base during installation procedure

10.1.3. Supports for the fuel cell emulator

To support the fuel cell emulator, a semi-circular bed consisting of a saddle made from semi-tube portions suitably cut and bent is proposed, the material chosen is still the AISI 310 for its mechanical properties for high temperature applications. Once the size of all the components of the support have been defined, the length of the saddle, function of the angle θ, has been verified, calculating the projected area on which the entire load will insist.

The procedure proceeded as usual with a precautionary approach, the first check carried out is the compression under hot conditions, in fact the system is static and therefore the only stresses that must be considered are: the weight of the structure supported by the supports and obviously the temperature factor that decreases the resistance of the material.

Having performed a thermodynamic study on thermal losses and evaluated the temperature value of the saddle with the presence of the insulating layer, the temperature of the material to be considered is T = 546 ° C.

At this temperature the calculated stress on the component results lower than the corresponding yield stress.

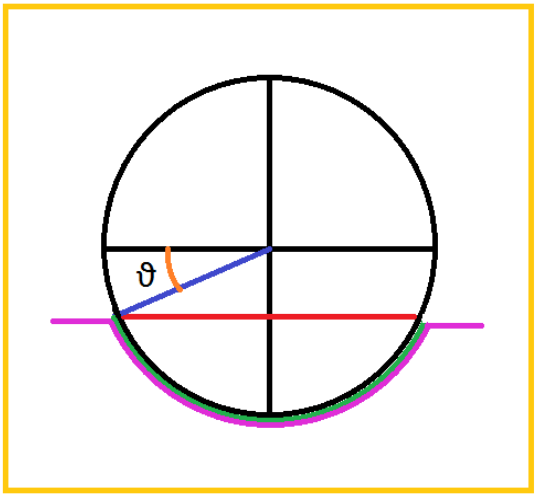

Figure 142: Sketch of the supporting saddle for the fuel cell emulator

The saddle will be folded at the ends where IPE 120mm beams (Figure 143) will be placed. The distribution of the load on the new surfaces was calculated and the verification of elastic instability on the shank of the beam was carried out.

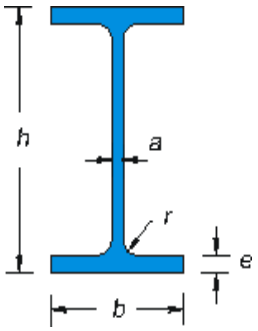

Figure 143: Detail of a IPE beam

Table 30: IPE beams dimensions

h mm	**b** mm	**a** mm	**e** mm	**r** mm	**Weight** kg/m	**Cross section** cm^2
80	46	3,8	5,2	5	6,0	7,64
100	55	4,1	5,7	7	8,1	10,32
120	64	4,4	6,3	7	10,4	13,21
140	73	4.7	6,9	7	12,9	16,43
160	82	5,0	7,4	9	15,8	20,09

A parameter to check is the stress distributed on the IPE beams, for a more conservative choice we analyze the most critical point, i.e. the shank of the beam.

Once again, after the calculation of the stressed area and of the overall stress imposed on this element, the current calculated stress results lower than the yield stress at the same working temperature.

For the fuel cell emulator movement, a solution has been adopted which provides for the superimposition of two UPN beams arranged one upside down with respect to the other, to create a track as shown by Figure 145 in which the rollers can rotate to allow the pipe to slide easily into its final seat.

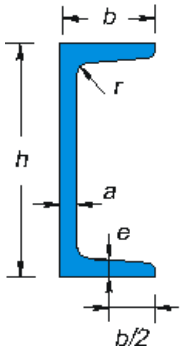

Figure 144: Detail of a IPE beam

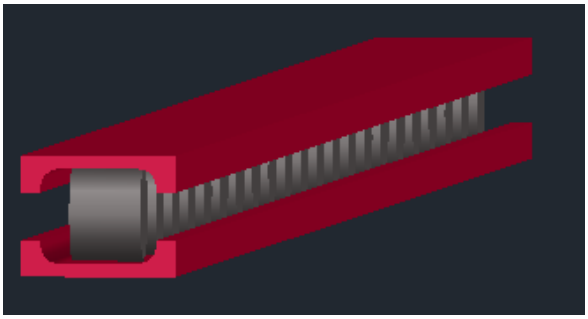

Figure 145: Rail for the fuel cell emulator movement

The UPN beans must be slightly modified to allow the movement of the rollers, dimensions of the original and modified versions are reported in Table 31.

Table 31: UPN dimensions, original and modified

	Original UPN [mm]	Modified UPN [mm]
h	65	65
b	42	15.5
a	5.5	5.5
e	7.5	7.5

The same verification procedure has been followed for the supporting metallic sheet and beams. In this case due to a lower working temperature estimated around 236°C, it is possible to switch to AISI 321.

The wheels chosen are RoCarr 710/84 wheels, visible in Figure 146, which are centered and therefore are the best solution for a symmetrical load distribution that avoids bending moments. These wheels have been chosen for their high temperature range of application.

Figure 146: Rocarr 710/84 symmetric wheels

The final supporting architecture is visible in Figure 147.

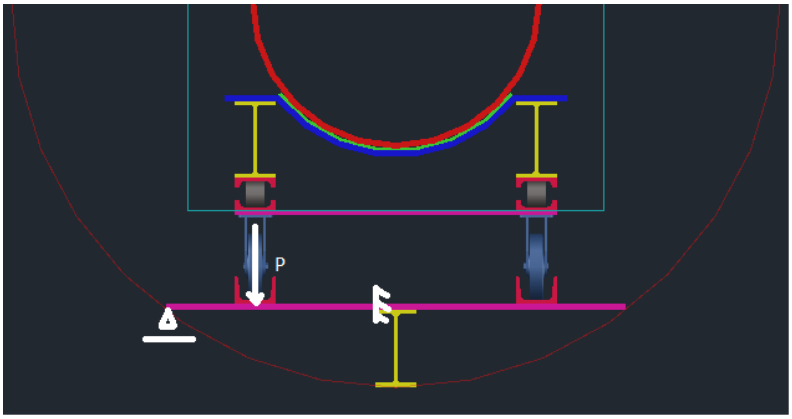

Figure 147: Layout of the modular supporting structure

Where the half portion of the bottoming part of the support has been imagine as in Figure 148 to perform a verification under static conditions.

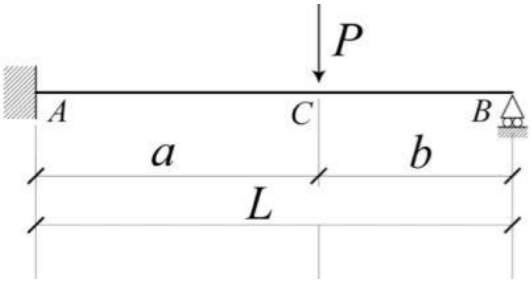

Figure 148: Bending stress model

Figure 149: Base of the thermal vessel on wheels, front view

Figure 150: base of the thermal vessel on wheels, side view

Figure 151: Picture taken during vessel assembling procedure, pressure vessel (in the back), insulated saddle on the internal vessel base (in the front)

10.1.4. Pressure vessel design procedure

This activity started with the choice of the steel necessary for the construction of the external tank. The priorities and at the same time the limits provided by the project were the thickness and dimensions of the external container. The activity concerned the analysis of the classifications of the steels according to the type of use and directing the research on specific steels for pressure vessels. The research began by interfacing with companies specialized in steels for boilers and pressure vessels.

The result of the research led to the choice of the material P275NH, this material meets the resistance requirements required for this use. Below are reported the main material characteristics.

Comp. chimica

Secondo UNI EN 10028-3

Elemento	Al	B	C	Ceq	Cr	Cu	Mo	Mn	N
Min.	0,02							0,80	
Max			0,16		0,30	0,30	0,08	1,50	0,012

Elemento	Ni	Nb	P	S	Si	Sn	Ti	V	Zr
Min.									
Max	0,50	0,05	0,025	0,015	0,40		0,03	0,05	

Propr. meccaniche

Secondo UNI EN 10028-3

Spessore nominale (mm)	≤ 16	> 16
Carico di snervamento (MPa)	≥ 275	≥ 265

Spessore nominale (mm)	16< t ≤ 60
Resistenza alla trazione (MPa)	390-510

Figure 152: P275NH information provided by Sidastico website

The required thickness is calculated from equation (82) valid for cylindrical shells (it corresponds to Eq.7.4-1 from UNI 13445_3)

$$e = \frac{P \,.\, Di}{2.f.z - P} \tag{125}$$

Where:

- P calculation internal pressure. The design pressure condition is 4 bar (0.4MPa)
- Di internal diameter equal to 1200mm.
- f nominal design stress. For the calculation of this parameter the standard reports two possible procedures, both are meant for "steels other than austenitic, as per 6.3 of UNI_13445_3: alternative route A<30%" where A is the rupture elongation. Equation (126) is used in the case of operation under normal conditions and the equation (127) in the case of 'exceptional load cases', which refers to operation in more stressing conditions with variations in events such as explosions and temperature increases.

$$f = fd = \min\left(\frac{Rp0.2/_{T}}{1{,}5}, \frac{Rm/_{T.amb}}{2{,}4}\right) \tag{126}$$

$$f = f_{exp} = f_{test=}\left(\frac{R_{p0,2/T}}{1{,}05}\right) \tag{127}$$

it has been decided to consider the most extreme case and to consider the possibility of possible temperature increases, in this way a more precautionary calculation is obtained compared to what will be the actual working conditions of the system. The

selected temperature, 400 ° C, is the maximum for which measurements and tests have been carried out on P275NH steel type and corresponds to a value of $R_{p0.2}$ equal to 156 MPa.
Table 32 reports data coming from the web database of company Salzgitter Flachstahl, these values are valid for thickness values ≤ 16 mm, [45].

Table 32: 0.2% proof strength at different temperatures for P275NH

T [°C]	50	100	150	200	250	300	350	400
$R_{P0,2}$	266	250	232	213	195	179	166	156

- z joint coefficient

Table 33: Joint Coefficient and corresponding testing group

Z	1	0.85	0.7
Testing Group	1.2	3	4

A value equal to 1 is chosen, it represents the more conservative case used also for exceptional and testing conditions.

The thickness calculation returns a value below 2mm.

The thickness given by this section is the minimum. Thickness may have to be increased at junction with other components, or to provide additional reinforcement at nozzles or openings, or to carry non-pressure loads.

A security factor of 2.5 is chosen so the final adopted thickness is **5mm**.

10.1.5. Torispherical ends

In this section the design of the end without holes is addressed. It was decided to adopt a torispherical geometry to match the need to have a compact geometry together with not excessive thickness (as it would have happened choosing a flat end).

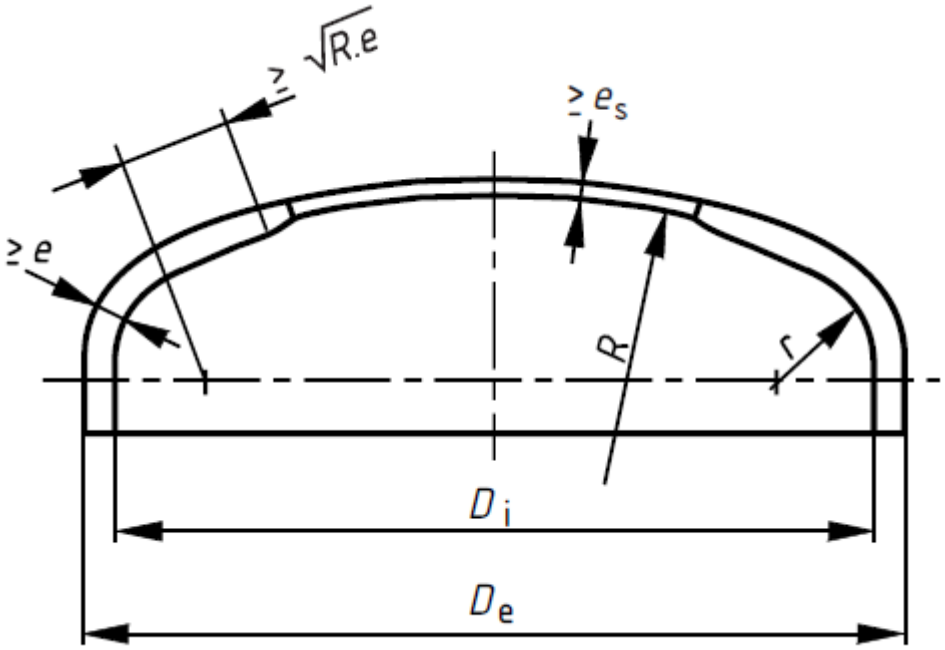

Figure 153: Geometry of torispherical end – from UNI 13445-3

The design procedure starts checking the condition of applicability for equations reported on UNI 13445_3.

The design started by setting a value for inside spherical radius of central part of torispherical end equal to $R=D_i=1200mm$.

All the following required conditions are met at the end of the iterative design procedure.

$$r \leq 0.2\ D_i \quad \textbf{(128)}$$

$$r \geq 0.06\ D_i \quad \textbf{(129)}$$

$$r \geq 2\ e \quad \textbf{(130)}$$

$$e\ \leq 0.08\ D_e \quad \textbf{(131)}$$

$$e_a\ \geq 0.001\ D_e \quad \textbf{(132)}$$

$$R\ \leq D_e \quad \textbf{(133)}$$

The required thickness e shall be the greatest between the required thickness of end to limit membrane stress in central part e_s, the required thickness of knuckle to avoid axisymmetric yielding e_y and the required thickness of knuckle to avoid plastic buckling e_b defined as follows

$$e_s = \frac{P.R}{2f.z - 0.5P} \quad \textbf{(134)}$$

$$e_y = \frac{\beta\ P\ (0.75R + 0.2D_i)}{f} \quad \textbf{(135)}$$

$$e_b = (0.75R + 0.2Di)\left[\frac{P}{111f_b}(Di/r)^{0.825}\right]^{\left(\frac{1}{1,15}\right)} \quad \textbf{(136)}$$

Where β is found from Figure 154 or the procedure in Equations (137) - (145) replacing e by e_y.

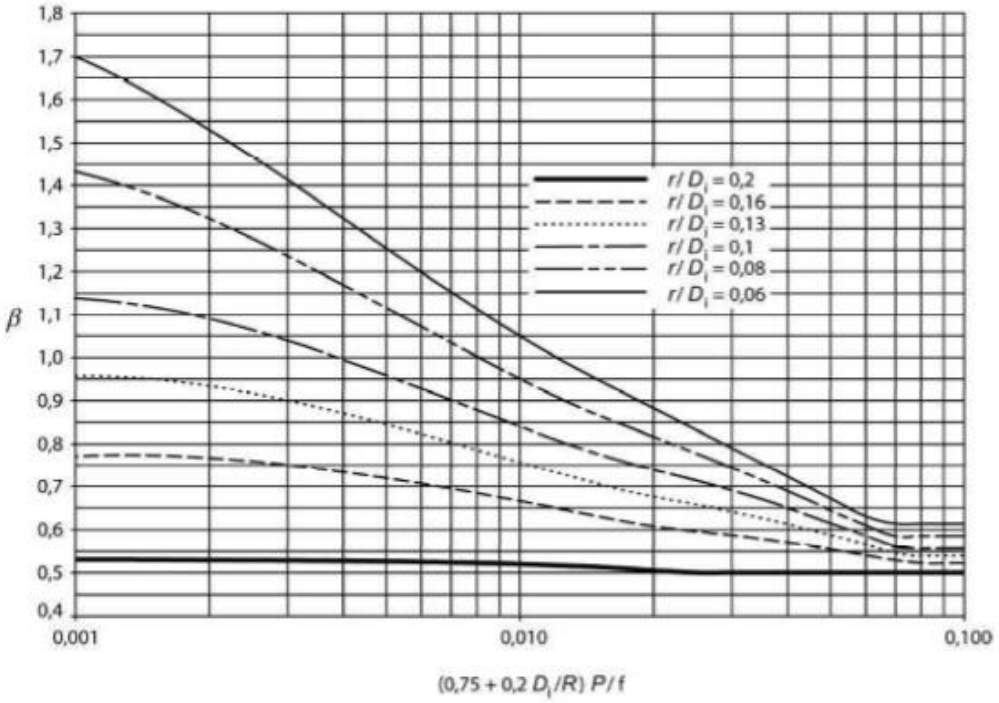

Figure 154: Parameter β for torispherical end – from UNI 13445-3

$$Y = \min\left(\frac{e}{R}\ ; 0.04\right) \quad \textbf{(137)}$$

$$Z = \log_{10}\left(\frac{1}{Y}\right) \quad \textbf{(138)}$$

$$X = \frac{\mathrm{r}}{D_i} \quad \textbf{(139)}$$

$$N = 1.006 - \frac{1}{(6.2 + (90\,Y)^4)} \quad \textbf{(140)}$$

For X = 0.06

$$\beta_{0.06} = N(-0.3635Z^3 + 2.2124Z^2 - 3.2937Z + 1.8873) \quad \textbf{(141)}$$

For 0.06<X<0.1

$$\beta = 25\{(0.1 - X)\beta_{0.06} + (X - 0.06)\beta_{0.1}\} \quad \textbf{(142)}$$

For X=0.1

$$\beta_{0.1} = N(-0.1833Z^3 + 1.0383Z^2 - 1.2943Z + 0.837) \quad \textbf{(143)}$$

For 0.1<X<0.2

$$\beta = 10\{(0.2 - X)\beta_{0.1} + (X - 0.1)\beta_{0.2}\} \quad \textbf{(144)}$$

For X=0.2

$$\beta_{0,2} = MAX\{0.95(0.56 - 1.94Y - 82.5Y^2); 0.5\} \quad \textbf{(145)}$$

Equation (134) returns a thickness of e_s = 1.616mm.

The impact of the inside radius of curvature of the knuckle r on the e_y calculation is then analyzed. Varying the value of r between 24cm and 12cm. It is clear how the resulting thickness increases as the radius decreases. The values obtained with the use of the graph are reported in Table 34.

Table 34: Influence of r on e_y graphical procedure

e_y [mm]	R [cm]	β
1.6574	24	0.54
2.271	19	0.74
3.284	12	1.07

The calculation using the formulas to obtain β do not highlight significant differences as

Table 35: Influence of r on e_y analytical procedure

e_y [mm]	R [cm]	β
1.53	24	0.5
2.18	19	0.712
3.16	12	1.03

Among the three required thicknesses the values of e_b turn out to be the highest.

Table 36: Values for e_b varying R

e_b [mm]	R [cm]
2.31	24
2.61	19
3.38	12

The final thickness for this end is chosen equal to **5mm**.

For this type of end a hub of 40mm is calculated following the specifications of UNI 13445-3. This will help during the manufacturing phase.

10.1.6. Flanges

Flanges represent in this case a constrain for the design because they are usually produced according to established standards, they are available in different dimensions and for predefined ranges of application.

UNI EN 1092-1 (before UNI 2276-67) is the reference standard for flat flanges.

Depending on the required size and on the design pressure of the application the type of flange is defined. The range of pressure of interest available in the standards is 2.5-10bar, among these the PN6 category is chosen. This type of flanges is designed for a slightly higher pressure (6bar); therefore, this choice ensures a further security margin to the overall design.

The standard does not specify the type of material used, indicates the generality of the family of usable material, limiting itself to specifying that they belong to the category of weldable steels as the one chosen in this case, P275NH.

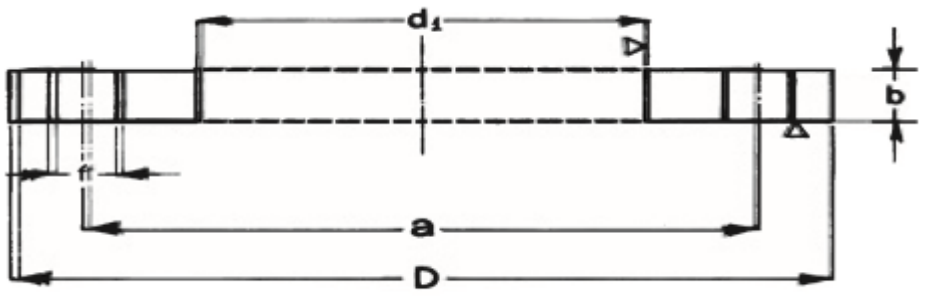

Figure 155: Flat flange cross section – from UNI 13445-3

Table 37: Sizing Chart for circular flanges in accordance with UNI EN 1092-1

DN	Ø TUBO		d_1		a	D	b	f	VITI	N. FORI	Kg.
	DIN	ISO	DIN	ISO							
10	13,5	17,2	14,0	17,5	50	75	10	11	M10	4	0,29
15	20,0	21,3	20,5	22,0	55	80	10	11	M10	4	0,33
20	25,0	26,9	25,5	27,5	65	90	12	11	M10	4	0,50
25	30,0	33,7	30,5	34,0	75	100	12	11	M10	4	0,61
32	38,0	42,4	38,5	43,0	90	120	14	14	M12	4	1,05
40	44,5	48,3	45,0	49,0	100	130	14	14	M12	4	1,23
50	57,0	60,3	58,0	61,5	110	140	14	14	M12	4	1,35
65	76,1		77,0		130	160	14	14	M12	4	1,68
80	88,9		90,0		150	190	16	18	M16	4	2,63
100	108,0	114,3	109,0	115,5	170	210	16	18	M16	4	2,92
125	133,0	139,7	134,5	141,0	200	240	18	18	M16	8	3,90
150	159,0	168,3	160,5	170,0	225	265	20	18	M16	8	4,78
200	219,1		221,0		280	320	22	18	M16	8	6,91
250	267,0	273,0	269,0	275,0	335	375	24	18	M16	12	9,04
300	323,9		326,0		395	440	24	22	M20	12	12,1
350	368,0	355,6	370,5	358,0	445	490	26	22	M20	12	17,0
400	419,0	406,4	422,0	409,0	495	540	28	22	M20	16	20,1
450	457,2		460,2		550	595	28	22	M20	16	25,8
500	508,0		511,0		600	645	30	22	M20	20	30,0
600	609,6		612,6		705	755	30	25	M22	20	37,9
700	711,2		714,2		810	860	32	25	M22	24	47,9
800	812,8		815,8		920	975	34	30	M27	24	62,9
900	914,4		917,4		1020	1075	36	30	M27	24	74,6
1000	1016,0		1019,0		1120	1175	36	30	M27	28	81,9
1200	1220,0		1224,0		1340	1405	38*	33	M30	32	–
1400	1420,0		1424,0		1560	1630	40*	36	M33	36	–
1600	1620,0		1624,0		1760	1830	42*	36	M33	40	–
1800	1820,0		1824,0		1970	2045	44*	39	M36x3	44	–
2000	2020,0		2024,0		2180	2265	46*	42	M39x3	48	–

DN is the reference diameter which in this case is 1200 mm. However, the real inner diameter of the flange requires a slight modification to the diameter of the cylindrical part of the vessel. To reach the value of 1220 mm (actual value that corresponds to the DN1200) the diameter of the vessel and consequently of the torispherical end have been increased by 10 mm.

The thickness calculations are verified with the new values showing limited difference compared to the previous results.

Table 38: New calculated values for minimum thickness

	e_b [mm]	e_s [mm]	e_y [mm]	R [cm]
New	2.33	1.6165	1.6602	24
Previous	2.31	1.616	1.6574	24

R is the same because it still satisfies the requirement to be less than or equal to the value of D_e.

10.1.7. Openings

An opening is considered isolated if the following condition is satisfied:

$$L_b \geq a_1 + a_2 + l_{so1} + l_{so2} \quad \textbf{(146)}$$

Where a_1 and a_2 are shown in Figure 156 while l_{so1} and l_{so2} are calculated according to

$$l_{so} = \sqrt{(2r_{is} + e_{c,s})\, e_{c,s}} \quad \textbf{(147)}$$

Where, for torispherical ends, r_{is} is equal to R (1200mm) and $e_{c,s}$ the assumed thickness (5mm).

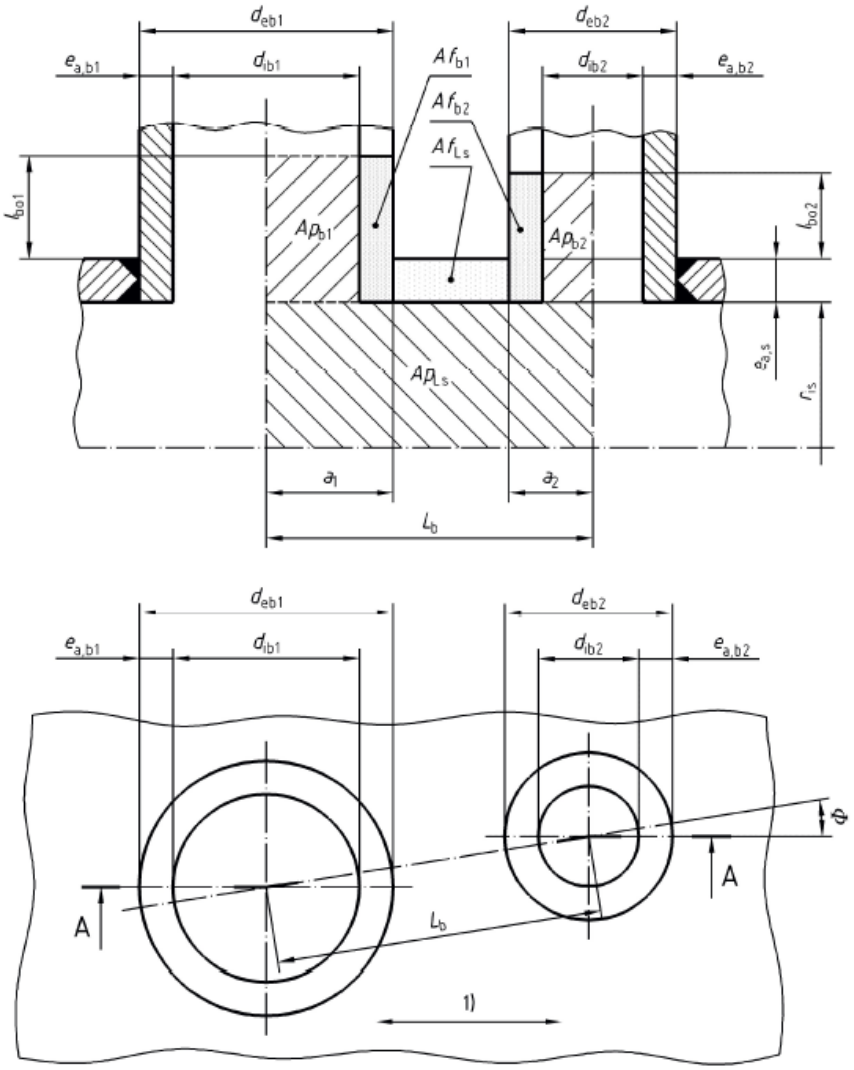

Figure 156: Ligament check of adjacent nozzles normal to a cylindrical shell – from UNI 13445-3

Since Lb = 0.1675m is lower than the RHS in equation (146) (0.413m), openings cannot be considered isolated.

Therefore equation (148) for isolated openings as for section 9.5.2.1.1 in UNI 13445-3 has to be satisfied

$$(Af_s + Af_w)(f_s - 0.5P) + Af_p(f_{op} - 0.5P) + Af_b(f_{ob} - 0.5P) \geq P\left(Ap_s + Ap_b + 0.5Ap_\varphi\right) \quad \textbf{(148)}$$

Moreover, standard in this case requires the calculation for multiple openings, section 9.6 of UNI 13445-3 page 115, where in our case a ligament check is needed, which, according to Figure 156, is satisfied if the following equation is met.

$$(Af_{Ls} + Af_w)(f_s - 0.5P) + Af_{b1}(f_{ob1} - 0.5P) + Af_{p1}(f_{op1} - 0.5P) + Af_{b2}(f_{ob2} - 0.5P) + Af_{p2}(f_{op2} - 0.5P) \geq P\left(Ap_{Ls} + Ap_{b1} + 0.5Ap_{\varphi 1} + Ap_{b2} + 0.5Ap_{\varphi 2}\right) \quad \textbf{(149)}$$

The calculation procedure returns for equation (148) that: LHS = 0.126 > 0.002 = RHS

And for equation number (149): LHS = 0.21 > 0.178 = RHS

According to this procedure every single opening must have a distance from each other greater than 33.5 cm.

Figure 157: Pressure vessel with torispherical ends

10.1.8. Squared ends and flanges

The design of the square-shaped flanges has followed the references indicated by various suppliers, among these, the indications found on the *Guru Gautam Steels* website [46], section *Squared Flanges*, were used. The website has provided the basis for the sizing of both the flanges and of the square background.

Since there is almost no pressure difference between the inner and the outer sides of this vessel, all the flanges and squared ends are designed with a thickness of 10mm, which is the minimum value suggested by the standard. It is important to specify that even if this is the lowest value of thickness reported in the standard, there is a wide security margin left for this application.

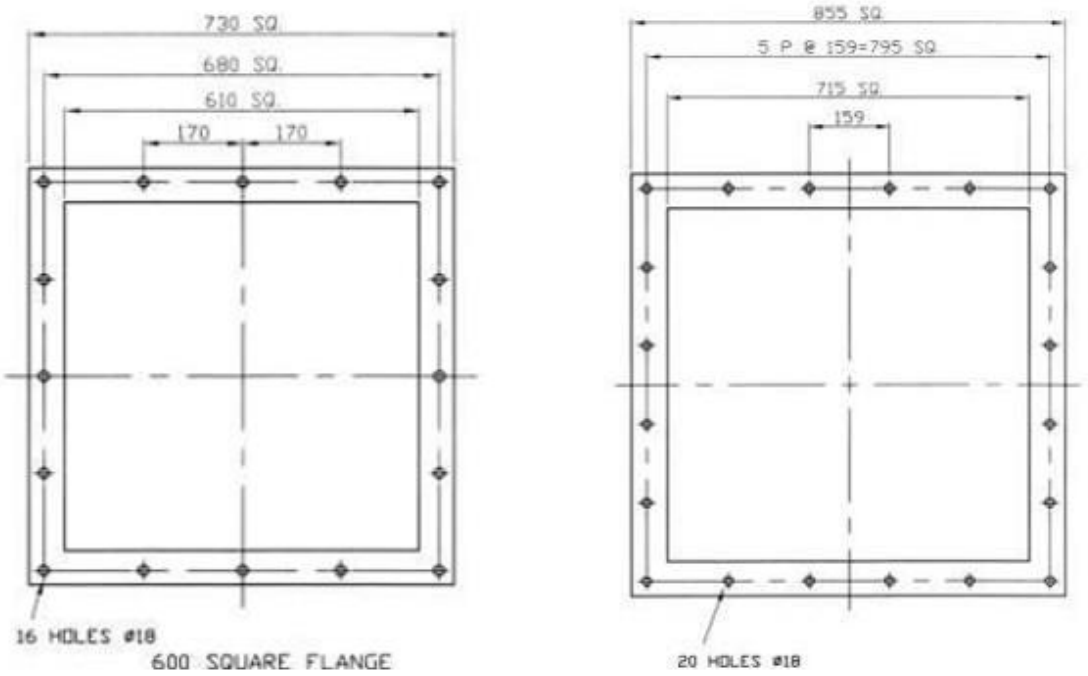

Figure 158:Example of squared flanges from the company Guru Gautam Steels

The squared end has the following dimensions:

- Side equal to 780mm
- Thickness 10mm
- 16 holes for bolts with diameter equal to 18mm
- Material: AISI 321

The squared flanges have the following dimensions:

- Inner side 660mm
- Outer side 780mm
- 16 holes for bolts with diameter equal to 18mm
- Material: AISI 321

Figure 159: Upper and side parts of the thermal squared vessel

10.1.9. Summary of technical specifications

Table 39: Final dimensions and characteristics for the Bio-HyPP vessel

Component	Specifications	Dimensions [mm]	Material	Quanti ty
External vessel without flanges (Pressure vessel)	Cylindric geometry with circular cross section	-Inner diameter: 1210 -Outer diameter: 1220 -Thickness:5 -Length:2040	P275NH	1
Internal vessel without flanges (Thermal vessel)	Cylindric geometry with squared cross section	-Inner side: 650 -Outer side:654 -Thickness: 2 -Length: 1800	AISI 321	1
Fuel cell emulator pipe (Thermal capacitance containment)	Cylindric geometry with circular cross section	-Inner diameter: 438 -Outer diameter: 457 -Thickness:9,5 -Length: 1315	AISI 310	1

Ceramic spheres (Thermal capacitance)		-Diameter: 20	ALUMINA	
Insulation layer	Saddle with constant radius of curvature	-Inner diameter: 457 -Outer diameter: 462 -Thickness: 5 -Length: 1200	Ceramic fiber	1
Supporting metallic saddle	Saddle with constant radius of curvature with side extension	-Inner diameter: 462 -Outer diameter: 481 -Thickness: 9,5 -Length: 1200	AISI 310	1
IPE beams	Supports for saddle	-h: 120 -b: 64 -a:4,4 -e: 6,3 -r: 7 -length: 100	AISI 310	2
UPN beams	Track for rollers	-h:65 -b: 15,5 -a: 5,5 -e: 7,5 -length: 1415	AISI 310	4

Rollers (obtained from rods)	To facilitate the movement of the inner vessel	-Diameter: 40 -Length: 30	AISI 310	44
Reinforcing plates	Sheet to fix the two UPN beams to the inner vessel	-Length: 504.94 -Width:100 -Thickness: 5	AISI 321	4
Cast iron wheels	Wheels for high temperature application h13	-Total height: 132 -Guaranteed load: 200 kg -Wheel width: 30	GHISA	8
UPN beams	Track for cast iron wheels	-h: 65 -b: 42 -a: 5,5 -e:7,5 -length: 2000		2
Reinforcing plates		-Length: 720 -Larghezza: 100 -Spessore: 10		6
IPE beams		-h: 120 -b: 64 -a:4,4 -e:6,3 -length: 2000		1
Flanges for inner vessel (thermal vessel)	Squared geometry	-Inner side: 660 -Outer side: 780 -Width: 60 -Thickness: 10	AISI 321	2

Inner vessel end 1	Squared flat end with openings	-Side: 780 -Thickness: 5 -number of openings: 2 -Opening diameter: 40 -number of holes for bolts: 16 -Diameter of openings for bolts: 18	AISI 321	1
Inner vessel end 2	Squared flat end	-Side: 780 -Thickness: 5 - number of holes for bolts: 16 - Diameter of openings for bolts: 18	AISI 321	1
Flanges for outer vessel (pressure vessel)	Circular geometry	-Inner diameter: 1224 -Outer diameter: 1340 -Thickness: 40 -number of holes for bolts: 32 -Bolts type: M30	P275NH	2
Pressure vessel end 1	Torispherical end with openings (UNI 13445-3)	-Inner diameter: 1210 -Outer diameter: 1220 -Thickness: 5 -number of holes for bolts: 32 -Diameter of holes for bolts: 33	P275NH	1

		-Hub length: 40 -R=1200 -number of openings: 5 (compressor delivery DN50, recuperator delivery DN50, recuperator return DN200, delivery to turbine DN150, instrumentation DN50) -Holes diameter: 1xDN200, 1xDN150, 3xDN50		
Pressure vessel end 2	Torispherical end (UNI 13445-3)	-Inner diameter: 1210 -Outer diameter: 1220 -Thickness: 5 -number of holes for bolts: 32 -Diameter of the holes for bolts: 33 -Hub length: 40 -R=1200	P275NH	1

11. References

[1] M. L. Ferrari, P. Silvestri, M. Pascenti, F. Reggio, A.F. Massardo, 2018, "Experimental Dynamic Analysis on a T100 Microturbine Connected With Different Volume Sizes", Journal of Engineering for Gas Turbines and Power, 140(2), 021701.

[2] M. L. Ferrari, 2015, "Advanced control approach for hybrid systems based on solid oxide fuel cells", Applied Energy, 145, 364-373.

[3] P. Pezzini, D. Tucker, A. Traverso, 2013, "Avoiding compressor surge during emergency shutdown hybrid turbine systems", Journal of Engineering for Gas Turbines and Power, 135(10), 102602.

[4] M. L. Ferrari, A. Traverso, A. F. Massardo, 2016, "Smart polygeneration grids: Experimental performance curves of different prime movers", Applied Energy, 162, 622-630.

[5] U. M. Damo, M. L. Ferrari, A. Turan, A. F. Massardo, 2015, "Test rig for hybrid system emulation: New real-time transient model validated in a wide operative range", Fuel cells, 15 7-14.

[6] N. A. Cumpsty, "Compressor Aerodynamics", 1989 , Krieger Publishing Company, Malabar, Florida.

[7] D. A. Fink, N. A. Cumpsty, E. M. Greitzer, 1992, "Surge dynamics in a free spool centrifugal compressor system", Journal of Turbomachinery 114, 321-322.

[8] G. Bartolini, A. Muntoni, A. Pisano, E. Usai, 2008, "Compressor surge active control via throttle and CCV actuators. A second-order sliding-mode approach. In Variable Structure Systems", VSS'08 International Workshop on (pp. 274-279), IEEE.

[9] J. S. Simon, L. Valavani, A. H. Epstein, E. M. Greitzer, 1992, "Evaluation of approaches to active compressor surge stabilization", International Gas Turbine and Aeroengine Congress and Exposition (pp. V001T01A065-V001T01A065), ASME American Society of Mechanical Engineers.

[10] M. L. Ferrari, P. Silvestri, F. Reggio, A. F. Massardo, 2018, "Surge prevention for gas turbines connected with large volume size: Experimental demonstration with a microturbine", Applied Energy, Vol.230, 1057–1064.

[11] P. Pezzini, S. Celestin, D. Tucker, 2015, "Control Impacts of Cold-Air Bypass on Pressurized Fuel Cell Turbine Hybrids", Journal of Fuel Cell Science and Technology, 12(1), 011006.

[12] E.M. Greitzer, "Surge and Rotating Stall in Axial Flow Compressors", 1976, Journal of Engineering for Power, 98.2, 190-211.

[13] A. Traverso, "TRANSEO code for the dynamic performance simulation of micro gas turbine cycles", 2005, ASME Paper GT2005-68101.

[14] Deltaflow DF12 Data Sheet: https://www.systec-

controls.de/files/deltaflow_df12_data_sheet_rev1_2__december_2010__1.pdf
[15] Rosemount 2051 Pressure Trensmitter Product Data Sheet: https://www.emerson.com/documents/automation/product-data-sheet-rosemount-2051-pressure-products-en-73206.pdf
[16] UNIK 5000 Data Sheet: https://www.gemeasurement.com/sites/gemc.dev/files/unik_5000_series_datasheet_italiano.pdf
[17] PICOTURN rotational speed sensor Data Sheet: https://www.pmt-fl.com/picoturn/picoturn-rotational-speed-sensor
[18] PCB Piezotronics 356A15 Data Sheet: https://www.pcb.com/contentstore/docs/PCB_Corporate/Vibration/Products/Manuals/356A15.pdf
[19] PCB Piezotronics 352C33 Data Sheet: https://www.pcb.com/contentstore/docs/pcb_corporate/vibration/products/manuals/352c33.pdf
[20] PCB Piezotronics 393B04 Data Sheet: https://www.pcb.com/contentstore/docs/PCB_Corporate/Vibration/Products/Manuals/393B04.pdf
[21] PCB Piezotronics 353B03 Data Sheet: https://www.pcbpiezotronics.fr/wp-content/uploads/2018/03/353B03.pdf
[22] GRAS 26CA ½" Data Sheet: https://www.gras.dk/products/preamplifiers-for-microphone-cartridge/constant-current-power-ccp/product/203-26ca
[23] Piezoeletric Charge Accelerometer Type 4374 Data Sheet: https://www.bksv.com/doc/Bp2038.pdf
[24] Piezoeletric Charge Accelerometer Type 4393 Data Sheet: https://www.bksv.com/doc/bp2043.pdf
[25] GRAS 40AE microphone Data Sheet: https://www.gras.dk/products/product/ss_export/pdf2?product_id=150
[26] W. Jiang, J. Khan, R.A. Dougal, 2005, "Dynamic Centrifugal Compressor Model for System Simulation", Journal of Power Sources, 158, 1333-1343.
[27] G. L. Arnulfi, P. Giannattasio, C. Giusto, A. F. Massardo, D. Micheli, P. Pinamonti, 1999, "Multistage centrifugal compressor surge analysis: Part II-numerical simulation and dynamic control parameters evaluation", Journal of Turbomachinery, 121, 312-320.
[28] I. J. Day, E. M. Greitzer, N. A. Cumpsty, "Prediction of Compressor Performance in Rotating Stall", 1978, Journal of Engineering for Power, 100, 1-12.
[29] J.T. Gravdahl, O. Egeland, "Centrifugal compressor surge and speed control", 1999, IEEE Trans. Control Syst. Technol., 7, 567 - 579.
[30] F. K. Moore, E. M. Greitzer, 1986, "A theory of post-stall transients in axial compression systems: Part I-Development of equations", Journal of engineering for gas turbines and power, 108.1, 68-76.

[31] J. T. Gravdahl et al, 2004, "Modeling of surge in free-spool centrifugal compressors: Experimental validation", Journal of propulsion and power, 20.5, 849-857.
[32] D. Tucker, L. Lawson, R. Gemmen, 2003, “Preliminary Results of a Cold Flow Test in a Fuel Cell Gas Turbine Hybrid Simulation Facility”, ASME Turbo Expo, Atlanta, GA, June 16–19, ASME Paper No. GT2003-38460.
[33] A. Abrassi, A.Traverso, L. Ferrari, 2018, “Turbocharger-Based Hybrid Systems: Modeling and Validation of a Free Spool Subject to Compressor Surge”, ASME Turbo Expo: Turbomachinery Technical Conference and Exposition (pp. V003T06A019-V003T06A019). American Society of Mechanical Engineers.
[34] S. G. Koff, EM Greitzer, 1986, “Axisymmetrically stalled flow performance for multistage axial compressors”, Journal of Turbomachinery 108, 216-249.
[35] M. L. Ferrari, M. Pascenti, R. Bertone, L. Magistri, 2009, “Hybrid simulation facility based on commercial 100 kWe micro gas turbine”, Journal of Fuel Cell Science and Technology, 6(3), 031008.
[36] M. L. Ferrari, A. F. Massardo, 2013, “Cathode–anode side interaction in SOFC hybrid systems”, Applied energy, 105, 369-379.
[37] Turbec T100 Series 3, 2002, “Installation Handbook”.
[38] N. Watson, M.S. Janota, 1982, “Turbocharging the internal combustion engine MacMillan”.
[39] T. B. Ferguson, 1963, “The centrifugal compressor stage”, Butterworths London.
[40] A. E. Nisenfeld, 1982, “Centrifugal compressors: principles of operation and control”, Instrument society of America.
[41] R. C. Pampreen. 1973, “Small turbomachinery compressor and fan aerodynamics”, Journal of engineering for power 95, 251-256
[42] M. L. Ferrari, M. De Campo, L. Magistri, 2018, "Design and Emulation of a Turbocharged Bio-Fuelled SOFC Plant”, ASME Turbo Expo: Turbomachinery Technical Conference and Exposition. American Society of Mechanical Engineers,
[43] https://en.wikipedia.org/wiki/Slip_factor
[44] S. L. Dixon, 1978, “Fluid Mechanics, Thermodynamics of Turbomachinery”, Pergamon Press, Third Edition.
[45] https://www.salzgitter-flachstahl.de/en/products/hot-rolled-products/steel-grades/weldable-fine-grain-structural-steels-for-pressure-vessels.html
[46] https://www.gurugautamsteels.com/flange-type-square-flanges.html